Development of quality assurance procedures and methods for the CBM Silicon Tracking System

Dissertation
der Mathematisch-Naturwissenschaftlichen Fakultät
der Eberhard Karls Universität Tübingen
zur Erlangung des Grades eines
Doktors der Naturwissenschaften
(Dr. rer. nat.)

vorgelegt von
Dipl.-Phys.Ing. Evgeny Lavrik
aus Gorodowikowsk, Russland

Tübingen
2017

Gedruckt mit Genehmigung der Mathematisch-Naturwissenschaftlichen Fakultät der Eberhard Karls Universität Tübingen.

Tag der mündlichen Qualifikation:	13.11.2017
Dekan:	Prof. Dr. Wolfgang Rosenstiel
1. Berichterstatter:	Prof. Dr. Hans Rudolf Schmidt
2. Berichterstatter:	Prof. Dr. Josef Jochum

Dedicated to my family

Abstract

The Compressed Baryonic Matter (CBM) experiment at the future Facility for Antiproton and Ion Research (FAIR) aims to study the properties of nuclear matter at high net-baryon densities and moderate temperatures.

It is expected that, utilizing ultra-relativistic heavy-ion collisions, a phase transition from hadronic matter to QCD matter will be probed. Among the key objectives are the determination of the nature and order of the transition (deconfinement and/or chiral) and the observation of a critical end-point. To measure and determine the physics phenomena occurring in these collisions, appropriate detectors are required. The Silicon Tracking System (STS) is the key detector to reconstruct charged particle tracks created in heavy-ion collisions. In order to assure the necessary detector performance, about 900 silicon microstrip sensors must be checked and tested for their quality. For these tasks highly efficient and highly automated procedures and methods have to be developed.

The first part of this dissertation reports on a novel automated inspection system developed for the optical quality control of silicon microstrip sensors. Proposed methods and procedures allow to scan along the individual sensors to recognize and classify sensor defects. Examples of these defects are: surface scratches, implant defects, metalization layer lithography defects and others. In order to separate and classify these defects various image-processing algorithms based on machine vision are used. The silicon sensors are also characterized geometrically to ensure the mechanical precision targeted for the detector assembly procedures.

Since the STS detector will be operated in a high radiation environment with a total non-ionizing radiation dose up to 1×10^{14} n_{eq}/cm^2 over 6 years of operation, the silicon sensors need to be kept in the temperature range of -5 to -10 ℃ at all times to minimize reverse annealing effects and to avoid thermal runaway.

The second part of this work is devoted to the development and optimization of the design of cooling bodies, which remove the thermal energy of overall more than 40 kW produced by the front-end readout electronics. In particular, thermodynamical models were developed to estimate the cooling regimes and thermal simulations of the cooling bodies were carried out. Based on the performed calculations an innovative bi-phase CO_2 cooling system of up to 200 W cooling power was built and allowed to verify the simulated cooling body designs experimentally.

Zusammenfassung

In der geplanten Experimentieranlage für Antiprotonen- und Ionenforschung (Facility for Antiproton and Ion Research, FAIR) wird das Compressed Baryonic Matter Experiment (CBM) nukleare Materie bei hoher Baryonendichte und moderaten Temperaturen untersuchen.

Der Phasenübergang zwischen hadronischer und QCD-Materie kann mithilfe von ultrarelativistischen Schwerionenkollisionen untersucht werden. Die wichtigsten Ziele sind die Bestimmung der Art des Übergangs (Deconfinement- und/oder chiraler Phasenübergang) und die Untersuchung des kritischen Endpunktes im Phasendiagramm. Um diese Phänomene zu untersuchen, sind geeignete Detektorsysteme notwendig. Das Silicon Tracking System (STS) ist der zentrale Detektor, mit Hilfe dessen die Spuren der in den Schwerionenkollisionen erzeugten geladenen Teilchen rekonstruiert werden. Um die volle Funktionsfähigkeit des STS sicherzustellen, müssen die mehr als 900 Siliziumstreifensensoren vor dem Zusammenbau überprüft und getestet werden. Hierfür müssen die hocheffiziente und automatisierte Prozeduren und Methoden entwickelt werden.

In erstem Teil dieser Dissertation wird über ein automatisiertes optisches Inspektionssystem berichtet. Das System erlaubt es, die einzelnen Siliziumsensoren auf potentielle vorhandene Oberflächendefekte zu untersuchen und sie zu klassifizieren. Beispiele hierfür sind: Kratzer auf der Oberfläche, Implantierungsdefekte oder Lithographiedefekte der Metallisierungsschicht. Für das Erkennen dieser Defekte werden mehrere "Machine Vision" Bildbearbeitungsalgorithmen benutzt. Außerdem werden die geometrischen Parameter der Sensoren, die für den Zusammenbau des STS wichtig sind, optisch kontrolliert.

Der STS Detektor wird bei extrem hohen Kollisionsraten betrieben. Innerhalb einer Betriebsbszeit von 6 Jahren wird eine Strahlungsdosis von bis zu 1×10^{14} n_{eq}/cm^2 akkumuliert, was zu einer deutlichen Erhöhung des Dunkelstrom führt und letztlich des "end-of-life" Kriterium darstellt. Die Siliziumsensoren müssen deswegen auf -5 bis -10 ℃ gekühlt werden, um "reverse Annealing" Effekte zu minimieren und das "Thermal Runaway" Phänomen zu verzögern.

Durch die Ausleselektronik werden andererseits mehr als 40 kW an thermischer Energie nahe der Sensoren produziert, die deshalb mit Kühlkörpern komplett abgeleitet werden muß.

Das zweite Teil dieser Dissertation wurde der Optimierung von Kühlkörpern gewidmet. Dafür wurden thermodynamische Modelle implementiert und entsprechende thermische Simulationen durchgeführt. Im Rahmen der Arbeit wurde ein 200 W CO_2 Kühlungssystem gebaut, das es erlaubt, die Modellberechnungen und Simulationen einer Kühlung mit 2-phasigem CO_2 zu überprüfen.

Contents

1. Introduction **7**

2. The Compressed Baryonic Matter Experiment **9**
2.1. The FAIR facility 9
2.2. Physics of the CBM experiment 10
2.2.1. The CBM experimental setup 10
2.2.2. Physics cases 12
2.2.2.1. Study of the dense nuclear matter 14
2.2.2.2. Collective phenomena 15
2.2.2.3. Event by event fluctuations 16
2.2.2.4. Dilepton spectroscopy 16
2.2.2.5. Strangeness and charm 17

3. The Silicon Tracking System detector **19**
3.1. Silicon Microstrip Sensors 20
3.1.1. Sensor logistics 20
3.1.2. Sensor read-out 23
3.1.3. Radiation damage effects in Silicon sensors 24
3.1.3.1. Type inversion 27
3.1.3.2. Temperature dependence and thermal runaway . 31

4. Quality assurance of the detector components **33**
4.1. Silicon microstrip sensors 33
4.1.1. Optical quality assurance 33
4.1.2. Electrical quality assurance 33
4.2. Sensor microcables 35
4.3. Sensor ladders 36

5. Optical quality assurance of the silicon sensors **37**
5.1. Optical setup 37
5.1.1. Hardware and Setup 37
5.1.2. Overview of the machine vision algorithms 39
5.1.2.1. Geometrical transformations 39
5.1.2.2. Color adjustment 40
5.1.2.3. Color operators 40
5.1.2.4. Color plane extraction 40
5.1.2.5. Image filtering 42

5.1.2.6. Edge detection . . . 42
5.1.2.7. Pattern matching . . . 44
5.1.2.8. Texture matching . . . 45
5.1.2.9. Caliper . . . 46
5.1.2.10. Color thresholding . . . 46
5.1.2.11. Binary image morphology . . . 47
5.1.2.12. Particle analysis . . . 48
5.2. Optical axis calibration and characterization . . . 48
5.2.1. Distortion corrections . . . 49
Image lens distortions . . . 49
Vignetting distortion and flat field correction . . . 50
5.2.2. Focus stage . . . 52
5.2.3. Zoom stage . . . 54
Exposure time . . . 54
Parcentricity . . . 55
Parfocality . . . 57
Magnification . . . 57
Field of view . . . 59
Depth of field . . . 60
Autofocusing . . . 61
5.2.4. Summary . . . 63
5.3. Linear motor stages calibration and characterization . . . 63
5.3.1. Summary . . . 65
5.4. Silicon sensor optical inspection . . . 65
5.4.1. Acceptance criteria for silicon microstrip sensors . . . 65
5.4.2. Sensor misalignment calibration . . . 66
5.4.3. Sensor scanning . . . 67
5.4.4. Surface defect detection . . . 68
5.4.4.1. Foreign object detection . . . 69
5.4.4.2. Scratch detection . . . 69
5.4.4.3. Aluminum strip defects . . . 70
Strip metal break . . . 70
Strip metal short . . . 71
Second metal line defects . . . 72
5.4.4.4. Implant defects . . . 73
Implant strip break . . . 73
Implant short . . . 75
p-stop and p-spray strip implant defects . . . 75
Dielectric defects . . . 76
Other implant openings . . . 77
5.4.4.5. Passivation layer defects . . . 78
Passivation layer opening . . . 78
Passivation layer degradation . . . 79

Surface chips . . . 79
5.4.4.6. Defect context . . . 81
5.4.5. Sensor electrical elements inspection . . . 81
5.4.5.1. AC pads . . . 81
5.4.5.2. DC pads . . . 82
5.4.5.3. Bias resistors . . . 82
5.4.5.4. Bias ring . . . 82
5.4.5.5. Guard ring . . . 83
5.4.6. Advanced defect analysis . . . 84
5.4.6.1. Machine learning approach . . . 84
5.4.6.2. Convolutional neural networks . . . 85
5.4.6.3. Method application . . . 85
5.4.6.4. Summary . . . 89
5.4.7. Inspection results . . . 91
5.5. Sensor metrology . . . 92
5.5.1. Sensor warp measurement . . . 92
5.5.1.1. Height measurement with the optical system . . . 92
Characterization of the method . . . 95
Method optimization . . . 96
Method comparison . . . 98
5.5.1.2. Method applications . . . 98
5.5.2. Sensor cutting edge inspection . . . 101
5.5.3. Sensor edge parallelism inspection . . . 103
5.5.4. Sensor thickness inspection . . . 105
5.5.4.1. Direct optical measurement . . . 105
5.5.4.2. Measurement by autofocusing . . . 108
5.5.4.3. Summary . . . 110
5.6. Quality assurance database . . . 111
5.6.1. FairDB . . . 112
5.6.1.1. Versioning concept . . . 113
5.6.1.2. Aggregation concept . . . 114
5.6.1.3. ROOT object model compatibility . . . 114
5.6.2. Storing the optical QA data in FairDB . . . 114
5.6.2.1. Inspection image storage . . . 117
5.6.3. Summary . . . 118
5.7. Optical inspection of other STS components . . . 118
5.7.1. Readout microcables . . . 118
5.7.1.1. Microcable geometry . . . 119
5.7.1.2. Quality assurance methods and procedures for microcables . . . 120
Trace break detection . . . 121
Trace profile control and defect detection . . . 122
Foreign object detection . . . 123

Metal surface defect detection 123
Microcable inspection under direct light 125
5.7.1.3. Summary 125
5.7.2. Ladder assembly tool 126
5.7.2.1. Optical inspection of the ladder assembly tool . . 127
5.7.2.2. Summary 132
5.8. Software solution 132
5.9. Performance limitations 136

6. Detector cooling 139
6.1. Bi-phase CO_2 cooling 139
6.1.1. Volumetric heat transfer coefficient 139
6.1.2. CO_2 phase diagram 141
6.1.3. Vapor quality 142
6.1.4. Equation of state for carbon dioxide 144
6.1.5. Thome model 148
6.2. Thermal simulations of cooling bodies 152
6.2.1. Motivation 152
6.2.2. Front-end board box simulations 152
6.2.2.1. SolidWorks setup 153
6.2.2.2. Thermal studies of the FEB boxes 154
6.2.2.3. Study of AlN heat sinks 155
6.2.3. Read-out board simulations 156
6.3. Open CO_2 cooling system 158
6.3.1. Motivation 158
6.3.2. Cooling assembly 158
6.3.3. Cooling setup 159
6.3.3.1. Cooling setup equipment 161
6.3.3.2. Cooling setup control and readout 163
Temperature sensors 164
Pressure sensors 166
Flow meter 167
Liquid chiller 167
Relative humidity control 168
6.3.3.3. Control software 169
6.3.4. FEB Box Measurement results 171
6.4. Further experimental work with the cooling system 172

7. Conclusions and Outlook 175
7.1. Conclusions 175
7.2. Outlook and project continuation 176
7.3. 1 kW closed cooling system TRACI XL 177

A. Optical setup hardware and equipment 179

B. Neural networks architecture **181**

C. Sensor warp data **183**

D. Sensor thickness measured with the autofocusing approach **185**

E. FEM Simulated materials **187**

F. Cooling system equipment **189**

G. List of devices read out by the cooling system's control software **191**

H. Cooling system piping and process connections **193**

I. Swagelok parts for cooling system **195**

List of Figures **196**

List of Tables **206**

Bibliography **209**

1. Introduction

Quantum Chromodynamics (QCD [1]), a quantum field theory formulated in 1970's, is based on the experimental observation of the hadronic substructure. Deep inelastic scattering experiments showed that the electrical charge of the hadrons is not smoothly distributed and is carried by the constituent charged particles — quarks, which are kept confined [2] in the hadrons by the strong force mediators — gluons. The implication color confinement is that the quarks and gluons can not be observed in a free state due to increase of the potential between quarks as they are further separated. Only color neutral groups of two quarks (quarks and antiquarks form mesons), three (baryons) or in exotic cases more quarks are allowed. Another important property of the QCD is the asymptotic freedom [3]: as distance between partons becomes small, the coupling strength decreases. At sufficiently high temperatures or net-baryonic densities a deconfinement transition of hadronic matter becomes possible. The system of deconfined quarks and gluons is called the Quark-Gluon Plasma (QGP).

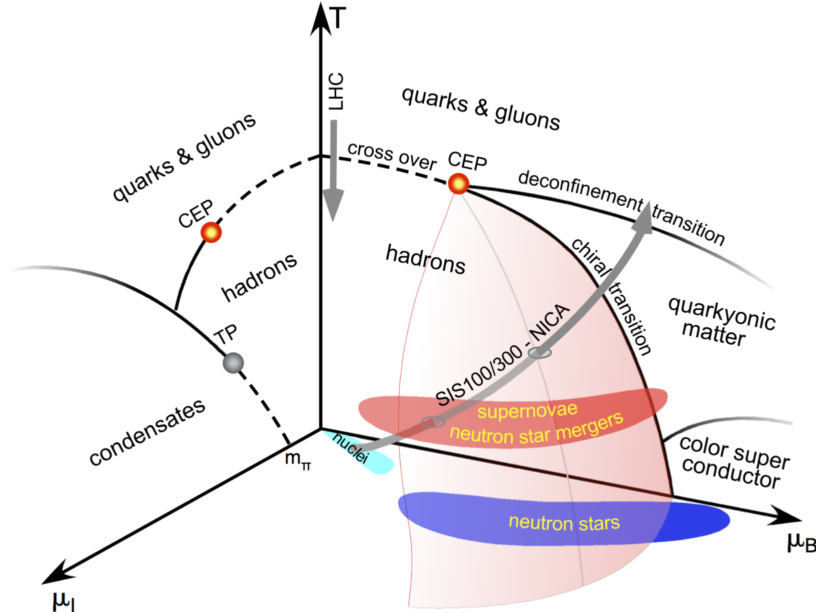

Figure 1.1.: 3-dimensional representation of the QCD phase diagram at high net-baryonic μ_B and moderate isospin μ_I densities. Different phases of the nuclear matter and critical end points (CEP) are shown [4].

Evidence of QGP formation was obtained in lattice QCD simulations and in high-energy heavy-ion collisions at the LHC[1] [5] and at RHIC[2] [6]. Thus, the QGP formed several microseconds after big bang can be recreated in the laboratory and its properties can be studied. So far only the properties of the QGP and phase transitions were studied at high temperature and vanishing net-baryon density of the QCD matter. The region at high net-baryonic density and moderate temperatures is only poorly studied due to the lack of the data and non-availability of lattice calculations.

Fig. 1.1 shows the phase diagram of the QCD matter in three dimensions [4]: temperature, net-baryonic density μ_B and isospin density μ_I. The critical end-points (CEP) separate the regions with different types of phase transition. In the region of high net-baryonic and moderate isospin densities the chiral and deconfinement phase transitions might be separated, yielding a confined phase with partially restored chiral symmetry, the so-called quarkyonic matter. At high densities of about 5 ρ_0 and at low temperatures conditions similar to those found in the neutron star mergers or in the cores of the neutron stars can be studied. Other phases of the deconfined matter, e.g. a color-superconductor, is expected to exist at very high net-baryon densities.

The CBM experiment [7] at FAIR [8] will be able to perform both integral and differential systematic measurements of almost all particles produced in the heavy-ion collisions. The SIS-100[3] synchrotron will provide beams of heavy ions, light ions and protons with energies up to 11 AGeV, 14 AGeV and 30 GeV, respectively. Thanks to uniquely high interaction rates of 10 MHz within this energy region the comprehensive study of the rare probes such as multi-strange hyperons and their antiparticles together with the excitation functions and flow, single and double hypernuclei is possible [9]. Collective phenomena of the dense matter, e.g., the flow of particles and antiparticles, event-by-event fluctuations, the production of open charm particles and charmonia can be addressed.

[1]Large Hadron Collider, CERN, Switzerland
[2]Relativistic Heavy Ion Collider, BNL, USA
[3]SchwerIonenSynchrotron, GSI, Germany

2. The Compressed Baryonic Matter Experiment

2.1. The FAIR facility

The future Facility for Antiproton and Ion Research (FAIR [8]) will expand the well established infrastructure of the GSI[1] heavy-ion research center. It will provide the unique research opportunities in the fields of nuclear, hadron, atomic and plasma physics. More than 200 institutions from 53 countries from all around the world participate in a reach scientific program devoted to the exploration of compressed baryonic matter. The program will start with primary beams from the SIS100 synchrotron (protons up to 30 GeV, Au ions up to 11 AGeV, nuclei with Z/A = 0.5 up to 14 AGeV). The planned SIS-300 synchrotron will provide protons up to 90 GeV, Au ions up to 35 AGeV and nuclei with Z/A = 0.5 up to 45 AGeV. Fig. 2.1 shows the layout of the FAIR with the experimental facilities.

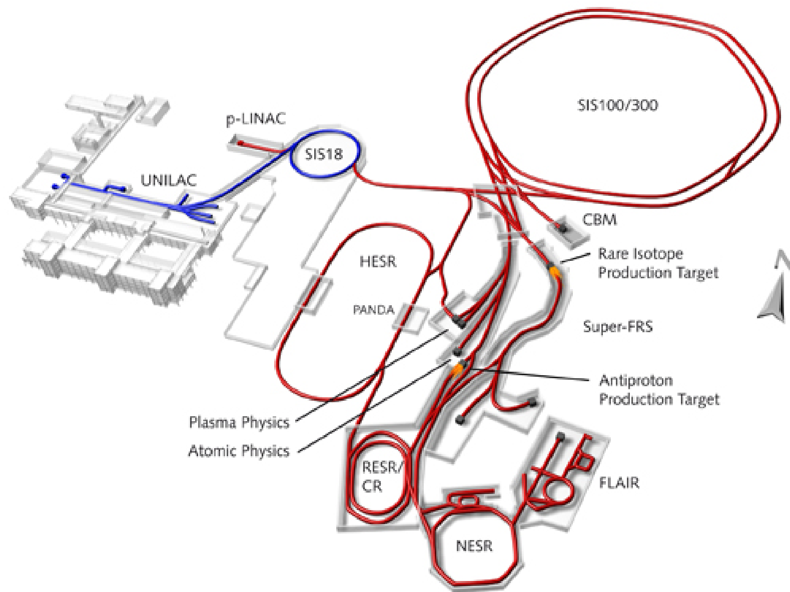

Figure 2.1.: A conceptual view of the FAIR facility [10].

[1] Gesellschaft für Schwerionenforschung.

2.2. Physics of the CBM experiment

The CBM experiment aims to perform both integral and differential systematic measurements of bulk as well as rare particles produced in nuclear collisions with unprecedented precision and statistics. The collisions of nucleus-nucleus and proton-nucleus systems, with a reference measurements from proton-proton collision, at unique interaction rates of 10^7 and 10^9 interactions per second will be conducted at different beam energies. These interaction rates open access to the rare probe measurements, such as multi-strange hyperons, hypernuclei, particles with charm quarks and vector mesons decaying into lepton pairs. The CBM experiment will run in a self-triggered, so called free streaming, data taking mode without hierarchical trigger system.

2.2.1. The CBM experimental setup

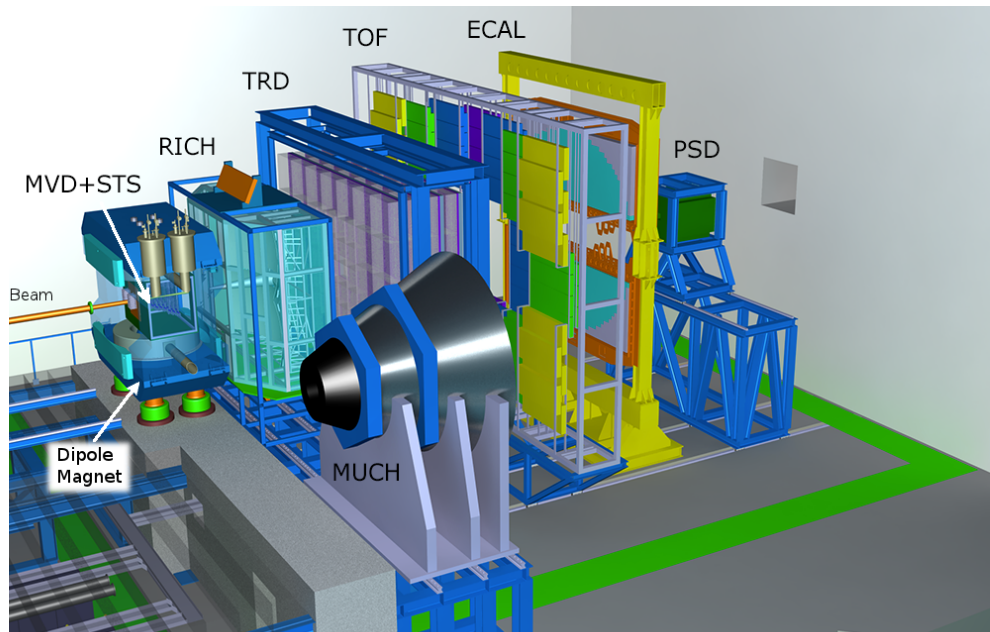

Figure 2.2.: The CBM experimental setup including, from left to right, Dipole Magnet, MVD, STS, RICH, MUCH, TRD, TOF, ECAL and PSD detector systems [11].

Fig. 2.2 shows the CBM experimental setup with the electron detection layout and the muon detection system which is in its parking position. The CBM experimental setup consists of following systems and detectors:

The **Superconducting Dipole Magnet** [**12**] has an aperture of ±25° polar angle. It provides a magnetic field integral of 1 Tm and accommodates the tracking detectors.

The **Micro-Vertex Detector** (MVD [7]) comprise of 4 MAPS[2] sensor layers in the close vicinity to the interaction point. The layers are placed 5, 10, 15 and 20 cm, respectively, downstream of the target. It provides the means to determine the primary decay vertices of short lived particles. It features the excellent position resolution of $\sigma = 3.5 - 6$ μm and has very low material budget to prevent the multiple scattering of the charged particles.

The **Silicon Tracking System** (STS [13]) provides the means to reconstruct the charged particle tracks and determine their momentum with a resolution of $\Delta p/p = 1 - 2\%$. It consists of 8 layers of double-sided silicon microstrip sensors. The sensors are based on the p^{+}-n-n^{+} technology, have a thickness of about 300 μm, 58 μm strip pitch and 7.5° strip stereo angle. The sensors are produced with four different strip lengths 20, 40, 60 and 120 mm. The sensors are mounted to the lightweight carbon fiber carrying ladders. To reduce the material budget the read-out electronics, cooling plates and other services are located on the periphery outside the acceptance zone. The sensors are connected to the read-out electronics with ultra light micro-cables with lengths up to 50 cm. The detector is positioned 30 cm downstream from target inside the dipole magnet.

The **Ring Imaging Cherenkov Detector** (RICH [14]) detector provides the identification of electrons and suppression of pions. It consists of a gas radiator, focusing mirrors and photo detector planes. The rings of Cherenkov radiation produced by the charged particles traversing the 1.7 m long CO_2 gas radiator are projected to the with the focusing mirrors on the MAPMT[3] detector planes. The detector will be positioned 1.6 m downstream from target outside the dipole magnet.

The **Muon Chamber System** (MUCH [15]) provides the possibility to detect the low-momentum muons by performing a moment-dependent identification. It consists of 5 layers of hadron absorbers and tracking detector planes between the absorber layers. The absorber layers consist of a 60 cm thick carbon plate followed downstream by four iron plates of 20 cm, 20 cm, 30 cm and 100 cm thickness, respectively. The tracking planes are based on GEM[4] and RPC[5] detectors. The MUCH detector is placed after the STS detector which provides the charged particle momentum identification.

The **Transition Radiation Detector** (TRD [7]) will allow further particle tracking, identification of electrons and positrons and further suppression of pions. It is consists of one or three detector layers for SIS-100 and SIS-300, respectively, which are based on MWPC[6] technology. The detector is placed 5 m downstream the target.

The **Time of Flight** (TOF [16]) will measure the velocity of the particles

[2] Monolithic Active Pixel Sensors
[3] Multianode Photomultiplier
[4] Gas Electrom Multiplier
[5] Resistive Plate Chamber
[6] Multi-Wire Proportional Chamber

from which the mass-to-charge ration can be determined. The detector is based on the Timing Multi-gap Resistive Plate Chambers (MRPC) technology. It is placed about 6 m downstream of the target.

The **Electromagnetic Calorimeter** (ECAL [7]) will measure the direct photons and other particles decaying into photons. It will consist of 140 layers of 1 mm lead and 1 mm scintillator. It can be arranged as a wall or as a tower with variable distance from the target.

The **Projectile Spectator Detector** (PSD [17]) will be used for the collision centrality determination and the reaction plane extraction. The detector is a hadronic calorimeter able to measure the number of non-interacting nucleons from a projectile nucleus in the heavy-ion collisions. It consists of 44 individual modules, which are built of 60 lead-scintillator layers. The scintillation light is read out via wavelength shifting (WLS) fibers by Micro-pixel Avalanche Photodiodes (MAPD) with an active area of 3×3 mm^2 and a pixel density of 10^4/mm^2.

Because the CBM experiment will be collecting data in a free streaming mode without hardware triggers [7] it is essential to provide an efficient online event selection. This allows to reject the events which contain no signal and implement the efficient software triggers for the targeted probes. The event selection system will be based on a fast on-line event reconstruction running on a high-performance computer farm equipped with many-core CPUs and graphics cards in the GSI GreenIT cube [18]. The track reconstruction, which is the most time consuming combinatorial stage of the event reconstruction, will be based on parallel track finding and fitting algorithms, implementing the Cellular Automaton and Kalman Filter methods.

2.2.2. Physics cases

The rich physics program of the CBM at SIS-100 energy regime is described in detail in [9, 19]. The CBM experiment at FAIR provides unique interaction rates of 10 MHz at moderate energies for 1% target.

Fig. 2.3 shows a comparison of interaction rates and center of mass energies of high energy experiments. The high interaction rate of the CBM experiment opens the possibility to measure the rare probes with high statistics. It is at least two orders of magnitude larger compared to the closest competitors such as BM@N[7] [20], HADES[8] [21] and NICA/MPD[9] [22] experiments.

Fig. 2.4 shows the particle yields for Au+Au and Pb+Pb collisions in the high baryon density region. The red and green data points were measured by other experiments, however the low-energy region denoted by the blue data points is uncharted so far and will be investigated by the CBM experiment.

[7] Baryonic Matter at Nuclotron, JINR, Russia
[8] High Acceptance Spectrometer, GSI, Germany
[9] Nuclotron-based Ion Collider fAcility/MultiPurpose Detector, JINR, Russia

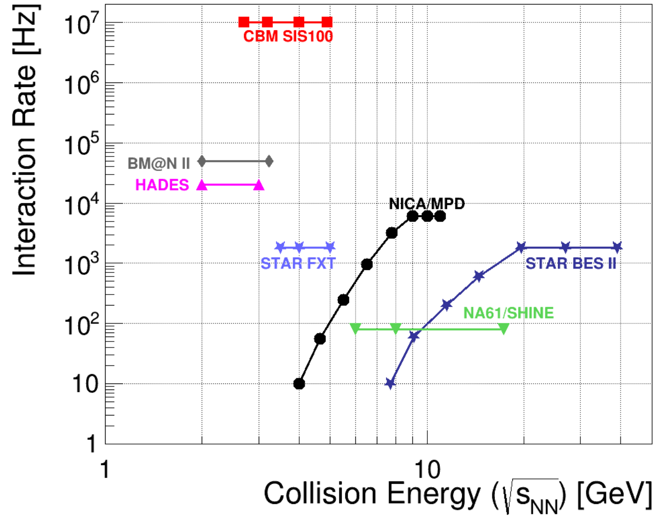

Figure 2.3.: A comparison of interaction rates and center of mass collision energies of high energy physics experiments [19].

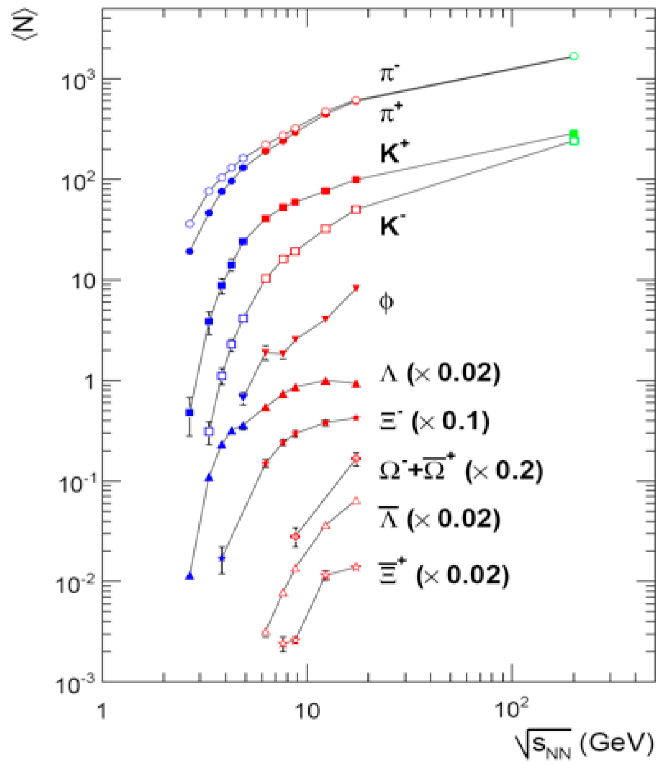

Figure 2.4.: Particle yields depending on the collision energy for central Au+Au and Pb+Pb collisions [23].

The CBM experiment will be able to address fundamental questions such as the equation of state and the relevant degrees of freedom at high net-baryon densities, the existence of exotic QCD phases, how the properties of the hadrons are modified in-medium, indications of chiral symmetry restoration, existence of the heavy multi-strange hypernuclei.

2.2.2.1. Study of the dense nuclear matter

The CBM experiment will operate at beam energies which produce high baryon densities in high-energy collisions. According to the model calculations [24, 7] shown in Fig. 2.5 the densities in the fireball produced will exceed 6 times the saturation density of normal nuclear matter ρ_0 at the beam energies of 5 AGeV and 8 ρ_0 at 10 AGeV.

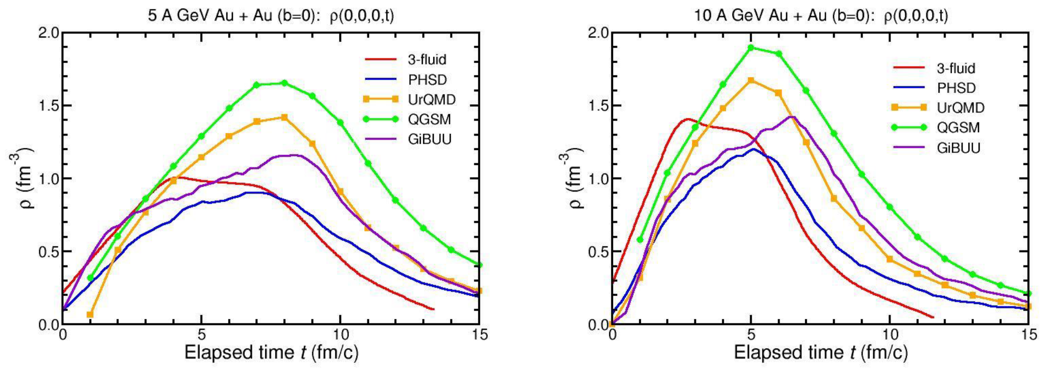

Figure 2.5.: Net baryon density evolution of the fireball at 5 (left panel) and 10 (right panel) AGeV [19].

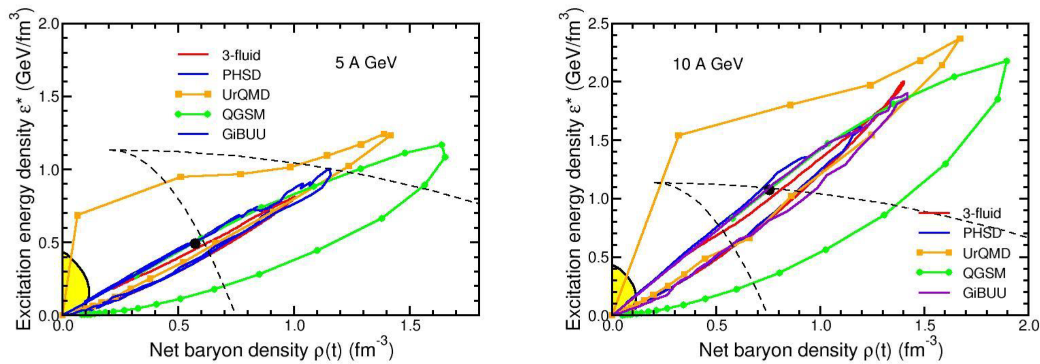

Figure 2.6.: Evolution of the excitation energy density and net-baryon density of a fireball. The step between data points is 1 fm/c [19].

The excitation energy density is a bulk property of the dense nuclear matter. It is defined as $\epsilon^*(t) = \epsilon(t) - m_N\rho(t)$, where $\epsilon(t)$ is the energy density and $m_N\rho(t)$ the mass density. Fig. 2.6 shows the evolution of the excitation energy density and net baryon density of a fireball calculated with a time step of 1 fm/c.

2.2.2.2. Collective phenomena

Collective phenomena like flow was already observed at LHC and RHIC. It is driven by the pressure gradient produced in the early stages of the fireball evolution. The flow effects are characterized by the azimuthal distribution of the emitted particles. The total flow can be expanded in a series:

$$dN/d\phi = C(1 + v_1 cos(\phi) + v_2 cos(2\phi) + \cdots + v_n cos(n\phi)), \quad (2.1)$$

where the ϕ is the azimuthal angle relative to the reaction plane. The coefficients v_n represent different flow contributions: directed, elliptic, triangular and other higher order contributions. The experimental observations indicate different flow behavior for different particle species.

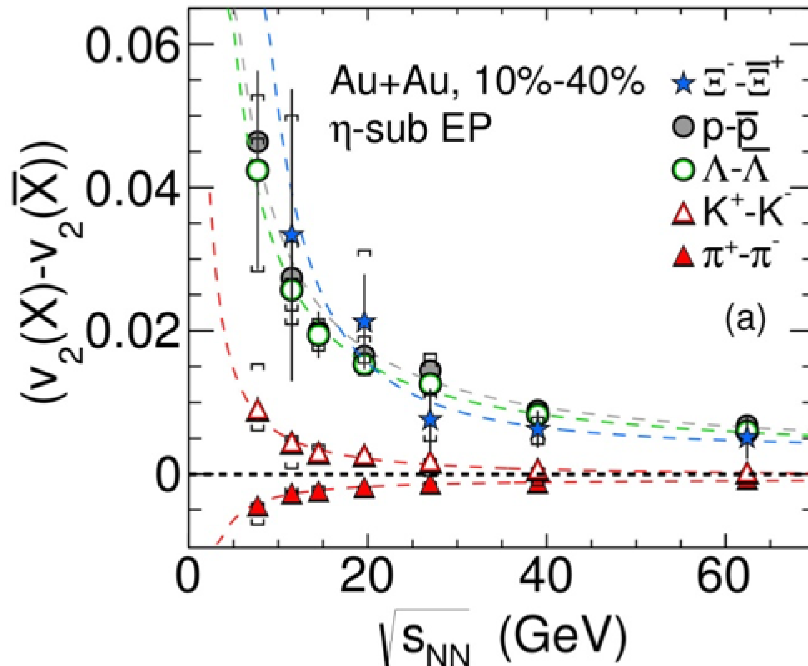

Figure 2.7.: The difference in elliptic flow v_2 of particles and antiparticles as a function of the collision energy for the 10%-40% central Au+Au collisions measured by the STAR collaboration [19].

Fig. 2.7 shows the difference in elliptic flow for particles and antiparticles measured by the STAR collaboration. The CBM experiment is able to increase the measurement statistics in the low energy regions as well as measure the flow of multi-strange hyperons and dileptons.

2.2.2.3. Event by event fluctuations

The fluctuations of the conserved quantities like baryon number, strangeness, charm and electrical charge and others can be measured by the CBM experiment. It is expected that higher order moments of these distributions are more sensitive to the phase transition and matter structure around the critical point [25].

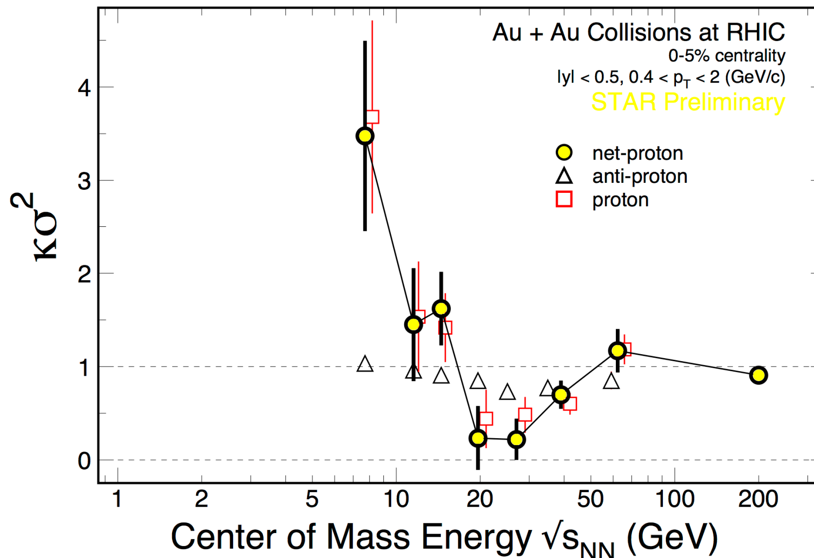

Figure 2.8.: The excess kurtosis times variance ($k\sigma^2$) of the proton, antiproton and net-proton distributions for most central Au+Au collisions as a function of collision energy measured at RHIC [26].

Fig. 2.8 shows the volume-independent cumulant ratio, the excess kurtosis times variance ($k\sigma^2$), of the proton, antiproton and net-proton multiplicity distributions as a function of a collision energy measured at RHIC. It is expected that in absence of a critical point, this ratio should stay constant. The results presented here will profit from high precision measurements in the low energy range available in the CBM experiment.

2.2.2.4. Dilepton spectroscopy

The leptons are emitted during the whole evolution of the fireball and carry the information about the medium properties. This is possible because they do not interact strongly. The yield of lepton pairs is sensitive to the temperature of the created matter and its expansion processes [27]. They are expected to be sensitive to chiral symmetry restoration [28].

Fig. 2.9 shows the invariant-mass spectra of electron-positron pairs radiated in central Au+Au collisions at 20 AGeV. The different underlying processes are presented. The slope of this distribution between 1 and 2.5 GeV/c^2 reflects the

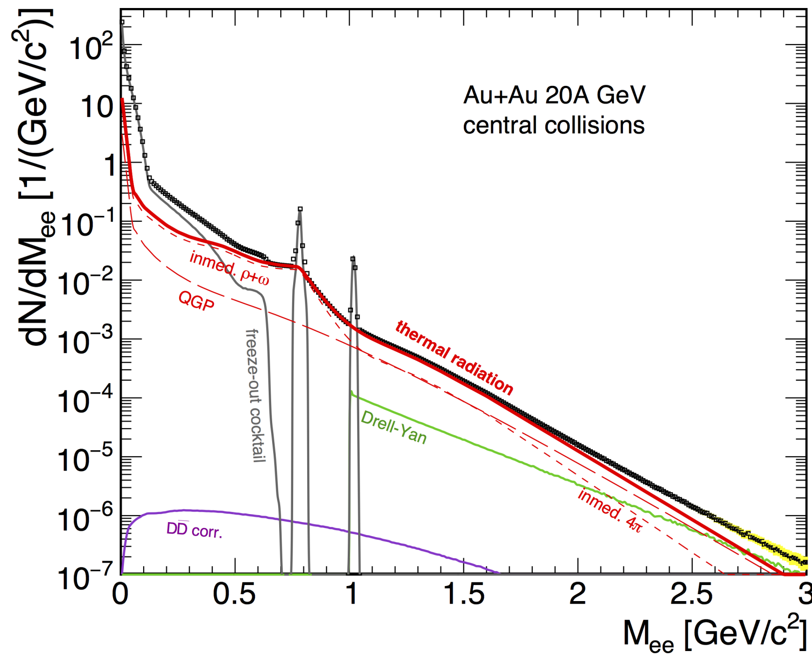

Figure 2.9.: Invariant-mass spectra of electron-positron pairs radiated in central Au+Au collision at 20 *A*GeV. Color coded are the contributions from different underlying decay processes [19, 29].

average temperature of the fireball created. The CBM experiment will perform high-precision measurements of the dilpeton invariant mass spectra allowing to calculate the excitation function.

2.2.2.5. Strangeness and charm

Particles containing strange quarks will be produced in heavy-ion collisions in the CBM experiment. The yields of these particles correlate with the density of the fireball produced. The heavier strangeness containing particles, e.g. Ω, Ξ, can be produced in sequential collisions involving lighter strange particles such as kaons and lambdas. The density sensitivity is largest at the lower beam energies close or even below the production threshold in elementary collisions.

The thermal models [30] predict the possibility to create single and double hypernuclei in the heavy-ion collisions. These nuclei contain at least one baryon carrying a non-zero strangeness quantum number. It is expected that around 3000 ${}_{\Lambda\Lambda}{}^{5}H$ and 60 ${}_{\Lambda\Lambda}{}^{6}He$ will be measured within one week of data taking. Fig. 2.10 shows the calculated yields of the hypernuclei for 10^6 central Au+Au collisions.

Charmed particles are created in the early stages of the heavy-ion collisions. The charmonium suppression observed earlier in central Pb+Pb collisions at RHIC [31] and LHC [32] indicate the formation of the quark-gluon plasma. This suppression happens due to the color screening of the heavy quark potential in

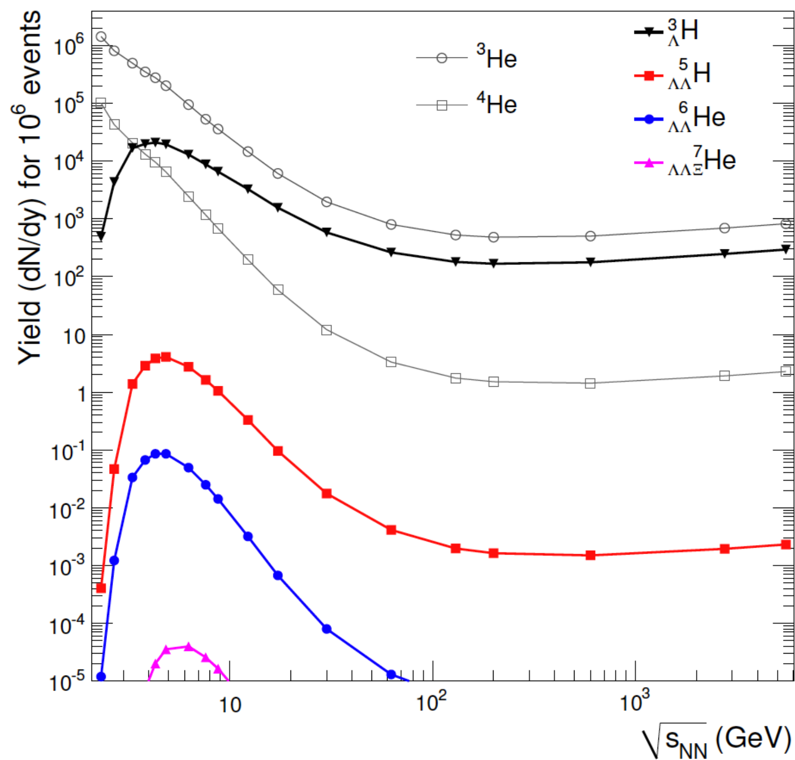

Figure 2.10.: The yields of hypernuclei depending on the collision energy for 10^6 central Au+Au collisions calculated with thermal model [30].

the deconfined state. With the CBM experiment in the SIS100 energy regime the charm production will be studied at the beam energies close to the threshold. It is expected to measure 300 J/ψ for central Au+Au collisions at 10 AGeV per one week of data taking.

3. The Silicon Tracking System detector

The Silicon Tracking System (STS) is the core detector of the CBM. It is located in the dipole magnet and provides track reconstruction and momentum determination of charged particles from beam-target interactions. The detection of rare probes requires the STS to be capable measuring Au+Au collisions at interaction rates up to 10 MHz. The track multiplicities reach up to 700 per central Au+Au collision in the aperture of $2.5° < \theta < 25°$.

The STS comprise 8 tracking stations from 30 to 100 cm downstream the target. It occupies a volume of about 2 m^3 with the thermal enclosure. The sensors will be kept at temperatures below -5 ℃ in a dry nitrogen atmosphere to prevent condensation. The STS will be placed inside 1 T superconducting dipole magnet. A schematic view of the STS detector without thermal enclosure and services is shown in Fig. 3.1.

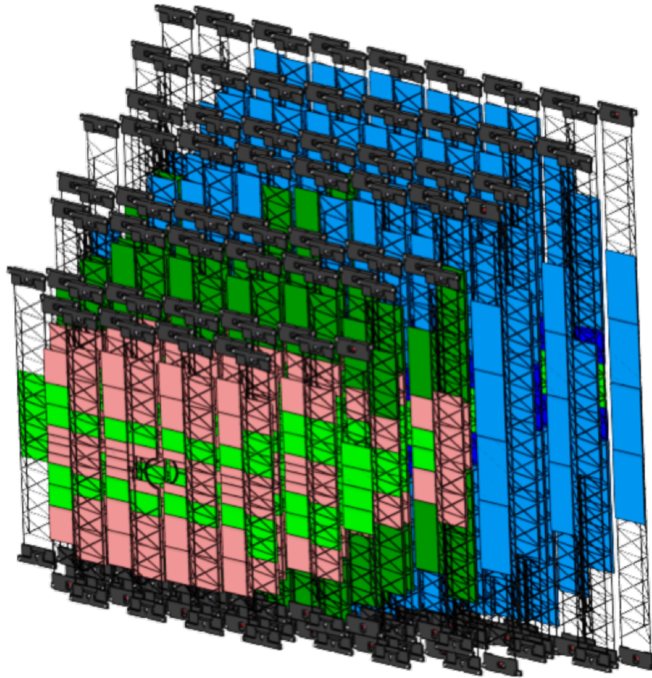

Figure 3.1.: View of the STS detector without thermal enclosure and services [33].

The STS detector will use the double-sided microstrip sensors based on the

p$^+$-n-n$^+$ technology. The silicon sensors have a thickness of about 300 μm, 58 μm strip pitch and 7.5°strip stereo angle. Depending on the sensor position, different-sized sensors will be used. The sensor sizes are 22×62 mm^2, 42×62 mm^2, 62×62 mm^2 and 124×62 mm^2 with 1024 strips each. Additionally the smaller sensors with fewer strips, so-called "baby" sensors, will be used to cover gaps close to the beam pipe. The sensors provide the spatial resolution of about 25 μm.

Momentum resolution of the STS is mostly dominated by the multiple scattering of the charged particles in the material. In order to achieve the momentum resolution of $\Delta p/p \approx 1 - 2\%$ required for the physics observables, the material budget of the detector have to be minimized and optimized. For this purpose the light-weight carbon fiber ladders for the sensor mounting are used. Additionally the read-out electronics, powering boards and cooling elements are placed outside the acceptance zone. To connect the sensors to the read-out electronics, the ultralight read-out cables with lengths up to 50 cm are used. Due to a very limited space for the detector cooling the efficient evaporative CO_2 cooling is used (see chapter 6).

3.1. Silicon Microstrip Sensors

Silicon microstrip sensors were used in numerous experiments differing in their strip length, strip pitch and other parameters. In the CBM STS detector we use double-sided silicon sensors, where both electrons and holes are collected on the respective sides of the sensor.

The silicon sensors used in the STS detector are produced by two manufacturers: CiS Forschungsinstitut für Mikrosensorik GmbH (later referred to as CiS) located in Erfurt, Germany [34] and Hamamatsu Photonics K.K. located in Hamamatsu, Japan [35]. Both manufacturers have an established 4 inch wafer technology. For the production of 12 cm long sensors a 6 inch technology is required. Hamamatsu has it already established, the CiS has only recently introduced it and it requires additional testing. The sensor layouts for CiS (left panel) and Hamamatsu (right panel) are shown in Fig. 3.2. Tab. 3.1 shows the specification summary of the sensors used in the STS detector.

The sensor active area is placed within the bias ring and guard rings. The strips are parallel to the edges on the n-side and inclined by 7.5° on the p-side. This allows to have both read-out planes oriented in the same direction unlike to the designs where the strips are perpendicular. The p-side corner strips are interconnected with the second metal layer lines. The implant strips are read out by the AC coupled aluminum read-out strips (cf. 3.1.2).

3.1.1. Sensor logistics

Fig. 3.3 shows the workflow diagram of the STS detector production and logistics. The optical quality assurance of the sensors happens as a first step after procure-

Parameter	CiS	Hamamatsu
Thickness	285 ± 15 μm	320 ± 15 μm
Technology	p^+-n-n^+, moderated p-spray	p^+-n-n^+, p-stop
Lattice orientation	<111>	<100>
Segmentation	double-sided single metal (early versions) double metal (later versions)	double-sided single metal (early versions) double metal (later versions)
Width	62 mm	62 mm
Height	22, 42, 62, 124 mm	22, 42, 62, 124 mm
Dicing	Diamond saw, up to 80 μm extra width per edge, ca. 10 μm precision	Laser (stealth), up to 10 μm extra width per edge, $<$ 5 μm precision
Strip amount	1024	1024
Strip angles, n/p	0°/7.5°	0°/7.5°
Biasing	Bias ring, poly-silicon resistors, 1 MΩ	Bias ring, poly-silicon resistors, 0.5 MΩ
Guard rings	n and p sides visible series of rings	n and p sides single ring, metal overhang

Table 3.1.: Specification summary of the silicon microstrip sensors used in the STS detector [36].

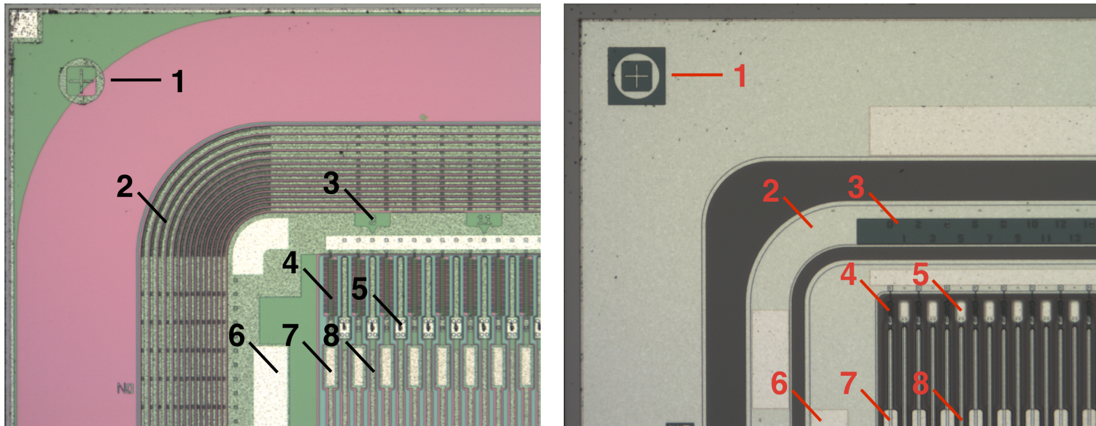

Figure 3.2.: Layout of the silicon sensors from CiS (left panel) and Hamamatsu (right panel) in the corner region, n side. Legend: 1) Alignment mark 2) Guard ring 3) Strip numbering panel 4) Polysilicon bias resistor 5) DC pad 6) Bias ring pad 7) AC pad 8) Aluminum read-out strip.

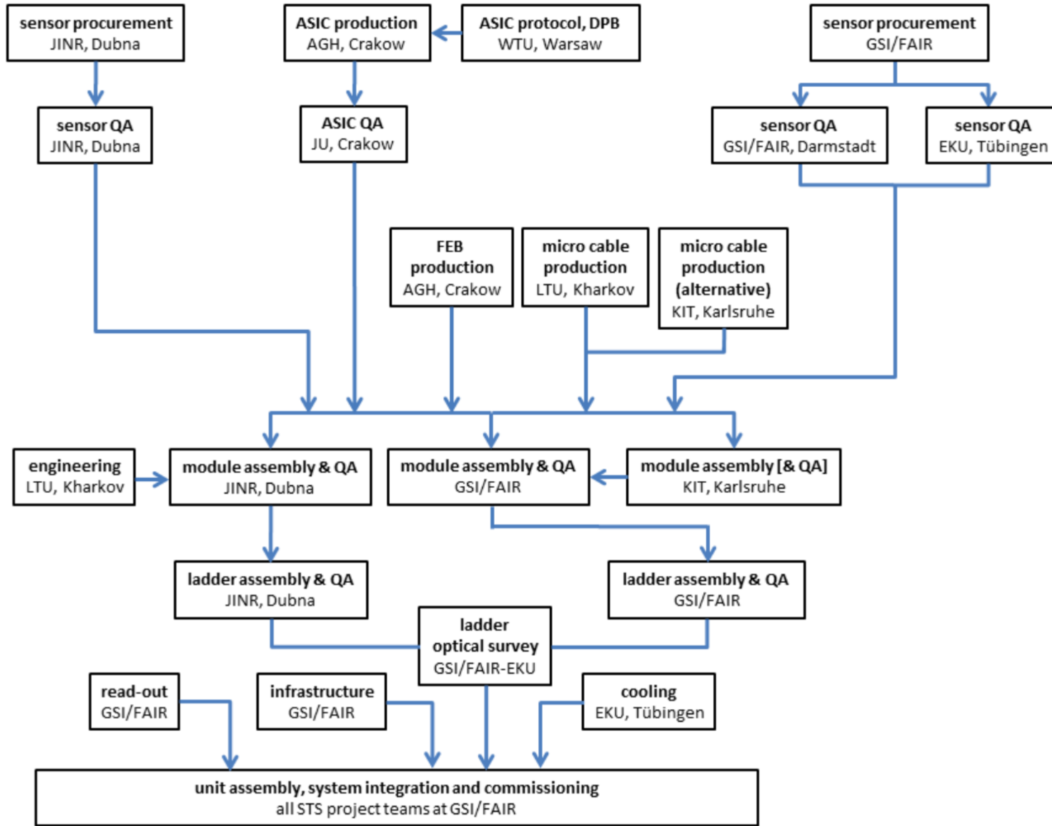

Figure 3.3.: The diagram of the STS detector production from procurement to the assembly [36].

ment. 100% of the sensors should undergo the optical QA. This allows to qualify the sensors and reject the faulty batches on the early steps as well to identify the “suspicious” sensors to be thoroughly inspected electrically.

To allow the unique end-to-end identification of the microstrip sensors between the quality assurance and production sites the following naming convention for the sensors is used:

$$\mathrm{CBM06C2} - 350714 - 18 - 2 - \mathrm{SM}$$

CBM06 identifies the sensor generation, C or H stands for manufacturer (CiS or Hamamatsu, respectively), 2 (or 4, 6, 12) for the strip length, 350714 for the batch number, 18 for the wafer number and 2 for the sensor id on the wafer. The optional SM suffix indicates that the sensor technology is single metal rather than double metal.

The sensor envelopes or cases should receive either a barcode or a QR code (Fig. 3.4) sticker to identify the sensor uniquely. Scanning either code allows to preconfigure the optical or electrical setup for the sensor.

Figure 3.4.: A barcode and QR code to identify the sensor.

3.1.2. Sensor read-out

The silicon sensors are operated fully depleted. As an ionizing particle traverses the silicon bulk it produces electron-hole pairs. The most probable value of the number of electron-hole pairs produced per 1 μm of silicon bulk thickness is 76 for a minimum ionizing particle [37]. The electrons and holes drift in an electrical field to the respective sensor sides and are collected on the implant strips. Fig. 3.5 shows the cross section of the sensor and illustrates the electron-hole production.

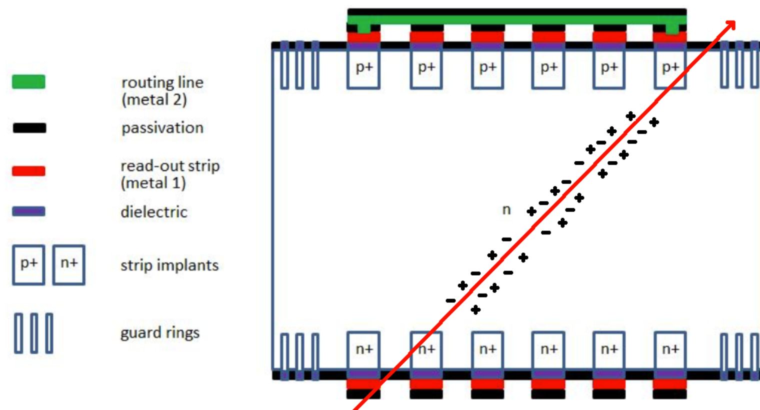

Figure 3.5.: Silicon microstrip cross section. The ionizing particle traversing the silicon bulk creates the electron-hole pairs which are drifting in the electrical field to the respective sensor side [36].

According to the Technical Design Report (TDR) [13] the end-of-life sensor noise should not be higher than 1000 electrons ENC (equivalent noise charge) and the signal to noise ratio (S/N) should be higher than 10. This implies that at least 10000 signal electrons should be read out. The ionization energy required to create a single electron-hole pair in the bulk silicon material is about 3.6 eV [38]. The mean energy loss due to ionization for minimum ionizing particle (MIP) is $dE/dx = 3.88$ MeV/cm or 388 eV/μm. Thus, the mean amount of electron-hole pairs produced per micrometer of silicon material is about 108,

while most probable value is factor 0.7 lower — about 76. This allows to estimate the expected signal for a non-irradiated 300 μm sensor — about 22800 electrons or about 3.65 fC.

The charge collected on the implant strips induces the current on the AC coupled aluminum strips. The signal is read-out from the AC pads, to which the signal transmission cables are bonded. The signal is then directed to the STS-Xyter ASIC chips to be digitized and sent to the first level event selection (FLES).

3.1.3. Radiation damage effects in Silicon sensors

The silicon sensors of CBM experiment closest to the beam line will be exposed to a total non-ionizing radiation dose up to 1×10^{14} n_{eq}/cm^2during the operation time of ca. 6 years [13].

This dose requires highly radiation tolerant materials. The overall detector material budget have to be minimized to avoid multiple scattering [39, 40]. In this section some aspects of radiation damage to silicon semiconductor detectors, the dependence of its properties on the radiation dose, on time (annealing) and most important for this work, temperature, are discussed.

The silicon microstrip detectors used in the CBM experiment are subject to ionizing and non-ionizing radiation damage. The ionizing damage comes primarily from photons produced in Compton effects and electron-positron pairs, but as well from charged particles and heavy ion fragments from peripheral collisions.

The process of ionizing energy loss (IEL) affects the structure of the silicon sensor. For example, the electrons produced in the SiO_2 layer and SiO_2-Si interface could lead to fixed positive oxide charge formation, the accumulation of electrons at the surface and the creation of additional interfacing states on SiO_2-Si border.

This in turn leads to increase of the interstrip capacitance, a decrease of the interstrip resistance, a change of the breakdown voltage and an increase of surface dark current. More information on IEL effects can be found in [41, 42].

Another aspect of radiation damage is the damage by non-ionizing radiation. In this case an energetic incident particle may scatter and displace (Fig. 3.6) the so called “knock on” atom out of its place in the crystalline lattice and create a Frenkel pair [43]. It consists of an interstitial atom and a vacancy.

The formed vacancies and interstitials are movable objects inside the lattice due to their possible thermal reconfiguration. They migrate inside the lattice until they find impurities and form defects, for example, a vacancy and an oxygen atom could form a defect. An incident particle can scatter in bulk material multiple times thereby creating the clusters of defects — regions of the lattice with many localized displacements — which persist for a long time. Formation of clusters predominantly happens at the end of the track.

To qualify and quantify the radiation damage impact from various particle

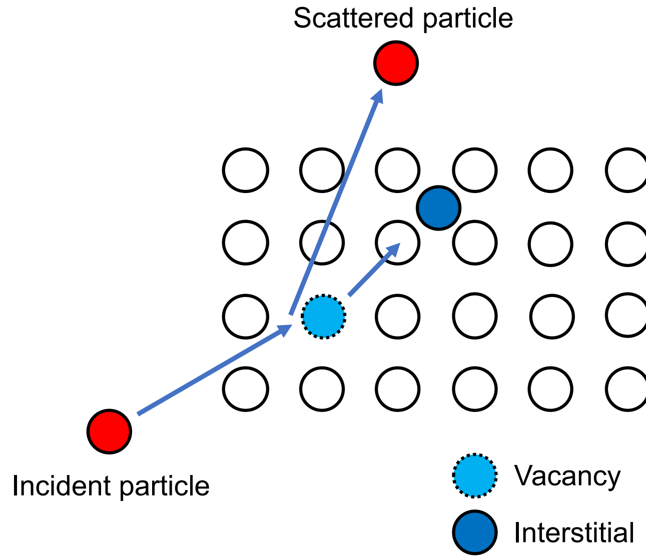

Figure 3.6.: A sketch of the Frenkel pair creation mechanism.

species we refer in this work to so called Non-Ionizing Energy Loss (NIEL) hypothesis which provides us the scaling mechanism to normalize radiation damage from theses species to 1 MeV neutrons.

$$k = \frac{1}{D(1 \text{ MeV neutrons})} \cdot \frac{\int D(E)\phi(E)dE}{\int \phi(E)dE} \tag{3.1}$$

Eq. (3.1) expresses the so called hardness factor k of a radiation field (or as well of a monoenergetic particle) normalized to to 1 MeV neutrons. E denotes the energy of particle, $D(E)$ is the displacement damage cross-section for a particle with energy E (for 1 MeV neutrons $D = 95$ MeV $\cdot$ mb), $\phi(E)$ is the energy spectrum of this radiation field. The integrals are evaluated for the interval $[E_{MIN}, E_{MAX}]$, where E_{MIN} and E_{MAX} are the minimum and maximum cut-off energy values, respectively, for particle types in the radiation field [44]. Fig. 3.7 shows displacement damage functions for 4 particle species.

According to our requirement, that the STS detector should remain operational for a non-ionizing dose up to 1×10^{14} n_{eq}/cm^2, it is crucial to assure, that the detector properties will deteriorate only within certain limits.

Let us take a look which properties of the detector will change or deteriorate with radiation dose.

First, the silicon microstrip sensors are operated fully biased to assure the high charge collection efficiency. Up to 22800 electrons of about 3.65 fC of charge is expected to be collected from a 300 μm thick non-irradiated sensor. The charge collection efficiency drops down with radiation dose resulting in a lower read-out signal (Fig. 3.8). This can be explained by the partial trapping of the electrons in bulk silicon defects as described in equation (3.2) and (3.3).

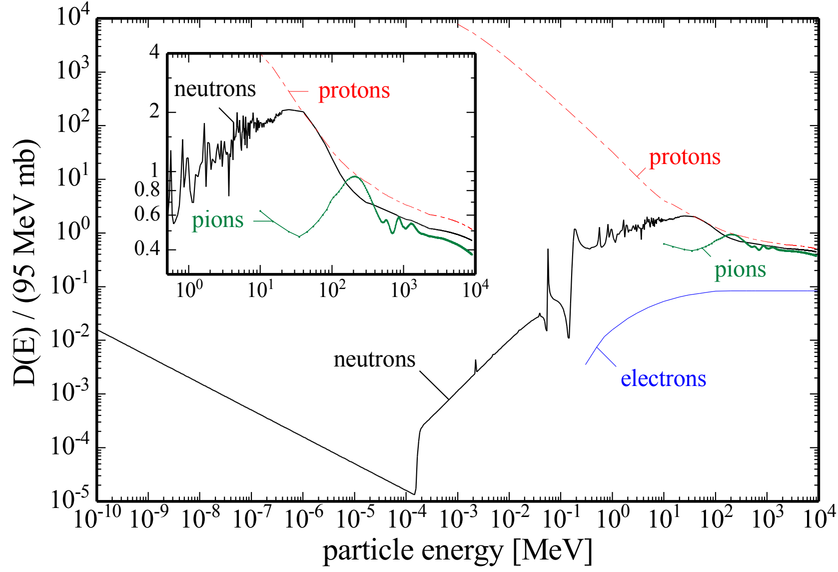

Figure 3.7.: Displacement damage functions normalized to 95 MeV · mb for neutrons, protons, pions and electrons. The inset displays a zoomed part of the figure [44].

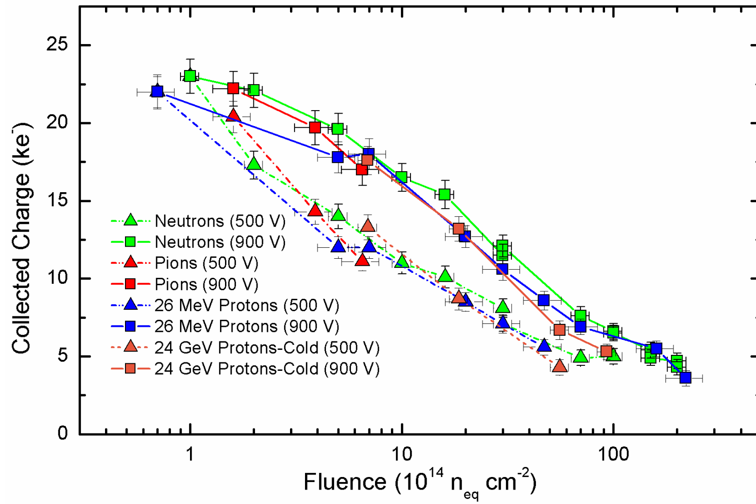

Figure 3.8.: Deterioration of charge collection efficiency with increasing particle fluence [45].

$$Q_{e,h}(t) = Q_{0e,h} \exp - \frac{1}{\tau_{eff\ e,h}} \cdot t, \tag{3.2}$$

where

$$\frac{1}{\tau_{eff\ e,h}} \propto N_{defects} \tag{3.3}$$

The inverse trapping time is subject to change with fluence and time. The

dependencies are shown in Fig. 3.9.

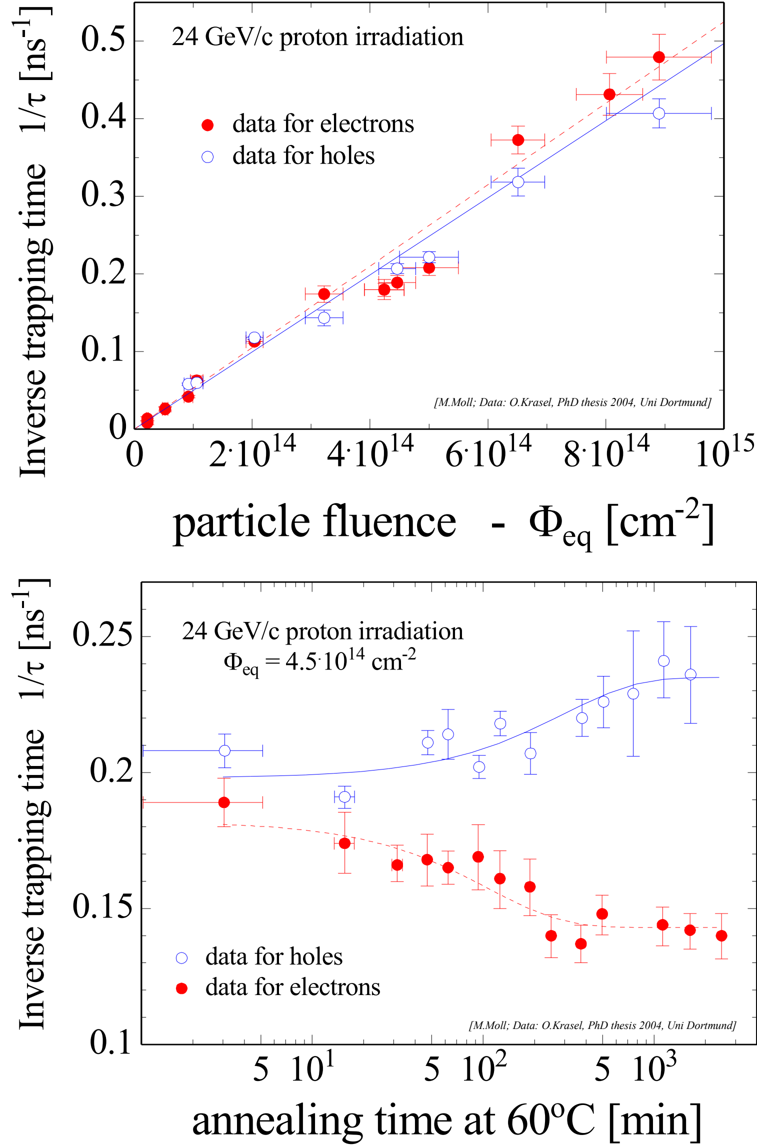

Figure 3.9.: Increase of inverse trapping time with fluence (top panel) and time (bottom panel) [44].

3.1.3.1. Type inversion

Another important property, which changes with the radiation damage, the full depletion voltage V_{dep} of the silicon sensor:

$$V_{dep} = \frac{q_0}{\varepsilon\varepsilon_0} \cdot |N_{eff}| \cdot d^2 \tag{3.4}$$

The depletion voltage as seen in eq. (3.4) depends on the effective space charge density N_{eff}, and emerges from Poisson's equation:

$$-\frac{d^2}{dx^2}\phi(x) = \frac{q_0}{\varepsilon\varepsilon_0} \cdot N_{eff}, \tag{3.5}$$

where d is the thickness of semiconducting material, ε and ε_0 are the permittivity values for material and vacuum (electric field constant) respectively, q_0 elementary electrical charge.

Radiation exposed n-bulk semiconducting materials change the effective dopant concentration, which affects the full depletion voltage. This is due to various effects such as Frenkel pair formation, defect cluster creation, electron-hole trapping as well as possible atom transmutation (the latter effect is used for bulk doping in a process called "Neutron Transmutation Doping" [46, 47]).

Fig. 3.10 shows the dependency of the detector's effective charge concentration (and, correspondingly, full depletion voltage on the left panel) from particle fluence and time (annealing). A very important phenomenon illustrated on left panel is the so-called *type inversion* — an effect when the semiconductor doping concentration changes such, that the detector bulk material transforms from n-type to p-type, due to sign change of the space charge N_{eff}. This process requires constant bias voltage adjustment, otherwise the detector might be underdepleted ($V_{bias} < V_{dep}$) or be in the region of breakdown ($V_{bias} \approxeq V_{breakdown}$). This can be seen in the fluence region of around $\Phi_{eq} = 10^{14}$ $\mathrm{n}_{eq}/\mathrm{cm}^2$, where full depletion voltage reaches already 600 V, which is greater than the $V_{breakdown}$. Furthermore, the effect of increased leakage current leads to thermal runaway as explained further below.

The right panel of Fig. 3.10 shows the time change of irradiated silicon ΔN_{eff} with time (annealing) at 60 °C.

$$\Delta N_{eff} = N_A + N_Y + N_C \tag{3.6}$$

Eq. (3.6) shows the contributions to effective space charge concentration. The short term beneficial annealing (expressed as N_A) leads to migration of defects with possible recombination with the counterpart, their gettering [48, 49] (e.g. at the surface); dissociation of complex defects in crystalline lattice if the lattice vibrational energy is greater than the binding energy. This beneficial defect annealing results to a certain degree in an improvement of the detector's properties. However, the long term reverse annealing (expressed as N_Y) leads to formation of new defects. The N_C term denotes the stable or irreparable damage to crystalline lattice.

The very important aspect of annealing effects for this work is their temperature dependence. Tab. 3.2 summarizes the observed annealing times from the detector operation temperature. Thus it is very important to keep the silicon sensors at around -10 °C at all times to mitigate the annealing effects and prevent formation of clusters of defects.

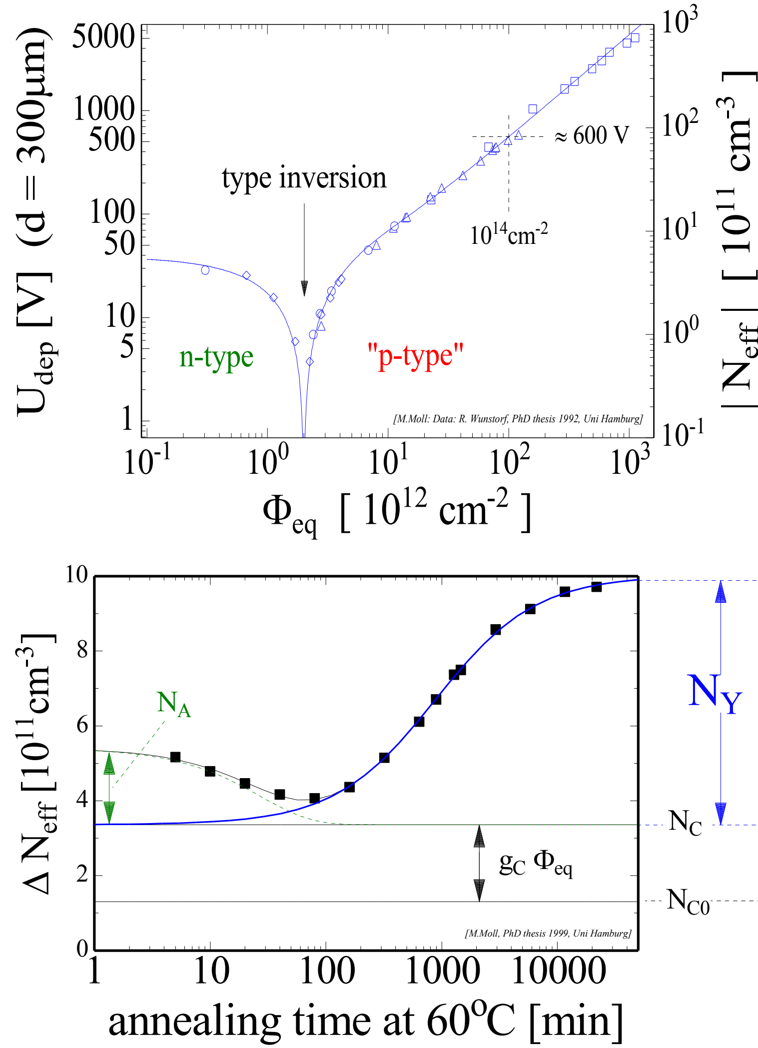

Figure 3.10.: Change of detector depletion voltage and effective charge carrier concentration with respect to fluence (top panel) and annealing time (bottom panel) [44].

Detector operation temperature, °C	Annealing time
-10	ca. 500 years
20	ca. 500 days
60	21 hours

Table 3.2.: Annealing time dependence from detector operation temperature

Last (but not least) important topic for this work is the leakage current I and its change ΔI induced by radiation. They could be expressed in following ways:

$$I = T^2 \; exp\left(\frac{E_{gap}}{2k_B T}\right) \tag{3.7}$$

and

$$\Delta I = \alpha \Phi = \alpha \int \phi(E) dE = \alpha \ V \ \Phi_{eq}, \tag{3.8}$$

where T denotes the detector operating temperature, E_{gap} is band gap energy of semiconductor, k_B is Boltzmann constant; α is the damage parameter (slope in Fig. 3.11) expressing the leakage current per unit volume V and particle fluence Φ_{eq}.

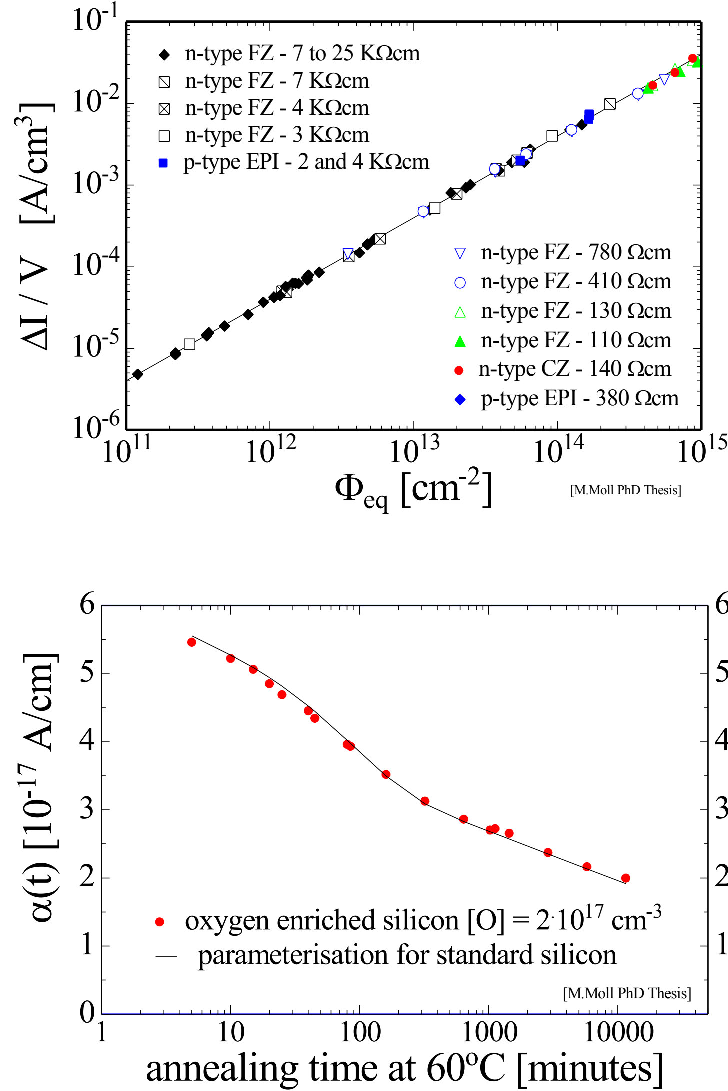

Figure 3.11.: Change of detector leakage current with fluence (top panel) and damage parameter with annealing time (bottom panel) [44].

α is a constant over several orders of magnitude of fluence. The value extracted from the slope in Fig. 3.11 is

$$\alpha = (3.99 \pm 0.03) \times 10^{-17}\mathrm{A/cm} \tag{3.9}$$

after 80 minutes at 60 ℃.

3.1.3.2. Temperature dependence and thermal runaway

The Leakage current shows a strong temperature dependence which, expressed in the form of a relation, reads as follows:

$$\frac{I_2}{I_1} = \left(\frac{T_2}{T_1}\right)^2 exp\left[\frac{E_{gap}}{2k_b}\left(\frac{1}{T_1} - \frac{1}{T_2}\right)\right] \tag{3.10}$$

According to eq. (3.10), the leakage current doubles with $\Delta T \approx 7$ ℃ or, as another example, $I(-10$ ℃$) \approx 1/16\ I(20$ ℃$)$.

The increase of the leakage current leads to an increase of the shot noise in the detector (which is proportional to $\sqrt{I}$ and deteriorates the signal to noise ratio) and internal heat power dissipation which further increases the leakage current as follows from eq. (3.7). This undesired positive-feedback phenomenon is called thermal runaway and should be avoided.

The strong temperature dependence of the leakage current and the annealing processes requires cooling of irradiated silicon detectors at all times, even when not operated. The aspects of the detector cooling are covered in the chapter 6.

4. Quality assurance of the detector components

The quality assurance of the detector components is an important step before the STS detector assembly. The sensors, microcables, read-out microchips have to be characterized individually. The larger building blocks such as detector modules and ladders have to be quality assured to ensure proper signal read-out from the sensor and the sensors spatial alignment on the ladder, respectively.

4.1. Silicon microstrip sensors

4.1.1. Optical quality assurance

After the procurement the sensors are checked optically for visible defects such as surface scratches, read-out strips and other electrical elements integrity. The metrology procedures are performed to qualify the sensor cutting edge and parallelism, its warp and thickness. So far the experiments using silicon microstrip sensors have performed the optical quality assurance and sensor metrology in a manual manner. This work is dedicated to the development of the automated optical quality assurance procedures and methods. The development is covered in the chapter 5.

4.1.2. Electrical quality assurance

The electrical characterization of the silicon sensor is an essential step to qualify the sensor performance. All sensors received during the preproduction stage have to be tested at the quality assurance centers. During the production stage a fraction of up to 10% of the sensors chosen randomly and those identified as faulty by an optical inspection have to be checked. Additionally 1% of the sensors, which corresponds to a single sensor from the batch, have to be tested in depth to verify the manufacturer data.

The electrical characterization is performed at three quality assurance centers: GSI, Darmstadt, University of Tübingen, Tübingen and JINR, Dubna. The equipment in all QA centers is nearly identical, however the electrical QA setup in the University of Tübingen features a custom build automated probe station, allowing the in-depth qualification of the sensor's electrical characteristics [50].

The basic tests are performed on all received sensors allowing to estimate the

sensor quality. These tests include measurement of current-voltage (I-V) and capacitance-voltage (C-V) characteristics of a sensor. From these measurements the full depletion voltage and breakdown voltage of the sensor can be extracted. Fig. 4.1 shows the I-V and C-V characteristics of the prototype sensors.

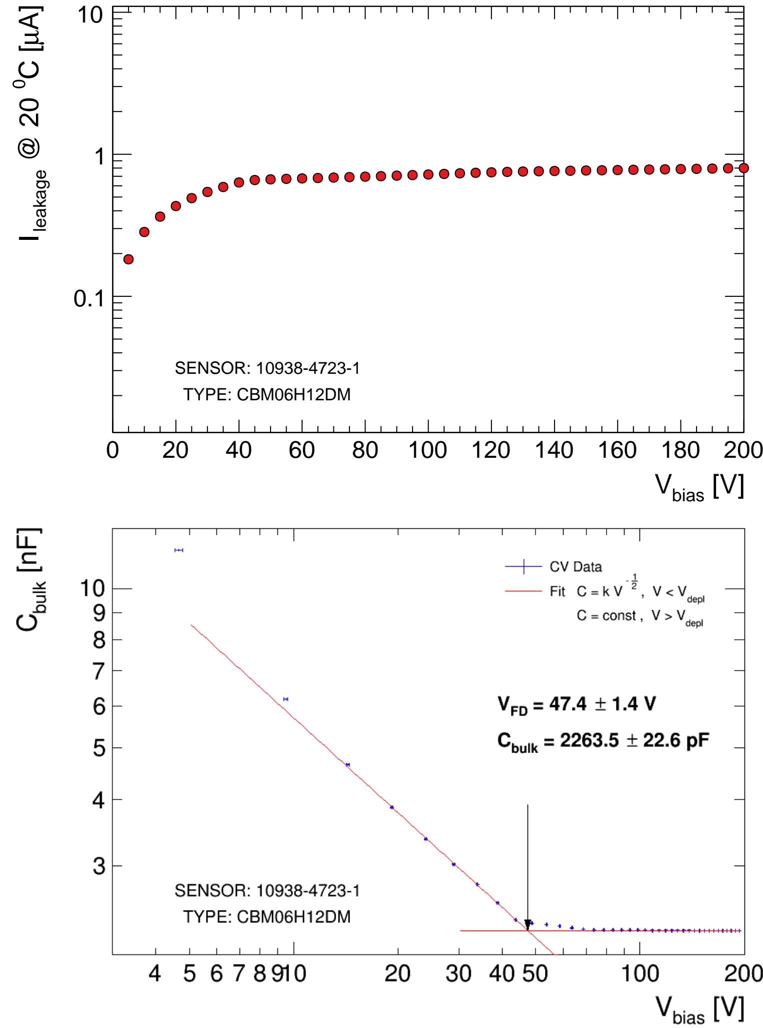

Figure 4.1.: The I-V (top panel) and C-V (bottom panel) characteristics of the prototype sensors measured during the electrical characterization at the University of Tübingen [50, 51].

During the subset tests (up to 10% of all sensor) the per-strip electrical measurements are conducted including the sensor's strip integrity and uniformity of the electrical properties. In this inspection the sensor is checked for the pinholes[1], measurements of the strip leakage currents and the coupling capacitances are performed. Fig. 4.2 shows the results of a pinhole scan. In this case the pinholes

[1]A short in the coupling capacitor between implant strip and read-out strip

(indicated with markers in the figure) were detected on the p and n-side of the sensor. The found pinholes correspond to the manufacturers data.

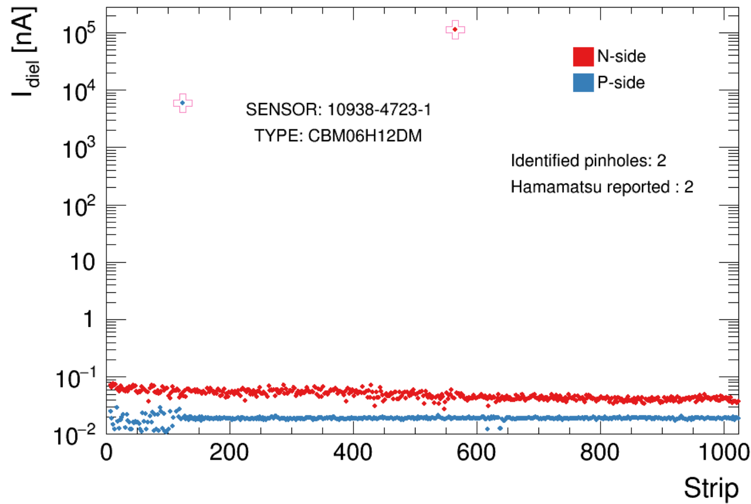

Figure 4.2.: The results of a per strip pinhole test for a prototype sensor [51].

The in-depth tests performed in the University of Tübingen on a smaller fraction of the sensors allow to characterize their more complex properties. These tests include the measurement of the interstrip capacitance, total strip capacitance, polysilicon resistance and coupling capacitor breakdown.

Further sensor performance studies are conducted on the non-irradiated and irradiated sensors to qualify the evolution of the charge collection efficiency and signal-to-noise ratio with fluence accumulated and annealing time as described in section 3.1.3.

4.2. Sensor microcables

The sensor ultralight microcables are essential to transmit the signal generated withing the sensor's silicon bulk to the read-out electronics, which is located in the periphery of the STS detector to decrease the material budget. The microcables have lengths between 10 and 50 cm which is determined by the sensor position on the ladder. The cable stack should have low total capacitance to minimize the noise. The electrical and optical quality assurance methods developed in the University of Tübingen allow to identify the electrical integrity of the individual traces of the cables as well as measure the total capacitance of the cable stack. Fig. 4.3 shows the obtained results for a sample microcable stack.

The individual signal layers of the non-assembled cable stack were inspected optically in this work. The developed automated methods and procedures are described in detail in the section 5.7.1. However the optical inspection of the microcables is only possible at the production site before their bundling into

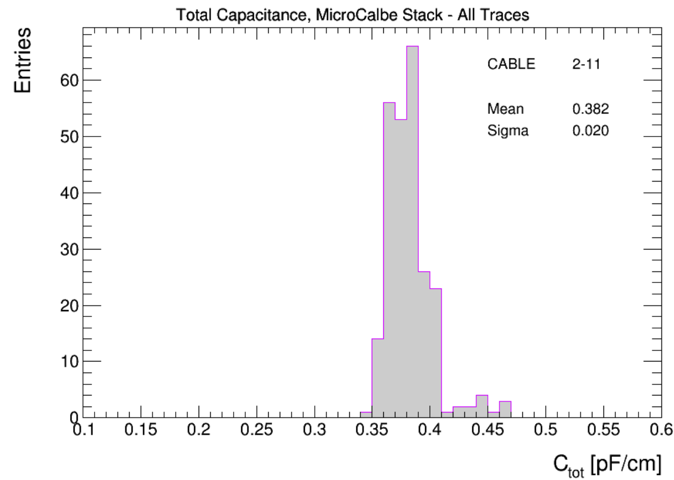

Figure 4.3.: Total cable capacitance distribution measured for a prototype microcable stack [51].

stacks. It was proposed to apply the inspection methods developed in this work at the production site.

4.3. Sensor ladders

The sensor ladders are important building block of the STS detector. The lightweight carbon fiber ladders carry the sensor modules. In order to control the quality of the assembled ladders the optical quality assurance methods and procedures were developed in this work. They are described in detail in the section 5.7.2. The developed methods provide the sensor spatial configuration information which enters the track reconstruction algorithms.

5. Optical quality assurance of the silicon sensors

The Silicon Tracking System detector of the CBM experiment will be built of about 900 silicon microstrip detectors. Because 100% of the sensors need to be inspected optically, the inspection methods and procedures should be highly optimized and automated. The optical inspection of the sensor's surface quality and its geometrical parameters is an important step before the detector assembly. Other experiments have already addressed this problem, this work however brings the optical inspection approach to the new level, when the images are acquired and analyzed fully automatically, the defects are identified and classified with flexible and powerful machine vision and machine learning algorithms. Furthermore, the geometrical and metrological parameters, such as warp, edge cut quality, and edge parallelism of the sensors are automatically measured.

This chapter describes in detail the development of the novel methods and procedures for the optical quality assurance of the silicon sensors of the CBM STS detector.

5.1. Optical setup

For the sensor quality assurance a modular and highly flexible optical setup was developed in the University of Tübingen. It features an XY motorized inspection table, a motorized Z-stage with a controllable zoom and focus stages. This setup allows the quality control of the surface and geometrical parameters of the silicon microstrip sensors.

5.1.1. Hardware and Setup

The base components of the optical inspection setup are the camera system mounted on a stable supporting frame and XY-linear stage to move the inspected object under the camera. The motorized Z-linear stage, focus and zoom stages give the setup flexibility to inspect the object under different conditions. The optical inspection setup built in this work is depicted in Fig. 5.1. It features a support frame made out of Item® 60×60 mm^2 aluminum profile resting on a massive granite table. An XY-linear table based on Faulhaber/Movtec® SMC-300 servo motors provides the moving range of 200 mm and 70 mm in X and Y

directions, respectively. This allows to mount and inspect all the STS sensors up to 124 mm. To inspect the newly considered 120 mm sensors the Y-stage has to be replaced by a larger one. A custom-made 3-zone vacuum chuck is attached to the XY stage to hold the different-size sensors 6.2×2.2 cm^2, 6.2×4.2 cm^2 6.2×6.2 cm^2 and 6.2×12.4 cm^2 sensors in place during the scanning. A Becker® 150 mbar abs. vacuum pump supplies the vacuum to the chuck. The Z-motor stage allows the vertical movement of the optical assembly in a range of 70 mm. The optical assembly consists of a motorized 12x zoom (0.58x - 7x) and a motorized 3 mm fine focus tube from Navitar®. The optical tube allows the direct light illumination by a ∅15 mm flexible light guide connected to a 590 lm, 5700 K model Roma LED3 direct light source from Starlight® company. The 5 megapixel microscope camera from Motic is attached to the optical tube with a C-ring connection. The vacuum pump bypass channel is controlled by an electromagnetic relay, allowing to release the sensors from the vacuum suction. The full list of hardware can be found in the appendix A.

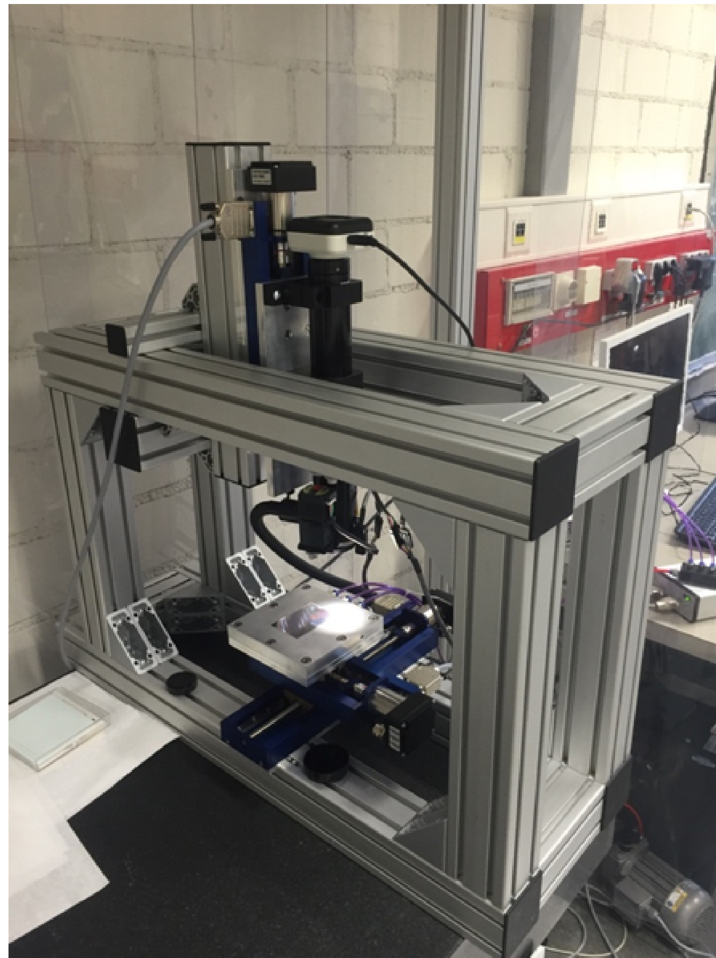

Figure 5.1.: Setup for the optical QA consisting of an XY-table and a microscope system.

The setup is installed in a clean area during the pre-production stage. At the production stage it will be installed in a clean room with a temperature 21 ± 2 ℃ and a humidity control. The required clean room class is 10000 (ISO 4 DIN EN ISO 14644-1) or better.

The setup is controlled with a PC running LabVIEW 2013 software [52]. The software features low hardware dependence and scalability. This means that any part of the setup could be replaced with a different hardware. The corresponding software is quickly set up by writing a driver for the API (Application Programming Interface) in order to be used with the control program.

5.1.2. Overview of the machine vision algorithms

The images obtained during the scan are processed with a variety of machine vision algorithms. They allow to do basic color and geometry manipulations as well as, when combined together, do sophisticated morphological analysis and defect finding. This section provides an overview of these algorithms as they will be often referred to throughout this work.

5.1.2.1. Geometrical transformations

The images obtained during the sensor scan often are rotated arbitrarily depending on the sensor misalignment on the vacuum chuck. In order to account for this effect, the images are rotated by the angle extracted during the calibration step. After rotation the sensor image is aligned properly with respect to the optical axis and can be used for further analysis. Fig. 5.2 shows the source image of a misaligned sensor and the corrected image.

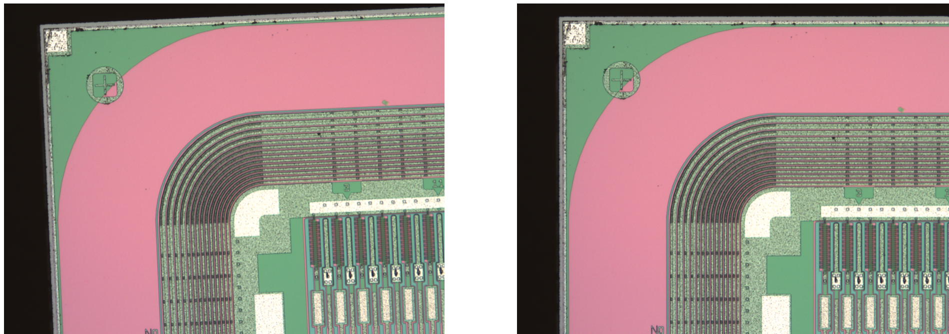

Figure 5.2.: The rotation correction of an image taken from misaligned sensor. The left panel shows the source image, the right panel shows the corrected image rotated by about 2.5 degrees clockwise.

The image rotation transformation is a provided by a *Geometry* tool from NI Vision package. Other options available for image geometry transformation are symmetry transformations, image resampling which allows to shrink the image and change its resolution if needed.

5.1.2.2. Color adjustment

Sometimes the color of the captured image should be corrected. It is needed to be adjusted, for example, for the images taken with a wrong exposure setting of the camera. At this step the brightness, contrast and the gamma of the image or individual color component (red, green or blue) can be adjusted. The color adjustment is provided by the *Brightness* tool from NI Vision package [53].

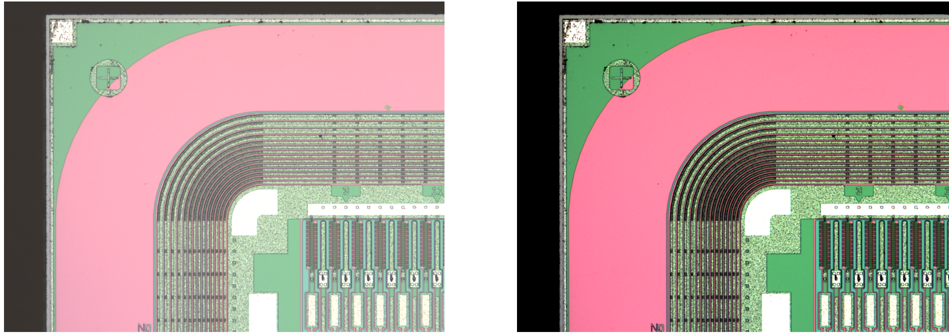

Figure 5.3.: The color adjustment principle of an image taken with a wrong exposure value of the camera, here overexposed. The source image (left panel) is adjusted for its brightness and contrast yielding sharper edges and more saturated colors (right panel).

Fig. 5.3 shows the color overexposed source image taken from the camera and the image with color adjustment applied. The adjusted picture has sharper edges, which improves the results of other machine vision algorithms such as edge detection.

5.1.2.3. Color operators

The *Color Operators* tool from the NI Vision package allows to apply arithmetical or logical operations on images. It allows the per-pixel addition, subtraction, multiplication, etc. by a constant color. Additionally the per-pixel arithmetical and logical operations are supported between two images. This allows to mask parts of the image by a boolean criterion or apply non-trivial image overlays as illustrated in Fig. 5.4.

Fig. 5.4 shows the overlay applied to the source image. Here the AC pads of a prototype sensor were detected with other machine vision algorithms and added to the source picture. This functionality is used extensively in the reporting module of the software solution developed in this work (cf. section 5.8) which allows to examine the results of automated inspections.

5.1.2.4. Color plane extraction

The extraction of color planes is an important step to process the sensor images acquired at different regions of interest. The extraction of a color plane allows to

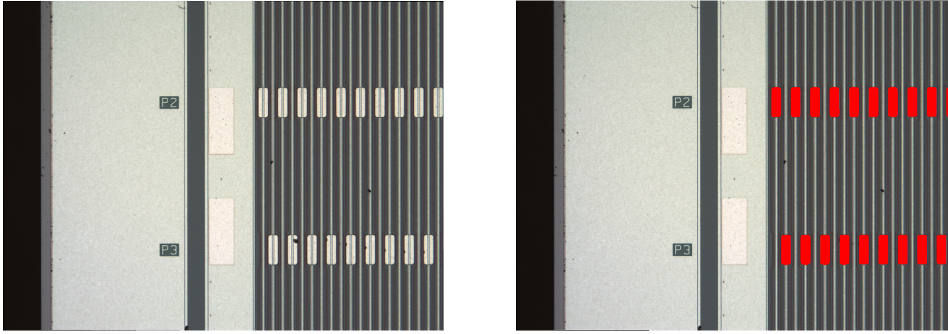

Figure 5.4.: The use of the Color Operator tool illustrated. The AC pads on the source image (left panel) are detected and overlaid with the per-pixel addition (right panel).

underline different aspects of a defect. The *Color Plane Extraction* tool from the NI Vision package allows to extract the red, green or blue pixel color planes to access the respective pixel components of a colored image. Alternatively the hue, saturation and luminance planes can be extracted.

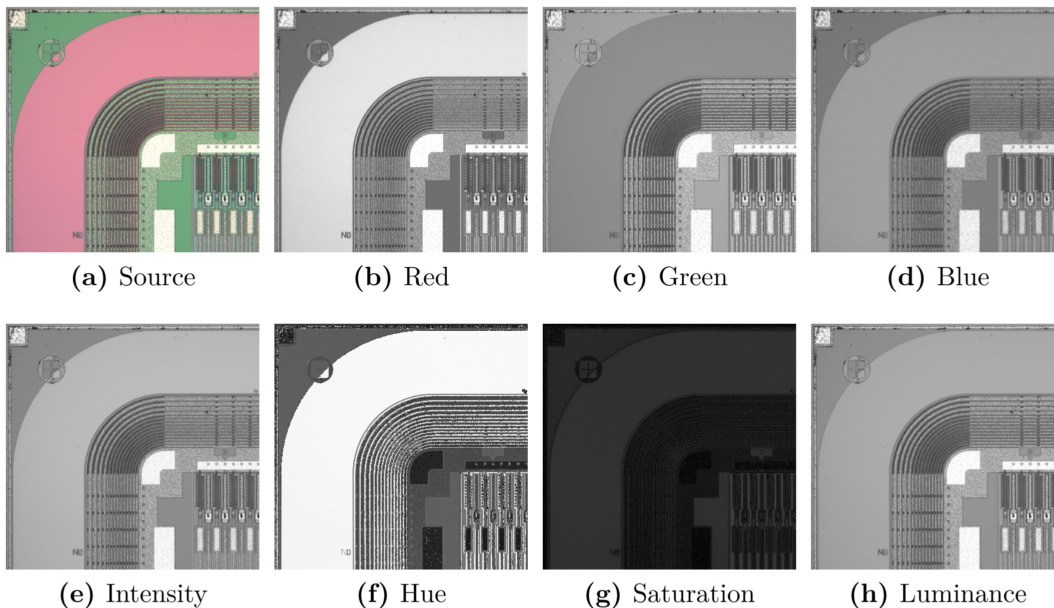

(a) Source **(b)** Red **(c)** Green **(d)** Blue

(e) Intensity **(f)** Hue **(g)** Saturation **(h)** Luminance

Figure 5.5.: An overview of different color planes extracted. Image is taken in the corner region of the CBM06C6-353090-11 prototype sensor.

Fig. 5.5 shows an overview of different color planes extracted with the described algorithm. Here only the pixel brightness values between 0 and 255 were preserved, effectively turning the image grayscale.

In this work majority of the inspection algorithms use the luminance plane to preserve the overall brightness information of the image being analyzed, while

keeping the red, green and blue color components not suppressed. The color plane extraction allows to transform the image from a 32 or 24-bit format to a 8-bit format. The 8-bit format images are required in order to use other specific image processing algorithms, such as image filters, pattern and texture matching and others.

5.1.2.5. Image filtering

The images taken from the camera can be transformed with different filters to smoothen, highlight details or detect edges. These transformations are mostly done by the image convolution [54] with different kernels. A convolution is computed as follows:

$$V = \left| \frac{\sum_{i=1}^{k} \left(\sum_{j=1}^{k} f_{ij} d_{ij} \right)}{F} \right|, \tag{5.1}$$

where V is the output pixel value, f and d are the kernel and data matrices to be processed, k is the kernel size and F is the weighting applied, which is a sum of kernel coefficients. Eq. (5.2) shows the selected kernels commonly applied for the image filtering in this work.

$$\underset{Gaussian}{\begin{bmatrix} 1 & 2 & 4 & 2 & 1 \\ 2 & 3 & 8 & 4 & 2 \\ 4 & 8 & 16 & 8 & 4 \\ 2 & 4 & 8 & 4 & 2 \\ 1 & 2 & 4 & 2 & 1 \end{bmatrix}} \quad \underset{Highlighting}{\begin{bmatrix} -1 & -1 & -1 & -1 & -1 \\ -1 & -1 & -1 & -1 & -1 \\ -1 & -1 & 30 & -1 & -1 \\ -1 & -1 & -1 & -1 & -1 \\ -1 & -1 & -1 & -1 & -1 \end{bmatrix}} \quad \underset{Laplacian}{\begin{bmatrix} -1 & -1 & -1 & -1 & -1 \\ -1 & -1 & -1 & -1 & -1 \\ -1 & -1 & 24 & -1 & -1 \\ -1 & -1 & -1 & -1 & -1 \\ -1 & -1 & -1 & -1 & -1 \end{bmatrix}} \tag{5.2}$$

Fig. 5.6 shows the results of image processing with different filters. The panel a) shows the source grayscale image. The panel b) shows the result of applying Gaussian smoothing filter used to decrease the variations of light intensities in the pixel neighborhood. The panel c) shows the highlighting convolution which increases the contrast of the pixels. The panel d) shows the Laplacian edge detection filter which extracts the contour of the objects and outlines the details. The panel e) shows the example of a Canny filter [55] which extracts only the edge information greatly reducing the rest amount of data to be processed. The image filtering and transformation is provided by the *Filters* tool from the NI Vision package.

5.1.2.6. Edge detection

The edge detection is an important application of the machine vision algorithms in this work. It allows to detect the object boundaries by analyzing the pixel intensity variations. Depending on the measurement purpose, the edge detection

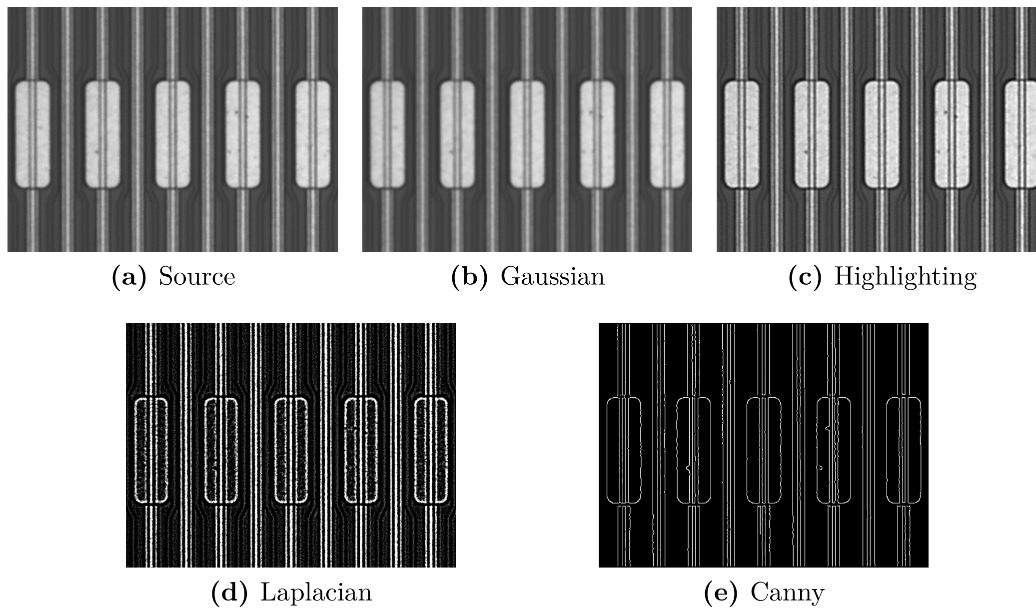

(a) Source **(b)** Gaussian **(c)** Highlighting

(d) Laplacian **(e)** Canny

Figure 5.6.: An overview of different image filters applied to a source grayscale image.

can be used to detect the edges along a single line, extraction of the straight edges or tracing the contours of the object.

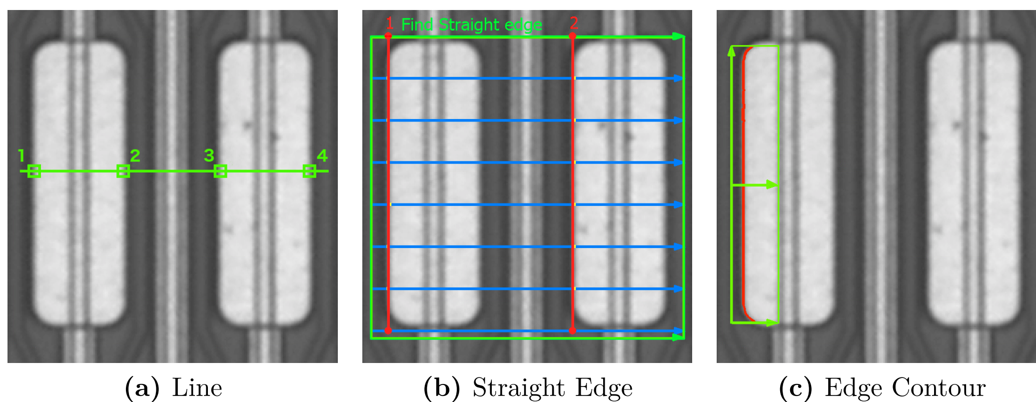

(a) Line **(b)** Straight Edge **(c)** Edge Contour

Figure 5.7.: An overview of different edge detection algorithms.

Fig. 5.7 shows different edge detection algorithms applied.

The left panel shows the edge detection along a single line. Here both dark to bright and bright to dark edges exceeding the set threshold are detected. On this example the width of an AC pad can be measured and controlled. This algorithm is available in the *Edge Detector* tool from the NI Vision package.

The middle panel shows the straight edge detection principle. Here the edges along multiple lines separated by a spacing parameter are detected. The search direction is left to right. The dark to bright edges detected are then fitted with a

straight line. The fit is weighted either by averaging or by median. This algorithm is available in *Find Straight Edge* and *Advanced Straight Edge* tools from the NI Vision package.

The right panel shows the edge contour tracing principle. Here the edges are detected, left to right, with no spacing, e.g. pixel by pixel. The extracted contours can be analyzed for their curvature and length or can be compared with a template edge to analyze the deviation from a preset edge profile. This algorithm is available in the *Contour Analysis* tool from the NI Vision package.

5.1.2.7. Pattern matching

The pattern matching algorithms [56] allow to compare the image under test with the reference images. In the simplest representation of these algorithms the pixel intensities of the reference image are compared with the regions of the source image. If the intensity difference for a certain region is lower than a set threshold a match is found. The *Pattern Matching* tool of the NI Vision package provides a number of different optimized pattern matching algorithms allowing to search for rotated and scaled patterns. These algorithms are used extensively in this work. The sensor alignment calibration uses the matched alignment marks to extract the sensor positioning on the vacuum chuck. Both color and grayscale pattern matching are supported.

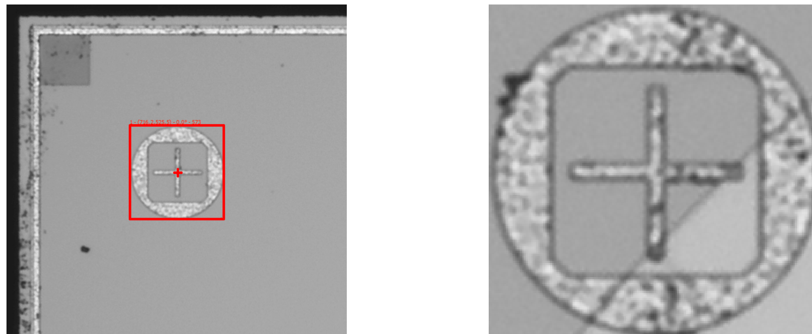

Figure 5.8.: An alignment mark detected on the corner of the prototype sensor from CiS (left panel) with a template (right panel).

Fig. 5.8 shows the detection of the alignment mark on the corner of a sensor. Note, that the reference image was taken from another sensor of the newest generation and applied to the earlier generation sensor. Here the pattern was matched with a Grayscale Value Pyramid algorithm [57] with the matching score 573 out of 1000. The score shows the discrepancy between the detected feature and the reference image.

The pattern matching is further used in this work to detect (and estimate their quality based on detection score) the electrical elements of the sensor like AC and DC pads, bias resistors and others.

5.1.2.8. Texture matching

Texture matching is an advanced analysis method, which allows to look for any deviation from the self-repeating reference image which could be seen as a texture of the object under test. This is very useful for the central regions of the silicon sensors where the read out strips are located, which is more than 95% of the sensor. The method is based on the wavelet transformations [58] and calculation of co-occurrence matrices. Various metrics of these matrices are called the Haralick features [59]. Fig. 5.9 shows the dissimilarity, contrast, homogeneity, correlation, entropy metrics (smaller panels) extracted for a source image (larger panel). Fig. 5.10 shows a scratch defect detected with texture matching algorithm. Left panel shows the source image, right panel shows the detected defect overlaid over the source image.

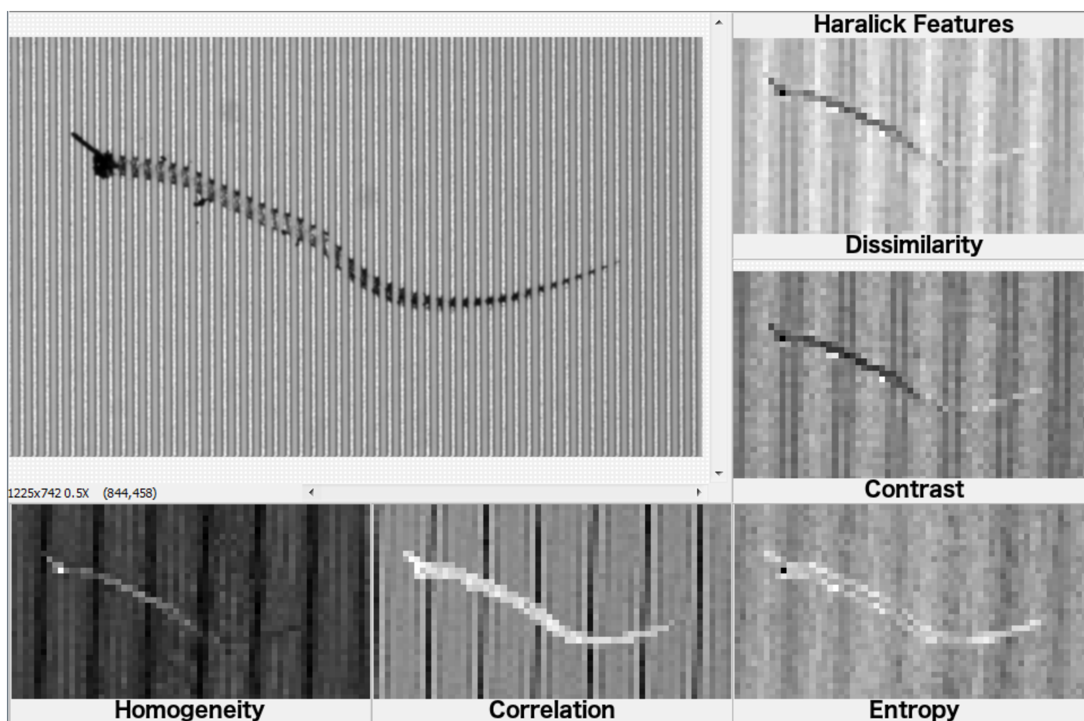

Figure 5.9.: Source image with a defect on a texture (larger panel) and calculated Haralick features, as seen in the Texture training interface of NI Vision. The features extracted are (from top to bottom, from left to right) dissimilarity, contrast, homogeneity, correlation, entropy.

The disadvantage of the texture matching method is that the type of the resulting defect (deviation from the texture) is unknown. However, this still can be assessed with a further analysis to classify the defect.

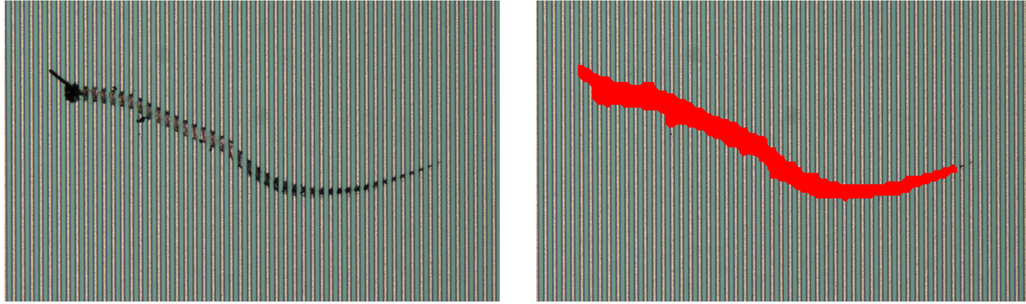

Figure 5.10.: A scratch defect detected with the texture matching algorithm.

5.1.2.9. Caliper

The *Caliper* tool provides the access to the geometrical calculations based on the reference points obtained on the previous steps like edge detection. Most commonly used functions used in this work are the distance measurements, calculation of perpendicular projections, line intersections and angles between lines. The caliper allows to analyze the sensor cutting edges and parallelism, measure the sensor thickness and other measurements.

5.1.2.10. Color thresholding

The *Color Threshold* tool allows to convert the analyzed images to the binary images. The threshold levels can be configured manually or with more advanced approaches like computing the cross-entropy between background and foreground regions, color clustering and inter variance [60, 61]. The thresholding can be configured to look for dark, bright or gray objects in order to reliably extract the appropriate features. Fig. 5.11 shows an example of the color thresholding, the left panel shows the source image, the right panel shows the resulting binary image. Note, that the thresholding here was on purpose done not optimal. This image will be used further in text.

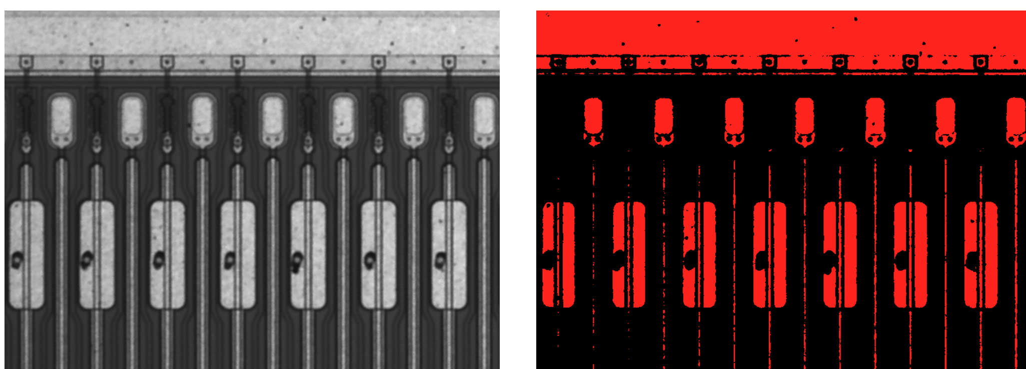

Figure 5.11.: Example of the color thresholding for gray objects.

5.1.2.11. Binary image morphology

Having the image thresholded and converted to a binary format, a number of machine vision algorithm can be applied for further transformations. The *Basic Morphology* and *Advanced Morphology* tools provide the possibilities to erode, dilate, close the objects using different transformation kernels. Additionally the falsely detected background objects could be filtered out based on their sizes or other metrics.

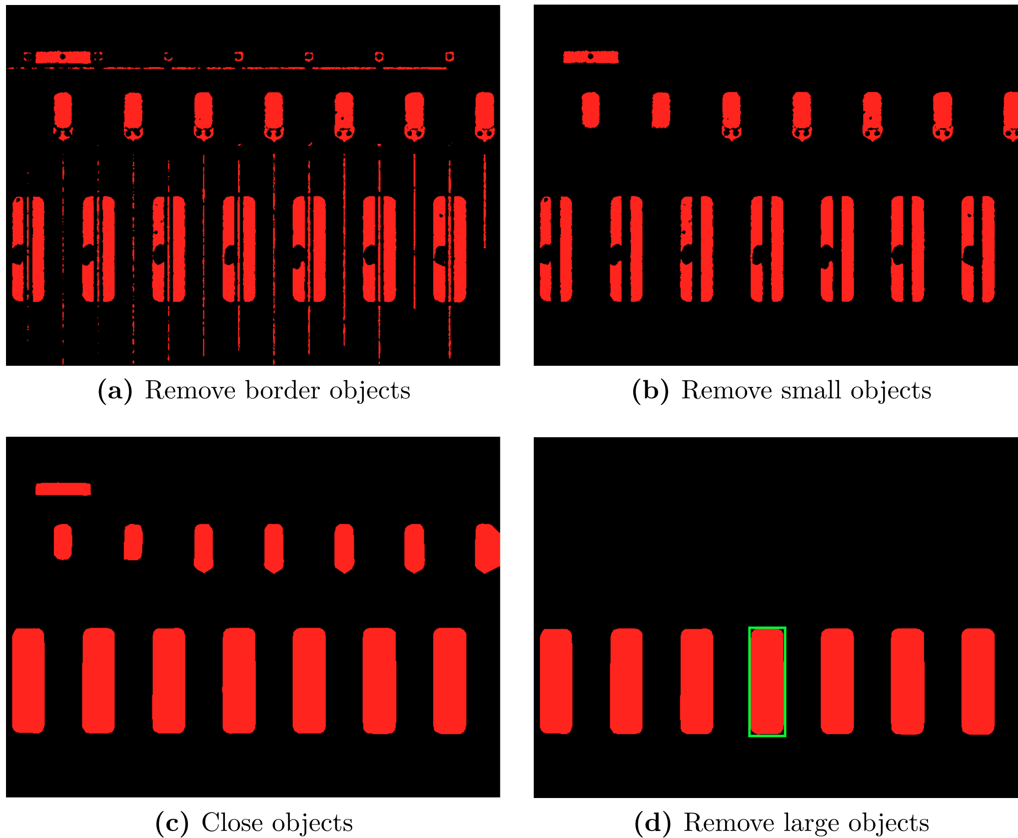

(a) Remove border objects

(b) Remove small objects

(c) Close objects

(d) Remove large objects

Figure 5.12.: Example of the binary morphology algorithms applied in series.

Fig. 5.12 shows the binary morphology algorithms applied in series. Here the last image of the Fig. 5.11 is taken for further analysis. The panel a) shows the results after removing the border objects. The panel b) shows the results after small objects removal. The panel c) shows the results after applying convex hull [62, 63] and object close algorithms to fill the gaps. The panel d) shows the results after removing of large objects, with a size threshold set to keep pad objects. After background removal the binary image is now ready for further analysis.

5.1.2.12. Particle analysis

When the image is cleaned up from the background objects as shown in Fig. 5.12, the extracted objects are analyzed with the *Particle Analysis* tool. Here a large variety of the object information is extracted: the position of the object on the image, its perimeter, area, the ratio between the object area to image area etc. Additionally the elongation, compactness and circularity factors are available. These factors allow to determine if object has a rectangle or circular shape and is useful for further analysis. The information extracted is available in pixels and as well in real-world units, if the image was previously calibrated by the *Image Calibration* tool.

The particle analysis is used as well to recognize and interpret the information put on a sensor's scratch pads. There are in total 16 small pads grouped by 4. They are used for sensor unique identification.

Figure 5.13.: Detection of the scratched pads.

Fig. 5.13 shows the example of the scratch pad detection. By analyzing their presence and position, the associated information (16 bits in total) about the sensor is decoded.

5.2. Optical axis calibration and characterization

It is very important to calibrate and characterize the optical axis of the inspection system. It allows to correct for image distortions, estimate the precision of the measurements, extract various properties of the optical system (field of view, depth of field, pixel-to-μm conversion factors, etc.). This chapter will cover the automated, hardware independent methods developed for the calibration and characterization of the optical axis.

5.2.1. Distortion corrections

Image lens distortions

The motorized zoom and focus optical assembly from Navitar employed in this work uses the conventional spherical lens objective. This renders the images taken subject to image lens distortions. Eventual use of the telecentric objective would mitigate the lens distortion problem, however, the use of autofocusing for the height measurements described in the section 5.5.1.1 will be impossible.

The effect that for a spherical lens the distance between points projected from a source to the sensing plane is not scaled linearly is called the fish eye effect or a barrel distortion. Fig. 5.14 shows an example of a barrel distortion (panel **b**) together with other distortion types for comparison.

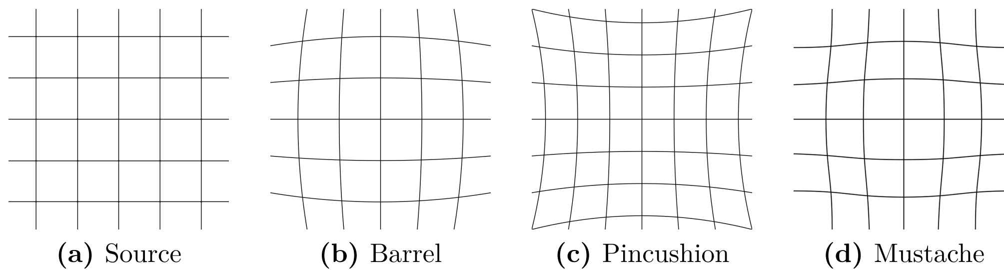

(a) Source **(b)** Barrel **(c)** Pincushion **(d)** Mustache

Figure 5.14.: An overview of the image lens distortions. The panels show the source image, barrel, pincushion and mustache(a combination of barrel and pincushion) distortions.

To quantify the effects and to correct for barrel distortions a dot array calibration plate can be used. Fig. 5.15 shows an example of a dot array calibration grid which is commonly used for distortion corrections.

The optimal array dot size and spacings for the optical system used in this work are estimated based on the field of view calculations [64, 65]. The individual dots should be visible and detectable at lowest magnification and as many as possible should be visible at highest magnification. The 50 μm dot size and 100 μm dot spacing have been chosen. Tab. 5.1 shows the summary of the estimation.

Magnification	FOV, μm	Dot size, px
0.58x	9831.2	13
1x	5704	23
7x	814	159

Table 5.1.: Summary for the dot array estimation for a 50 μm dot size and 100 μm dot spacing

The barrel distortion correction is done using the NI Vision software package.

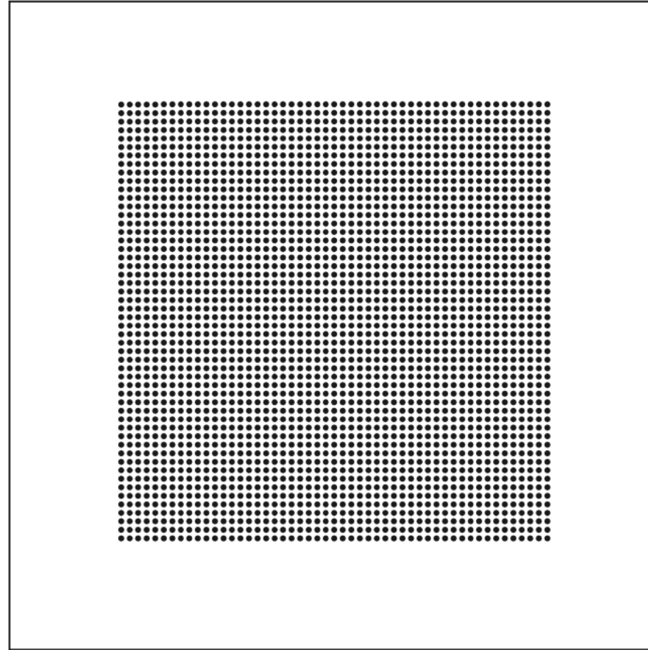

Figure 5.15.: An example of a dot array calibration plate.

The dots of the calibration plate are recognized by the detection algorithms, their centers and spacings are taken into account. Then, using a polynomial distortion model based on a Brown-Conrady model [66, 67] the dot corrected positions are calculated. The residuals from this normalization are represented as the vectors of correction size pointing into the direction of the corrected position.

Fig. 5.16 shows the vector field of the residuals. The vector sizes are scaled by a factor of 45 for the presentation purposes. Note, that the distortion central point in this example does not correspond to the image central point. This effect arises from the fact that in this example optical axis is not calibrated for parcentricity.

As an alternative to using dot arrays, any other reference object could be used for the calibration, if the precision of the motor stage is good enough. In this approach an alignment mark of a silicon microstrip sensor is taken as a reference. By moving the object table with the reference object under the microscope camera and detecting its central point position with the pattern matching algorithms the dot grid arrays are created. For this approach it is important to keep the spacing between the dots constant and cover as much image area as possible for the distortion correction algorithms to provide the best accuracy.

Vignetting distortion and flat field correction

In optical systems the objects are illuminated in various ways, for example by indirect illumination or by using ring or direct light sources, based on the properties of the objects inspected. Depending on the parameters of the illumination

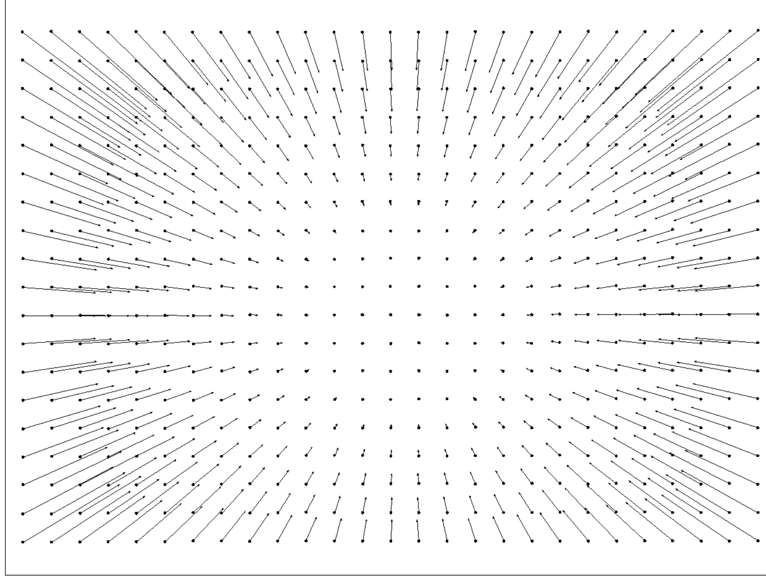

Figure 5.16.: Correction for the barrel distortions of the image. The errors are scaled by a factor of 45 for presentation purposes.

used, the optical axis misalignment, the object surface non-linearity and lens effects the object might be lit unevenly. This effect is called vignetting or bright field distortion. It is most clearly seen on the lowest magnification powers of the optical system, where the light spot size is comparable with the system's field of view. Several approaches exist to correct for the vignetting (e.g. [68] or [69]). In this work we use the *Flat Field Correction* tool set from the NI Vision package to account for these effects. It supports several ways of correcting the lighting distortions. One could use mathematical bright field modeling. The background estimation methods supported are: polynomial with specified degree, background correction by color thresholding and Niblack [70, 71] binarization (eq. (5.3)):

$$T(x,y) = m(x,y) \cdot \left[1 + k \cdot \left(\frac{s(x,y)}{R} - 1\right)\right], \tag{5.3}$$

where $m(x,y)$ and $s(x,y)$ are the mean value and standard deviation calculated in the processing window, k is the thresholding parameter, R is the filter radius.

The use of mathematical models is advised if there is no possibility to acquire an image of the background only. Fig. 5.17 shows an example of the Niblack model correction output (denoted in red) overlaid on the original image. The processing window is set to 32×32 pixels and the thresholding parameter k is set to 0.2. The patterned profile depicts the uneven lighting of the source image. The field center does not correspond to the image center, indicating slight misalignment of the coaxial lighting axis relative to the optical axis.

Another approach for the correction of the vignetting distortion is to acquire a number of images of the monochromatic background only, for instance, images

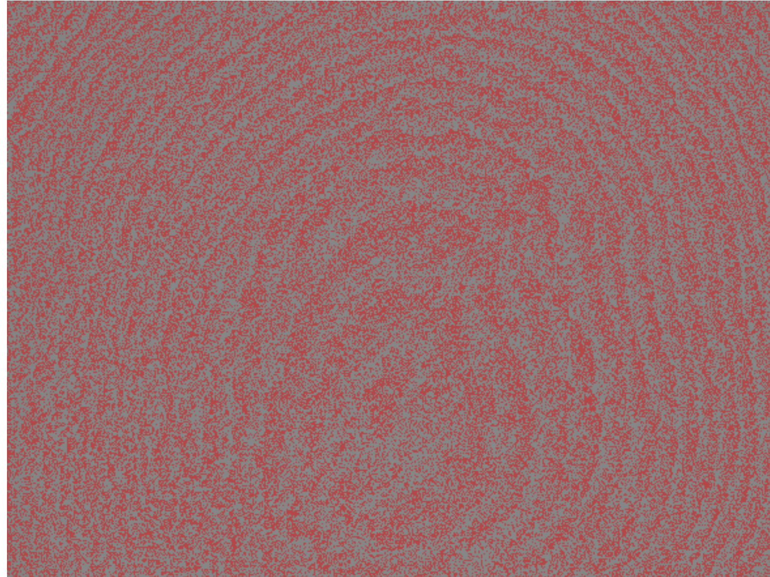

Figure 5.17.: Example of the Niblack correction for the bright field distortion.

of the calibration plate region without calibration crosses visible. This approach allows to estimate the bright field by computing an average or median metric for the image set. In this approach the mean or median color channel brightness is calculated for the entire image (or a set of several images for the best result). The standard deviation around the mean or median value shows the unevenness of the background.

In order to further improve the flat field correction, the so called dark field (or dark frame) pattern is measured. It allows to account for the camera gain, pixel pedestals and temporal noise due to the dark currents (covered in [72] for CMOS and in [73] for CCD sensors). This is done by tightly covering the camera sensor and take digital images in the absence of light. The images taken for the digital camera used in this work show, that in the absence of light, the color channel brightness values do not correspond to a value of 0 (for the black color) but rather to a value range between 12 and 15, which indicates the temporal noise in a pixel around the pedestal levels. The computed dark field pattern further improves the flat field correction.

Fig. 5.18 shows the flat field correction by applying the trained bright and dark field patterns. This correction allows to lower the image brightness unevenness (or standard deviation around mean value) from 14 units down to 3 units of brightness per color channel.

5.2.2. Focus stage

In order to characterize the focus motor stage of the optical axis a set of calibration algorithms have been developed. The calibration is done with a certified

Figure 5.18.: Principles of the correction for the flat field distortions. The images are downsampled artificially for the presentation purposes. This allows to illustrate the unevenness of the light spot. The left panel shows the source image of the background with the light spot from the coaxial lighting visible. The middle panel shows the thresholded image. The right panel shows the corrected image.

micrometer precision gauge block set from Mitutoyo Corp. [74]. The gauges from the set have exceptional surface flatness allowing to cold-weld them together for a short time, hence the height of a gauge stack is exactly the sum of the heights of individual gauges. This allows one to cover the full range of the heights possible to measure with the autofocusing algorithms introduced in this work (see section 5.5.1.1).

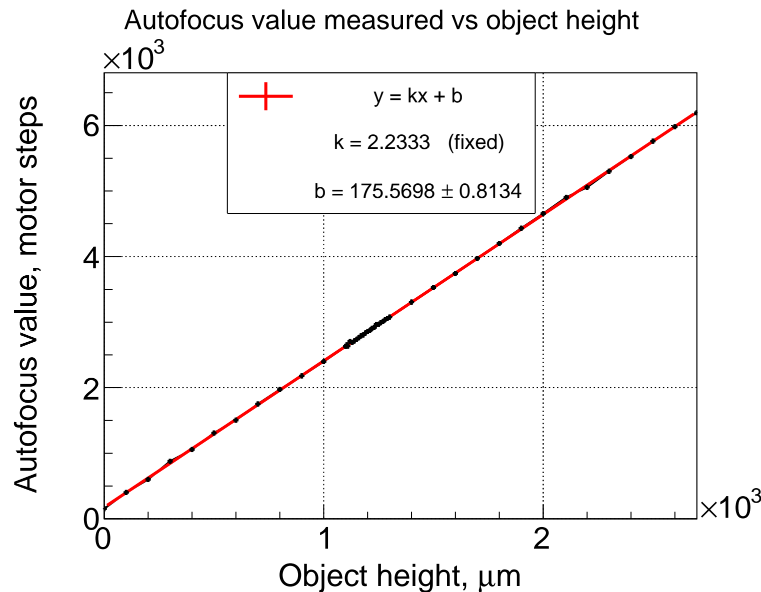

Figure 5.19.: The autofocus values measured for different object heights.

Fig. 5.19 shows the measured autofocus value for different gauge (or gauge stack) heights. The dependence fitted with a linear function with a slope coefficient $k = 2.2333$ which exactly corresponds to the motor steps to micrometer conversion ratio for the focus motor stage used.

5.2.3. Zoom stage

The optical axis of the optical inspection setup consists of the digital microscope camera, the 1x magnification extension tube and motorized zoom and focus stages. The Z-stage of the closed-loop linear motors allow them to be moved in vertical direction adjusting the focused position to inspect different objects placed on the inspection table.

In order to characterize the optical axis and establish the dependencies of its properties with respect to the zoom motor stage, an automated calibration algorithm set has been developed. In the following paragraphs the different aspects (such as the optimal camera exposure time, parfocality, parcentricity, etc.) of the system are described and dependencies between them are extracted.

Exposure time

First, as the base for all following measurements, the dependence of the optimal digital camera exposure time on the zoom should be extracted, to guarantee the optimal lighting conditions. When zoomed in, given that the external lighting is not adjusted in the progress and stays the same, the field of view decreases, as does the amount of light reflected back to the camera sensor, thus the camera exposure time should be increased. This allows for more light collection and brighter images acquired. And vice versa, when zoomed out, the field of view and the amount of light collected by the camera increases and the exposure time should be decreased to lower the brightness of the images acquired. For the calibration routines described below a calibration cross from the macro calibration plate was used (Fig. 5.20).

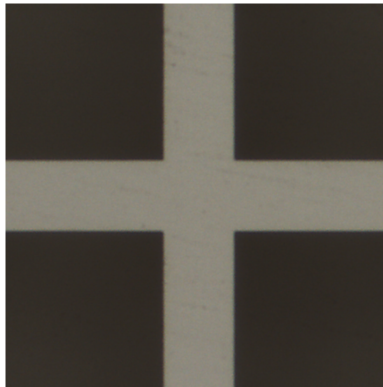

Figure 5.20.: A close-up image of the reference calibration cross used for various measurements in the zoom calibration.

The approach used for the exposure time calibration is as follows. We define an image to be well illuminated if its brightness per color channel corresponds to a mean value of 150 within the measurement window of 32×32 pixels. Then we

step throughout the full zoom motor stage range and on every step adjust the camera's exposure time accordingly to reach the same brightness levels. Due to the hardware limitations, the camera's exposure time could be changed only in discrete steps of around 0.25 milliseconds, thus the brightness value of 150 could be reached only within a certain error. This is reflected by the vertical error bars in the Fig. 5.21, which shows the data obtained fitted with an exponential function.

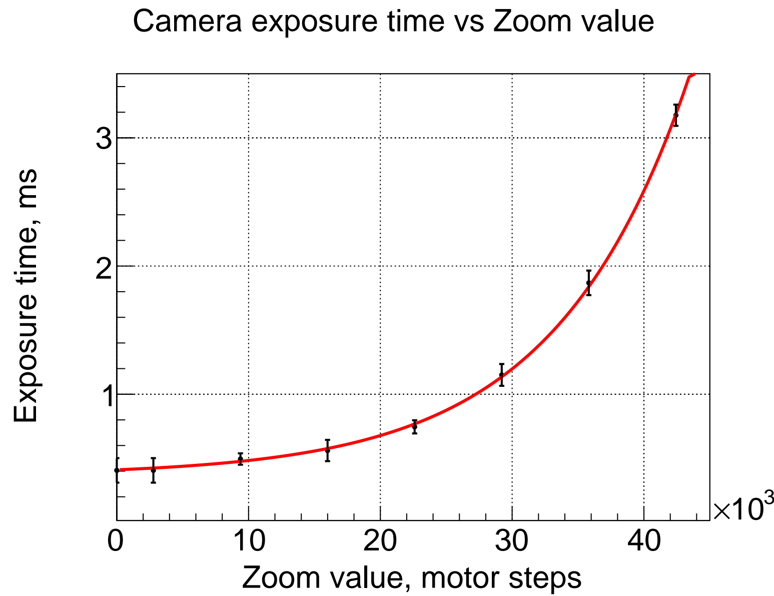

Figure 5.21.: The dependence of the camera exposure time on the zoom value extracted from the calibration.

Parcentricity

A parcentric optical system by definition has the centers of its optical lenses and camera sensor aligned along one axis. In order to establish if the optical system is parcentric, the images of a still object are taken at different zoom values, e.g. if the image of the object does not get displaced while changing zoom. This technique was used in the automated calibration algorithm set to establish the discrepancy from the parcentricity and correct for it.

As a reference object, the cross of the calibration plate have been chosen. The object was aligned under the microscope such, that the center of the image taken corresponds to the crosses' top-left edge (see Fig. 5.22 for reference). Then the system zoom value was changed throughout the whole value range and the distance from the center of the image to the fitted top-left edge was measured in X and Y directions.

Fig. 5.23 shows the obtained parcentricity deviations for an unaligned optical

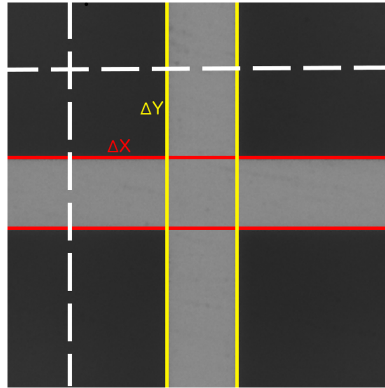

Figure 5.22.: The close-up visualization for the parcentricity discrepancy measurement. The center of an acquired image is denoted by a white dashed line. The distances are measured to the fitted edges of the cross.

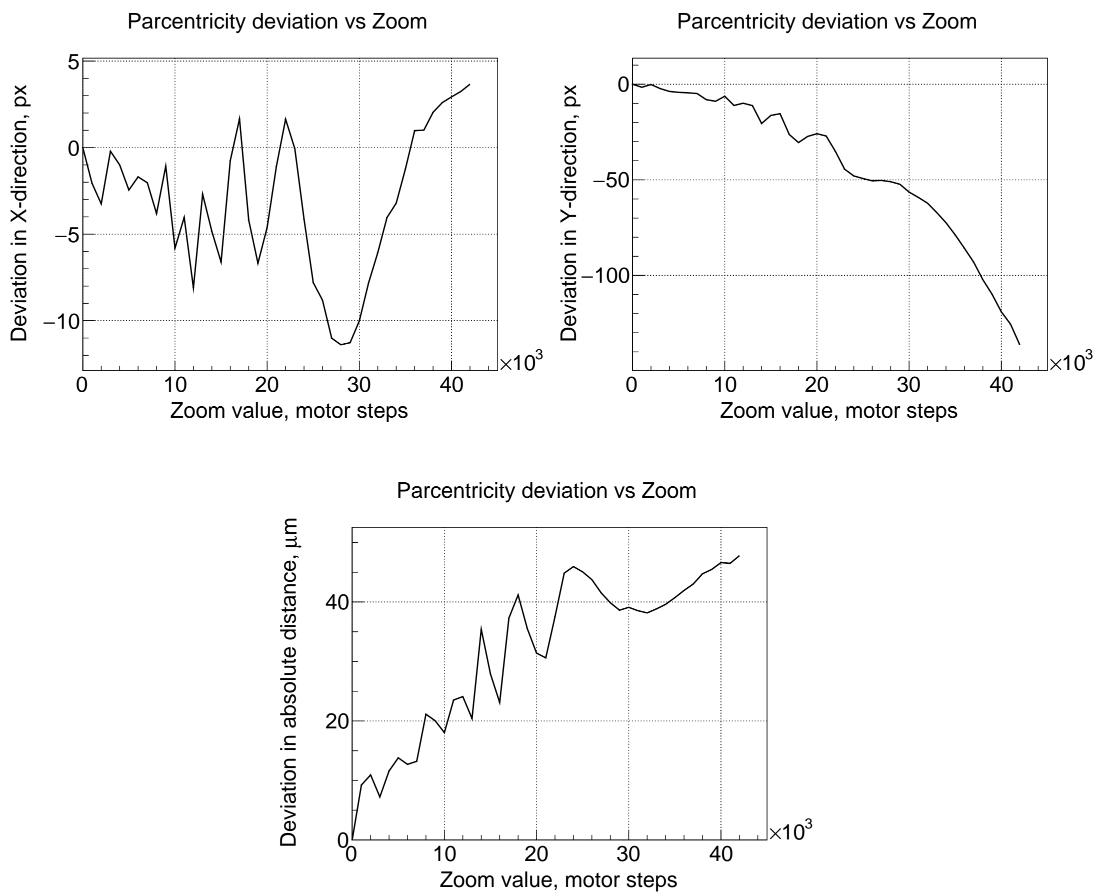

Figure 5.23.: Parcentricity deviation in X and Y directions measured in pixels (top left and top right panels, repsectively) and absolute distance deviation measured in micrometers (bottom panel)).

axis. The top two panels show the parcentricity deviation measured in pixels along the X and Y directions. The bottom panel shows the absolute distance deviation in micrometers. For an aligned and parcentric system, the deviations should be zero when zoom value is changed, resulting in flat trends. If the corresponding alignment adjustment is not available, the parcentricity can be achieved artificially by the XY-table adjustment extracted from calibration.

Parfocality

The camera exposure time dependence extracted on the previous step allows to provide the optimal lighting conditions throughout the whole range of the zoom motor stage. The next issue to be addressed in the optical axis calibration is the parfocality of the system. A parfocal lens system allows the observed object to stay sharply focused when its zoom value changes. It is possible to configure the microscope systems to be parfocal mechanically. However, due to many degrees of freedom it is a rather tedious task. Even after good mechanical arrangement the small focus error remains. This effect is negligible at low magnification when depth of field is rather large, however it becomes more significant at higher magnifications when the depth of field becomes very narrow. The calibration algorithm provides a way to mitigate this influence by adjusting the focal length of the system not by changing the focus motor stage value, but by adjusting the system vertical position with the Z motor stage.

In this series of measurements the focus value is set to a predefined value, then a zoom stage scan is performed. During the scan at each zoom stage position the autofocusing algorithm finds the most focused position as described in section 5.5.1.1. The Z motor stage position is corrected by the difference between the focus reference and measured value.

Fig. 5.24 shows the obtained data. Since there is a strong correlation between the Z motor stage position and the optimal focus stage position (they both change the focal length of the system), they can not be disentangled easily or described by a simple model. Rather, the data obtained is fitted with a high order polynomial function. The extracted dependence provides the means to correct for the parfocality error of the optical system and ensure the sharpness of the image obtained at any magnification power.

Magnification

To estimate the dependence of the system's magnification power from the zoom value, a series of measurements were carried out. In these measurements at every zoom value the pixel width of a reference object from the calibration plate have been measured and compared to its real value. The reference object of the available calibration plate is a cross of 1×1 cm^2 size with a line thickness of 100 μm. The crosses are produced by photolitography process with the

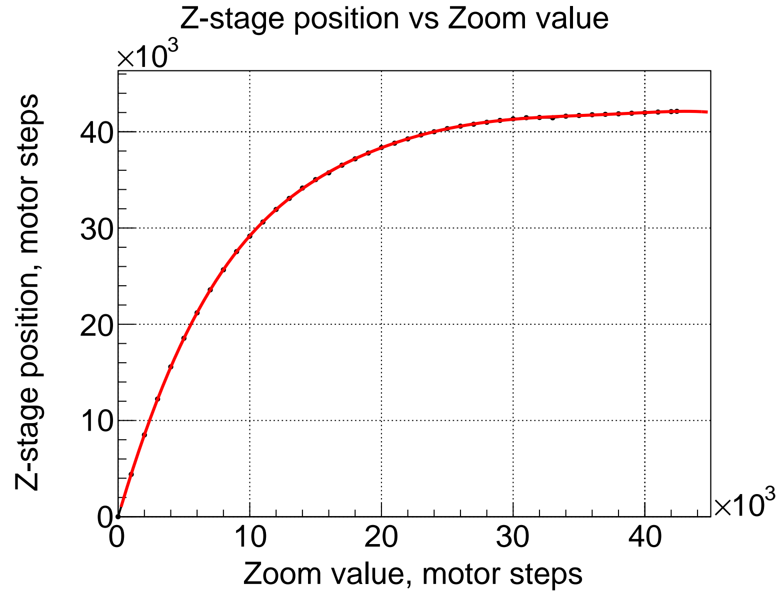

Figure 5.24.: The dependence of the Z-stage position of a linear motor stage on zoom value extracted from the calibration. It provides the means of parfocality corrections.

chrome structuring elements deposited on a fused silica substrate with a precision $< \pm 0.5$ μm. In order to measure the cross' line thickness the edge detection algorithms from the NI Vision package have been used.

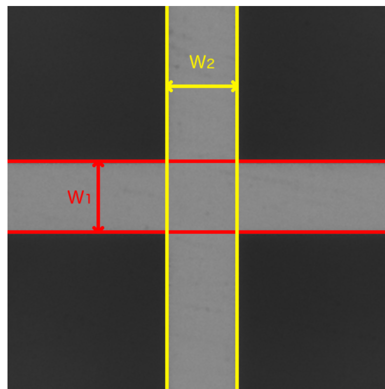

Figure 5.25.: A closeup of the calibration cross with its edges fitted to extract the object horizontal and vertical size.

Fig. 5.25 shows the horizontal (red lines) and vertical (yellow lines) extracted for the digital image of a calibration cross taken at 1x magnification. Having the edges extracted one uses the *caliper* functionality to measure the distance between two lines by a right angle projection. The average pixel distance between horizontal and vertical edges is then taken as the input for the field of view measurements. The accuracy of the width measurement was estimated by repeating

the measurements for different cross position in the acquired image (including rotations applied). The variation of this measurement is < 1 px.

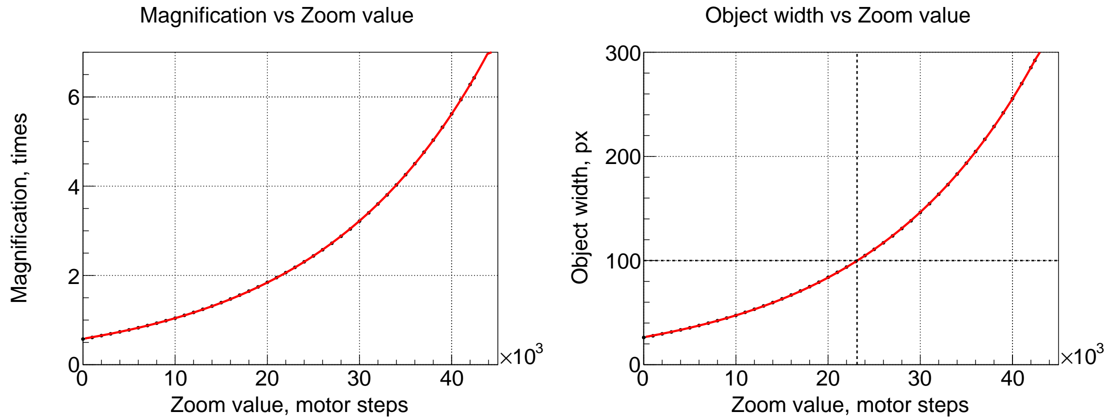

Figure 5.26.: Dependence of the optical system's magnification power (left panel) and observed 100 µm wide object width (right panel) on the zoom value.

Fig. 5.26 (left panel) shows the system magnification dependence on the zoom position. The data points are fitted with an exponential function.

The same data acquired for the reference object width measurement allows to establish the pixel-to-µm conversion for arbitrary zoom values. Fig. 5.26 (right panel) shows the obtained dependence for the pixel-to-µm conversion. The data points are fitted with an exponential function. It needs to be noted, that 1x system magnification factor does not correspond to 1 pixel per µm. The vertical dashed line denote the zoom value where 100 µm wide object appear 100 pixel wide on the image.

Field of view

In this work we define the field of view not as solid angle (also referred to as *angle of view*) but rather as the width of the image projected to the camera's sensor, which is commonly used in machine vision applications, where the focal length and camera sensor sizes are fixed.

In order to establish the dependence of the system's field of view in relation to the zoom motor position we use the following equation:

$$FOV = m \times w_S, \tag{5.4}$$

where m is the actual system magnification measured with calibration plates and w_S is the width of the microscope camera's sensor. We define the width of the sensor being the larger spatial dimension. The field of view is calculated from the single pixel size multiplied by the number of the pixels the camera has in the horizontal direction. The camera used has a sensor size of 1/2.5" with a 4:3

aspect ratio and characteristic pixel size of $2.2 \times 2.2\ \mu m^2$. Using the magnification dependence acquired previously one is able to establish the field of view to zoom value dependence. Fig. 5.27 illustrates this dependence. The data is fitted with an exponential function.

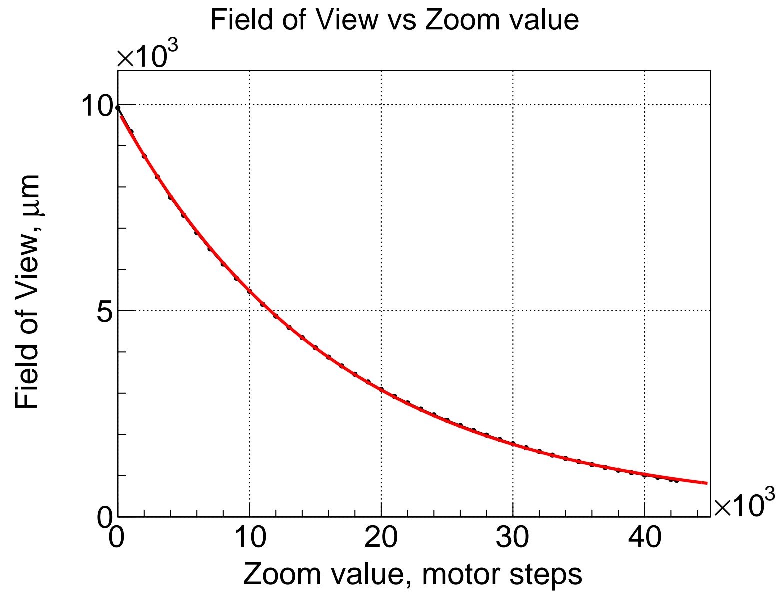

Figure 5.27.: The dependence of the projected field of view on the zoom value extracted from the calibration.

Depth of field

Another optical characteristic important for microscope applications is the depth of field. The focal distance limits become narrower at higher magnification power according to the approximation valid for microscopy:

$$DOF \approx 2Nc\,\frac{m+1}{m^2}, \tag{5.5}$$

where N is an optical system's equivalent lens f-number related to the aperture, c is the circle of confusion of the image format, and m — the magnification factor. The $2Nc$ factor is a constant characteristic for a given optical system. It has been fitted to the depth of field data provided by the manufacturer's technical documentation for the optical system.

Fig. 5.28 shows the derived dependence of optical systems depth of field on the system's magnification power and zoom value. The data are fitted with a function from eq. (5.5) and an exponential function.

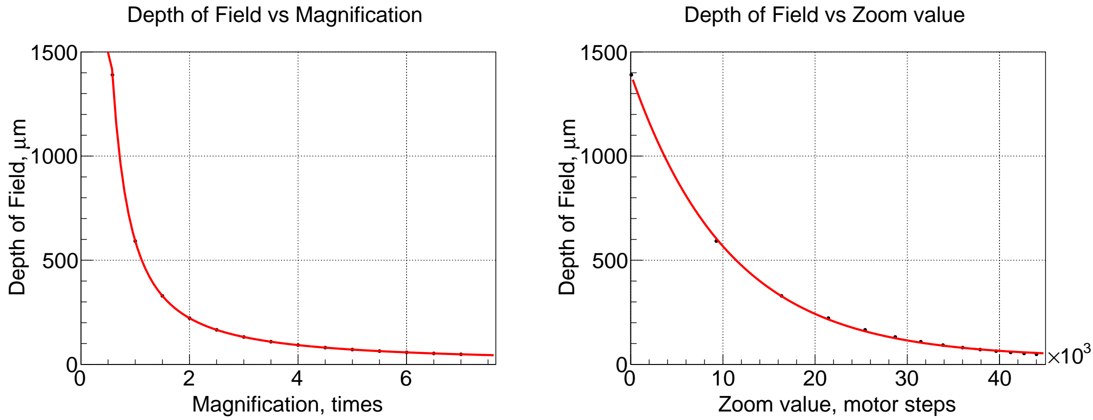

Figure 5.28.: The dependence of the optical system's depth of field on the zoom magnification power (left panel) and the zoom value (right panel).

Autofocusing

The Lorentzian distributions (cf. eq. (5.9)) used for autofocusing (cf. section 5.5.1.1) show as well a dependence on the zoom value. Fig. 5.29 illustrates this dependence. On the left panel the total amplitude values for the lowest magnification power are shown. The right panel shows the same distribution for the highest magnification power.

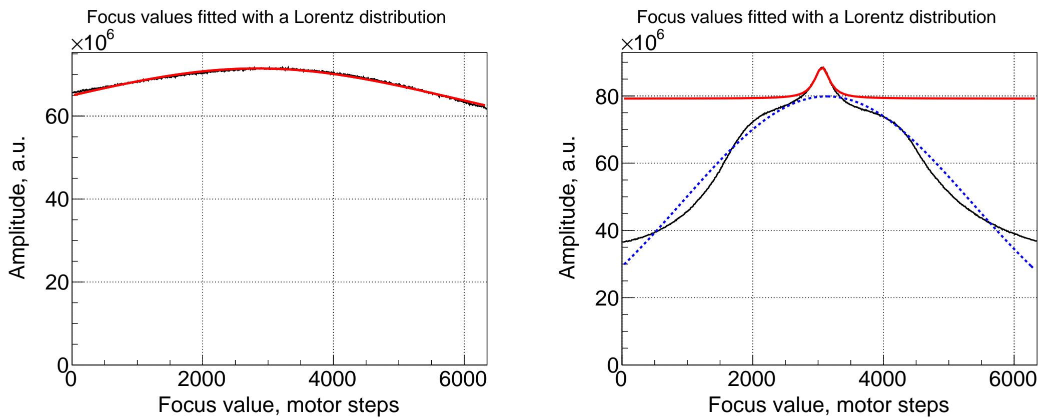

Figure 5.29.: The dependencies of Lorentzian distribution amplitude on the focus motor stage observed at minimal (left panel) and maximal (right panel) magnification power of the optical system. Solid red line denotes the Lorentzian fit, dashed blue line denotes the Gaussian fit.

These distributions show that the Lorentzian's half width at half maximum and amplitude are highly dependent on the magnification power. This is effect

is especially detrimental at high magnification powers, where the distribution transforms into a combination of Gaussian-like and Lorentzian distributions. A Gaussian-like contribution arises due to a higher susceptibility to the background. In this regime only the Lorentzian part should be fitted, which requires a careful picking of the initial fit parameters and fit ranges, otherwise this could decrease the robustness of the fit and may lead to wrong results or even failed fits. To mitigate this problem a series of measurements throughout the full zoom range have been performed. In these measurements the fit parameters have been stored and analyzed. The half width at half maximum and the amplitude of the distributions are the most important to be assessed.

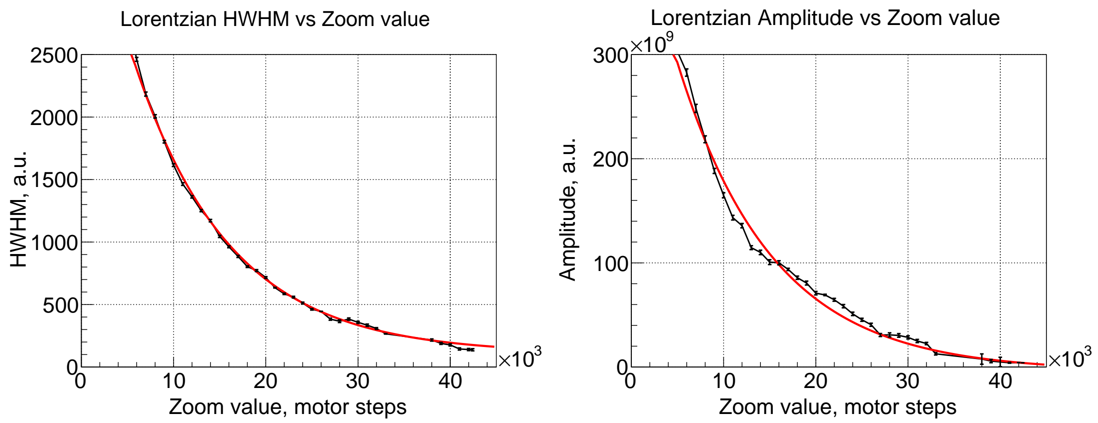

Figure 5.30.: The dependence of the Lorentzian distribution's parameters half width at half maximum and amplitude on the zoom value extracted from the calibration.

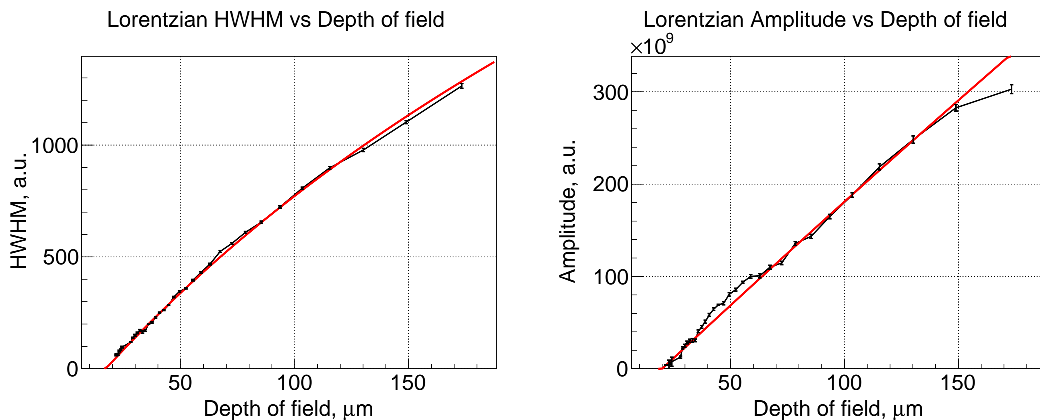

Figure 5.31.: The dependence of the Lorentzian distribution's parameters half width at half maximum and amplitude on the optical system's depth of field extracted from the calibration.

Fig. 5.30 shows the obtained dependencies. Both dependencies are fitted with the exponential functions. Although, the discrepancy between the data and the fit is not negligible, the extracted fit functions are providing the correct input for the Lorentzian fitting algorithm increasing its robustness and reducing the fit errors.

Fig. 5.31 shows the obtained dependencies for the half width at half maximum and the amplitude of the Lorentzian distribution on the optical system's depth of field value. The dependencies are fitted with logarithmic functions.

5.2.4. Summary

The optical axis calibration and characterization methods allow to qualify and establish dependencies between many properties of the system. The calibration and characterization is done in an automated way by means of a LabVIEW subprogram. The methods are hardware independent thanks to the hardware abstraction layer implemented, given that the zoom and focus stages of the optical system are motorized. They provide the parfocality corrections, if the optical axis is mounted on the motorized Z stage.

5.3. Linear motor stages calibration and characterization

The microscopy and metrology applications require a good XY positioning of the test object under the optical axis as well as movement of the optical assembly along the Z axis. This paragraph describes the calibration approach.

The linear motors tend to accumulate the linear positioning error when moved to a distant point. In order to estimate the motor positioning precision and repeatability, a set of measurements were carried out. In this calibration the motors were set to move to a certain position. The actual position was checked with the target value, then reset to the starting point and the measurement was repeated several times. In such a way the whole movement range was measured.

The obtained dependencies (Fig. 5.32) show the distribution of the positioning errors fitted with a Gaussian distribution. The motor position repeatability is then extracted from the fitting.

The linear motors used in this work are based on the closed loop feedback correction. This means that on a hardware level the motor's actual position in the idle state is constantly checked against the target position internally. If these positions do not match the feedback loop corrects the actual position to match the target one. This behavior results in a situation that the actual motor position, when read at a certain time, might not correspond to a target position. To estimate this motor idle positioning error a statistically significant amount of measurements were performed. The standard deviation of the actual position

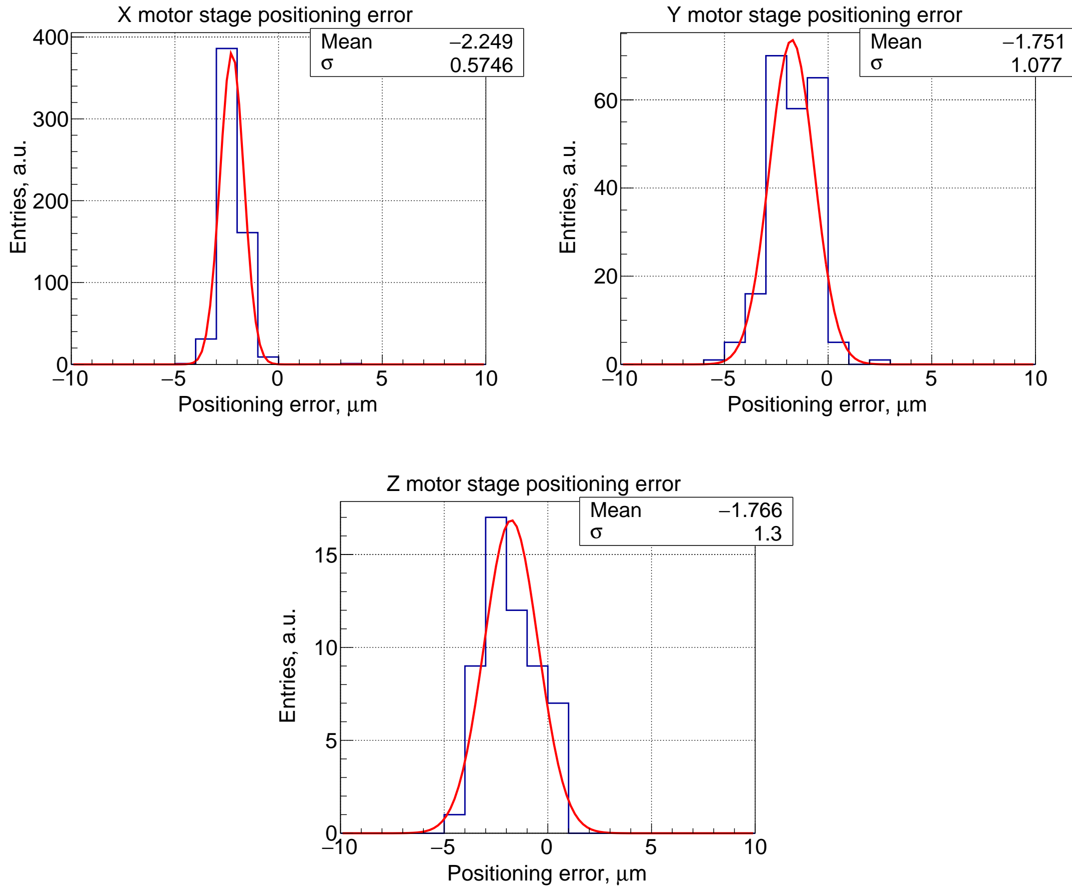

Figure 5.32.: Estimation of motor stage positioning repeatability by measuring the actual arrival position vs targeted position.

read back was taken as a motor idle error.

To estimate the calibrated positioning error the calibration described in section 5.4 was used based on measuring the position of the calibration plate's cross (see section 5.2.3) was used instead of sensor's alignment mark. The measurement was done for 133 crosses in the full 19×7 cm^2 range of the X and Y linear motor stages. The resulting calibrated positioning error does not show linear growth dependence, indicating that motors' feedback correction compensates for this effect.

Fig. 5.33 shows the obtained error vector field. The error vectors point in random directions, indicating that the error has a statistical nature rather than a systematic one. The summary of motor stages' positioning errors is presented in the Tab. 5.2.

The described calibrations are performed in an automated fashion. They are independent of actual motor hardware, thanks to the hardware abstraction layer. This means that they can be repeated for any linear motor hardware.

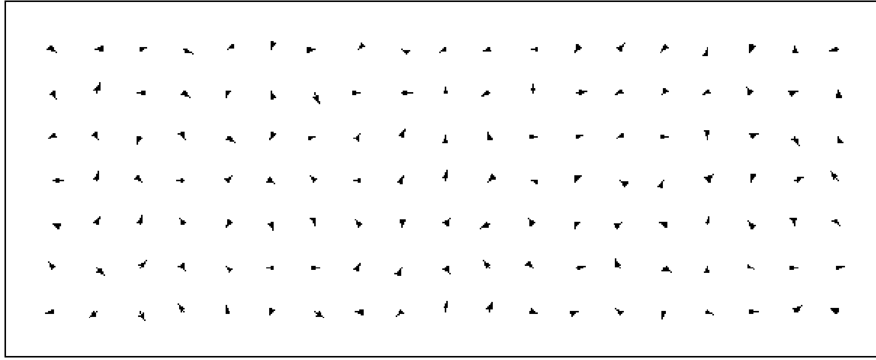

Figure 5.33.: Error vector field. The errors are scaled by a factor of 1000.

Motor Stage	Positioning, μm	Idle, μm	Calibrated, μm
X	0.55	0.2	2.4
Y	1.12	0.2	3.1
Z	1.24	0.2	

Table 5.2.: Extracted motor stages' positioning errors.

5.3.1. Summary

The automated linear motor stages calibration was implemented. It allows to estimate the positioning errors for uncalibrated and calibrated movement and perform linear stages characterization. Being hardware independent, the algorithms developed allow to perform the calibration and characterization for any linear motors.

5.4. Silicon sensor optical inspection

5.4.1. Acceptance criteria for silicon microstrip sensors

The acceptance criteria defined in the STS Technical Design Report [13] allow a maximum of 1% defective strips per sensor. This strict requirement takes into account an eventual malfunction of further strips during the 6 years of operation of the STS detector. The optical inspection setup permits to define more accurate acceptance criteria based on defect information and geometrical parameters extracted during the scan. This includes the information about the defect class and how severe the defect is. For example, the dust particles found on the surface are much less severe compared to the surface scratch.

The defect information collected during the element integrity check is gradual — the element will get a score from 0 (absence or completely destroyed) to 100 (fully intact) which allows to perform more flexible analysis of the sensors

quality. The current acceptance criteria (deduced from prototype sensors) are as follows [36]:

• broken strips, shortened strips	$< 1\%$
• defective bias resistors	$< 1\%$
• defective AC pads	$< 1\%$
• defective DC pads	$< 1\%$
• bias ring	No crossing scratches, biasing pad integrity 90%, no shorts to guard rings
• guard rings	No crossing scratches, overall defect area < 1 mm^2*, no shorts to bias rings
• sensor edge quality	Deviation from ideal cutting edge < 20 µm
• sensor edge un-parallelism	$< 0.05°$
• sensor warp	< 100 µm

Table 5.3.: Silicon sensors acceptance criteria

The values marked with an asterisk (*) are assumed for this work so far. They are however still preliminary and subject to change when the first batches of the final sensors arrive at the QA centers allowing to gather more defect statistics. In order to improve the defect severity scoring system and the overall decision taking on the sensor quality in the optical inspection system, it is necessary to compare the inspection results with the results coming from electrical inspection.

5.4.2. Sensor misalignment calibration

After the placement of the sensor on the vacuum chuck it is manually aligned to a certain extent. However, the absence of the rotational motor stage in the optical system does not allow to align it perfectly. Thus the misalignment of the sensor with respect to the motor stage should be extracted.

The key element for the misalignment calibration are the passer marks, or the alignment marks as they will be referred to throughout this work. Every sensor has at least 4 of these marks placed on the sensor's corners in a close vicinity to the edges. Fig. 5.34 shows the schematic representation of the sensor misalignment calibration. The black outermost rectangle represents the vacuum chuck and the motor movement plane. The blue rectangle with 8 crosses represents the misaligned sensor placed on the vacuum chuck. As the calibration is initiated (red dot), the closest alignment mark is looked for in the spiraling out movement pattern. As the first alignment mark is detected with pattern matching algorithms (here top-left), its position in the motor coordinates is saved. Furthermore, it's rotation is extracted to have a first estimate for the sensor misalignment. Then the calibration continues with other 3 corner alignment marks.

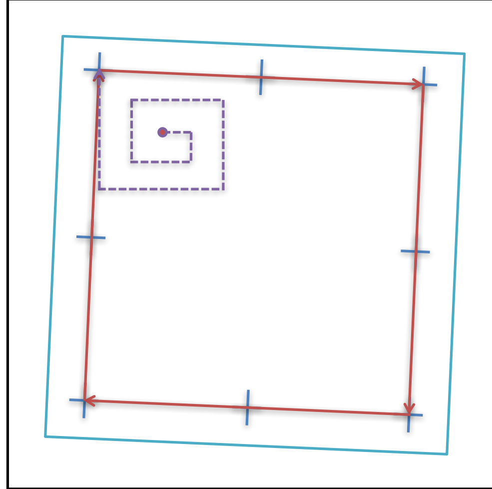

Figure 5.34.: Sensor misalignment calibration principle. Black rectangle denotes the motor coordinate space, blue rectangle denotes the sensor coordinate space. The initial search for the alignment mark is denoted by the dashed purple line. Further scan over four corner alignment marks is denoted by the red arrows.

Having all the alignment mark positions in the motor coordinate space and knowing the topology of the sensor from the CAD files, it is possible to solve the equation (5.6) to convert between coordinate spaces:

$$\vec{x}_m = \mathbf{C} \cdot \mathbf{R} \cdot \left(\vec{t} + \vec{x}_s\right), \tag{5.6}$$

where $\vec{t}$ is the translation vector between origins of coordinate spaces, C is the conversion matrix which converts motor steps to micrometers; R is the rotation matrix which extracts the rotation angle between the sensor coordinate space and the motor coordinate space. The 2-dimensional (the Z-direction and Roll and Pitch angles are not taken into account) expansion of the matrix equation (5.6) is fitted by a ROOT [75] based fitting macro. The fitting is performed by a MIGRAD [76] algorithm from a MINUIT [77] package. The fitting is done by minimizing the χ^2 of the equation system which is the sum of the χ^2 of both equations of the system. After solving the equation it is possible to convert between coordinate spaces, thus the motors will scan along the sensor. The positioning precision after the calibration is estimated to be $\pm$ 2.4 µm for the X- and $\pm$ 3.1 µm for the Y-motor stage (see section 5.3 for the estimations).

5.4.3. Sensor scanning

Having the sensor misalignment information extracted the scan along the sensor can be performed. The sensor is divided in a grid of rectangles which are slightly less than the camera's field of view at a given magnification. These rectangles are referred to the regions of interest (ROI) further in this work. The scan is then

performed in a snake-like movement pattern as schematically illustrated in the Fig. 5.35.

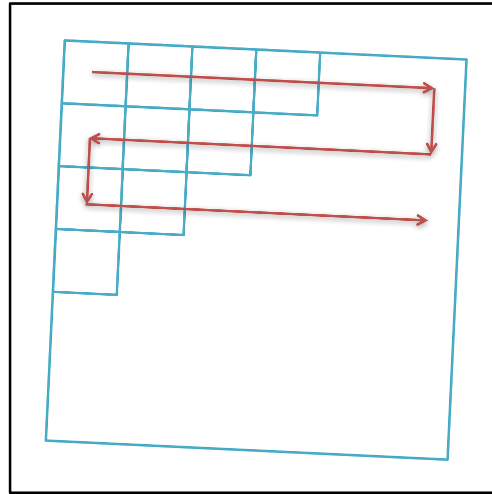

Figure 5.35.: Sensor scan movement pattern scheme. Black rectangle denotes the motor coordinate space, blue rectangle denotes the sensor coordinate space. The actual surface scan is done in the sensor coordinate space. Scan movement pattern is denoted by the red arrows.

When the motors move the sensor to the next region of interest, a digital image of this region of interest is taken. It is processed with a series of machine vision algorithms as well as saved on disk for later analysis. The machine vision algorithms are applied in order to find the potential defects, target different features and perform metrology measurements of a sensor on a given image and will be described further.

The optical inspection performance should be optimized: on the one hand, the inspection time of a single sensor side should be minimized, on the other hand the magnification of the system should be as big as possible to be able to observe most fine structure of the sensor and possible defects in details. The magnification of about 4x was chosen for the sensor scan in this work for the reason that it has a size of a single pixel equal to one micrometer (see section 5.2.3 for corresponding calculations). The corresponding time for a single scan at 4x magnification is about 20 minutes with the current setup. However this could be further optimized with faster camera (see section 5.9).

5.4.4. Surface defect detection

The images obtained during scans are analyzed by a variety of the machine vision algorithms to inspect the sensor surface quality and detect the defects. In this subsection the defect detection principles are described.

5.4.4.1. Foreign object detection

During the sensor logistics and due to the sensor handling the surface of the sensor can accumulate various foreign objects. Mostly these are the dust grains. Though the sensors are handled under clean room conditions and dust grains are removed with a nitrogen gun or a soft brush before inspection, not all of them could be removed. The dust grains or other electrically conductive particles convey a potential danger of shortening the strips if they are found on the passivation layer openings of the sensor. Another important aspect of the foreign objects on the surface is that they can hide the underlying defects such as strip scratches, opens or shorts.

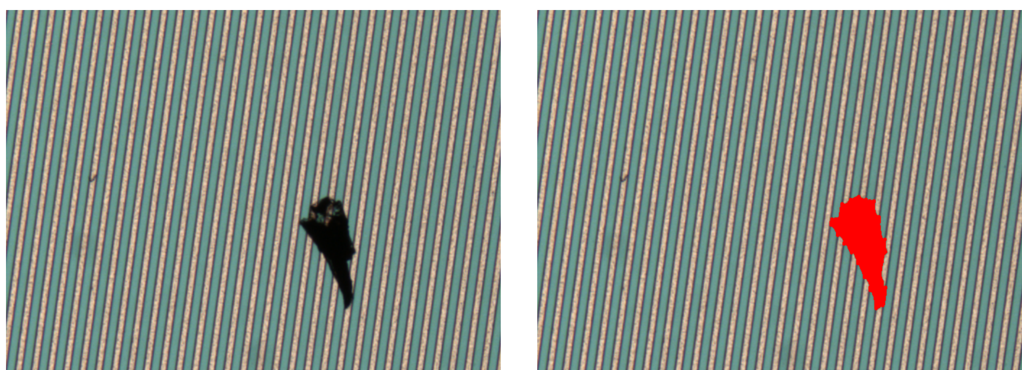

Figure 5.36.: Detection example of a dust particle covering a large area and 4 strips on a p side of a prototype sensor. The left panel shows the source image, the right panel shows the detected defect.

Fig. 5.36 shows an example of a dust detection. Here for presentation purposes a big particle was chosen. It covers four strips on the p side of a prototype sensor and potentially masks a scratch. The left panel shows the source image and the right panel shows the detected defect overlaid over the source image. Here the luminance plane was extracted and the image was thresholded using a metric auto-threshold. Then small background objects were removed with the morphology tools. The particle size was measured by a particle analysis tool and estimated to be 6330 μm^2.

5.4.4.2. Scratch detection

The scratches are dangerous defects which can lead to a broken sensor aluminum strip. If the scratch is deep enough the implant strip can be broken as well. Both lead to a deteriorated readout signal. Another effect is that the metal from a torn strip can electrically shorten the neighboring strips. This results in deterioration of the reconstructed hit position resolution due to the charge redistribution between the shortened aluminum strips.

Fig. 5.37 shows an example of a scratch detection. This scratch was introduced

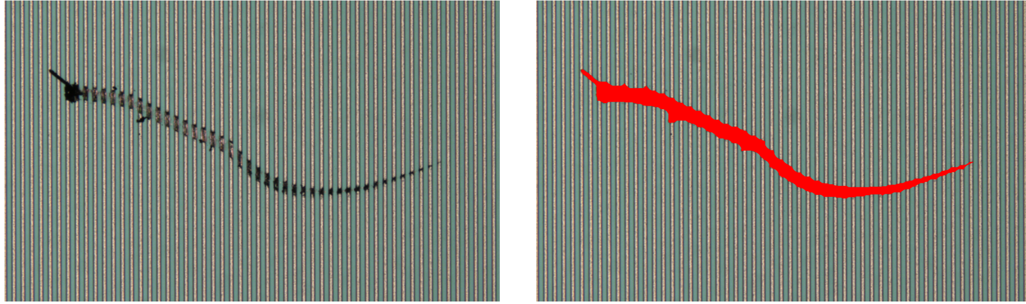

Figure 5.37.: Detection example of a scratch traversing many strips on an n side of a prototype sensor. The left panel shows the source image. The right panel shows the scratch defect detected.

by purpose to a low-quality prototype sensor during the development of the detection algorithms. It serves as an example of a severe defect damaging multiple sensor strips. The left panel shows the source image and the right panel shows the detected scratch overlaid over the original image. In this example the luminance plane of the image was extracted and thresholded manually to extract the dark objects with brightness values lower than 70 only. The thresholded binary image was then cleaned from small background objects and the interstrip gaps were closed. The resulting single object was analyzed, its total area was measured to be 30130 μm^2. The analysis tool also indicates a big elongation factor of around 9. This illustrates how the *Particle Analysis* tool can be used for an offline defect analysis and classification.

Another advanced approach for the scratch detection using the texture matching was shown previously in the section 5.1.2.8.

5.4.4.3. Aluminum strip defects

Aluminum strips of the silicon microstrip sensors are electrically decoupled from the implant strips by an insulation layer forming a coupling capacitor. The charge produced by an ionizing particle impinging the sensor is collected on the implant strips. It induces the electrical charge on the aluminum strip which is amplified and read out by the read-out electronics. Thus, it is important to assure the integrity of the aluminum read-out strips. A metal break (or several) on the metal strip leads to segmented read-out line and potentially lost signal due to this segmentation. The metal shorts and breaks might be caused by a scratch or a foreign object, this was covered in a previous subsection. Here we discuss the defects not caused by these effects.

Strip metal break

The metal break defect was observed for first versions of a prototype $6.2 \times 2.2\ cm^2$ sensor from CiS. This defect is due to manufacturing process. Like with

the scratches, breaking the metal line results in a defective readout channel.

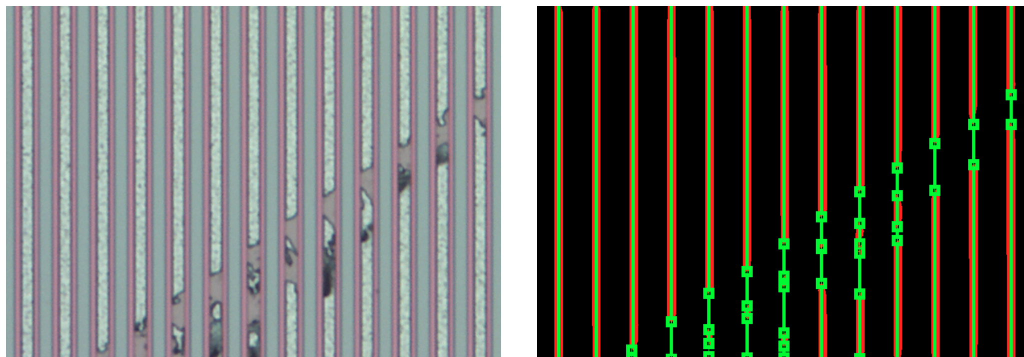

Figure 5.38.: Detection example of a metal break region on a prototype sensor. Left panel shows the source image, right panel shows the processed image with edges detected, edge numbering is suppressed.

Fig. 5.38 shows a detection example of the metal break defect type. Here the luminance plane was extracted and image was then thresholded with a background correction criterium, where the interstrip gap was selected as a background element. The resulting binary image was additionally cleaned up from small objects and the strips were filled with a convex hull morphology algorithm. Then a set of an edge detection lines were put over the strips. For the first two non-defective strips there are zero edges detected as expected. The defective strips show at least one edge detected, which indicates the defect.

Strip metal short

The metal short defects coming from manufacturing process were not observed for the prototype sensor available in this work. However, in order to illustrate the detection principle, an example image of a strip metal short found on a CMS-OB2 silicon strip sensor used in the LHCb experiment [78] was analyzed.

Fig. 5.39 shows the example of the metal short detection. Here the same approach was used as with metal breaks. The colors were thresholded to those of a strip. Then the edge detection lines were placed in the interstrip gap. If any edge is detected this would indicate a defect.

Few metal short defects of other origin were observed on the prototype sensors from CiS. Here the defect was caused during the electrical inspection (see Fig. 5.40). Seemingly, a defect was formed by a pinhole formation in a discharge process between the strip implant and the aluminum strip. Due to high currents flowing in the localized region, the metal from one strip has flown to a neighboring strip causing an electrical short.

Fig. 5.40 shows a detection of a strip metal short observed. The detection principle is similar to the described previously, except that strip metal colors

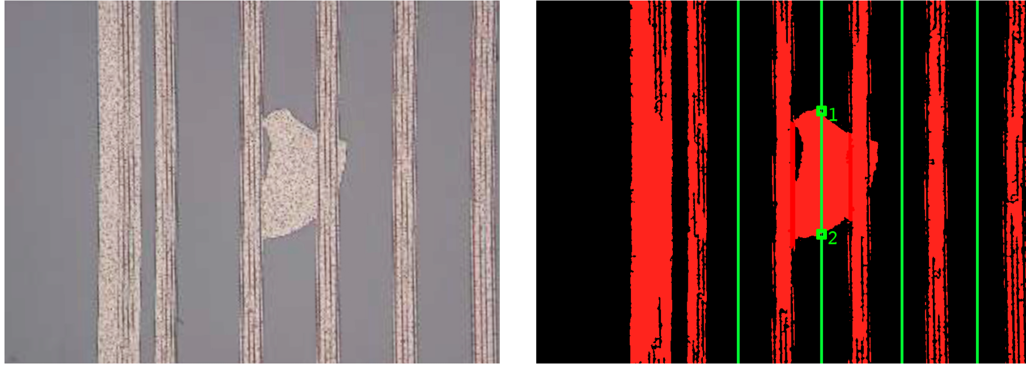

Figure 5.39.: Detection example of a metal short between two strips of a CMS-OB2 silicon strip sensor used in the LHCb experiment. The left panel shows the source image. The right panel shows the detected defect.

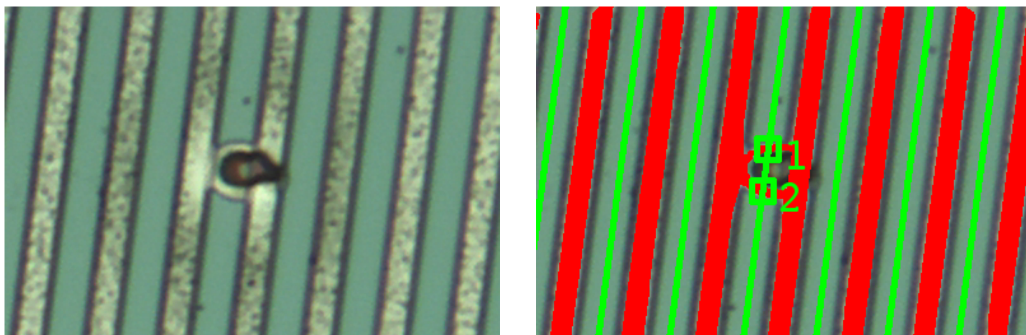

Figure 5.40.: Detection example of a metal short caused by a discharge. Left panel shows the source image. Right panel shows the defect detected by edge detection algorithms.

thresholded were adjusted accordingly and the edge detection lines were put at 7.5 degrees for the p-side.

Second metal line defects

The second metal lines interconnect the inclined corner strips on the p-side of the sensor. Their integrity is important to control since they can be shorted with other strip they run over or they can be broken resulting in a segmented strip. They are prone to the surface scratches since are formed by the top-most lithography layer, which is insulated with ~ 0.5 µm passivation layer.

For the quality inspection of the second metal lines the modified foreign object and scratch finding algorithms are used in the extracted regions of interest. Fig. 5.41 shows a detection example of the defects on the second metal line for a CiS (top panels) and Hamamatsu (bottom panels) sensors. Left panels show the source image, right panels show the processed image with the defects detected and overlaid.

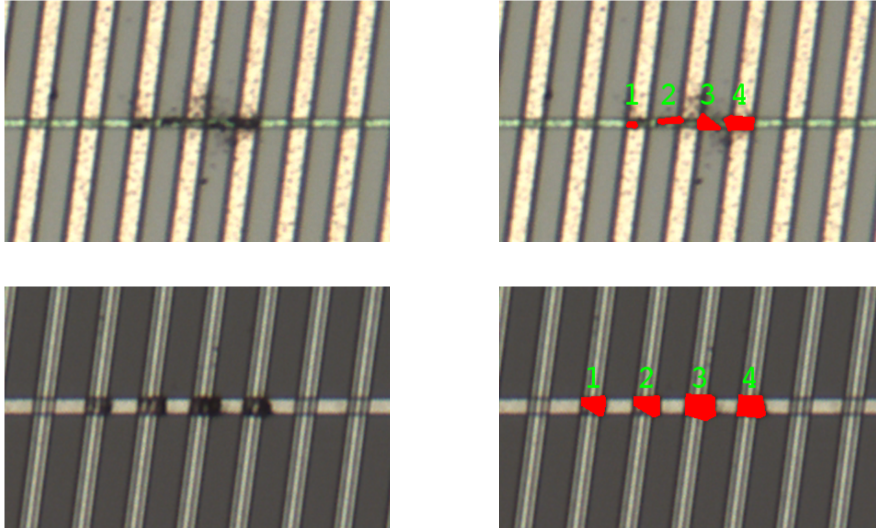

Figure 5.41.: Detection example of second metal line defects for CiS (top panels) and Hamamatsu (bottom panels) sensors. Left panels show the source images, right panels show the defects detected and overlaid.

5.4.4.4. Implant defects

The strip implant defects are very important to detect. They govern the charge collection from the ionizing particles impinging the sensor. A broken implant electrically decouples the implant strip in two (or more) regions resulting in modified electrical characteristics of the strip such as strip coupling capacitance and resistance.

The strip implant defects can be introduced by deep scratches, however, in the absence of the scratches the implant defects are only possible due to the manufacturing process faults such as over- or underetching of dielectric or the layer deposition.

The fact that the widths of the implant and aluminum strips differ and that aluminum strip thickness is on the order of the < 1 μm (which renders it semi-transparent) allow to inspect the implantation regions of the strips.

Implant strip break

Several strip implant breaks were observed on the very first prototype 12×6 cm^2 sensor from Hamamatsu.

Fig. 5.42 shows a detection example of the implant break defect type. The detection is done by recognizing the strips with pattern matching and using the edge detection algorithms over the detected strips. The fact that any edges are detected indicates a defect along the edge detection line. The left hand side panel shows the source image. The right hand side panel shows the implant strip break detected.

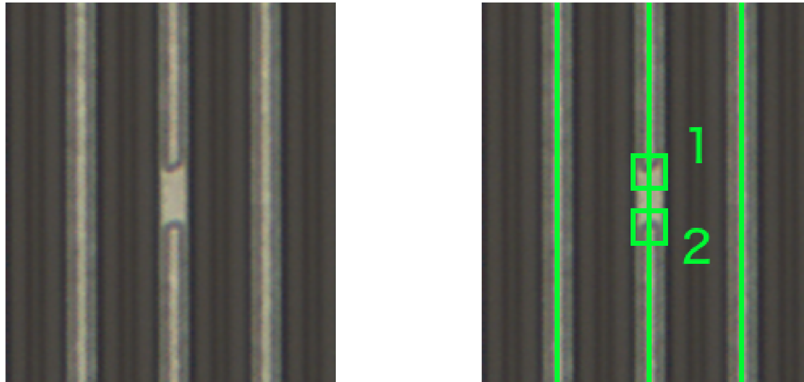

Figure 5.42.: Detection example of the implant strip break. Left panel shows source image, right panel shows the detected defect.

The sensor with implant breaks detected was as well inspected electrically. The measurement sensitive to the implant break defect was found out to be the strip coupling capacitance.

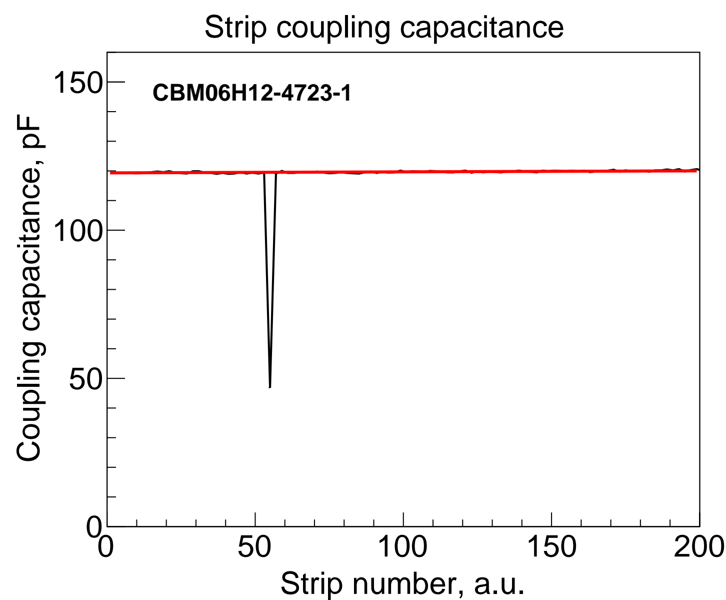

Figure 5.43.: Strip coupling capacitance measured during the electrical inspection. Low value measured for the strip 58 indicates the defect. Data measured by I. Panasenko [79].

Fig. 5.43 shows the strip coupling capacitance measured for the prototype sensor. The lower capacitance of the strip 58, compared to the neighbors, verifies the defect observed during optical inspection.

Implant short

Fig. 5.44 (left panel) shows a complex defect which extends over 8 strips and includes the implant short, implant breaks and a p-stop implantation defect types. It was found on the same prototype 12 × 6 cm^2 sensor from Hamamatsu, where the individual implant breaks were found.

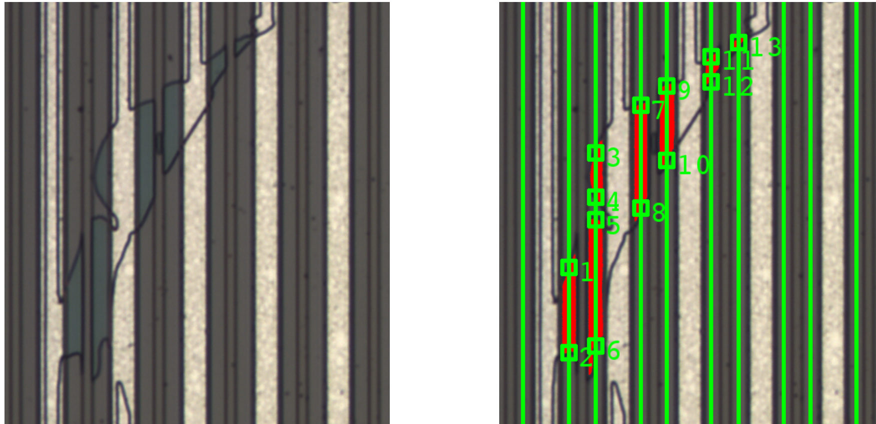

Figure 5.44.: Detection example of the implant opening defect type.

Fig. 5.44 (right panel) shows the detection principle for the implant short defect. Here the luminance plane have been extracted, the colors were auto-thresholded for color clustering and edges were detected along the interstrip gaps matched with pattern matching algorithms.

p-stop and p-spray strip implant defects

The p-stop (Hamamatsu) and moderated p-spray (CiS) implantation on the sensor n-side serves for electrical insulation between neighboring strips. Large defects of this type might disrupt the electrical insulation between neighboring strips, change the field configuration, interstrip capacitance and lead to increased strip leakage current.

Fig. 5.45 shows so far the only observed p-stop implantation layer defect which was caused by the n+ implantation short. In the observed case the defect is rather small and localized. The optical detection principles here are the same as for the implant strip inspection, except, the p-stop implantation "strips" are matched and edge detection lines are placed accordingly.

Fig. 5.46 shows the interstrip capacitance (left panel) and strip leakage current (right panel) characteristics measured in the region containing the defect. The observed higher interstrip capacitance and leakage current indicate a localized short between strips 426 and 427 caused by n+ implantation over the p-stop implantation.

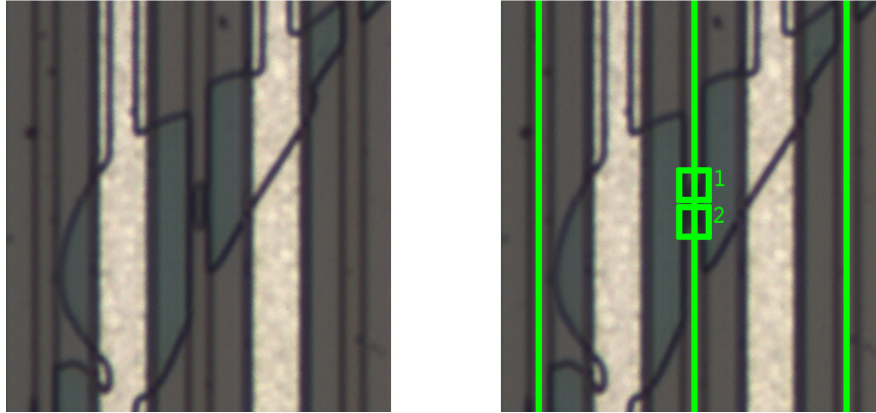

Figure 5.45.: A close-up photograph of the p-stop implantation defect.

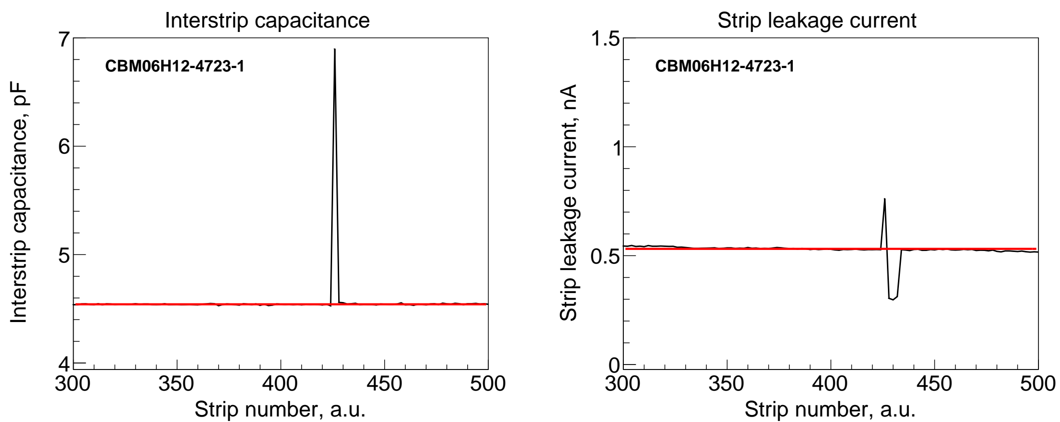

Figure 5.46.: Interstrip capacitance (left panel) and strip leakage current (right panel) characteristics measured in the defective region. The deviation from the average values indicate the presence of a defect. Data measured by I. Panasenko [79].

Dielectric defects

Some silicon wafer Si_3N_4 dielectric deposition defects were observed for the very first version of a prototype 6.2×4.2 cm^2 sensor from CiS. The implant strip, insulation layer formed from Si_3N_4 and SiO_2 and aluminum strip form a coupling capacitor. Thus if such a defect is introduced the coupling capacitance of the strip should change.

The cross section of a CiS sensor is shown in Fig. 5.47. Left panel shows the non-defective layer configuration, right panel shows the Si_3N_4 dielectric deposition defect.

This defect is most probably formed due to not fully established manufacturing process at the time. This defect type was not observed for other sensors so far.

Fig. 5.48 shows the dielectric defects detection principle. The left panel shows

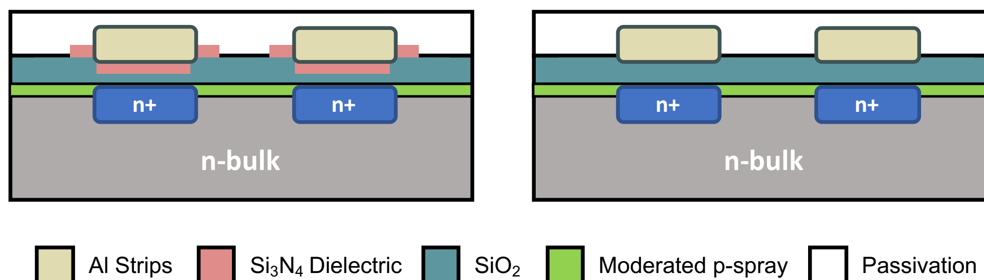

Figure 5.47.: A simplified sketch of a cross section of a CiS sensor. Left panel shows the non-defective layer configuration, right panel shows the defect of a Si_3N_4 dielectric deposition.

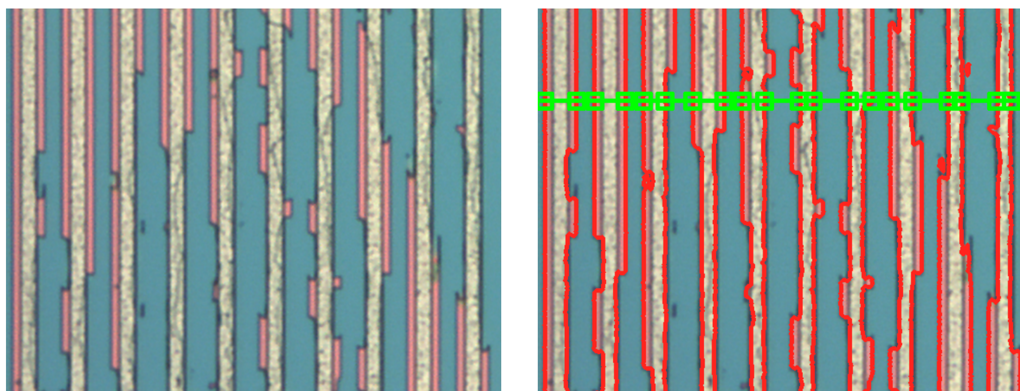

Figure 5.48.: Detection example of a dielectric defect on an n-side of a prototype 6.2×4.2 cm^2 sensor from CiS. Left panel shows the source image, right panel shows the processed image with the edges detected, edge numbering is suppressed.

the source image and the right panel shows the detection output overlaid over the source image. Here the source image is thresholded for the background color and the strip profile is extracted. Then with the *Advanced Morphology* tool set, the small particles are removed, the holes are filled and boundaries of detected strip profiles are extracted. At the detection step, the edge detection is applied line by line and width profile of the strip profiles is analyzed. Any deviation from the targeted width is considered to be a defect.

Other implant openings

The implant openings were as well observed outside the sensor's strip zone. They were found on the bias rings, guard rings and in the sensor's edge vicinity. These defects are not critical when small. However, if the opening is large enough compared to the implantation width of the respective electrical element it can disrupt the electrical field configuration or electrically decouple the implantation layer under the bias ring or guard ring.

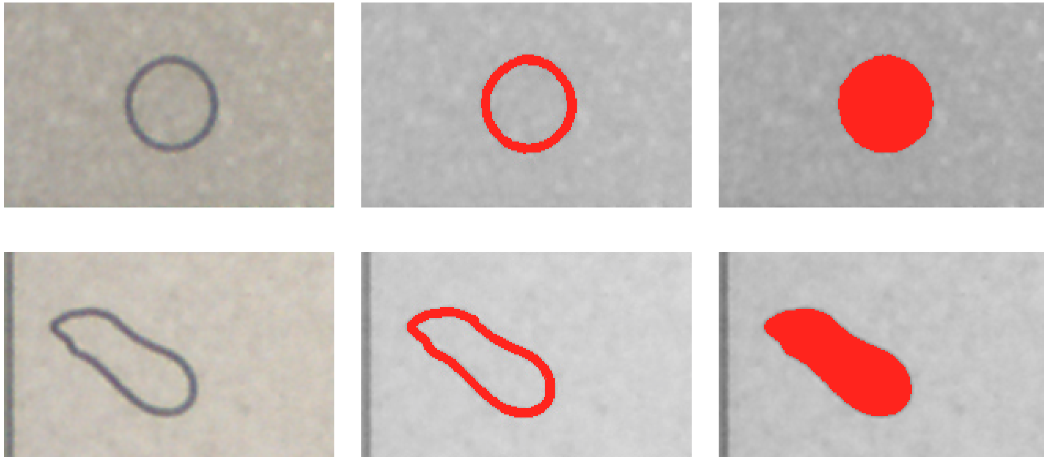

Figure 5.49.: Detection example of an implant opening defect over the bias ring (top row) and near the edge of a sensor (bottom row). Left panels show the source images of the defects. Middle panels show the defect detected with contour tracing. Right panels show the defect detected with color thresholding.

Fig. 5.49 shows a detection example of the implant openings over the bias ring (top row) and near the edge of a sensor (bottom row). Left panels show the close-up regions of the source images where the defects are found. Middle panels show the defects detected with the contour tracing algorithms overlaid over the source image. Right panels show the defects detected with the color thresholding algorithms configured to detect dark objects. The thresholded areas are filled with “Fill Holes” algorithm from the *Advanced Morphology* tool set. The extracted areas of the defects are about 3000 and 3300 μm^2, respectively.

5.4.4.5. Passivation layer defects

The silicon microstrip sensors are covered with a silicon oxide passivation layer of a 0.5 µm thickness. It serves as an insulation between the aluminum strips and atmosphere and hinders the aluminum oxidation processes. By design there are openings in the passivation layer over the AC and DC pads, biasing pads and contact pads on the guard rings.

Passivation layer opening

The opening in the sensor’s passivation layer exposes the underlying metal layer. The metal layer of the strips exposed is subject for possible electrical shorts caused by the conductive objects laying on them. Furthermore, the metal might undergo corrosion processes which will change its electrical properties, for example increase the noise of the read-out channel.

Fig. 5.50 shows a detection example of a passivation layer opening due to manufacturing process faults found on a Hamamatsu prototype sensor. Left panel

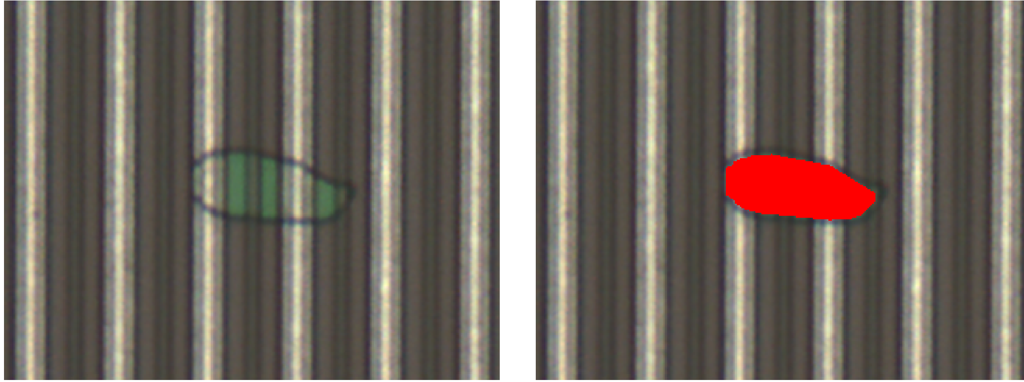

Figure 5.50.: Detection example of a passivation layer opening due to manufacturing process faults. The left panel shows the source image. The right panel shows the defects detected.

shows the source image close-up. Right panel shows the detected defect overlaid on the source image. The detection is based on the color thresholding and binary image morphology transformations.

Passivation layer degradation

The passivation layer is a subject to its quality degradation. If the sensor was handled inappropriately, stored in a high humidity conditions or exposed to other substances, the passivation layer can be gradually damaged or removed locally. Usually the passivation layer defects show some color patterned structures (see Fig. 5.51, left panel).

Fig. 5.51 shows aa detection example principle for the passivation layer openings due to degradation. The left panel shows the source image of the region of interest containing the defect. The passivation layer was dissolved over three strips, exposing the underlying metal and producing a color patterned spot. The right panel shows the defects detected. Here the image was thresholded for the color of the strip metal, the small and large objects were removed. The defects extracted were overlaid on the source image.

Surface chips

The surface chips on the sensor edges or their close vicinity can as well be detected with machine vision algorithms developed. They are introduced to a sensor during its handling and clamping in the test fixtures. They might change the configuration of electrical fields, increase the total leakage current of the sensor due to increased surface current over the edge of the sensor.

Fig. 5.52 shows two examples of the sensor surface chips found on prototype Hamamatsu sensors. The source images (left panels) have their luminance color

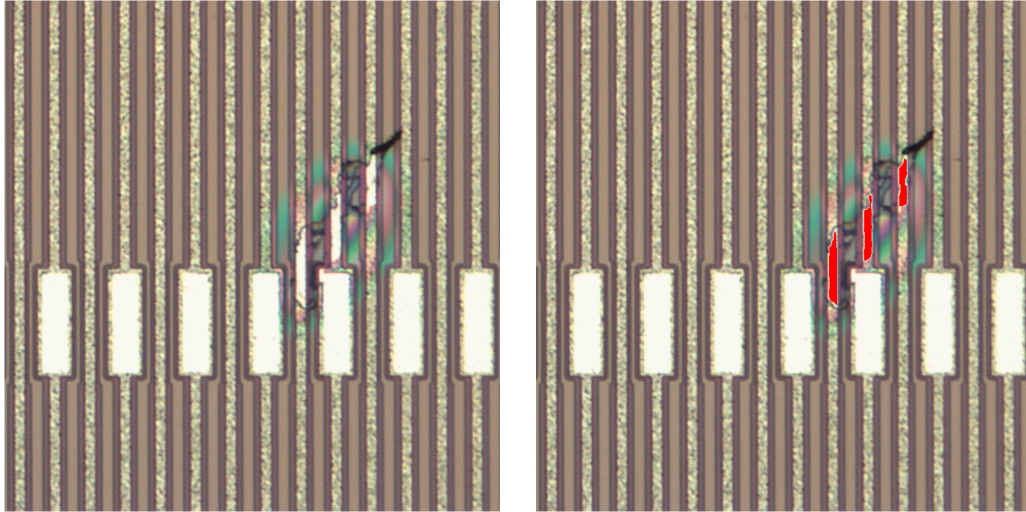

Figure 5.51.: Detection example of a passivation layer opening due to its degradation found on the n-side of a prototype sensor from CiS. The left panel shows the source image. The right panel shows the defects detected.

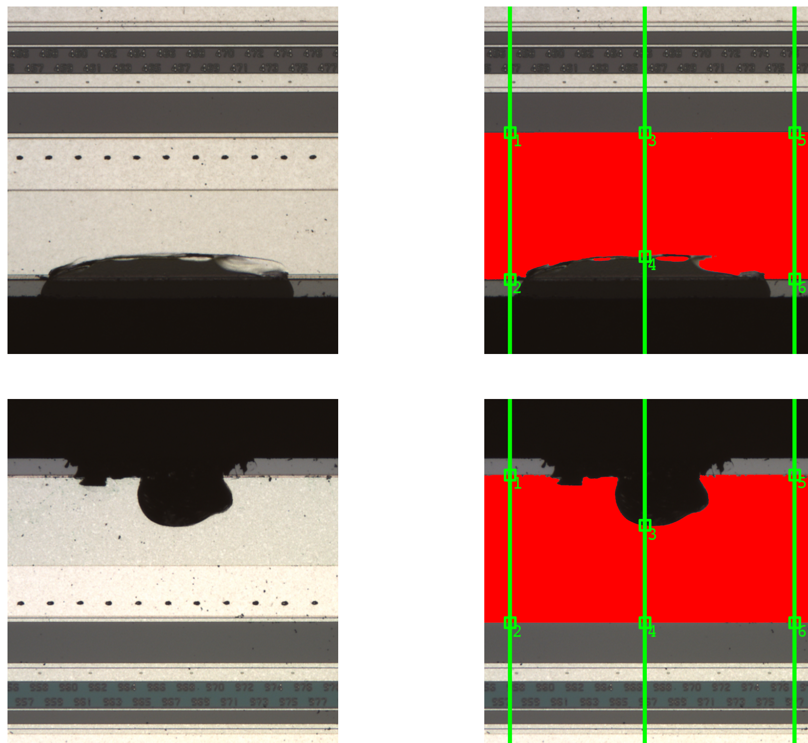

Figure 5.52.: Detection example of sensor surface chips found on prototype Hamamatsu sensors. Left panels show the source image, right panels show the defects detected.

planes extracted and thresholded for the sensor metalization colors. The binary

images are then processed with the *Binary Morphology* tool set. The edges of the extracted regions are detected and analyzed. Observed deviation in the edge distance is considered to be a defect.

5.4.4.6. Defect context

In order to reliably assign the defect severity it is essential to know the context of the defect found. For example a dust particle or a scratch found in the area near the sensor's edge does impact the sensor quality as those found in the strip area of the sensor. Thus the defect context should enter the analysis and play a significant role during defect severity calculations. We distinguish between following defect contexts: strips, AC pads, DC pads, bias resistors, guard ring and sensor's edge. For the context extraction we use the pattern matching with lowered threshold values, so that the region around the defect will be as well analyzed. However it is not always possible to properly identify the defect context with the standard machine vision algorithms. For this we use the advanced analysis methods to augment the machine vision methods (see section 5.4.6).

5.4.5. Sensor electrical elements inspection

The electrical components (AC and DC pads, bias resistors and guard rings) of a sensor are very important for its operation. Their presence, integrity and quality can be inspected automatically with the machine vision algorithms. The presence and integrity of the electrical elements is checked by the pattern matching algorithms with lowered detection threshold values.

Fig. 5.53 illustrates the electrical element integrity check. Here the elements are matched with a reference plate. Any deviation below the threshold value results in an element being not detected. If there are less elements than required in a region of interest is an indication of a defective element.

5.4.5.1. AC pads

The AC pads are used for the sensor readout. The microcables are tab bonded to them in order to connect them to the readout microchips. The quality of the AC pads is essential for the bonding process to be carried out and for the bond quality. The AC pads are as well used for the electrical quality assurance of the sensors both at the manufacturing companies and at the quality assurance sites of the STS detector. In this work we require that all the AC pads are present on the first two rows of the readout of the sensor. Due to the quality control on the production sites there is always a small defective spot to be found on each AC pad. It is caused by a probe needle when measuring the strip-by-strip electrical properties of the sensors. We require that the maximum defective area on an AC pad caused by the probes is less than 10 percent of its total area. With the detection principles shown in the Fig. 5.12 the total area of an AC pad

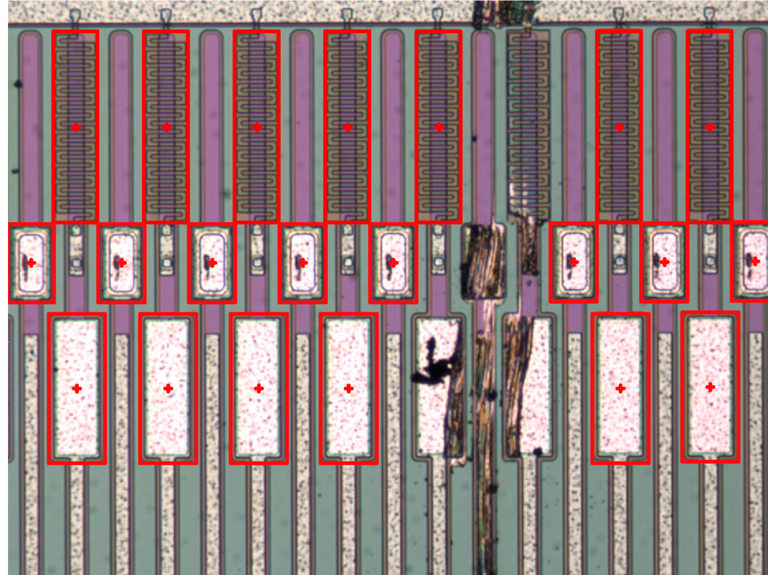

Figure 5.53.: The electrical element integrity principle based on the pattern matching. The defective elements are not detected here due to the high, thus strict, matching score threshold.

was estimated to be around 9000 μm^2 whereas the typical needle spot size was estimated to be around 400 μm^2, which is no more than 5% of an AC pads area and is in accordance with the quality criteria set.

5.4.5.2. DC pads

The DC pads are used for the electrical quality assurance. They are not used during the quality control at the manufacturing sites. Their presence is required during the optical quality assurance. They are required to contain no foreign objects covering them and no scratches crossing them. Their integrity score is set to 95%.

5.4.5.3. Bias resistors

The bias resistors connect the implant strips to the bias ring. A defective resistor leads to the inability to bias the implant strip. Their presence is required during the optical quality assurance. Same as DC pads, they should not have any foreign objects covering them, no scratches should cross them. The integrity score is set to 99%.

5.4.5.4. Bias ring

The bias ring allows to bias the sensor by applying the potential $\geq V_{fd}$ (full depletion voltage). Thus it is important that the bias ring is not segmented by

deep scratches into different regions which may lead to the inability to bias the implant strips in the segmented out region. The bonding pads allow to contact the bias ring by bonding to it or using pogo pins. Thus their integrity should also be checked and not be less than 90%.

5.4.5.5. Guard ring

The guard rings are placed outside of the active zone of a sensor. They are gradually decreasing the electrical field in the outermost regions of a sensor (see Fig. 5.54). Thus a defective guard ring will result in a modified I-V and C-V characteristics of a sensor. The most recent masks of the CBM STS sensors have the guard rings on both p- and n-sides of the sensor. The CiS sensors have their 14 guard rings visible and exposed for testing via small passivation layer openings. The width and distance between the rings differs, which helps to decrease the electrical field potential on the edge of the sensor. The Hamamatsu sensors have only one wide bias ring. Both sensor types employ the metal overhang technology, which improves the electrical field potential decrease.

A possible conductive foreign object covering the guard ring might shorten the individual rings of a CiS sensor bringing them to the same electrical potential, which should be avoided. A conductive object can as well shorten the guard rings and the bias rings, which brings them to the same potential and should be avoided. A number of scratches on the guard ring can electrically decouple and segment the guard ring into insulated regions, which will distort the electrical field of a biased sensor. This should be avoided.

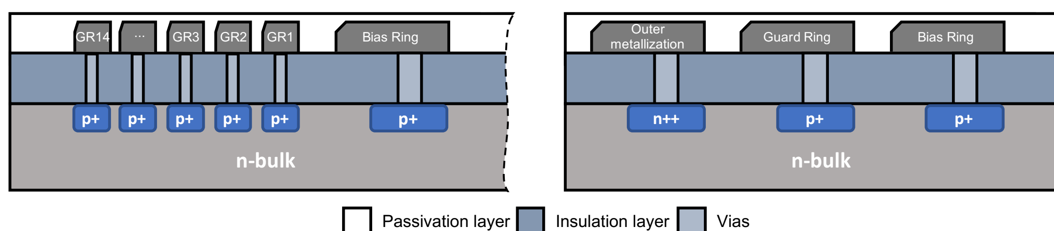

Figure 5.54.: The sketches of the edge region of the CiS (left panel) and Hamamatsu (right panel) sensors.

We require and check with the machine vision algorithms that there are no foreign objects and no crossing scratches on the guard rings and outer metalization layer.

Fig. 5.55 shows an example of the defect detection in the guard ring region of the sensor. Top panels show the detection of defective area over several individual guard rings of a CiS prototype sensor. Bottom panels show the foreign object detection which lies on the bias ring and guard ring and potentially shorts them

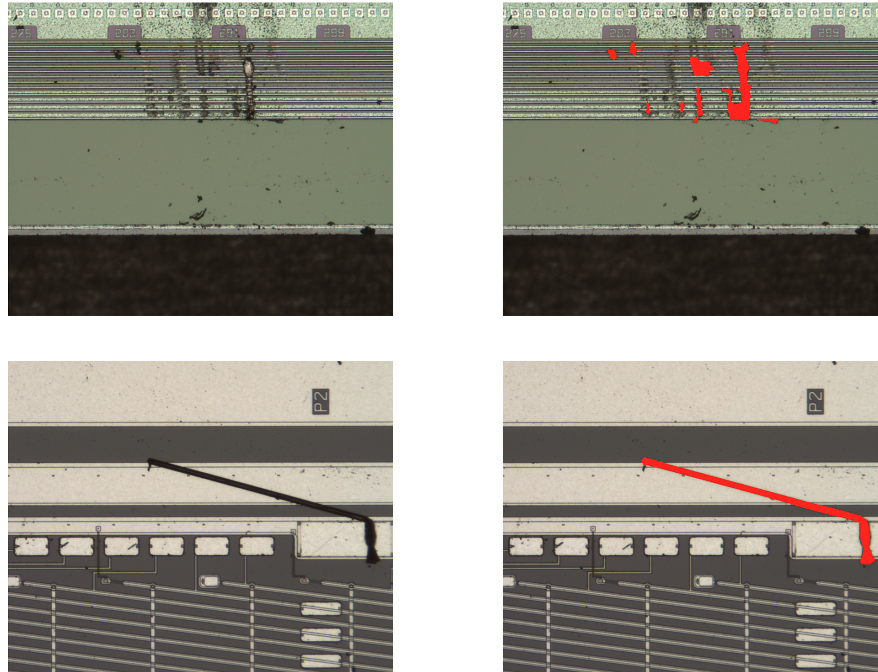

Figure 5.55.: Detection example of the deeply scratched guard ring of a CiS sensor (top panels) and a foreign object laying over bias and guard ring of a Hamamatsu sensor (bottom panels), potentially shortening them.

and brings them to the same potential. Left panels show the source images, right panels show the processed images with defects detected and overlaid over the source images. The detection is based on color thresholding, binary morphological analysis and reconstruction.

5.4.6. Advanced defect analysis

The methods described above provide a powerful set of defect detection algorithms. However they are very configuration dependent. For example the wrong value set for color thresholding might yield wrong result. The same applies for the pattern matching. Here we want to set the detection threshold as high as possible to detect the discrepancies from the reference images. The defects extracted with texture matching have no classification information, thus providing no possibility to distinguish between scratches and dust particles. Furthermore the defect context information is not always available. For the advanced analysis we use the machine learning and deep learning approaches.

5.4.6.1. Machine learning approach

The machine learning attracts a lot of industry and academic attention. The machine learning frameworks and libraries such as Caffe [80], TensorFlow [81]

and mxnet [82] provide the infrastructure to flexibly implement, train and visualize the neural network models. They support both the CPU based as well as the accelerated GPU based computations. The neural networks were already used in high energy physics to distinguish between the QCD phase transition order [83], the search for top quark pair associated Higgs bosons decaying into bottom quarks [84] in the CMS experiment, the measurement of the atmospheric muon spectra [85] with IceCube neutrino experiment and others.

In this work we investigate the possibility of the neural network application for the defect detection and classification.

5.4.6.2. Convolutional neural networks

The convolutional neural networks (CNN) feature multiple convolution layers. They allow to extract the so called multi-dimensional feature maps receptive for distinct features of the input images. The responses of the convolutions can then be pooled for the corresponding minimum, average or maximum values in order to reduce the dimension of the next layer. In the deep neural networks there are many convolutional and pooling layers which gradually reduce the dimension of the source image and increase the dimensionality of the feature maps. For image classification the detection layer is used as the last layer of the network, which outputs the class of the detected object with a certain probability.

5.4.6.3. Method application

In this work we use convolutional deep neural networks for defect detection and classification as well as to recognize and classify the defect context. We implement the defect detection and the context detection networks separately to reduce the misidentification, since the object to be detected are often intermixed. The networks are based on the Darknet [86] framework implementing the modified Faster R-CNN [87] network model. It allows to detect the objects which look similar to those trained against as well as predict the object's location.

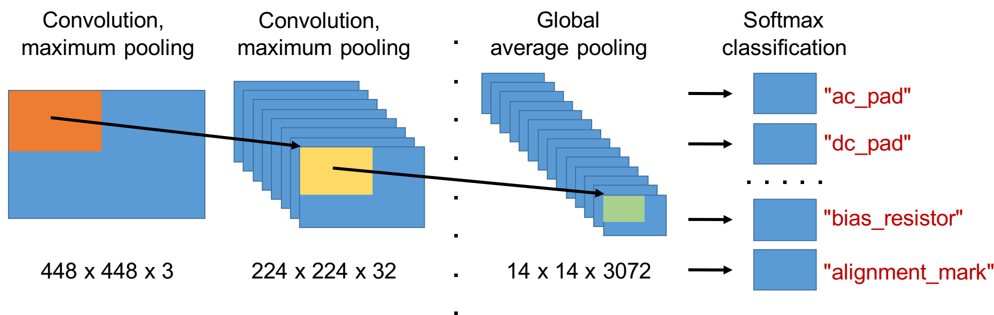

Figure 5.56.: A simplified sketch of the neural network architectures used in this work.

Fig. 5.56 shows a simplified sketch of the deep convolutional neural networks

used in this work, the full network architecture is provided in the appendix B. It features many convolutional layers, which apply image convolution operations with different kernels (cf. section 5.1.2.5). The convoluted images are then processed with an activation function which governs the propagation of the information to the next layers of the network. Fig. 5.57 shows different activation functions. In this work we use the parametrized rectified linear unit function.

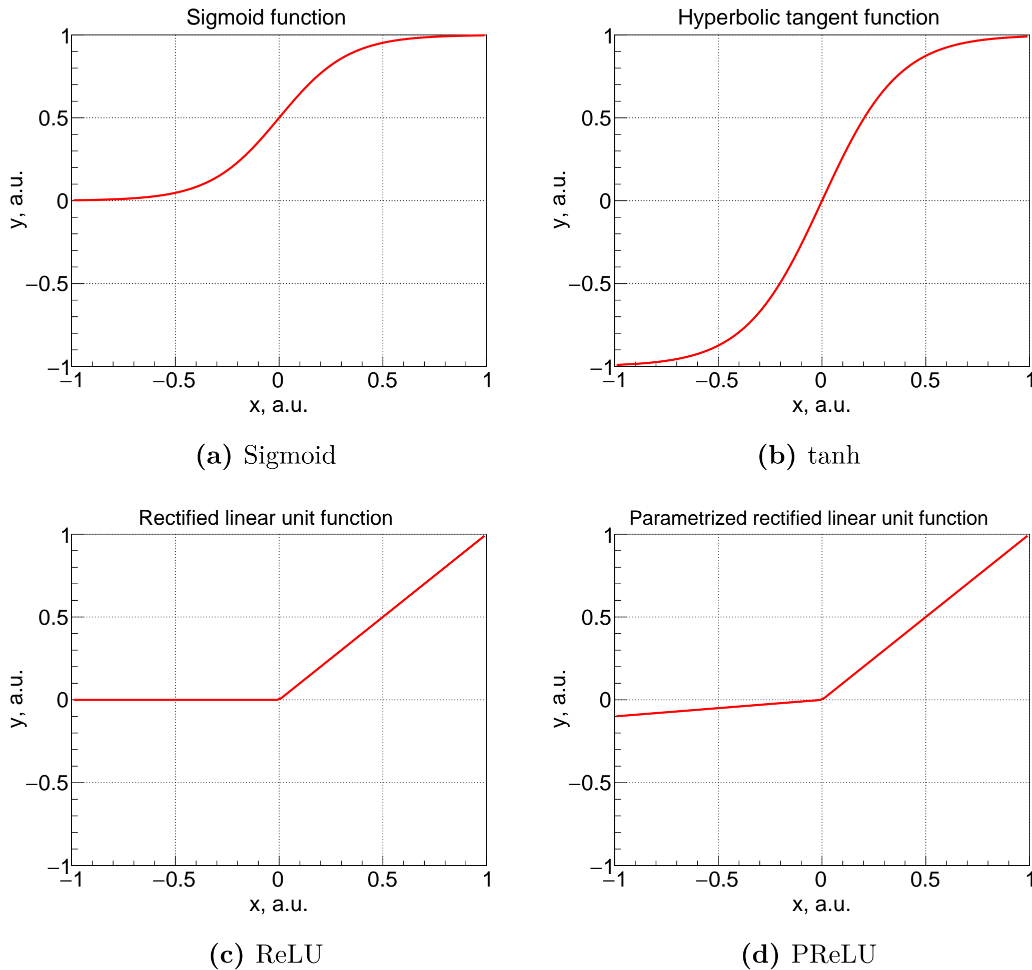

(a) Sigmoid **(b)** tanh

(c) ReLU **(d)** PReLU

Figure 5.57.: Activation functions used for data propagation between the neural network layers. The sigmoid (a), hyperbolic tangent (b), rectified linear unit (c) and parametrized rectified linear unit (d) functions are shown. This work uses the PReLU activations between convolution layers.

The maximum pooling layers extract the maximum pixel values of the filtered images and propagate them to the next layers of the network, thus increasing the dimensions of the feature maps. By repeating this approach, the high-dimensioned feature maps are obtained (in this work up to $14 \times 14 \times 3072 \approx 6 \cdot 10^5$ features).

The maximum pooling principle is illustrated in Fig. 5.58. Here the pooling

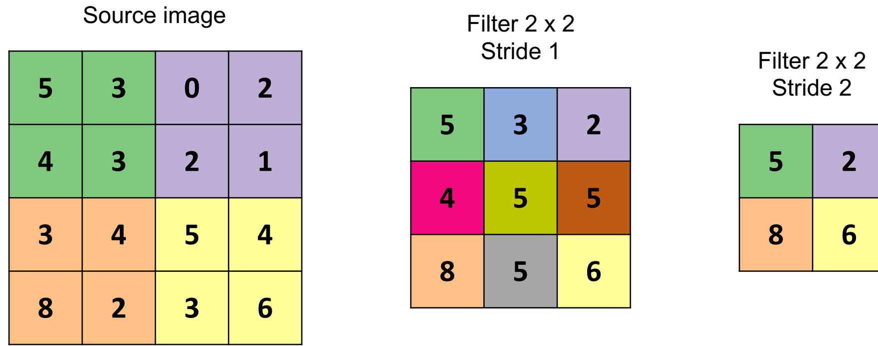

Figure 5.58.: A sketch of the maximum pooling principle. Left panel shows the source image. Middle and right panels show the result of a pooling filter with a size of 2×2 and stride of 1 and 2, respectively.

filter of size 2×2 is applied to the source image shown on the left panel. The maximum value of the pixel value is propagated to the reduced output image. The stride parameter governs the movement of the filter over the image. For example, with a stride value of 1 the filter is moved by one pixel in the corresponding direction and the computation of the maximum value is repeated. The middle panel and the right panel of the figure show the application of the filter with a stride value of 1 and 2, respectively.

The extracted feature maps are analyzed for the probability of a certain class of object appearing based on the softmax logistic function [88]:

$$p(C_k|x) = \frac{exp(a_k)}{\Sigma_j exp(a_j)}, \tag{5.7}$$

which allows to compute the probability $p(C_k|x)$ of certain object class k to be observed among j total classes defined.

The source data for the input of the neural networks was produced both automatically and selected manually. For the automated data pre-selection the output of the optical inspection was taken. For the context-detection source-data the pattern matching algorithms with lowered detection threshold values were used. For the defects the results of the morphological analysis were used. In both cases the location and size of the feature were used to automatically form the input for the neural network.

The training was done on an OEM NVidia GTX 745 GPU with 2000 MB of RAM available and CUDA [89] support. The full 5 MP source images can not be used due to the memory and performance limitations of the GPU. Instead the regions of interest around a defect or feature of about 450×450 pixels were extracted for further processing. The models were trained for 10000 iterations taking 5 days each. The data sets were automatically augmented by the framework by automatic source image rotation, crop and resizing. This allows to improve the robustness of the detection by increasing the generalization of the

feature detection.

The Faster-RCNN neural network model used in this work allows both to classify the object detected and propose the region in the image where the object is located. To qualify the performance of the network the sum of precision of both metrics is taken into account. Faster-RCNN defines the optimization function, or the loss functions as:

$$L(\{p_i\}, \{t_i\}) = \frac{1}{N_{cls}} \sum_i L_{cls}(p_i, p_i^*) + \lambda \frac{1}{N_{reg}} p_i^* \sum_i L_{reg}(t_i, t_i^*), \tag{5.8}$$

where L_{cls} and L_{reg} are loss terms related to the object class and object region identification. Details can be found in [90] and [87].

To qualify the quality of the bounding regions of the detected objects proposed by the Faster-RCNN various metrics can be used such as precision, recall and intersection over union (IOU) (see Fig. 5.59).

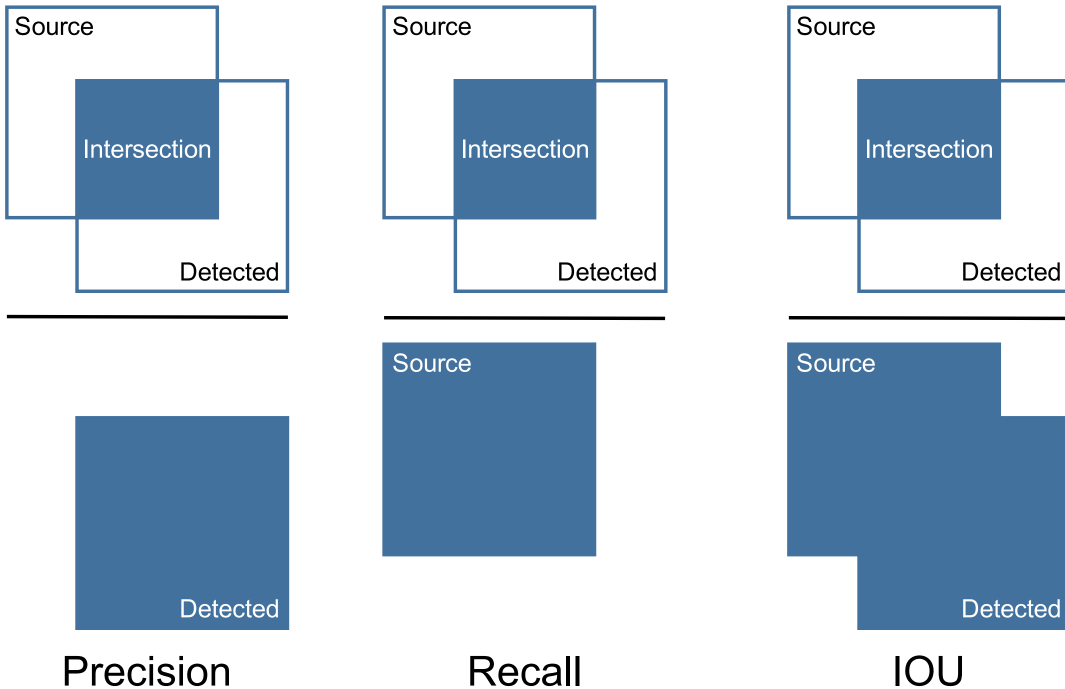

Figure 5.59.: Different metrics used to estimate the performance of the region proposal networks: precision (left panel), recall (middle panel) and intersection over union (IOU, right panel).

The *Precision* metric is the ratio between the intersection area of the predefined source object region (so called ground truth) and the detected object region area. The *Recall* metric defines the ratio of the intersection region and the source object. The *IOU* metric denotes the ratio between the region of the intersection area of the source object and the detected object and the union of their areas. We use the latter parameter to estimate the performance of the model in this work.

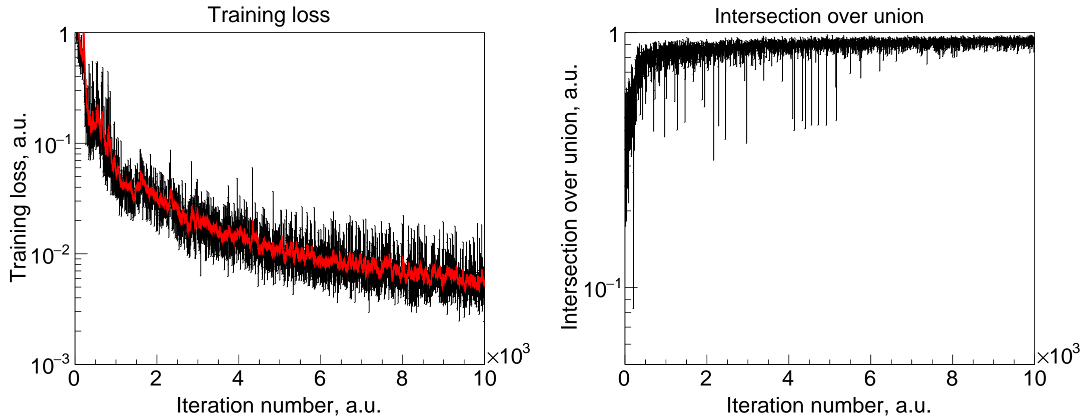

Figure 5.60.: Training progress illustrated in terms of training loss (left panel) and intersection over union (right panel).

Fig. 5.60 illustrates the progress of the training of the neural network for defects detection. The iterations represent a full training data set processing step. The training loss (left panel, black curve) represents the sum of errors made for each prediction and is the minimization parameter, the evolution of the training average loss is depicted with a red curve. The IOU metric evolution if depicted on the right panel. In a well trained network this metric should tend to be equal to unity.

Fig. 5.61 shows the output of the trained context detection neural network. It allows to identify the electrical elements and other features of the sensor.

Fig. 5.62 shows the output of the trained defect detection neural network. Here the dust particles and scratches are detected. The associated regions where the defect are found are as well extracted.

The defect detection neural network is continuously trained on the new data from the sensors as they are inspected. This allows to account for the defects which have different spatial configuration.

The network trained on the GPU can be run on the CPU as well. A single 448×448 source image takes about 0.16 seconds to be processed on the GPU and about 7.9 seconds to be processed on the CPU. For a single 5 MP image taken from the camera results in 30 source images for the network input, yielding the total time of about 5 seconds for the GPU and about 4 minutes for the CPU based detection.

5.4.6.4. Summary

The correct defect and context detection with the standard machine vision algorithms is not always possible due to the preconfigured detection thresholds and other detection parameters. For the prototype sensors available in this work the

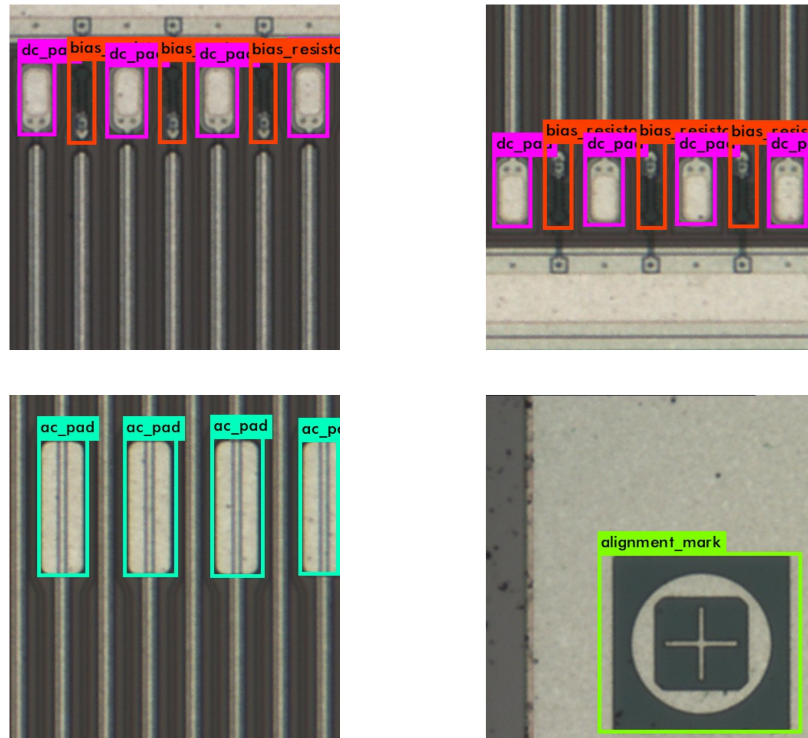

Figure 5.61.: Different contexts of the sensor identified with a neural network.

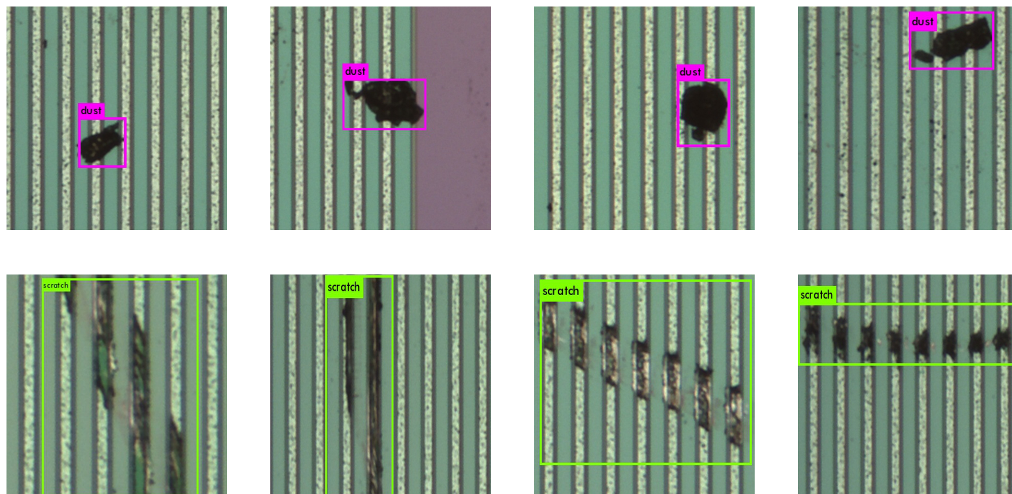

Figure 5.62.: The dust particles and scratches identified with a neural network.

detection rates were estimated to be 87% and 80% for defect and context detection, respectively. The usage of the neural networks has improved the defect detection to 96% and the defect context detection to 93%.

5.4.7. Inspection results

24 prototype sensors from different generations and sizes available in this work have been inspected for their surface quality. The sensor quality grading have been done in the following way. For every defect found, based on its type and size, the “penalty points” have been added up. The penalty points are then converted to the sensor quality score ranging from 0 to 4 and the quality grade from D to A. The results are presented in Fig. 5.63.

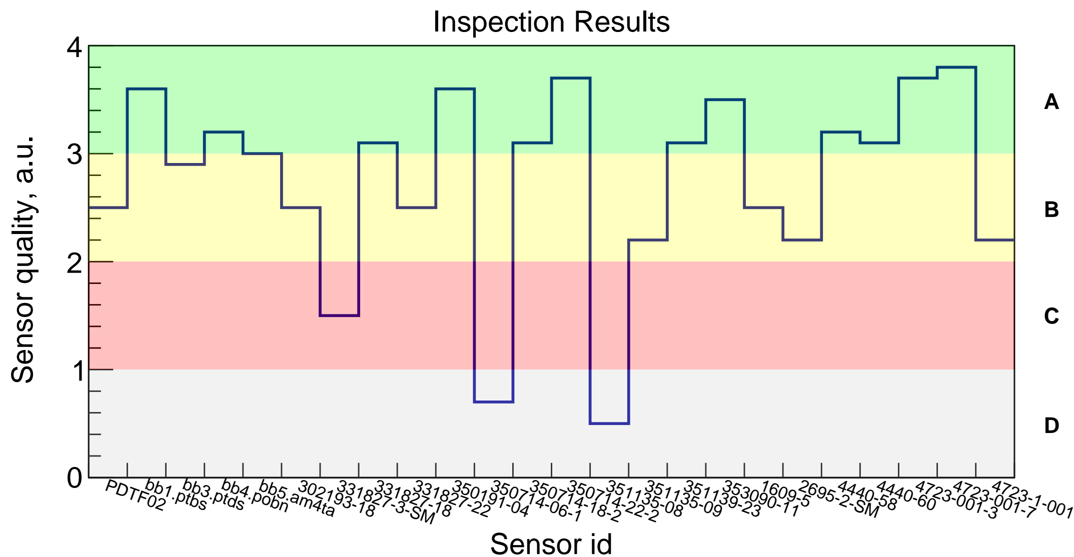

Figure 5.63.: Summary for the sensor quality inspected. The sensor quality score and grade range from lowest (0, D) to highest (4, A), respectively.

Grade A sensors have only minor defects such as small dust particles, no strip defects and the electrical element integrity is above 95%.

Grade B sensors are allowed to have some medium sized dust particles, non-critical surface scratches, strip interruption due to metal open or others for no more than 5 strips for both sides. The AC and DC pads are allowed to have less than 75-95% integrity score due to previous electrical measurements.

Grade C sensors have medium to large sized dust particles, deeper surface scratches, strip interruptions for 5 to 15 strips for both sides. The electrical element integrity score is 50-75%. There are some edge defects.

Grade D sensors have very dirty surface, deep surface scratches, more than 15 strip interruptions, electrical element integrity lower than 50%. There is a significant chipping of the sensor edges.

5.5. Sensor metrology

The geometrical metrology is an important part of the silicon sensor quality assurance. It allows to verify and control the geometrical properties of the sensor such as their warp, cutting edges and their parallelism, the thickness of the sensor. This section describes the metrology procedures and methods developed in this work.

5.5.1. Sensor warp measurement

From other high-energy physics experiments it is known that the silicon sensors have a height profile or warp [78]. Measurements of the warp of the silicon microstrip sensors of the STS detector is important for the precision during module assembly or, ultimatively, for the improvement of the tracking performance. Furthermore, the warp information is important for adjustment and positioning of the probe needles during the electrical characterization of the sensors.

5.5.1.1. Height measurement with the optical system

The precise positioning of the camera in Z-direction or change of motorized focus stage value allows the height measurement. This is done by analyzing the image sharpness at different motor positions.

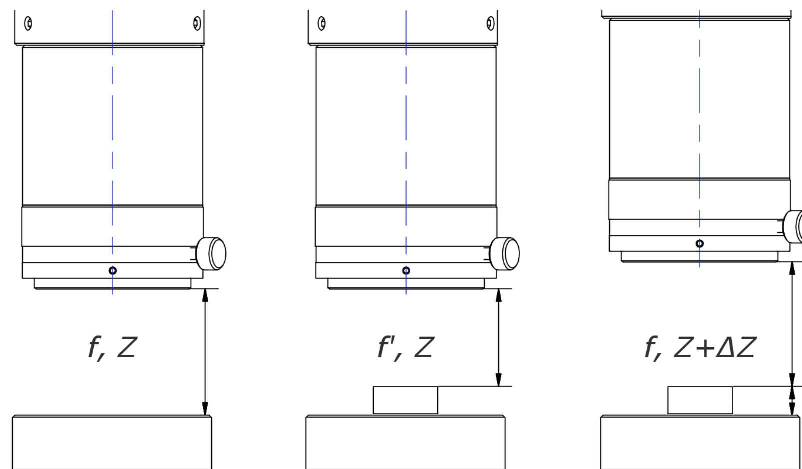

Figure 5.64.: The object height measurement principle by adjusting the focus of the system in a calibrated fashion (middle panel) or by adjusting the vertical position of the optical system (right panel). Optical tube CAD drawing used here is taken from [91].

Fig. 5.64 shows the principle of the height measurements. When inspecting a certain object, the focus of the system is first adjusted such that the image of the underlying surface is sharp and well focused (left panel of the figure). Then

an object under test is put on the underlying surface, and the optical system is adjusted once again for the most focused image. This is done by adjusting focus of the system (middle panel) or by adjusting the distance from the focal plane to the object by moving the whole system in an according Z-direction (ΔZ on the right panel). The calibrated change of the system focus is converted to the real-world coordinates, which allows to extract the height of the object. In this work the focusing approach is chosen due to its higher precision compared to the movement of the whole system. Refer to the sections 5.2.2 and 5.3 for precision estimation.

Having the focus stage motorized allows to implement the automated search of the most focused state of the optical system, i.e., autofocusing. The most simple implementation of the autofocusing is as follows. One steps over the range of motor positions and corresponding images from the camera. Every image is then transformed with a fast Fourier transformation [92] to the frequency domain[1], then, as a measure for image sharpness, the sum of all frequencies of the complex image is calculated and associated with a particular motor position. The acquired 2D array of values is fitted with a Lorentz [93] probability density function as presented in (5.9):

$$f(x; x_0, \gamma) = y_0 + A \cdot \frac{1}{\pi\gamma \left[1 + \left(\frac{x - x_0}{\gamma}\right)^2\right]}, \tag{5.9}$$

where y_0 is the y-offset, x_0 is the x-offset, A is the amplitude and γ is the half-width at half-maximum (HWHM). These variables are the parameters to fit the distribution either with Levenberg-Marquardt [94, 95] algorithm in LabVIEW or with the ROOT Minuit fitter [77] during offline analysis. The fitted x_0 value corresponds then (within the extracted fit error interval) to the motor position of the most sharp image.

Fig. 5.65 shows the distribution which has the most focused value around 3209 motor steps (roughly the mid interval of focus motor space) produced after scanning procedure with a step size of 10 motor steps. The fit parameters are presented in Tab. 5.4.

	Fitted Value	Fit error
x_0	3209.09	± 0.69
y_0	$4.34 \cdot 10^7$	$\pm 7.58 \cdot 10^4$
γ	442.97	± 1.26
A	$1.79 \cdot 10^{11}$	$\pm 4.51 \cdot 10^8$

Table 5.4.: Fit parameters for Fig. 5.65

[1] In the frequency domain every pixel represents the particular frequency contained in spatial domain.

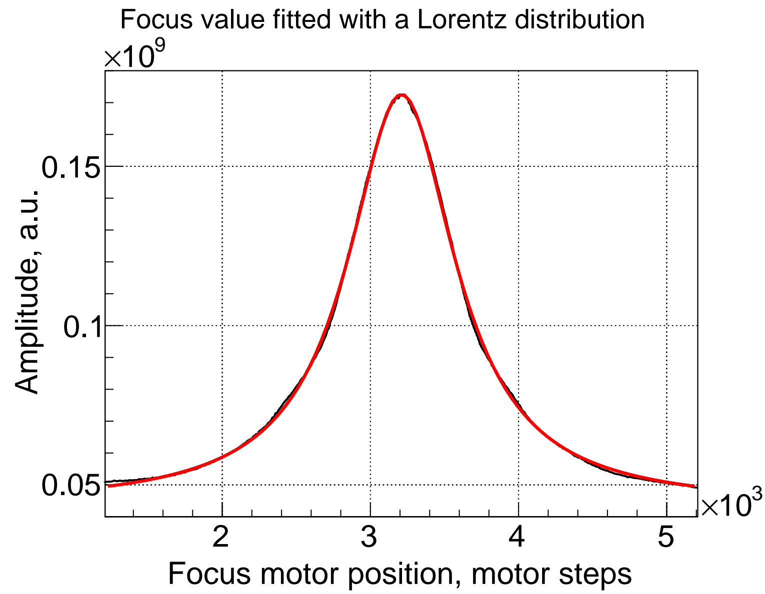

Figure 5.65.: Image frequency response vs. motor step.

The procedure is visualized in Fig. 5.66. The left panel shows the image taken from the camera, the middle panel shows graphical representation of a Fourier transformed image and the right panel shows the total amplitude distribution obtained from processing transformed images.

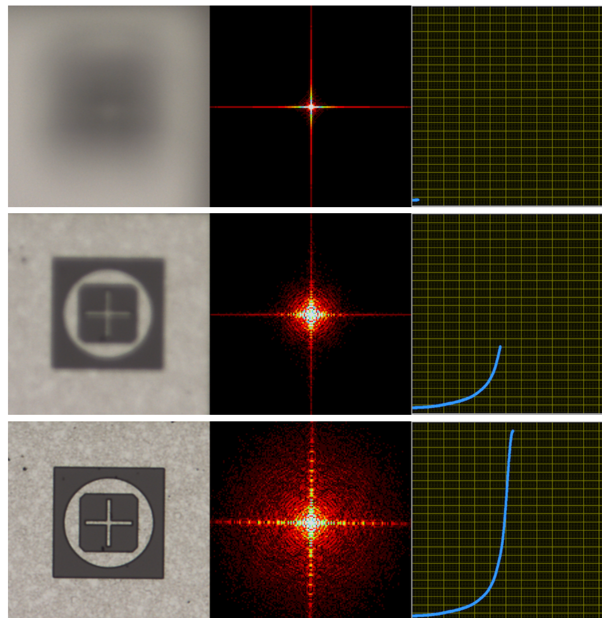

Figure 5.66.: An instant cut of the autofocusing process at 3 different motor positions, corresponding to non-focused image (top row), more focused image (middle row) and fully focused image (bottom row).

Characterization of the method

In order to characterize the method used to measure the height profile of the objects under test, a series of statistical measurements were conducted. In these tests the same height value was measured 50 times to estimate the mean measured autofocusing value and its standard deviation. The tests were then repeated for different stepping parameters in range from 1 to 500. Fig. 5.67 shows the obtained results. The plots show the autofocus value measured (left panel), autofocus fit errors (right panel) and single measurement time (bottom panel) as a dependence of motor stepping width.

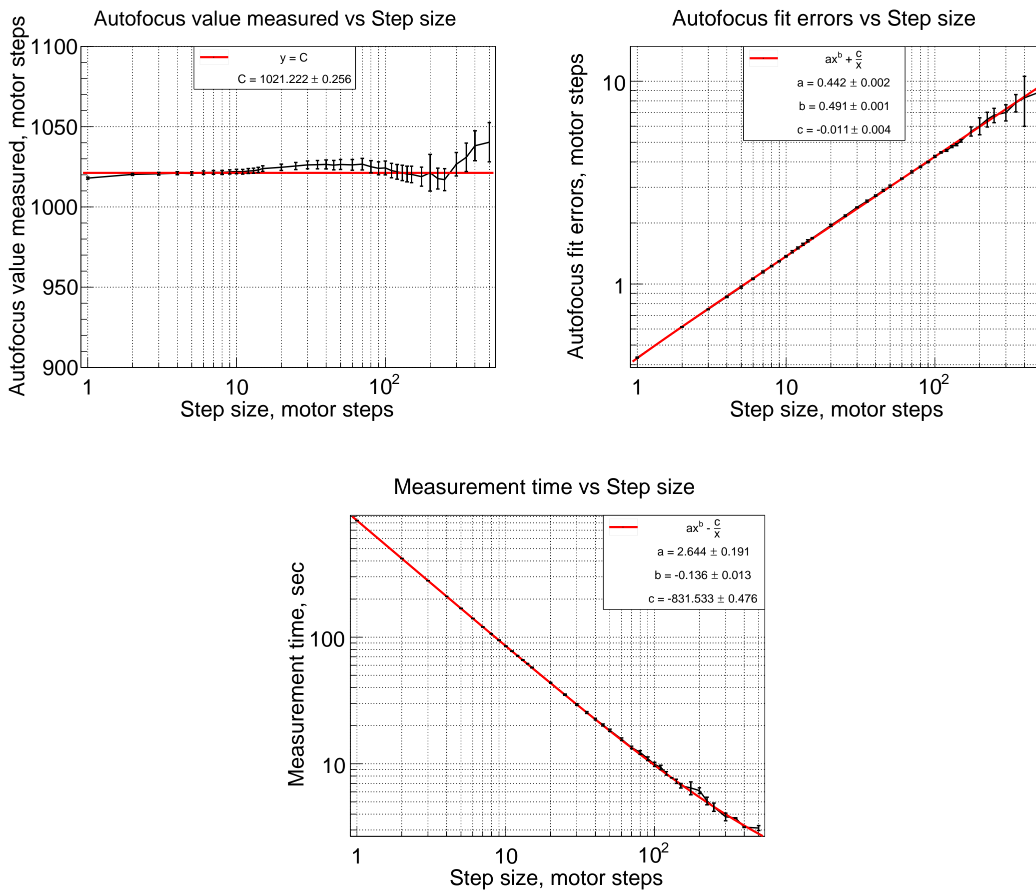

Figure 5.67.: The results of the autofocusing method characterization — the autofocus value measured (left panel), the fit errors (right panel) and the single measurement time (bottom panel) depending on the motor step size.

As seen from the pictures above the smaller the motor step width the more precise is the resulting autofocus value. However the time needed for a single measurement increases exponentially. The measurement time optimization will be presented further below. Note, that, as the motor stepping width goes above 200 the low number of data points around the Lorentzian distribution peak results in

a degraded estimate of the peak position as well as a large rise of the measurement errors. It is not advised to use theses stepping values, as the results would be too unreliable.

The time needed to scan a single side of a 6.2×6.2 cm^2 sensor with a precision of one motor step and a scan step width of 1 mm takes up to 174 hours. This estimation is done without the motor movement time, which adds some more overhead. Thus the optimization is needed to reduce the measurement time.

Method optimization

In order to speed up the warp inspection one could implement an adaptive approach which takes the previous autofocus value measured into account, and looks for the next autofocus peak around this value. The introduction of an *approach parameter* allows to speed up the inspection. In this method the motor stepping width is reduced by a factor, controlled by the approach parameter, as it approaches the expected peak and increases by the same factor as the peak value is passed. This results in more statistics around the true peak, which improves the fitting. An additional introduction of a stop criterium that the current amplitude should be not less than 0.5 of the maximum amplitude allows to exit the measurement loop at an early stage, thus saving more time.

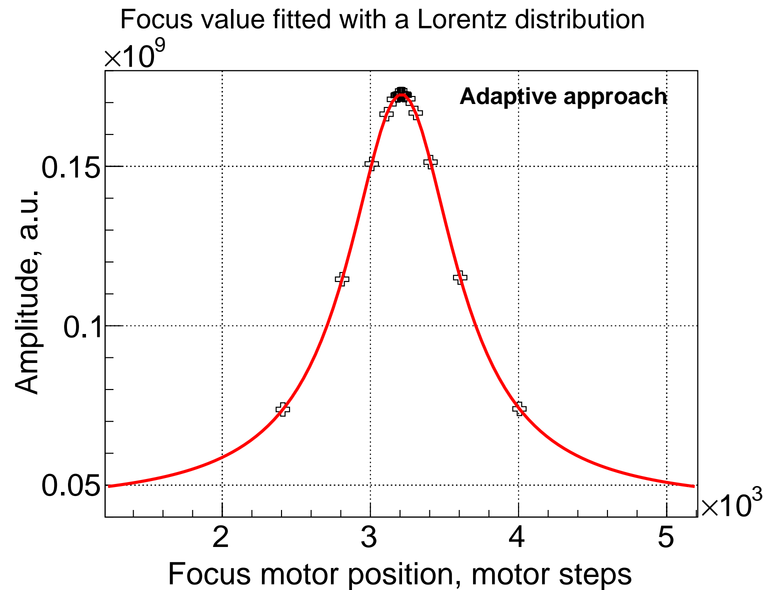

Figure 5.68.: Image frequency response vs. motor step for an approach parameter value of 2.

Fig. 5.68 illustrates the adaptive approach. Here the image frequency response is plotted for the data obtained with an approach parameter value of 2. Note how the distance between the data points along the X axis is first decreased by a factor

of 2 and, after passing the distribution peak, it is increased by a factor of 2.

The characterization procedure was repeated for the adaptive approach described above with the values of the approach parameter ranging from 1 to 30. Fig. 5.69 show the summary of the obtained results. Note that for the approach parameter equal 1, the results are naturally very imprecise, since the motor position on the first step will be immediately set to the anticipated peak position thus severely limiting the analysis statistics and yielding a large dispersion of the extracted peak position.

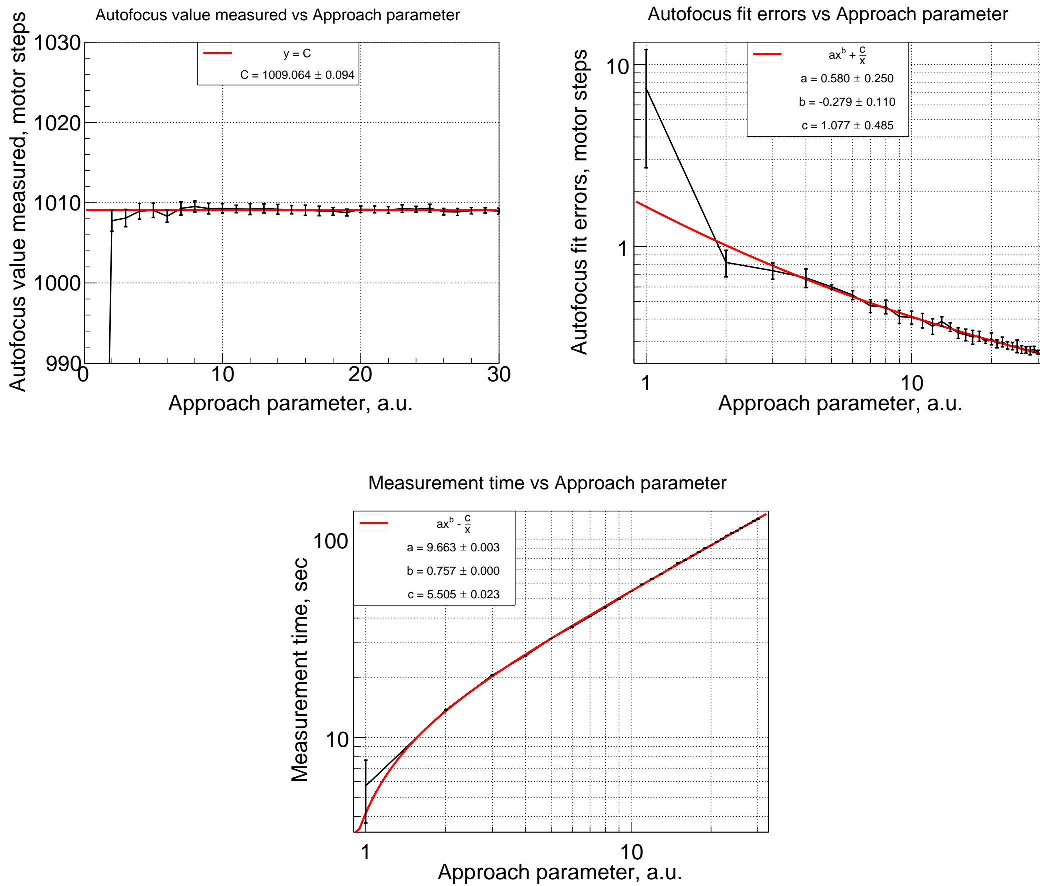

Figure 5.69.: The results of the adaptive method characterization — the autofocus value measured (left panel), the fit errors (right panel) and the single measurement time (bottom panel) depending on the approach parameter.

From the results shown above, it follows that this adaptive method is not only faster but has a much higher precision with measurement errors being below one motor step for an approach parameter value greater than two. When comparing the measurement times of both methods for a criterion, that the measurement errors should be below one motor step, the adaptive method is at least 8 times faster for a single measurement. This improvement reduces the total measurement time for the same parameters to 21.3 hours.

Method comparison

Fig. 5.70 show the precision (in terms of fit errors) and single measurement time comparison.

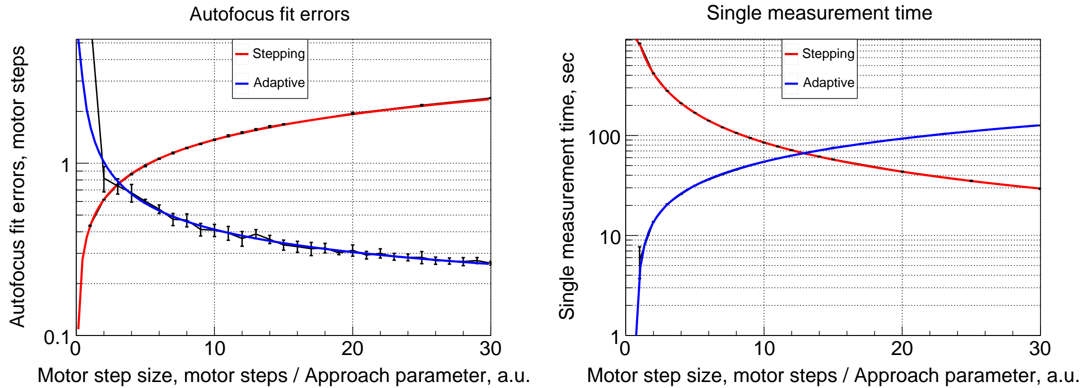

Figure 5.70.: Method comparison for the stepping and adaptive approaches in terms of fit errors (left panel) and measurement times (right panel).

Though being about 8 times faster for the adaptive method, the inspection time is still somewhat long. In order to optimize it and speed it up, one would need to give up the scanning granularity, since it is a quadratic dependence on the scanning step.

Fig. 5.71 shows the total inspection time dependence from inspection granularity (the stepping size between measurements) for the approach parameter value of 2. The finer the measurement step, the better the inspection and more features could be seen on the surface. However, this means as well, that the inspection time increases dramatically.

5.5.1.2. Method applications

Having a possibility to measure autofocus value at a single point with a good precision enables one to measure the height maps deduced from differential measurements of autofocus values at different points of the object under test. The focus stage motor position is converted by a ratio of 2.2333(3) steps per micrometer as presented in section 5.2.2. The conversion ratio allows to transform the height maps obtained in motor steps into real-world measure — micrometers.

Fig. 5.72 shows such a height profile measurement for the vacuum chuck used in the optical setup. To obtain a corrected picture shown on the right panel of this figure, we fit the data with a plane and subtract it. Knowing the Z-profile of the vacuum chuck is important for optical inspection, since it improves the movement over the sensor and ensures avoidance of the focus loss and sharpness of the images taken.

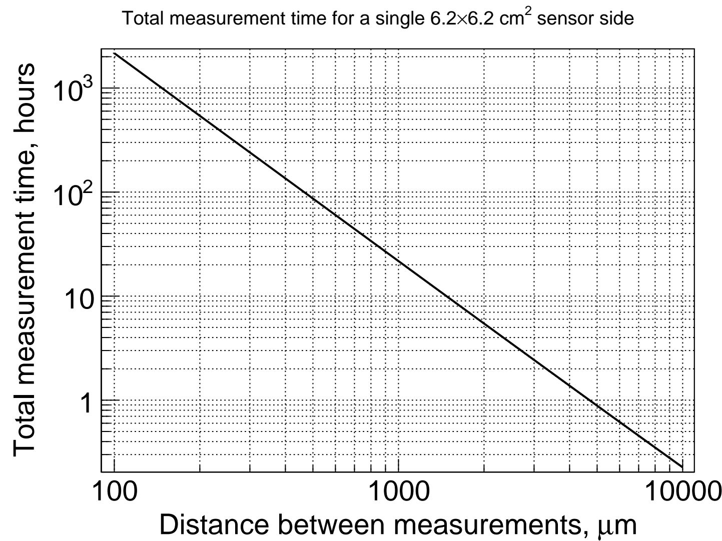

Figure 5.71.: Log-log dependence of single measurement time vs. approach parameter value.

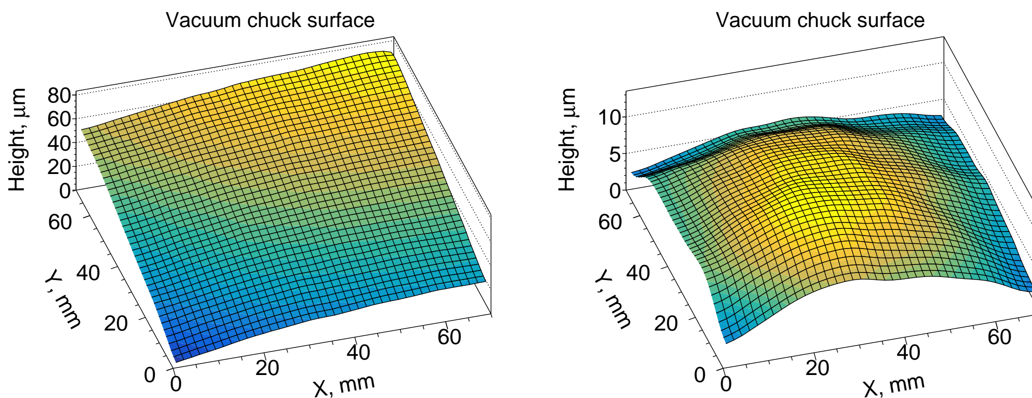

Figure 5.72.: Height profile of a most central 7×7 cm region of the vacuum chuck obtained with autofocusing method to measure object heights. The left panel shows uncorrected map. The right panel shows the corrected one.

The developed methods allow a contactless optical measurement of the sensor warp. However, simultaneous optical inspection and measure of the sensor warp are impossible, since the optical inspection as for now requires the vacuum pump turned on and sensor being sucked to the chuck. The warp of the sensor with the supplied vacuum is substantially modified and does not represent the real height profile of the sensor in its free state. This could be seen in Fig. 5.73.

All the prototype sensors available in this work were characterized and their respective Z-profiles were extracted and analyzed. Refer to the appendix C for

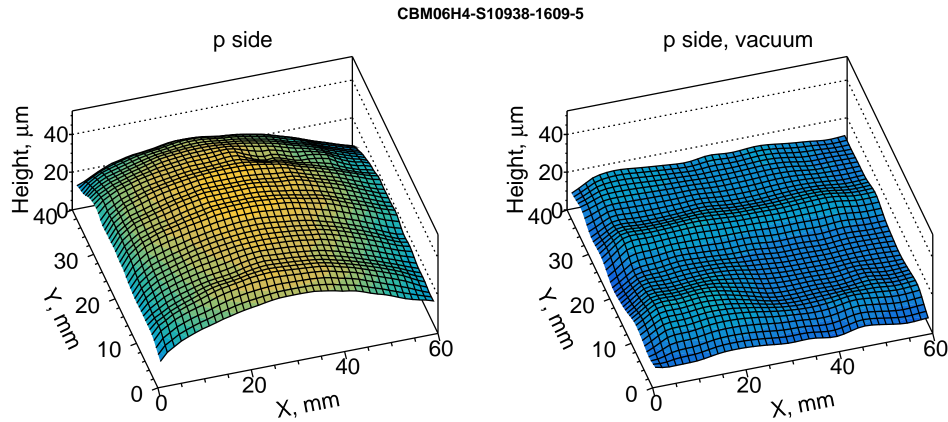

Figure 5.73.: The warp of the prototype 6×4 cm^2 sensor measured without and with vacuum supplied to the chuck. The maximum warp value measured without vacuum is 44 µm and with vacuum applied 19µm.

further details.

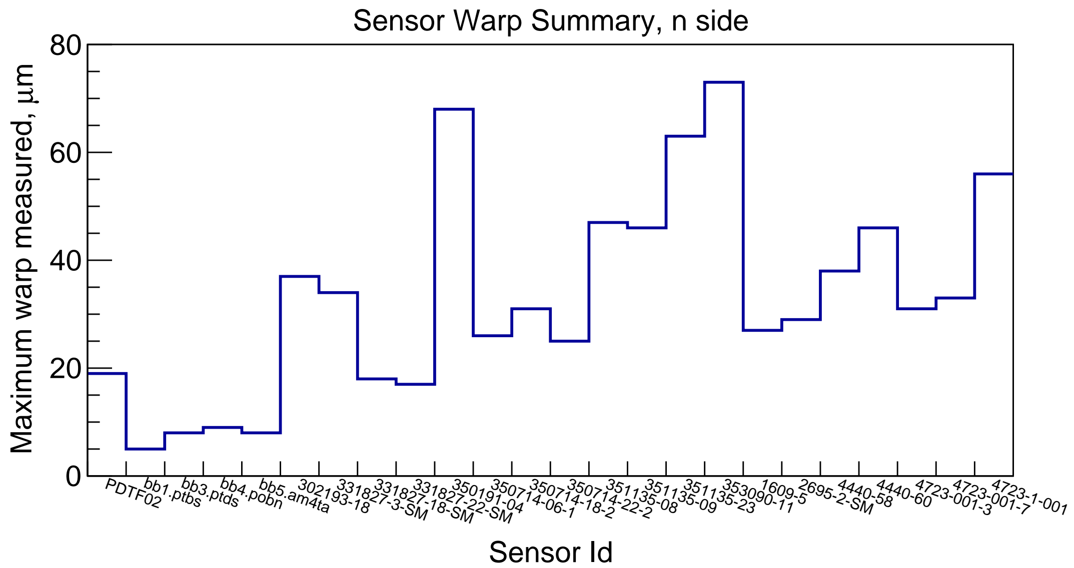

Figure 5.74.: Summary of a measured warp of the n side of the prototype sensors available.

Fig. 5.74 shows the warp summary data for the sensors available in this work. The maximum measured warp (Fig. 5.75) is about 80 µm and is within the quality criteria of 100 µm set for this property of the sensor.

Knowing the sensor warp is important for the electrical quality assurance. Here the sensor needs to be positioned vertically in a way, that the probe needles

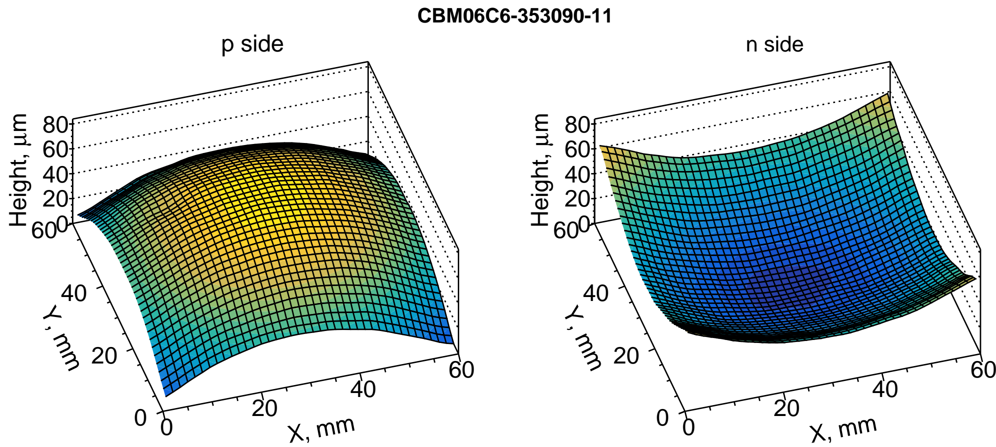

Figure 5.75.: Sensor warp measured for a prototype silicon sensor from CiS.

have a reliable contact to the test pads. Not adjusting the vertical position will lead either to a lost contact or to the deep scratches on the test pads, which should be avoided. Furthermore, the sensor warp is important for the micro cable bonding to the sensors during the module assembly.

A further application of the height measurements described above is the metrological inspection of the sensor mounted to the carbon fiber ladders. These metrology procedures are covered in the section 5.7.2.

5.5.2. Sensor cutting edge inspection

Sensor cutting quality is important to control. The defects on the edge, such as edge chipping, might lead to a local change of electrical characteristics. This can happen if the edge has a rough structure, which might increase the leakage current, change local electrical field reconfiguration, which in turn might lead to an electrical discharge between sensor sides causing damage to the readout electronics. The chipped microstructure of the sensor edge increases its overall surface area and might lead to a water vapor trapping and diffusion deeper into the crystalline lattice. Furthermore the sensor edges are important for the ladder assembly, where the sensor is pushed against the ladder assembly tool to align it properly. The required alignment precision for the sensor is defined to be < 100 µm over 12 cm.

The machine vision algorithms were used to extract the information about the sensor edge quality. Here, the luminance color plane was extracted preserving the brightness information. Then a combination of Gaussian filter and highlighting convolution was used to increase the sharpness of the edges. The *Contour Analysis* tool from the NI Vision package is used to extract the per-pixel contour of the sensor edge. The extracted contour is then compared to the sensor edge fitted

with a linear function. By computing the deviations from contour to the fitted edge the edge profile is extracted for a single image.

Figure 5.76.: A sensor edge profile analyzed using machine vision algorithms.

Fig. 5.76 illustrates the edge profile analysis principle. It shows a closeup picture of the sensor edge obtained during the surface scan. Here the green rectangle denotes the analysis boundaries for the applied algorithms, the blue line is the fitted edge. The edge contour extracted is shown in red. The algorithms are applied for 35 images comprising the full edge of a 6.2×6.2 cm^2 sensor inspected at 4x zoom, allowing to extract the full edge profile.

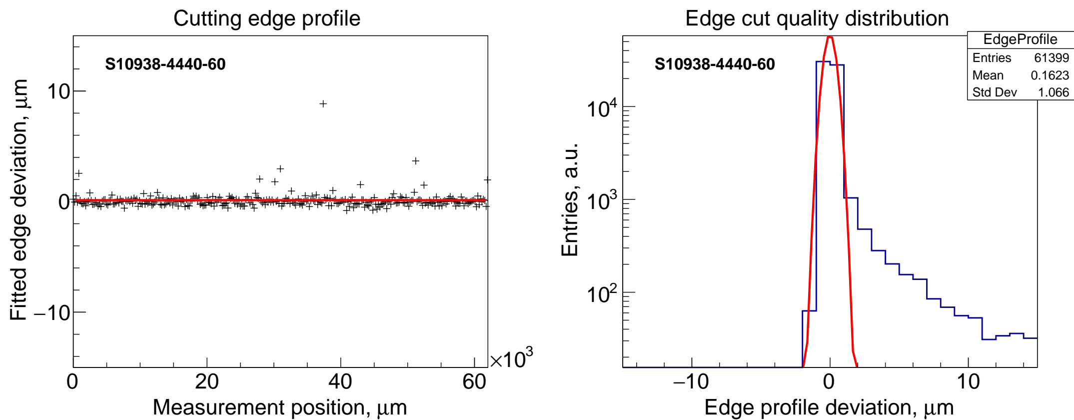

Figure 5.77.: Deviation of a measured edge along a single side of a sensor (left panel) and its distribution (right panel).

Fig. 5.77 shows the edge quality measured along a single edge of a prototype Hamamatsu sensor. The left panel shows the deviation of a measured edge contour from a fitted edge along a single sensor side. The right panel of the figure shows the distribution of the measured deviations. The precision of the method was estimated to be < 1 µm. The deviation of the data points in a positive direction indicates a chipped sensor edge. The deviation in a negative direction indicates that the inspected region of the sensor contains edge microstructure which might come from the dicing process. This microstructure, if its contribution is big enough, will affect the sensor positioning precision during the ladder assembly. The sensor edge quality criterion was defined as maximum $\pm$ 20 µm deviation. From the measurements described in this approach this quality criterion can be automatically controlled for the sensors being inspected.

5.5.3. Sensor edge parallelism inspection

Another quality criterion for the sensor geometry is the sensor cutting edge parallelism and precision. The sensors are cut out from the wafer outside the dice line resulting in the sensor being larger than the nominal dimensions [36]. The CiS company currently uses the diamond blade dicing yielding up to 80 μm extra sensor width per edge with a precision of about 10 μm. The Hamamatsu company uses the laser dicing technology with 10 μm extra sensor width per edge with a precision of few micrometer. The additional sensor width and the finite cutting precision might lead to the edge un-parallelism. The ladder assembly procedures require the contribution of the edge un-parallelism of maximum 100 μm per 6.2 cm of the sensor side as a quality criterion.

To assess this quality criterion the sensor edge un-parallelism is measured with the machine vision procedures in this work.

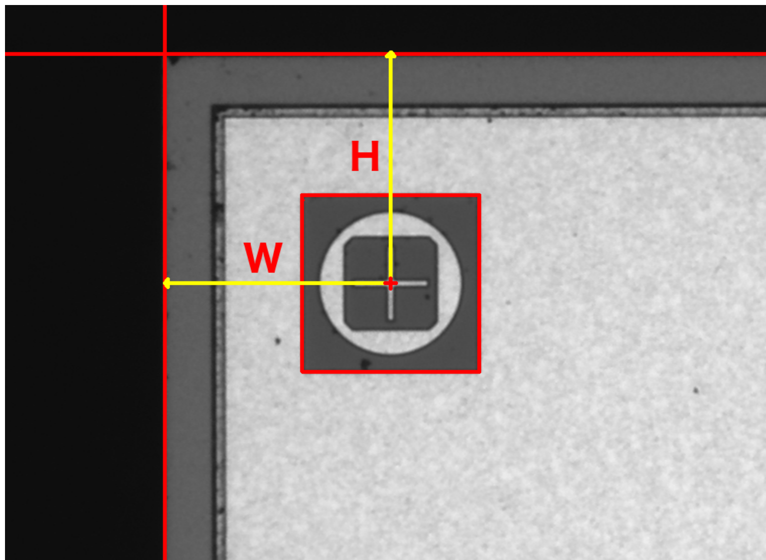

Figure 5.78.: Illustration of the edge parallelism measurement principle.

Fig. 5.78 shows the measurement principle. Here the outermost feature of the sensor, the alignment mark, is taken as a reference. The distances from its center to the neighboring edges of the sensor are measured and compared with those, measured at other sensor corners. Same as with the cutting edge quality control, the analyzed image is first prepared for the measurements by extracting the luminance plane, applying Gaussian filter and highlighting convolution to improve its sharpness. Then the pattern matching algorithm is used to locate the alignment mark and extract the coordinates of its center. The edges of the sensors are fitted with an edge detection algorithms with median weighting. Then vertical **H** and horizontal **W** perpendicular projections are made to the fitted edge lines and the distances are measured with a *Caliper* tool. By comparing the horizontal distances measured e.g. for top-left and bottom-left corners, one can compute the

sensor cut out line. These measurements are carried out for every corner of the sensor.

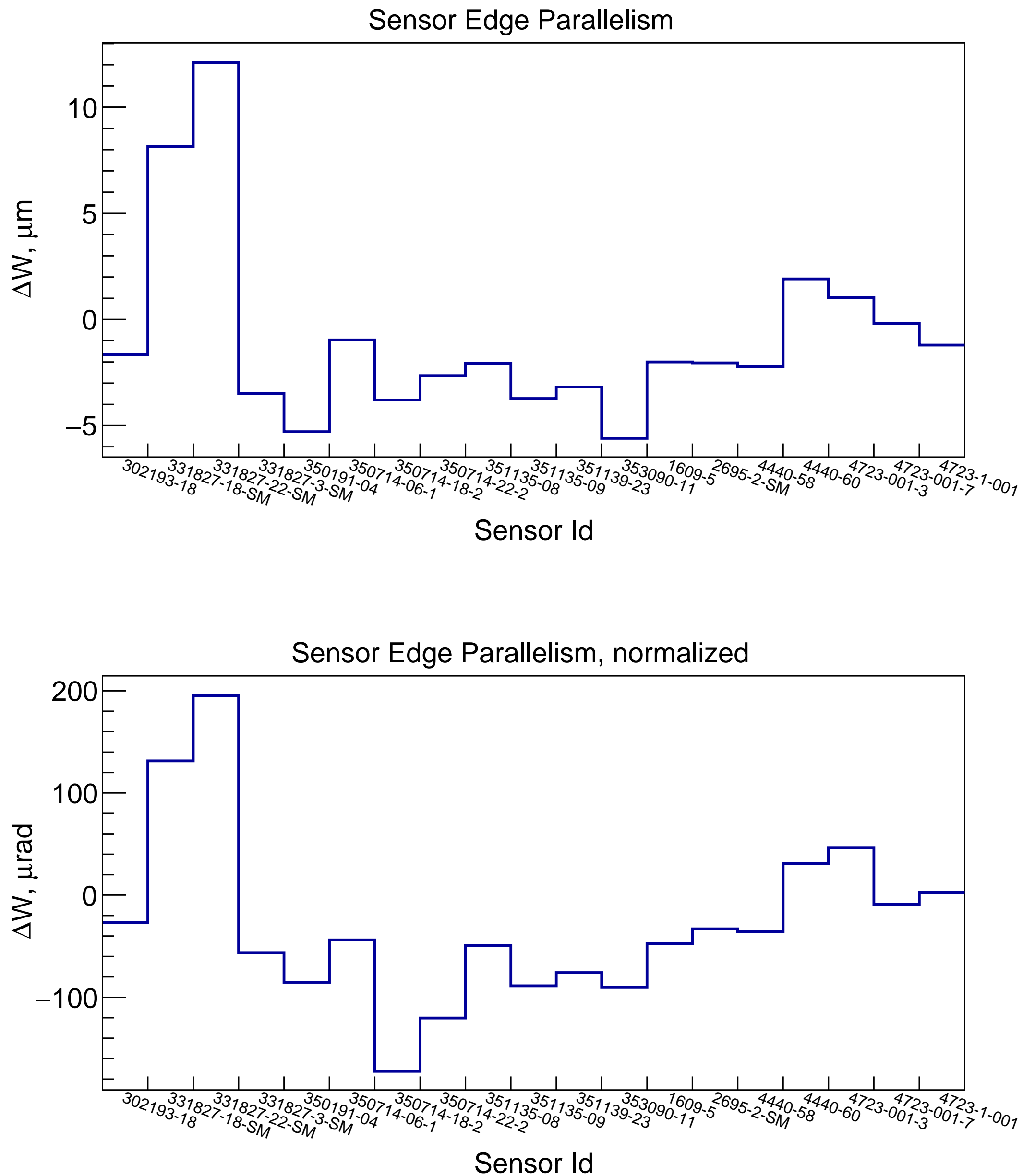

Figure 5.79.: Summary of the parallelism measured for available prototype sensors. Top panel shows the absolute values measured. Bottom panel shows the values normalized to the edge length expressed in microradians.

Fig. 5.79 shows the summary on the edge parallelism data obtained for the prototype sensors available. The values extracted lay within a range of ± 12 μm that satisfies the quality criterion of ± 20 μm set for this metrology measurement.

The precision of this method was estimated to be < 1 µm.

5.5.4. Sensor thickness inspection

The thickness of the silicon sensor is an important characteristic. It directly affects its electrical properties, most notable it is responsible for the electron-hole pair amount produced, when a charged particle traverses the silicon bulk. The amount of electron-hole pairs generated is important for the read-out of the sensor. As it was shown in the section 3.1.3, about 76 electron-hole pairs are produced per µm of silicon bulk. Thus knowing and controlling the thickness of the silicon sensor is essential for its operation. The declared sensor thickness for CiS sensors is 285 ± 15 µm and 320 ± 15 µm for Hamamatsu. This section describes the methods and procedures developed to optically, thus contactless, control this quality criterion.

5.5.4.1. Direct optical measurement

The thickness of the prototype sensors was measured using the optical inspection system. The vacuum table was removed and replaced with a makeshift holding structure. The holding structure was made from aluminum base plate, with the sensor clamped softly between dampening elements while keeping the sensor oriented upright. The soft clamping allows to preserve the sensor warp. The edges perpendicular to the sensor readout plane were inspected since they are used for the alignment procedures during ladder assembly.

The clamped sensor was aligned under the optical assembly to allow the inspection of the sensor thickness along one of its edges. The alignment precision was controlled by ensuring that the top and bottom edges are within the sensor thickness range, as well as left and right edges over 62 mm range stay in focus. Several sensors were inspected, both single metal and double metal types from CiS and Hamamatsu.

Fig. 5.80 shows sample microscope images taken of the selected prototype sensors differing in their production technologies. As expected there is no significant difference in the cutting edge between single metal and double metal sensors. The difference between the cuts from CiS and Hamamatsu arise from different cutting technologies. The silicon used at CiS has a <111> orientation and the wafers are cut with a diamond saw, while Hamamatsu uses <100> silicon and use the laser cutting technology, so called stealth dicing [96].

The edge inspection was carried out at the maximum system magnification of 7x to increase the precision of the thickness measurements. Using the same scan algorithms developed for the sensor surface, the sensor edges were inspected over their full length. A single full length edge inspection for a 6×6 cm^2 sensor takes about 2.5 minutes.

The machine vision algorithms were used to extract the information about the top and bottom edges of the sensor. First, the luminance color plane was extracted

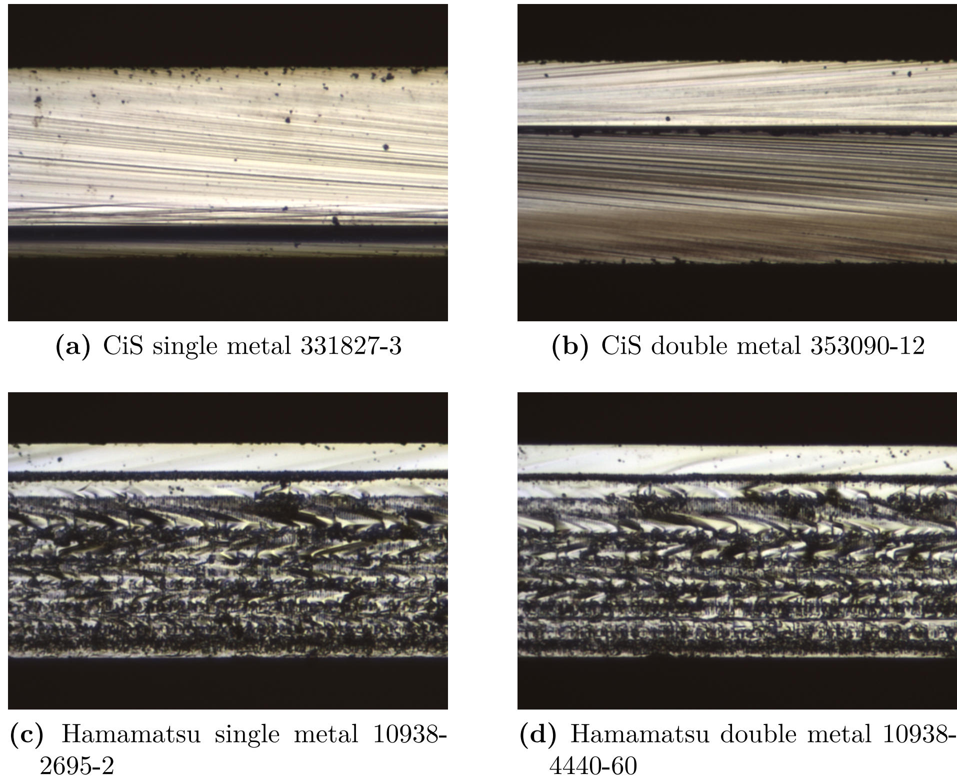

(a) CiS single metal 331827-3

(b) CiS double metal 353090-12

(c) Hamamatsu single metal 10938-2695-2

(d) Hamamatsu double metal 10938-4440-60

Figure 5.80.: A comparison of the sensor edges by their type and manufacturer.

to convert the image into an 8-bit grayscale format preserving the brightness information. Then a combination of the Gaussian filter and highlighting convolution was used to increase the sharpness of the edges. Then the top and bottom edges of the sensor were fit with median weighted edge detection algorithms, to reduce the influence of eventual visible surface roughness of the sensor edge. Using the pixel-to-micrometer conversion ratio extracted from the calibration (see section 5.2.3), the distance between the extracted edges **W**, i. e. sensor thickness in micrometers, was measured. Additionally the distance **D** to the top edge was measured to estimate the warp of the sensor. The distances were measured with the caliper algorithm.

Fig. 5.81 shows the measurement principle. The measurement was done for 74 images comprising the full edge of a single 62×62 mm^2 sensor under test. Information used on each step allows to extract the mean sensor thickness and the measurement error. The obtained results are shown in Fig. 5.82. The data is fitted with a linear function. The deviation from the fit line is due to the sensor edge surface defects. The measurement precision is estimated to be $\pm$ 1 μm.

The extracted data for the Hamamatsu sensors were compared to the sensor thickness data extracted from the electrical characterization [79]. In these measurements a silicon sensor is approximated as a parallel-plate capacitor. The

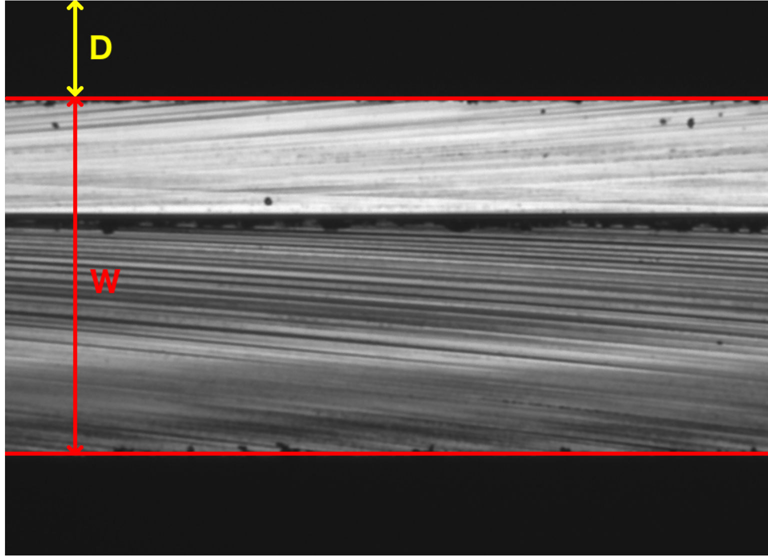

Figure 5.81.: Sensor thickness **W** and distance to the top edge **D** measured using machine vision algorithms.

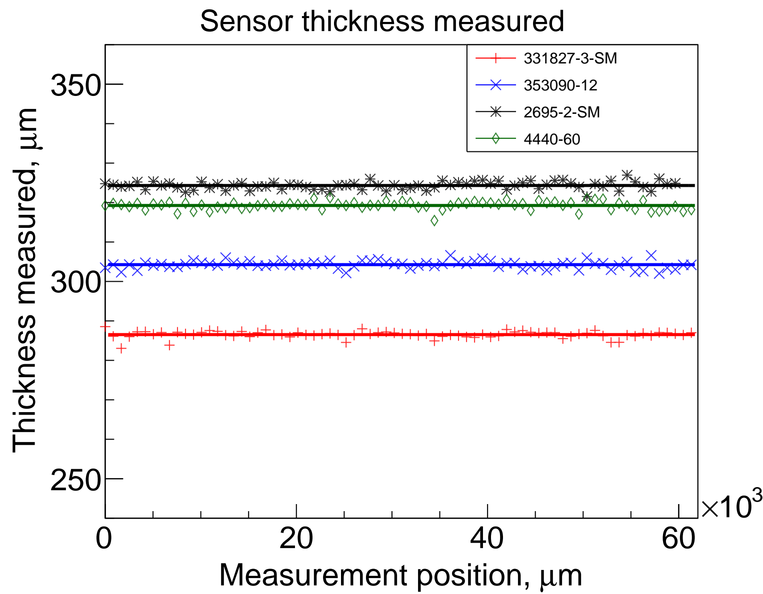

Figure 5.82.: Summary of the thickness profiles measured for four prototype sensors which were presented in Fig. 5.80.

sensor capacitance here is measured at different biasing voltages applied to the sensor. The capacitance saturates after voltage values exceed the full depletion voltage (V_{fd}) of the sensor. The extracted capacitance is used to calculate the distance between parallel plates of a capacitor using eq. (5.10):

$$W_{depl} = \frac{\varepsilon A}{C}, \tag{5.10}$$

where W_{depl} is the depletion depth, or distance between the parallel plates of the capacitor, A is the plate surface, C is the measured capacitance and ε is the dielectric permittivity of the silicon material. Fig. 5.83 shows the summary of the sensor thickness measurements with electrical characterization for Hamamatsu sensors. The thickness data obtained for all seven sensors from Hamamatsu available in this work correspond to those presented in the Figure within a precision of ± 3 μm.

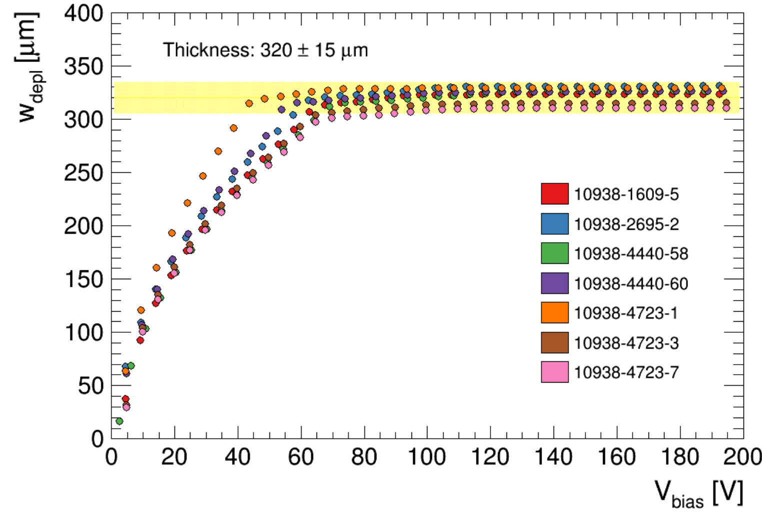

Figure 5.83.: Summary of the sensor thickness measured with electrical characterization for the Hamamatsu sensors. Courtesy of Iaroslav Panasenko [79].

The vertical distances **D** measured from a reference point to the top edge allow to inspect the sensor edge warp. The raw data was fitted with a linear function, the linear contribution was subtracted. The observed deviation indicates the contribution of the sensor warp.

Fig. 5.84 shows the obtained warp for the sensor edges of the prototype sensors. The data is fitted with a quadratic function. Same as with thickness measurements, the deviation from the fitted line is due to the sensor edge surface defects, affecting the measurement precision. The measurement precision is estimated to be ± 1.4 μm. The observed edge warp of 30 μm for the CBM06C6-353090-12 might pose the problems with the micro cable bonding to the sensors during the module assembly in case if the warp structure is as well present along the edge where the sensors are bonded. This issue needs to be further investigated.

5.5.4.2. Measurement by autofocusing

The methods for the direct optical thickness measurements require the optical system to be modified accordingly to accommodate the holding structure, which

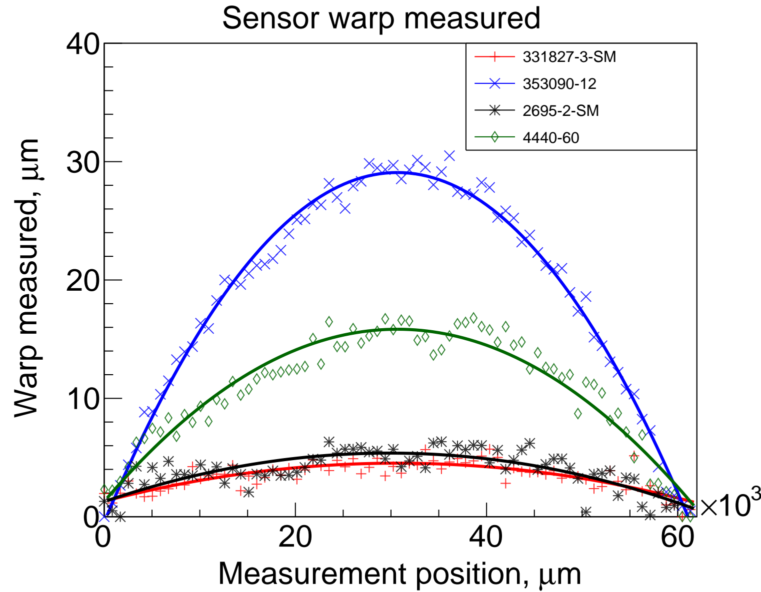

Figure 5.84.: Summary of the sensor warp measured along a single edge of four prototype sensors which were presented in Fig. 5.80.

replaces the vacuum chuck. Moreover it has a measurement set-up times of about 15 minutes and inspection time of about 5 minutes per sensor. The set-up requires the careful sensor clamping in the holding structure, positioning and alignment of the holding structure under the microscope camera, etc. In this paragraph we discuss an alternative approach to measure the sensor thickness based on the autofocusing height measurements as described in section 5.5.1.1. This method allows to measure the sensor thickness with almost no extra time needed as part of the sensor surface scan.

Here, the outermost feature of the sensor such as an alignment mark or a pad numbering print is used (see Fig. 5.85). The motors are positioned such, that the selected feature of a vacuum-sucked sensor is placed within the integration window of the autofocusing algorithm. The feature must be free of dust or other objects potentially influencing the measurement. Then the autofocusing height measurement is carried out for this region. The motor positions and the height value are saved. After the sensor inspection, when it is removed from the vacuum chuck, the motors are once again moved to the saved position and the height measurement is carried out once more, now to focus on the vacuum chuck surface. The extracted difference between two height measurements should then be the thickness of the sensor's silicon bulk plus additional height contributions from the structure of the sensors. These contributions include the thickness of aluminum strips, double metalization layer, passivation layer, etc.

The obtained data from autofocusing measurements were compared with the direct optical thickness measurements. The comparison allows to extract the

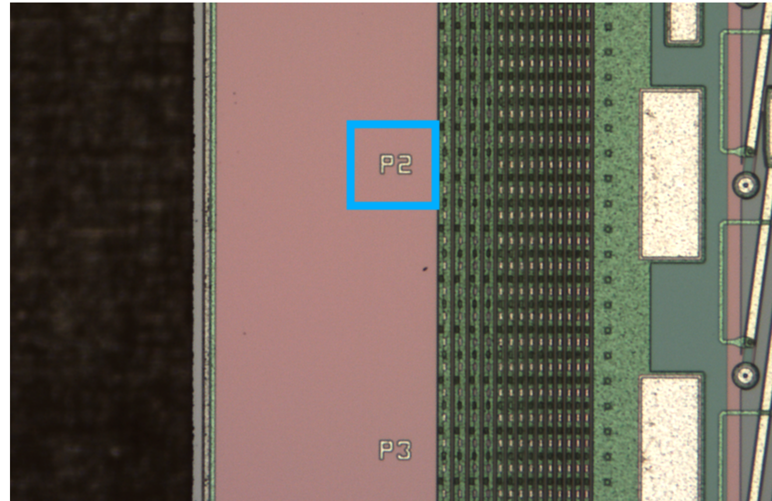

Figure 5.85.: Sensor thickness measurement principle based on the differential height measurement of a outermost sensor feature. Here the metal print with the pad number **P2** is used.

average correction factor of -20 μm. The corrected autofocusing data corresponds to the direct measurement within the precision of ± 3.5 μm.

Fig. 5.86 shows the corrected thickness data for the sensors from CiS and Hamamatsu. The yellow bands denote the declared sensor thickness, 285 ± 15 μm for CiS and 320 ± 15 μm for Hamamatsu. The error bars denote the arithmetical sum of 3 measurement error contributions — the thickness measurement error from direct optical measurement and autofocusing height measured on the sensor and chuck. For the CiS sensors measured, the group of 5 last sensors measured outside the yellow band belong to the same batch, thus the error should have a systematic nature. The data is presented in the appendix D in form of tables.

5.5.4.3. Summary

The methods and procedures developed for the sensor thickness measurements allow a contactless way to control for this important quality criterion. The direct optical measurement approach based on the machine vision metrology yields the measurement precision of ± 1 μm. However it requires the optical inspection setup to be modified accordingly and has rather long preparation times of about 20 minutes per sensor. The alternative approach based on the autofocusing based height measurements has a measurement precision of ± 3.5 μm. However, it does not require extra preparation time and can be done for all sensors inspected optically. Alternatively, a two-camera system can be used with one camera perpendicular to the sensor surface and another camera put parallel to the surface of the sensor.

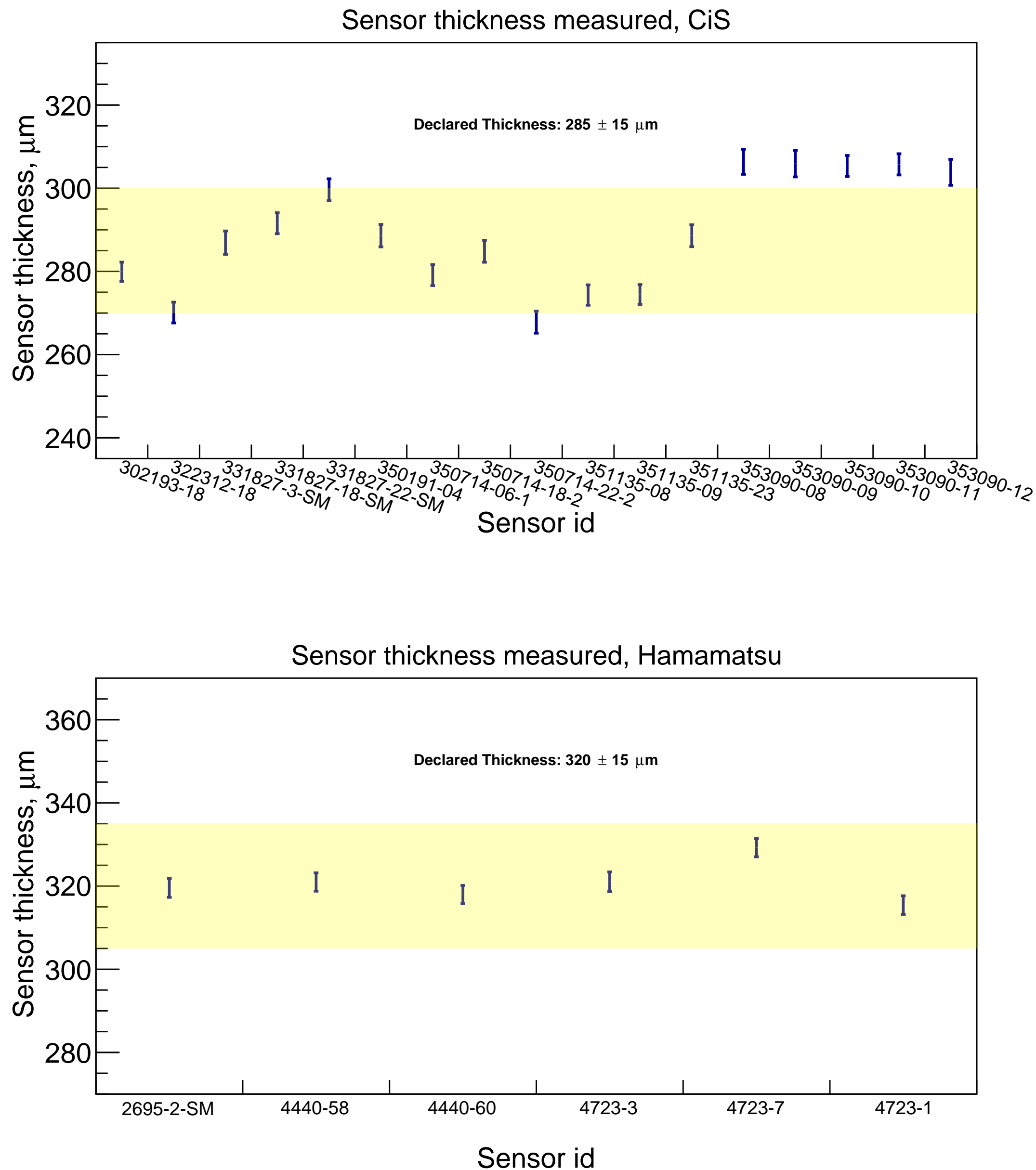

Figure 5.86.: Sensor thickness obtained by autofocusing height measurements for the prototype silicon sensors from CiS (top panel) and Hamamatsu (bottom panel).

5.6. Quality assurance database

The results obtained from the optical inspection of the silicon microstrip sensors need to be stored in a central database for a later use during the STS detector assembly. The detector assembly will be carried out based on the overall sensor quality. This enables for example the placement of the best performing sensors (or

the sensors with fewest defects) closer to the beam pipe where the radiation field and the number of charged particle tracks is higher. The sensors with defective channels are then more safe to use on the detector periphery where fewer tracks are expected. The database is also used to store the static sensor data such as sensor geometry, sensor batches etc. The sensor logistics information has to be stored centrally as well to track the sensor's movement information between the institutions involved in STS detector development and its current owner within the institution.

5.6.1. FairDB

FairDB, the FairROOT Virtual Database [97, 98], provides the end-user a way of centralized data storage for the FAIR experiments. It is based on the FairROOT framework [99] and extends the built-in database support of an underlying ROOT framework by creating a layer of abstraction to store and access data using different database technologies. Fig. 5.87 depicts the architecture of the FairDB.

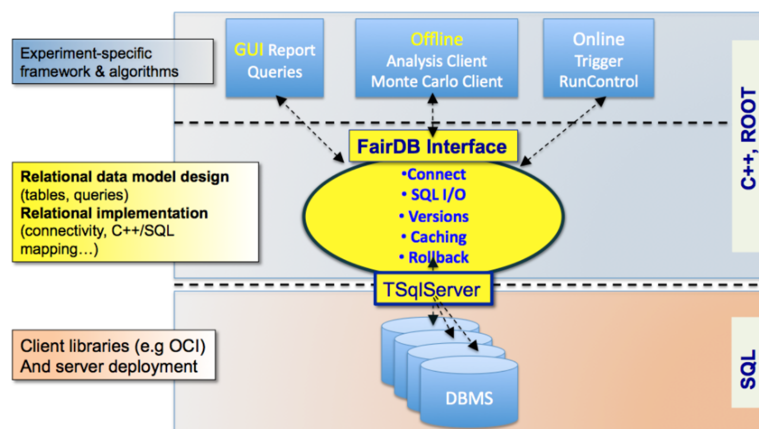

Figure 5.87.: A schematical representation of the FairDB architecture [97].

The FairDB separates the connectivity to the specific DBMS[2] into a front-end and a back-end. The front-end part exposes the application programming interfaces to implement the user defined relational data model. It provides the means of the platform independent database connectivity, permission management and the object relational mapping, e.g. allows to execute the queries to the database tables and returns the C++ objects which can be accessed within the ROOT framework. The front-end allows the stored data visualization in the user-defined format. For example the users are accessing the Web Application to view (all users) and manage (users with appropriate access permissions) data.

The back-end implements the platform and database specific interaction with the underlying DBMS. Presently the FairDB (being based on the ROOT frame-

[2]Database Management System

work's TSQLServer) supports following relational database backends: MySQL, Oracle, PostGreSQL and SQLite. The data is transparently cached to balance the network and disk load. The FairDB by design allows an important mechanism to stage data bunches to be *commited* at once as a single logical transaction between so called consistency points. If the transaction validity check will fail, none of the data will be written to the underlying database ensuring the data consistency. The *rollback* functionality allows to discard the latest state of the database and revert it to the previous consistent state based on the database state journaling.

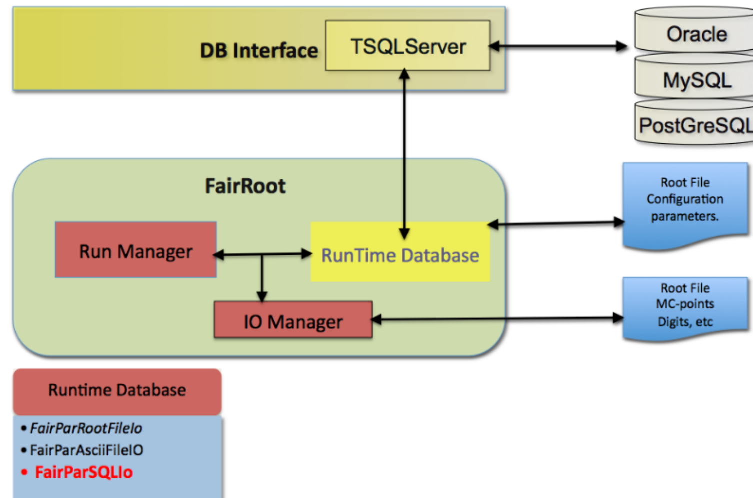

Figure 5.88.: The FairDB integration into FairROOT [97].

Fig. 5.88 show the integration of the FairDB into the FairROOT scientific framework. The FairROOT virtual parameter database is able to access FairDB to read and display the stored data for given detector systems, ROOT binary files, detector configurations etc.

5.6.1.1. Versioning concept

The FairDB has been designed to intrinsically support the entity versioning. This means that certain entity could change its properties throughout its lifetime, however the information of the previous state (or states) will not be lost by overwriting, but rather a *new version* of the entity will be created. This concept allows for example to access the historical state of a detector configuration assigned to a certain beam time. The important consequence of this design is that the FairDB could be seen as an *insert-only database* which allows to simplify its architecture and increase its robustness.

Fig. 5.89 shows the FairDB time-based versioning concept. The entity *cal* has three versions, and the historical version v_1 could be retrieved when querying the data in the time frame between UNIX time stamps t_1 and t_2.

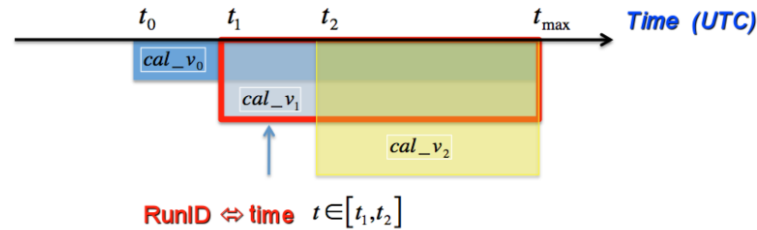

Figure 5.89.: The concept of the FairDB versioning [97].

5.6.1.2. Aggregation concept

Another important concept of the FairDB is the data grouping by the aggregation. This concept allows to simplify a *one-to-many* relation pattern. For example, a certain silicon microstrip sensor could have only one geometry type. Thus querying geometry data for this sensor will always return a single sensor geometry description entry. On the other hand a single sensor will have several quality inspections, thus querying the quality inspection data for a particular sensor will return several entries. This concept allows to free the FairDB engine from the conditional `WHERE` queries and further simplify its architecture and increase its robustness. The drawback of this concept is that the database entities should be designed appropriately and only have one foreign key defined.

5.6.1.3. ROOT object model compatibility

Being a part of the FairROOT, FairDB allows the storage of the object instances inherited from `TObject` class in form of serialized byte arrays. This provides the possibility to store the histograms, plots, canvases or even ROOT binary files using FairDB. For instance, in this work we store the sensor warp profile as a serialized TGraph2D and the cutting edge profile as a serialized TH1D.

5.6.2. Storing the optical QA data in FairDB

In order to store results of the optical inspections the ROOT/C++ object model and corresponding database schema was implemented in this work.

Fig. 5.90 shows the developed schema for the data storage. The sensor unique identification information, its geometrical type data, vendor and batch information are grouped in the first two columns of entity tables. The arrows indicate the relations between these entities.

The `sensor_location` entity allows the logistic tracking of the sensor between the institutions and different current owners within the same institution. The sensor geometry `sensor_type` entity contains the static data of all sensor types from all the sensor generations. It contains the information about sensor sizes, strip number per sensor side, strip angles and pitch, sensor's nominal thickness as

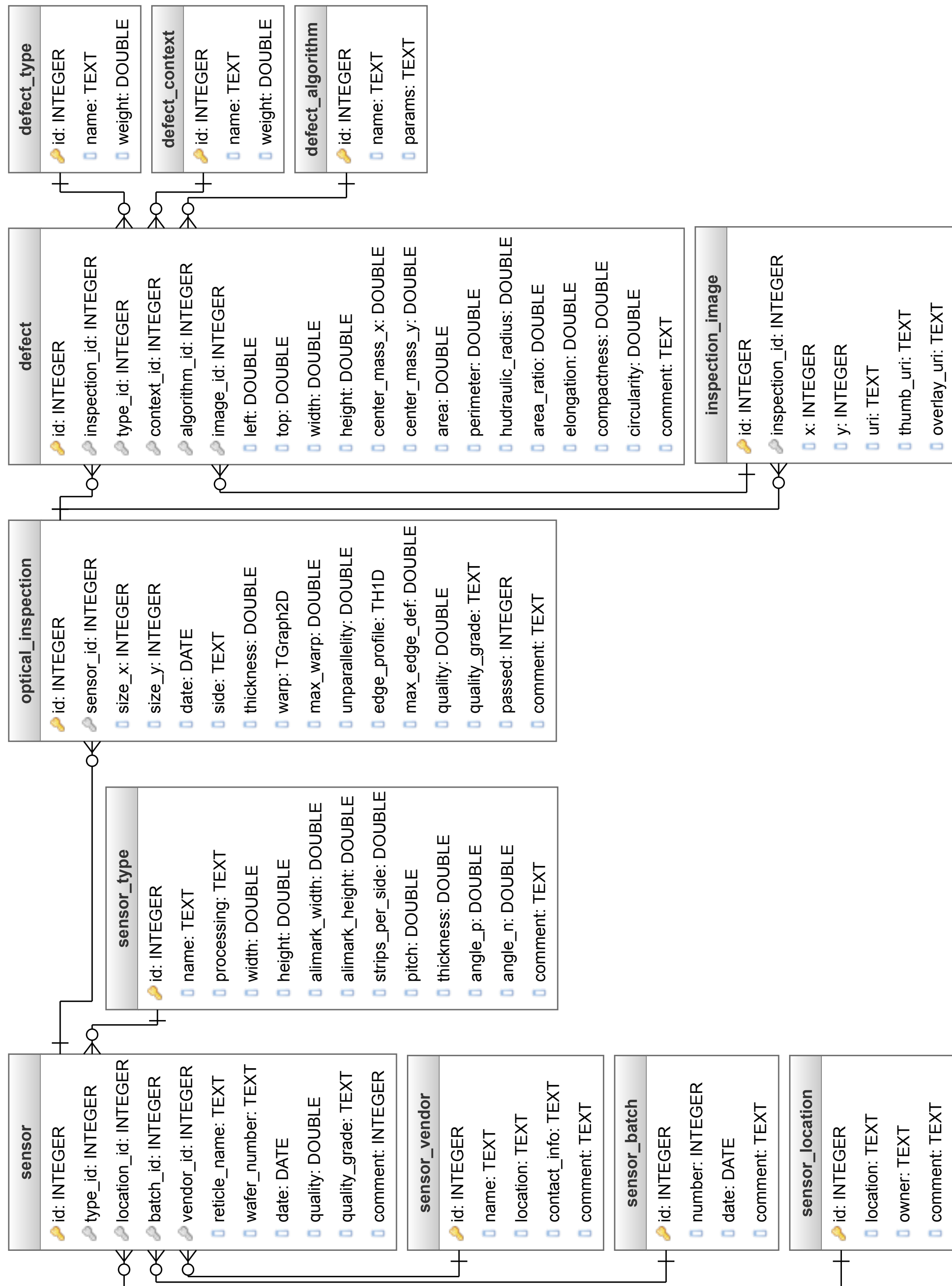

Figure 5.90.: The developed FairDB database schema for the data storage.

well as information about the alignment marks, which is particularly important for this work. This geometry static data is used in the inspection setup's software solution to properly configure the inspection.

The `optical_inspection` entity contains the information about the information and the results of a single optical inspection. The sensor characteristics such as measured thickness, height profile map (warp) and its maximum value, cutting edge un-parallelism, cutting edge profile and its maximum value are stored there. The sensor quality, quality grade and the flag if the sensor have successfully passed the optical inspections are set by analyzing these data and the data from the detected defects of this sensor.

The `optical_inspection` entity may contain the detected sensor surface defects. The information about them is stored in the `defect` entity. The fields of this entity contain the location of the defect on the image, its size and other geometrical parameters that have been used in the defect analysis. This entity as well points to the static data from other tables: `defect_type` to distinguish the defect class (e.g. scratch, metal short, metal open etc.) and its impact on the decision outcome (weight), `defect_context` to identify where the defect have been found (e.g. strips, AC or DC pads etc.) and its weight, `defect_algorithm` with which the defect have been detected (e.g. pattern matching, neural network etc.) and its parameters.

A single inspection consists of many digital images taken with the microscope camera, the information about these images is stored in the `inspection_image` entity. The fields of this entity point to the actual storage place (identified by URI[3], which could point to the SMB share, NFS location, etc.) of the original image, the processed image overlay with all defects and the thumbnail miniature of the original image to be shown to end-user in order to balance the network and disk loads.

The ROOT objects implementing this database relational model presented in the Fig. 5.90 have been developed in this work. The static data is put into the database with the special priming macros when the actual table structure within the database is created. The developed objects allow the partial data loading from the related tables on the fly and only when they are needed. This *lazy loading* pattern allows to balance the load on the database and only query the information needed instead of populating the whole object dependency tree. During the schema and object development numerous issues have been identified and reported to the head of the FairDB project development. Additionally, the feedback and suggestions on the end-user experiences developing the relational data models have been submitted in form of patches, further improving usability of the front-end APIs of the FairDB. Finally, the classes for the ROOT objects developed have been accepted by the project maintainer and put to the central FairDB repository [98].

[3]Universal Resource Identifier

5.6.2.1. Inspection image storage

It has been decided, that the original raw images of the inspected sensors should not be discarded after the quality assurance and stored for later use for analysis purposes. This poses a particular challenge — the resolution of original images is 5 megapixel resulting in a file size of a single region of interest of 14.4 megabytes, already compressed by the lossless algorithms in a PNG[4] format. Taking into account that a single sensor side inspection of a 6×6 cm^2 sensor consists of 910 regions of interest, the same amount of thumbnails and defect overlays, the resulting disk size usage is estimated to be 12.9 gigabytes. A full sensor inspection comprising both n- and p-sides the disk usage is then 25.8 gigabytes. Extrapolating this number for 900 sensors results in total estimated disk usage of 23.22 terabytes. To ensure the fault-tolerance (avoid the loss of data due to hardware faults) the data is usually replicated at least twice. This requirement brings the disk usage to the value of 46.44 terabytes for ≈10 million files stored.

Storage Type	Advantages	Drawbacks
Local	Ease of use during R&D phase Currently used	Locality of the storage limits the data access from outside
Cloud	Relatively low cost per gigabyte	Subscription based payment Data retrieval is paid Long data retrieval times 3rd party owns the data
NAS	Fast file access over network Single rack capacity up to 24 TB Data ownership local to experiment	Relatively high cost (24 TB rack costs around 2000$)
GSI gStore Tape Storage [100]	Designed to store archived data which is rarely accessed Data ownership local to experiment	Long data retrieval times
GSI HPC clusters [18]	Same network as the FairDB Fast access, 14.3 PB capacity Data ownership local to experiment	The HPC cluster is designed for computing, not storage

Table 5.5.: Overview and analysis of the data storage technologies

Such amount of the image data can not be stored in the FairDB or other DBMS. Instead only image metadata, which points to the physical storage location by URI, will be stored in the FairDB. However this amount of data to be

[4]Portable Network Graphics

stored does not pose a big problem for the state of the art IT systems.

Tab. 5.5 shows an overview of potential solutions on the data storage with their respective advantages and drawbacks. The NAS solution is very good for local data storage, however it has initial cost and has to be maintained in a long term perspective. The GSI in-house High Performance Computing clusters Hera and Nyx look most promising with their storage capacities and its usage as a primary fast access data storage should be investigated. The gStore tape storage technology seems to be ideal for data archivation and indefinite storage. It is most fitting solution to store the data after detector assembly.

5.6.3. Summary

FairDB allows the ROOT/C++ users from FAIR experiments to store and retrieve their experiment specific data (e.g. detector configuration, detector geometry, quality assurance results). In this work the interfaces for the silicon microstrip sensors' quality assurance data both in form of database entity schema and object relational model implementations have been developed. This allows to transfer the locally stored optical inspection results data into the central database. During the development process, the performance issues have been reported to the project head. The end-user feedback and improvement suggestions in form of patches have been filed and accepted into main code repository. The schema and object relational model implement have been accepted and became the part of the project repository. The optimal file storage solutions have been investigated and the usage of GSI High Performance Computing clusters for hot storage and GSI gStore service for long term data storage have been proposed.

5.7. Optical inspection of other STS components

5.7.1. Readout microcables

The readout microcables (or signal cables) are important components for the sensor module assembly. 16 of them (a sensor cable stack) are wire-bonded to each sensor in order to bias the sensor and transfer the electrical signal from the sensor to the read out ASIC[5] chips, which are mounted on the front-end electronic boards. They can have different lengths of up to 0.5 m depending on the distance from the sensor position on the carbon frame ladder to the read-out plane on the periphery of the STS detector.

Fig. 5.91 shows a prototype sensor module consisting of (from left to right, for each sensor side) a front-end electronic boards with 8 read-out ASIC chips, a signal transmission cable stack with electrical shielding, which is wire-bonded to the chips, and the sensor.

[5] Application-specific integrated circuit

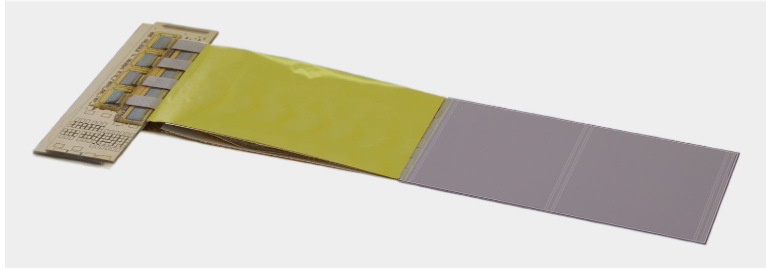

Figure 5.91.: A photograph of a prototype sensor module [101].

5.7.1.1. Microcable geometry

The microcables are produced by the chemical etching of the aluminum from the polyimide-aluminum compound. After the etching process, the individual signal traces are formed according to the developing mask. They have a width of 42 µm and a spatial depth of 15 µm.

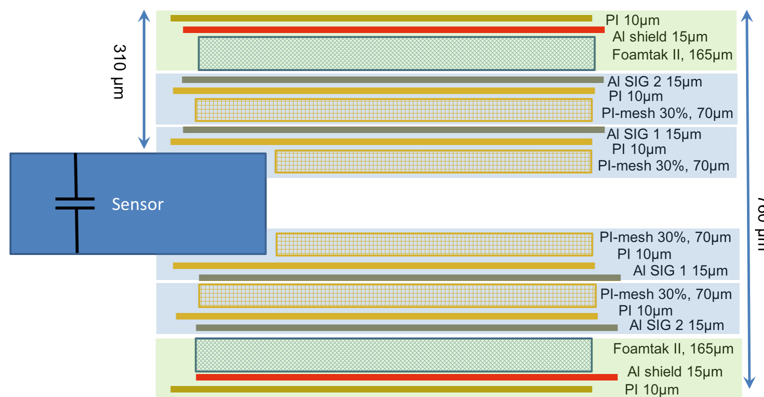

Figure 5.92.: A principal scheme of the cable stack connected to the sensor [101].

Fig. 5.92 shows the cable stack geometry. The innermost layers consist of 16 individual 64-channel microcables. The layers are insulated from each other and the distance between them is ensured by so called meshed spacers which are shown in Fig. 5.93. They are 70 µm thick and comprise only 30% of the material compared to a solid spacer. The meshed spacers ensure the low electrical capacity and low material budget of the cable stacks.

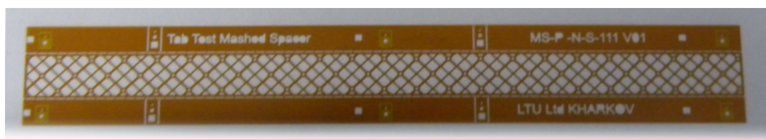

Figure 5.93.: A photograph of the polyimide meshed spacer with removable test structures [101].

After identifying the technology the microcable production line was established at the “LED Technologies of Ukraine” Ltd [102]. The first sets of prototype microcables were produced in 2015. Tab. 5.6 shows the summary on the microcable production process yield[6] at LTU. The columns show the nominal production yield without cable traces repaired and with 1 trace repaired by identifying it on the cable by manual optical inspection and restoring the broken trace by soldering.

Microcable Type	Yield, %	
	As is	1 trace repaired
111 mm	58.3	70.4
212 mm	51.5	71.9
252 mm	37.5	59.6

Table 5.6.: Microcable production yield by microcable type as is and with traces repaired [101].

The observed low yield arises from the production process where underetching or overetching of the polyimide-aluminum compound occasionally occurs[7]. The underetching results in thicker and wider cable traces and aluminum residues on the polyimide. The overetching results in thinner and narrower cable traces which may be partially dissolved or become fragile. The yields are improved after repairing one ore more broken traces. In order to identify the broken traces an optical inspection quality assurance is carried out. However, on the production site the optical inspections are carried out manually, which is tedious and prone to errors. The manual optical inspection takes up to 1/3 of the total production time resulting in 57.8 person hours of manufacturing effort for one microcable set to be produced [101].

Since the microcables are assembled into the cable stacks at the production site (rendering the metal traces invisible for inspection), the only viable location for their quality assessment is directly at the production site. The investigation of the inspection automation is presented in the following subsections.

5.7.1.2. Quality assurance methods and procedures for microcables

Due to the yield and manual inspection issues described above, it was decided to investigate the possible optical inspection automation for the microcable stacks using the optical inspection system developed for the sensor inspection. Two sets of prototype cables (early prototypes from 2014 and the latest prototypes from 2016) were delivered to the University of Tübingen from the GSI detector laboratory for this investigation.

[6] A ratio between fully functional and defective cables produced
[7] This depends on time the compound was submerged into the etching chemicals

In order to inspect microcables the vacuum chuck of the inspection system has been replaced with a porous amorphous aluminum chuck. It allows the suction of the object under test with its all active area. By placing the cable on this chuck and covering the inactive area with a rubber one acquires a good and uniform underpressure distribution below the cable to reliably fix it in place. Additionally this allows to avoid major distortions in the Z direction ensuring the microscope digital pictures to stay focused. The movement range of the X motor stage is limited to 19 cm, thus inspection of longer cables must be done in several steps by dividing the cable into partial inspection regions. This arises from the fact that motor stages were designed for sensors inspection. This limitation is easy to overcome by replacing the X motor stage with one with wider movement range. The inspection procedures do not need to be modified.

For the first prototype cable set circular illumination have been used. For the latter one the direct illumination.

Trace break detection

The broken traces are major defect of the microcable. They result in a dead readout channel of the sensor. Visually they appear as a discontinuity of the color spectral information. Using this fact we are able to extract the trace thresholded color profile and look for the falling and rising edges.

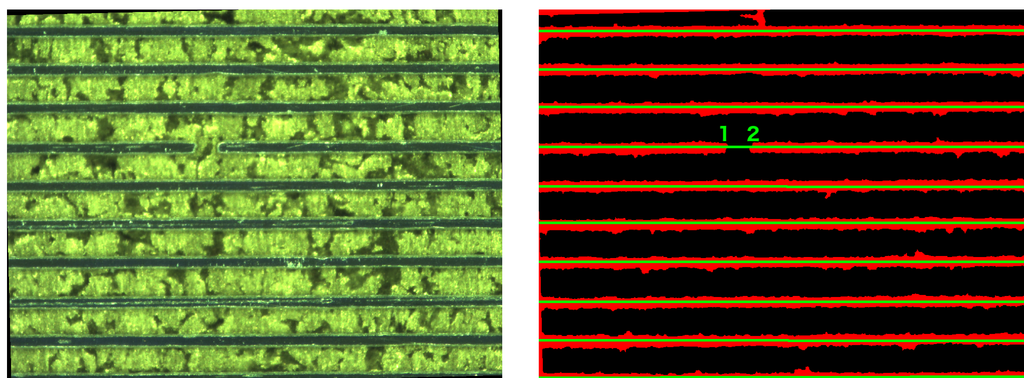

Figure 5.94.: The original (left panel) and the processed images (right panel) of the cable with a broken trace.

Fig. 5.94 shows the original and the processed microscope images taken of a region of interest on the microcable. The broken trace is detected by extracting and thresholding the color spectrum to match the cable traces. Extraction artifacts are removed by applying a particle size filter for small objects. The trace break is detected by an edge detection algorithm for a fitted trace. It looks both for falling and rising edges. The extracted edges allow to identify the start and endpoints of the break, hence the defect size.

Fig. 5.95 shows an alternative approach to detect the broken trace. Here, the

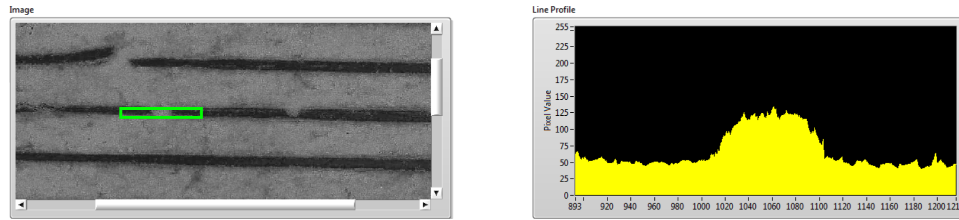

Figure 5.95.: Trace break detection by constraining the pixel color value. The left panel shows the saturation color plane extracted for the original picture. The right panel shows the pixel value histogram for the region of interest selected.

color saturation information of the original image is extracted in a set region of interest. Then the histogram containing the pixel value line profile is built. By setting a threshold on the pixel value, one extracts the start and endpoints of the break and defect size.

Trace profile control and defect detection

To assess the effects of the underetching and overetching the trace width profile is controlled all over the microcable. The underetched wider traces might affect the electrical characteristics of the trace and thus the signal read out. Eventual residual and etch left overs might short to the neighboring trace. The overetched traces might as well affect the electrical properties of the trace and the thinned out regions of the trace might become the predetermined breaking point. The latter effect is important because it could lead to the broken trace during handling of the cable throughout its lifetime.

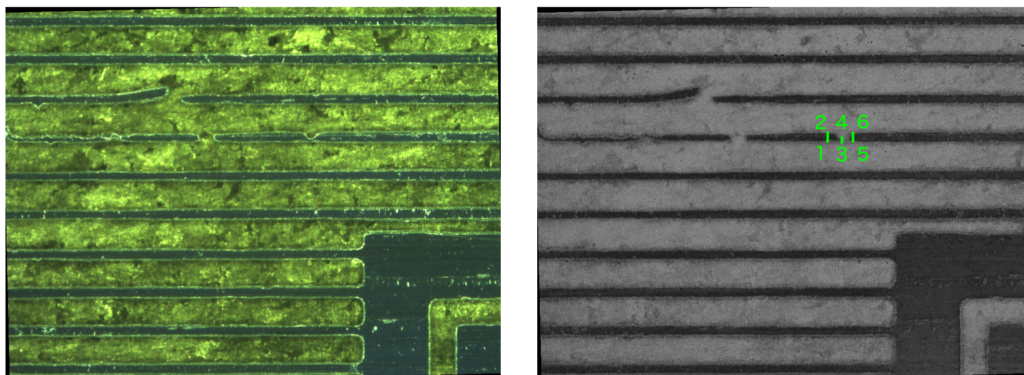

Figure 5.96.: The original (left panel) and processed image (right panel) of the cable traces with thinnings.

Fig. 5.96 shows an example of the trace thinning detection. First the saturation color plane is extracted to suppress the background influence to the detection algorithms. Then the edge detection algorithms are used to estimate the width of the trace in 3 different positions. When applied throughout the full trace length

the width profile is extracted. From the obtained width profile, the thinnings of the traces are identified and the severity of an observed defect is estimated.

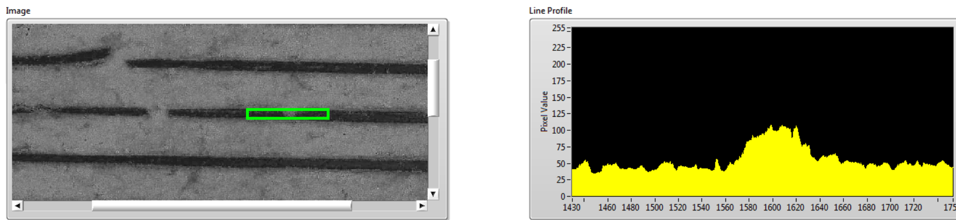

Figure 5.97.: Trace thinning detection by constraining the pixel color value. Left panel shows the contrast plane of the source image extracted. Right panel shows the pixel value histogram for the region of interest selected

Fig. 5.97 is similar to Fig. 5.95 and shows an alternative approach to look for trace thinnings by analyzing pixel value profile histograms. Both methods described previously are used in order to provide the best defect detection.

Foreign object detection

The detection of a foreign objects on the cable surface is an important step in assuring the quality of the microcables. For example the electrically conductive objects on the surface such as lifted-off traces or — to a minor extent — the dust grains, have a potential to short the neighboring traces. The current from the biasing line could flow to the ASIC chips' readout channels and damage the chip. This should be avoided in any case.

Fig. 5.98 shows a lifted off trace laying on the cable surface shortening the neighboring traces. The detection principle for this occasion is similar to those described above. However, the detection algorithms are configured to detect the light reflected from these objects, since they reflect much more light (due to their surface properties) compared to the homogeneously lit background. The same approach is applied for the dust grain detection (shown on the 2 bottom panels of the Fig. 5.98) since dust grains in the circular light are well illuminated from the sides and appear highlighted.

Metal surface defect detection

Metal surface defects appear on the microcable surface due to overetching. They are typically localized and clustered together indicating initial thinning of the aluminum layer on the polyimide substrate. This initial thinning is then dissolved further during the etching.

Fig. 5.99 shows the cable metal surface defects due to overetching. Though in this example they are found on the test structures, which will be removed later, they could possibly be found elsewhere on the active part of the microcable. The

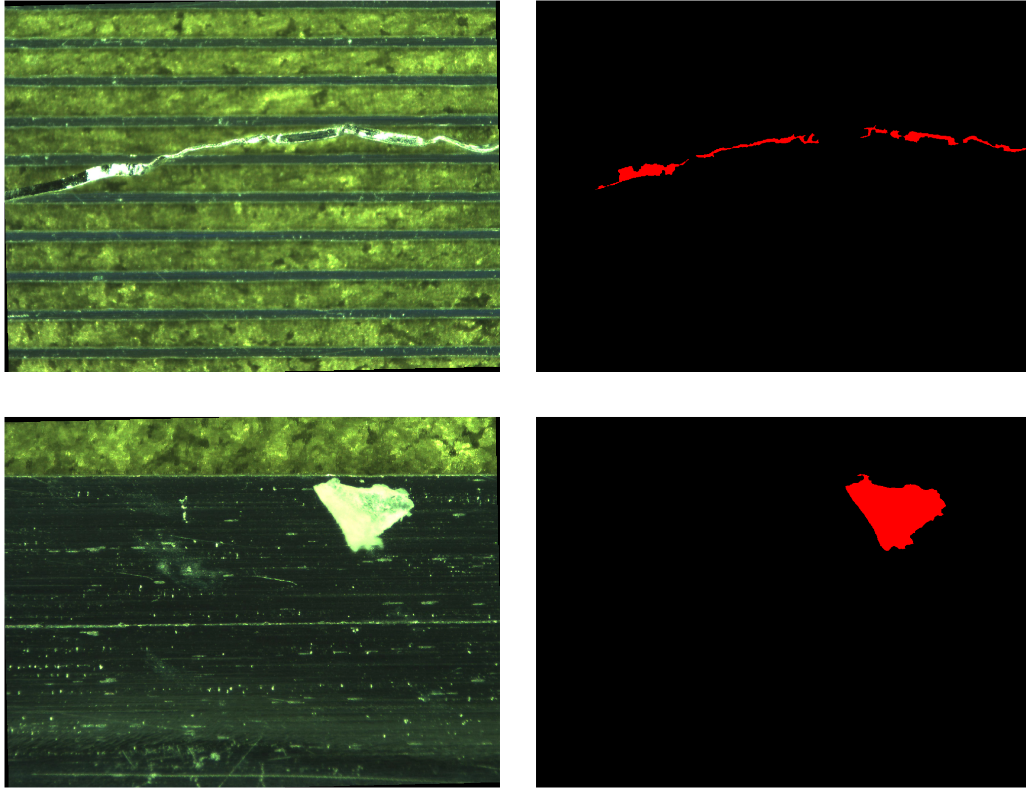

Figure 5.98.: The original and processed image of the cable traces lifted off (top panels) and a dust grain (bottom panels).

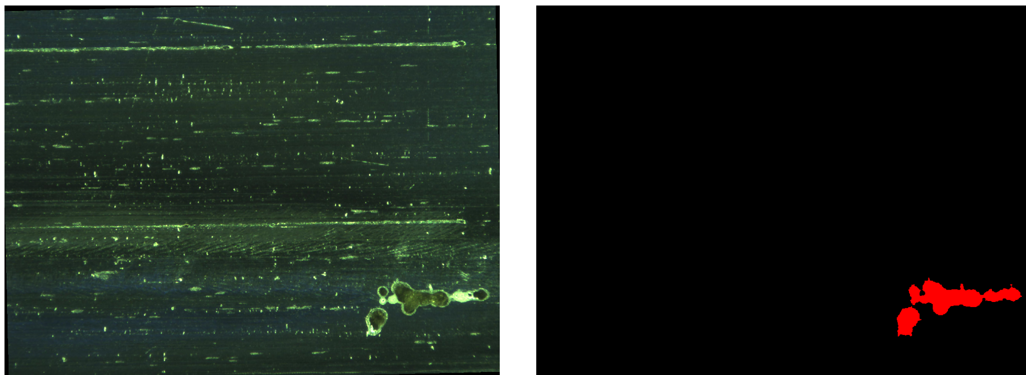

Figure 5.99.: The original (left panel) and processed (right panel) image of the cable metal surface defects.

information extracted during this test step contains all the geometrical data of the defect, e.g. area and perimeter, which is used to judge on the severity of the defect.

Microcable inspection under direct light

The examples above are showing the defect detection principles under the scattered light coming from a ring light source. At the time of the inspection of the second microcable set from the latest prototype batch, the optical inspection setup had been upgraded to use a direct light source. For the microcable inspection this poses a certain complication. Since much more light coming from the direct light source is reflected back into the camera, it becomes saturated by the shear amount of it, reducing the dynamic range and sensitivity to the background objects. To mitigate this effect, the prototype microcables were inspected twice: with high and low camera exposure (which is equivalent to the light sensitivity). The general approach to the defect finding however remained the same, with the detection parameters being tuned accordingly.

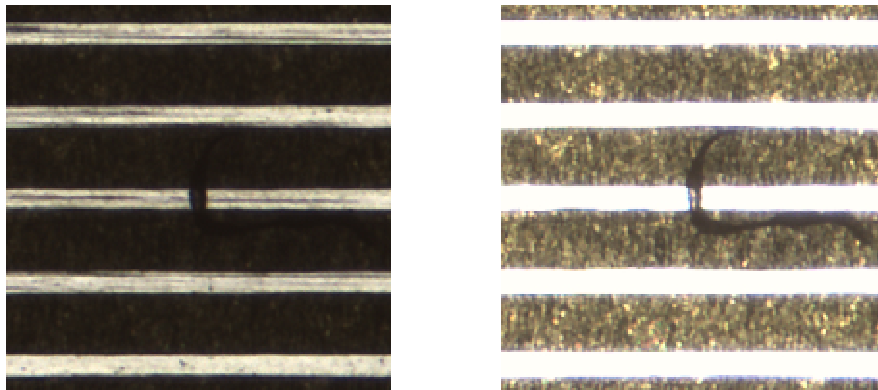

Figure 5.100.: The microscope image taken of the same region of interest with low (left panel) and high (right panel) camera exposure.

Fig. 5.100 illustrates the complication of the microcable defect detection under the direct light source: what appears to be a broken trace as seen with low exposure on the left panel turns out to be a dust grain laying on the surface as seen with high camera exposure.

5.7.1.3. Summary

The optical inspection and metrology setup is a flexible tool for arbitrary object inspection. Thanks to its modular composition, the individual components such as vacuum chucks and the light sources are interchangeable and allow to optimize the inspection conditions as well for the sensor microcables. The methods and procedures developed for the microstrip silicon sensors are as well applicable for the inspection of the microcables. The extracted defect information allows to speed up the repairing process of the broken traces and further increase the production yields.

The quality of two prototype microcable sets of different generations have

been assured with the optical inspection setup automated methods and procedures. For the latest set of the microcables the defect summary from the manual inspection have been provided (see Tab. 5.7). The defects from this summary have been successfully identified. Taking into account the capabilities of the cable inspection methods and efficiency of the defect detection the manufacturer has been encouraged to adopt this at the production site.

Cable number	Defects on the cable
40-2	1 break, 2 traces cut-off, 2 thinned traces
186-2	2 breaks, 2 traces cut-off, 1 thinned trace
163-3	1 break, 2 traces cut-off, 1 trace lift-off
181-1	Hole in Pi, deformation in the bond area
116-3	2 breaks, 1 trace cut-off, 1 trace lift-off
176-2	1 trace cut-off, 2 thinned traces
192-2	2 trace cut-off
194-2	1 thinned trace, deformation in the bond area
168-1	5 traces cut-off
169-2	1 break, 3 traces lift-off

Table 5.7.: Information on the cable defects from the manual inspection enclosed in the package.

5.7.2. Ladder assembly tool

The ladder assembly jig (Fig. 5.101) is an important tool for the assembly of the silicon sensor modules into ladders.

The ladder assembly procedure is done as follows. First, the carbon frame is fixed in the jig, then the so called L-legs [103] (Fig. 5.102) are glued to them. The L-legs are made of fiberglass and carry the sensors above the ladder. After gluing the L-Legs to the ladder, a sensor module is grabbed by the sensor holder tool and sucked to it by applying an underpressure. The sensor module with the holder structure is then laid over the L-Legs, pushed against the ladder tool edge to align it, and glued to the L-Legs. The module front end boards are then mounted to the FEB cooling box. The carbon fiber ladder populated with sensor modules and cooling boxes are attached to the fixtures.

A prototype ladder assembly tool for two sensors has been produced in the Detector Laboratory of GSI. In order to verify the assembly procedures, two prototype sensors were mounted to a carbon ladder. To characterize the machining precision, verify and qualify the sensor spatial placement, the assembly tool was transported to the University of Tübingen. The flexibility and modularity of the setup allowed to install and integrate the (rather bulky) ladder assembly tool into the optical inspection setup by replacing the vacuum chuck and adjusting the optical axis accordingly (Fig. 5.103).

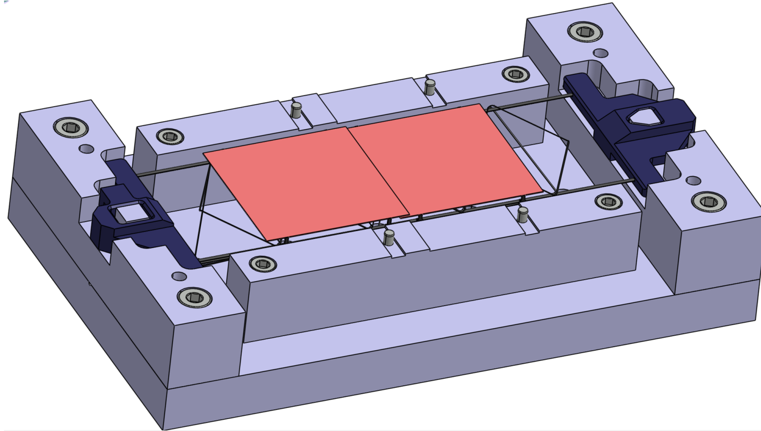

Figure 5.101.: A CAD view of the ladder assembly tool. The carbon fiber (CF) ladder frame (black color) is fixed on the holding and alignment structure (grey color). The silicon microstrip sensors (red color) are glued to the L-Legs previously glued to the CF frame. Image courtesy of O. Vasylyev, GSI [104].

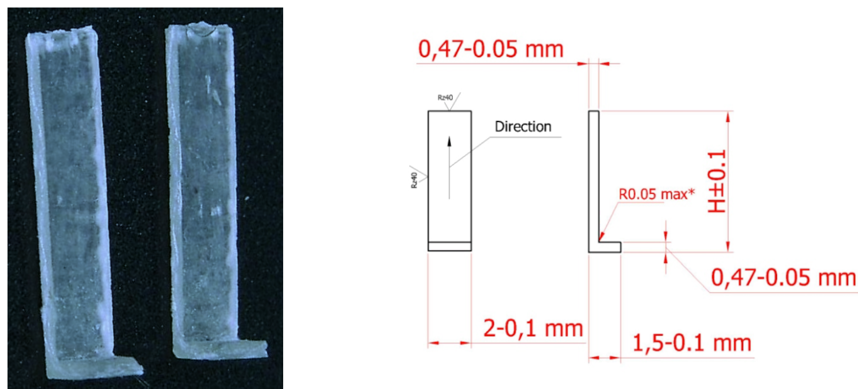

Figure 5.102.: A macro photograph of the fiberglass L-Legs carrying the sensor (left panel) [105]. A CAD drawing of a L-Leg (right panel) [103].

5.7.2.1. Optical inspection of the ladder assembly tool

After mounting the ladder assembly tool in the inspection setup (Fig. 5.103), its optical inspection and metrology has been done. The manual optical survey allowed to study the object and develop the inspection methods and procedures. This was done by inspecting the reference points on the assembly tool itself and the mounted sensors. Fig. 5.104 illustrates the spatial configuration of the sensors mounted on the ladder. The left sensor is a CBM06C6 prototype, oriented with its n-side towards the optical axis, its readout plane is rotated by 90° counterclockwise. The right sensor is an obsolete CBM03C6 prototype from the year 2009, laying spatially below the left sensor with its p-side being visible. Having the outdated mask, it only has 6 (instead of 8) alignment marks. Having 3 alignment marks covered by the left sensor complicates the inspection. For this reason

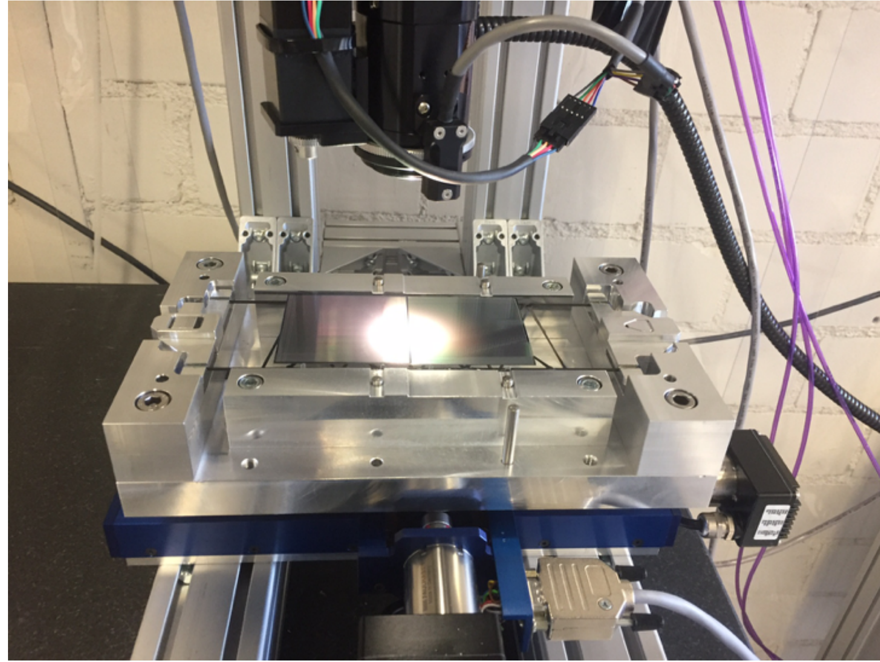

Figure 5.103.: The ladder assembly tool integrated into optical inspection setup.

other outermost feature have been taken as a reference point — the first visible strip number (47) mark being close to the horizontal line of the alignment marks. The information on these reference points were taken directly from CBM03C6 sensor CAD model provided by the manufacturer.

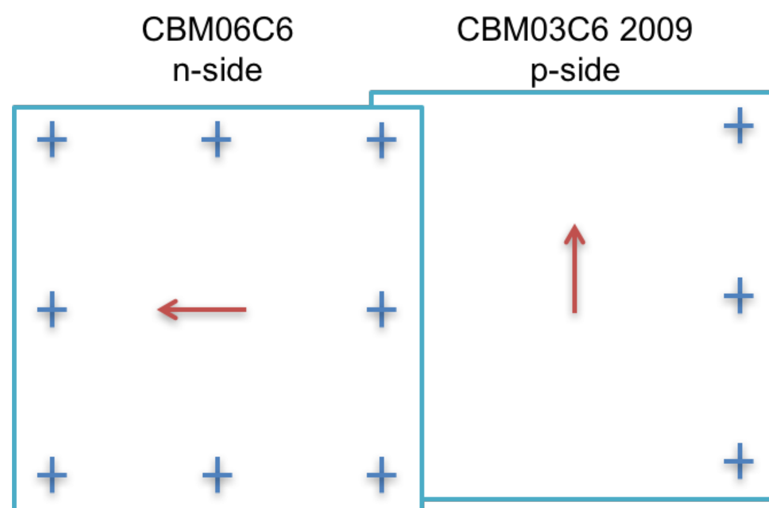

Figure 5.104.: The spatial configuration of the sensors mounted on the ladder. The red arrows denote the readout plane orientation.

Fig. 5.104 illustrates the fact that sensors are not perfectly overlapped spatially. To estimate the overlap geometry both at the top and bottom, the sensor

edges have been extracted. The edge extraction has been done by fitting the sensor edges with edge detection algorithms described previously. Using the metrology algorithms from the NI Vision package the planar information of the overlap has been measured. The depth of the overlap was measured by using the autofocus approach to measure the height of the objects as described above. Tab. 5.8 and Fig. 5.105 summarize the extracted information.

Measurement	Value
Width (top)	3919 µm
Height (top)	37 µm
Depth (top)	536 µm
Depth (bottom)	297 µm

Table 5.8.: Summary of the information extracted from the sensor overlap.

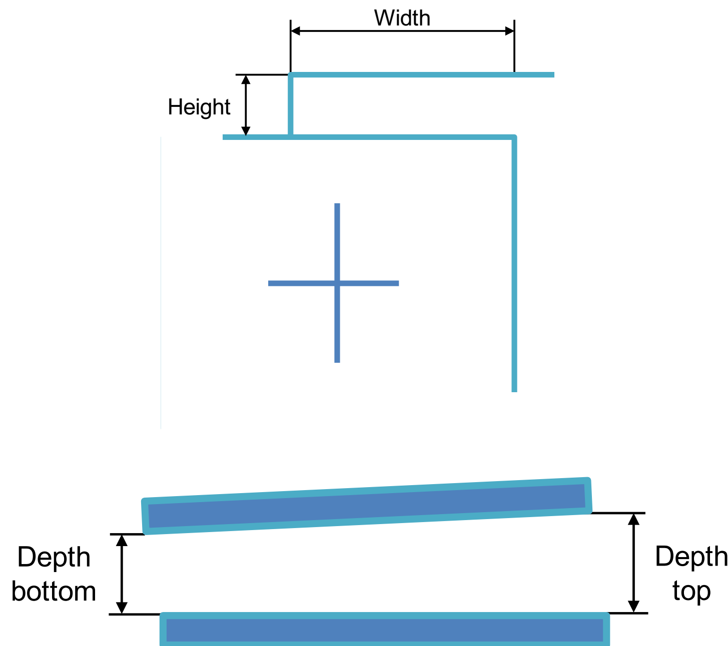

Figure 5.105.: A sketch of sensor overlap. Top panel shows the overlap in the corner region in the sensor plane. Bottom panel shows the side view of the sensor spatial configuration out of the sensor plane.

The information extracted from the reference points allows the measurement of the sensor planes with respect to the base-plane of the ladder assembly tool's mounting surface plane as well as estimation of sensor to sensor misalignment. To extract the in-plane rotational misalignment (Euler angle ϕ) of the sensors, the spatial information of the right edge alignment marks has been used by estimating

the individual rotation relative to the global coordinate space. The summary on the angular misalignment of the sensors is shown in tab 5.9

Euler angle	Value
ϕ	0.011°
θ	0.247°
ψ	0.225°

Table 5.9.: Summary of the angular misalignment of the sensors relative to each other.

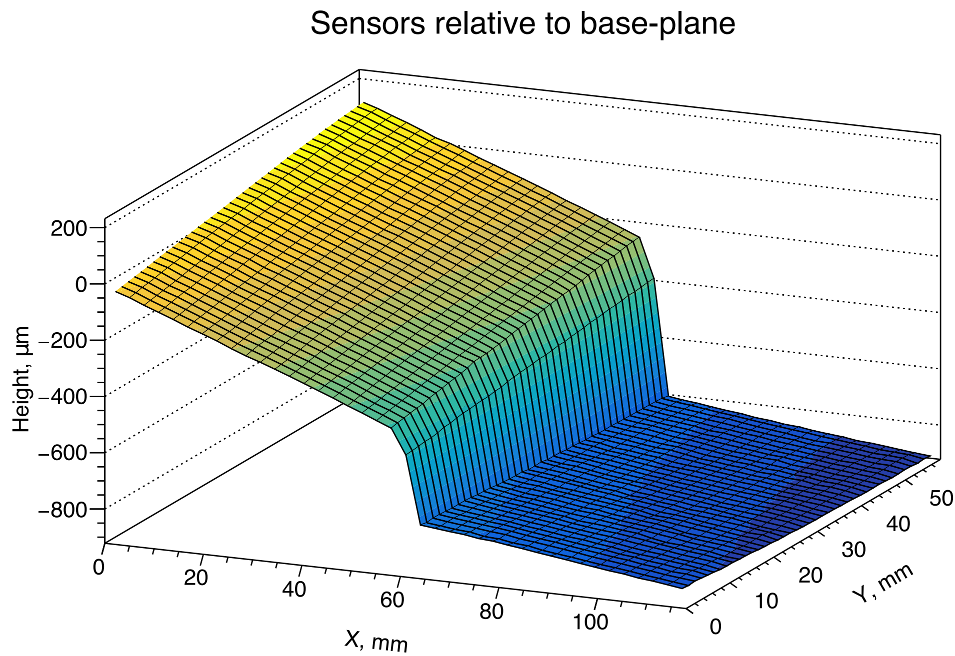

Figure 5.106.: The spatial configuration of the sensors mounted on the ladder relative to the mounting base plane.

Fig. 5.106 shows the spatial configuration of the sensors mounted on the ladder relative to the ladder assembly tool's mounting base-plane. The graph shows the results of the auto-focusing height measurement approach applied to both sensors at once. The observed shape indicates a problem with the sensor placement precision. The problem was due to the too long (relative to expected) hardening time of the glue, resulting in the glue flowing and sensor sagging after releasing it from the suction chuck. The requirements for the sensor placement precision are defined in the technical design report [13]. According to it the sensor base planes have to be parallel, the sensor edges have to be parallel and the gap between sensors have to be 700 µm.

In order to exclude the possible contribution to the sensor misalignment due to the cutting edges of the sensors, they have been inspected by the procedure

described above in section 5.5.2. The results are shown in the Tab. 5.10. The values measured are in accordance with the quality criteria and do not exceed 10 μm, though a slight trapezoidal form for the right sensor indicate that the cutting precision of the CBM03C6 sensor series is worse that those of the CBM06C6 series.

Edge	Left Sensor Parallelism, μm	Right Sensor Parallelism, μm
Top	<1	-7.5
Bottom	-2.6	3.3
Left	<1	N/A[1]
Right	4.7	2

Table 5.10.: The sensor cutting edge quality of the sensors on the ladder.

In order to estimate how the gluing process could possibly introduce the mechanical stress to the sensors, the height maps of both sensors have been taken. Additional warp structure would indicate the mechanical stress.

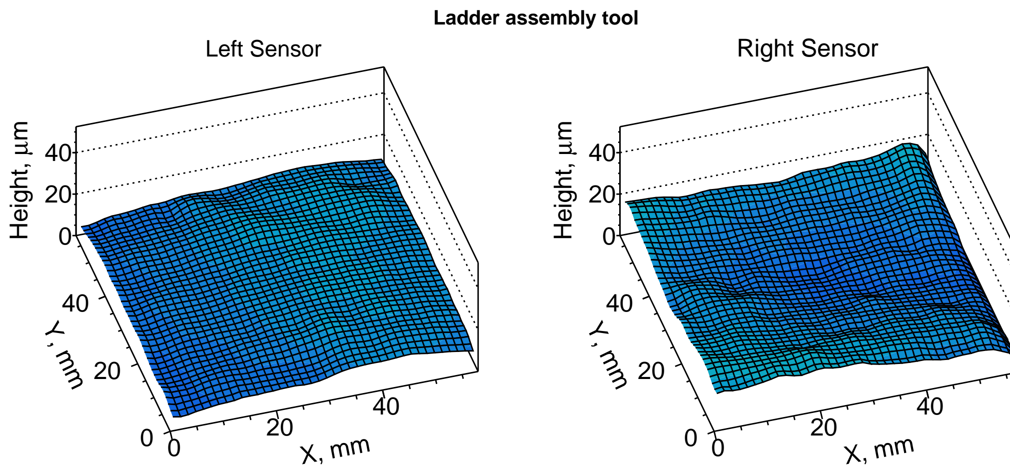

Figure 5.107.: Height map (warp) of the sensors on the ladder.

Fig. 5.107 shows the height scan results with a resolution of 2×2 mm^2. Being actively used even before being mounted on the ladder, the sensors during their lifetime have accumulated surface defects such as scratches and dust, which could not be removed with a nitrogen gas gun. Hence non uniform surface microstructure could be seen on the height maps. The maximum measured warp for the left sensor is 19 μm and 24 μm for the right sensor. No additional deformations in

[1] Left edge un-parallelism information for the CBM03C6 sensor is not available due to the sensor overlap.

the Z-direction indicate the absence (or negligibility) of the additional mechanical stress introduced to the sensor by the gluing process.

5.7.2.2. Summary

The developed procedures and methods for the ladder assembly tool allows to qualify its mechanical manufacturing process in order to ensure the correct sensor placement and alignment. Despite being carried out manually these procedures, taking into account the capabilities of the optical setup, can be automated in further work.

The developed procedures provide the data on the spatial misalignment of the sensors mounted to the ladder. This data is essential for the ladder, unit and station assembly of the STS detector. Before the assembly of the detector, which is foreseen to take place in two to three years from now, one could use this information as an input for the detector misalignment studies. These studies allow to simulate the real misalignment of the sensors in the STS detector and perform the track reconstruction efficiency analysis.

The ladder assembly tool after its optical inspection was sent back to the GSI Detector Laboratory with provided feedback and inspection results. At GSI, the results were verified and confirmed by the mechanical metrology methods. The reasons for the sensor misalignment were identified to be due to the glue hardening time and flow.

The described methodology will be automated and integrated at the two ladder assembly sites: at GSI, Darmstadt and at JINR, Dubna.

5.8. Software solution

The described methods and procedures developed in this work were implemented in LabVIEW 2013. It features a hardware abstraction level, which allows to use it with different hardware. It is possible for an end user to replace for example the XY motor stage if its drivers comply to the API[8] of the inspection system. The software solution comprise of control, measurement, analysis and visualization modules. It provides the operator's graphical program, which allows to configure the inspection parameters, control the XYZ motor stages, adjust the properties of the camera and optical assembly. It should be operated by a trained technician when the batches of the sensors start to arrive.

Fig. 5.108 shows the front panel of the inspection program. A window to display the images captured by the camera takes the most space of the front panel. It allows to zoom the image in and out to inspect different regions of interest of the sensor. The scale cross is drawn over the image to indicate the center of the image, additional "cross-hair" with the configurable size is drawn

[8]Application Programming Interface

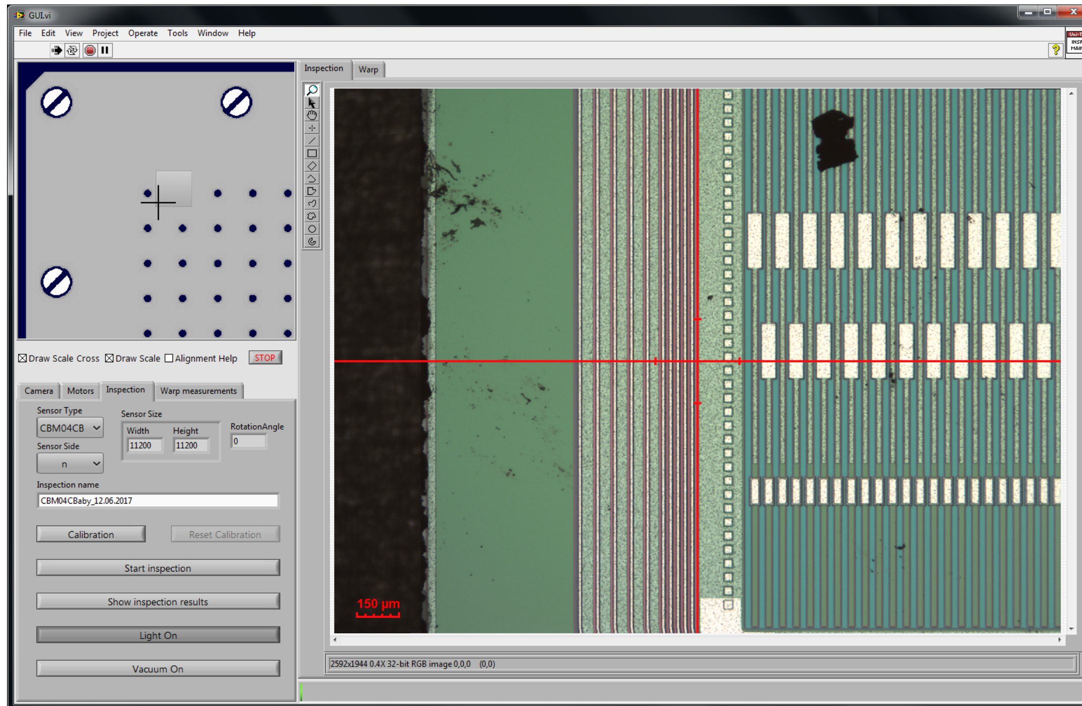

Figure 5.108.: The graphical user interface of the optical inspection setup.

around the center of the image to allow the estimation of the size of the object under investigation. A configurable scale bar with the current scale information is drawn and updated for different zoom values of the optical system.

In the top left corner of the figure the graphical representation of the inspected sensor on the vacuum chuck is shown. It allows to navigate the XY motors to position the sensor under the camera. The small black cross indicates the field of view of the camera over the sensor.

The bottom left paged block of controls allows to configure different properties of the inspection setup. On the presented page the configuration controls for the sensor surface inspection are shown. After placing the sensor on the inspection table and roughly aligning it, the operator choses the type of the sensor, its current side visible for the camera and performs a calibration to extract the sensor misalignment as presented in the section 5.4.2. After the calibration the sensor surface scan is initiated. The results are first stored locally under the system path indicated by the automatically generated inspection name. After the analysis of the data acquired is finished, the results are transferred to the database. From this panel the lighting and the vacuum pump are as well controlled.

Fig. 5.109 shows the other controls of the inspection program. The panel a) shows the camera information and the frames per second counter. It allows the adjustment of the camera properties, such as its current resolution, exposure time, gamma, color intensity, brightness, color correction etc. Further options are available by clicking on “Show more options” button. In case of a camera miscon-

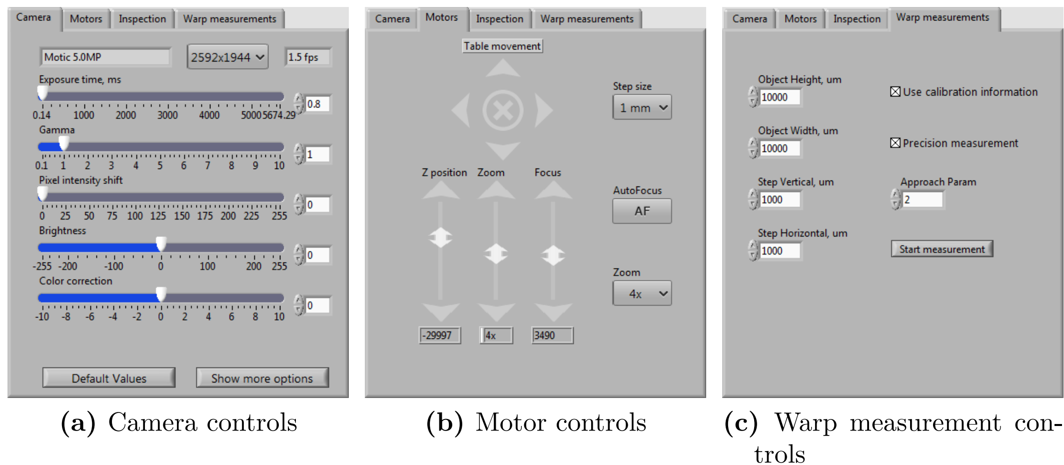

(a) Camera controls

(b) Motor controls

(c) Warp measurement controls

Figure 5.109.: Configuration panels of the optical inspection graphical program.

figuration, its properties can be reset to the predefined at current magnification (see section 5.2.3).

The panel b) shows the controls for the XYZ motor stage and for the motorized zoom and focus stages. From this panel the vacuum chuck can be moved in a calibrated and non-calibrated manner with a step resolution set by corresponding control. The "X" button allows to position the system over the alignment mark if it is visible in the current field of view of the camera. The zoom and focus of the system can be changed here arbitrarily or set to the predefined values. The "AF" button allows to autofocus the system on the object under test.

The panel c) shows the controls for the sensor warp measurements. Here the height and width of the object or its part and the stepping width are set. The "Precision measurement" and "Approach Param" (see section 5.5.1.1 for explanation) controls allow to adjust the precision of the warp measurement.

After the sensor surface scan, the inspection results can be accessed from the "Inspection" panel.

Fig. 5.110 shows the front panel of the inspection result overview program. Here a map of individual images which comprise the sensor inspected is shown. The small pictograms on the top right corner of each image shows the summary of the inspection in that region of the sensor. The green check-mark indicates, that no defects were found. The yellow exclamation sign shows that there is a defect with a low severity found, e.g. a dust grain. The red cross denotes a problem found in this region of interest: a large dust grain, a scratch or other critical defect. By selecting a single image, the image preview program is opened.

Fig. 5.111 shows the front panel of the image preview graphical program. Here an image of the sensor's region of interest is shown with the detected defects overlaid in a white color. This figure features a large dust grain found on the sensors strips. Due to its large area of 25223 μm^2 it is classified as a severe

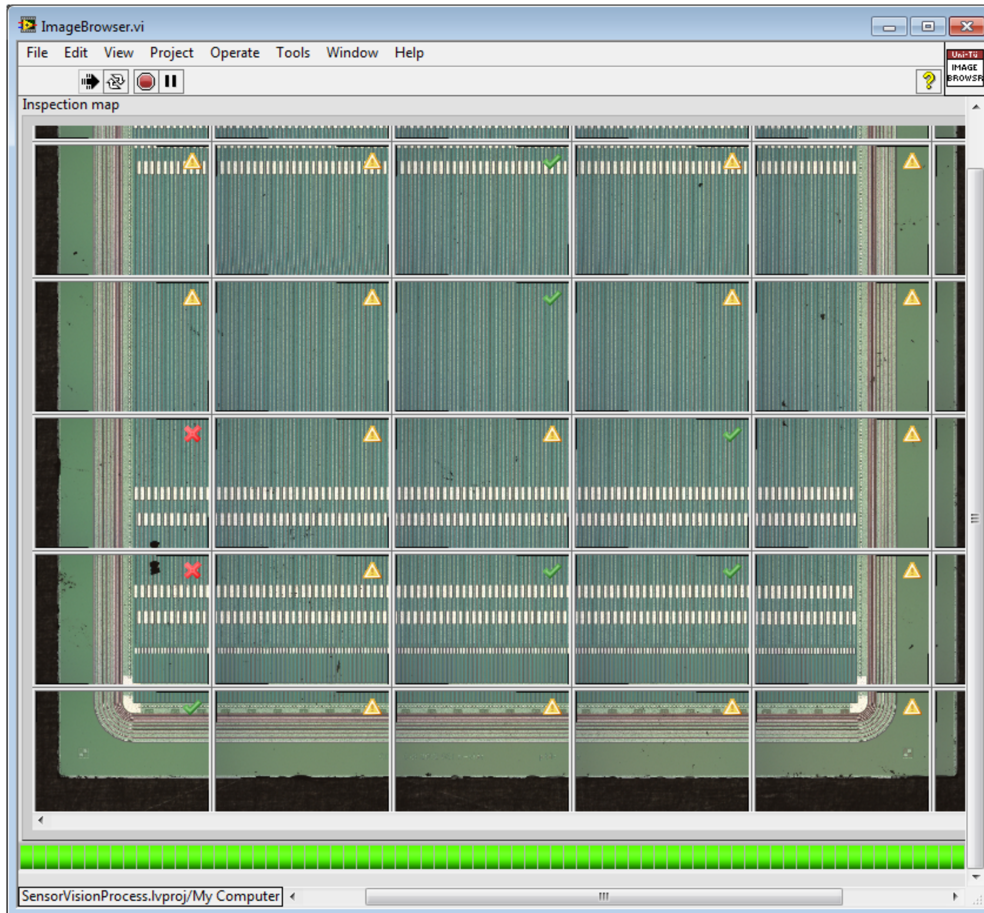

Figure 5.110.: Inspection overview program.

defect. The panel on the right hand side allows to navigate through all the defects found in this region of interest. For every defect the information about its context, position and geometry is available. The advanced information extracted during the defect finding is shown here. It contains the circularity, elongation, compactness factors and others. These data can be used for further defect analysis and tuning of the detection algorithms.

From this interface the operator can navigate between different regions of interest of the sensor, browse through the defects, switch the defect overlay on and edit the inspection results in case of misidentification. If the data were edited it is synchronized with the database.

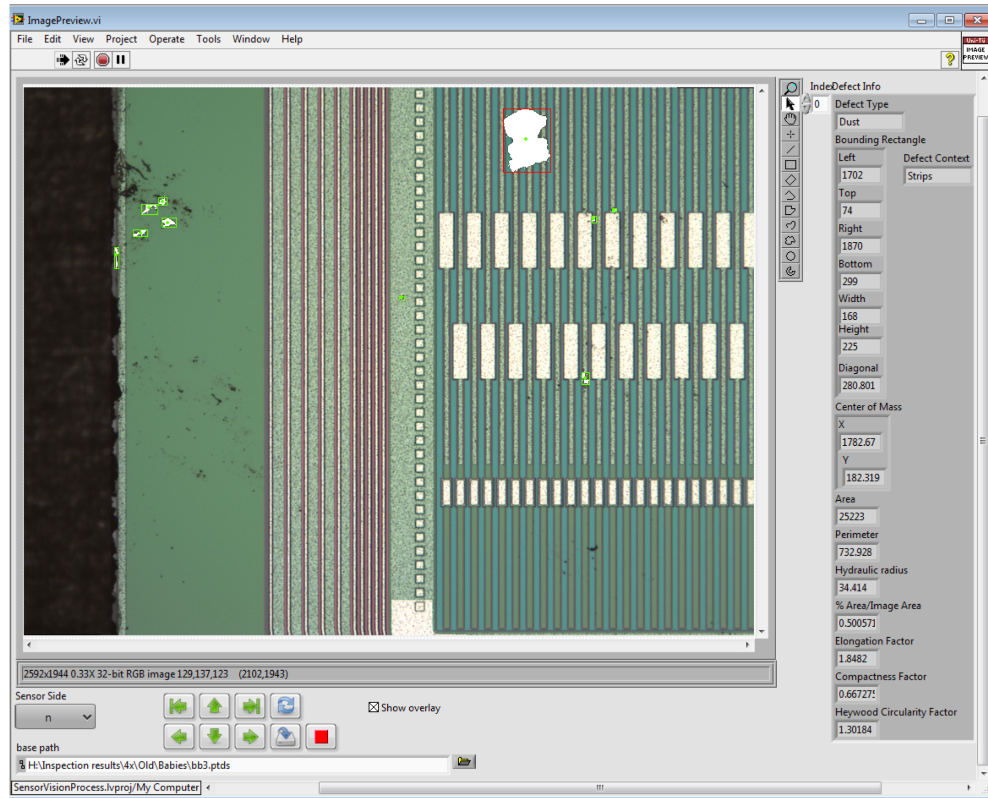

Figure 5.111.: Interface for the region of interest preview.

5.9. Performance limitations

It should be noted that results obtained and described in this work are for a camera with a low frame rate. It took roughly 1.8 second to acquire a full 5 MP image in LabVIEW. For the autofocusing and height measurements only a small region of interest of 300x300 pixels is taken, which speeds up the process but still takes roughly 0.3 second per captured image.

One more performance deteriorating effect of this camera is the so called *Rolling Shutter* effect, which distorts the image taken of the fast changing scenes. This effect was observed both during the fast movement of the sensor under the camera and for fast changes of the focus value. The effect of rolling shutter is shown in Fig. 5.112, which shows the undistorted original image of a cross on the calibration plate, followed by a series of distorted images taken.

The rolling shutter effect arises from the fact that the camera sensor (characteristic to CMOS sensors) is read out row by row. Combined with slow readout this leads to a situation, where upper part of the image belong to one scene and lower part to a different one.

To mitigate the rolling shutter effect two consecutive images should be taken in a row after motors arrive to designated position: first will take the distorted image

Figure 5.112.: Rolling shutter effects. From left to right: undistorted image, sudden start of motor movement, fly-by at a set speed, arrival moment.

and thus flush the frame buffer, the second captured image will be undistorted and viable for analysis.

The procedures described in sections 5.4 and 5.5.1.1 thus are about two times slower (together with the image processing overhead) compared to a global shutter camera (usually based on CCD technology), where all pixels are read out instantaneously and no distortions are possible.

Using a camera with a global shutter is considered as a possibility for improvement. Another point of improvement would be a camera with higher FPS (frames per second), allowing to speed up both the visual inspection and autofocusing height measurements. Thus having a faster camera (in terms of FPS) as well would increase the overall performance of the optical setup significantly. Furthermore, splitting the software between two machines allows a further speed up. In this scheme one machine is dedicated to the image acquisition only and the other is responsible for the image processing and defect analysis, allowing them to work in parallel and to share the same computing resources.

6. Detector cooling

6.1. Bi-phase CO_2 cooling

The requirement of keeping the silicon sensors below -5 ℃ coupled with severe space constraints pose a problem for the detector cooling. This challenge arises due to a very limited space between the sensor stations in the STS detector and a high density of the detector arrangement. Thus, the front-end electronics cooling bodies, their materials and coolant itself is a subject of thorough research and optimization. Substantial part of this work was dedicated to the optimization of cooling body geometry and cooling assembly performance.

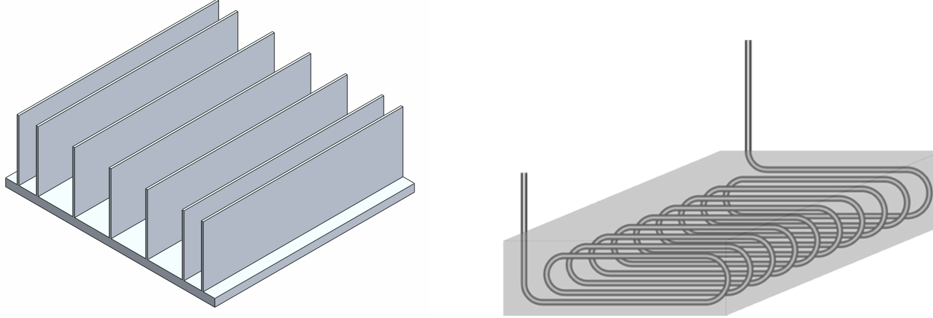

Figure 6.1.: Schematic view of a cooling body (left panel) and cooling block (right panel).

The cooling body (Fig. 6.1, left panel) is based on a classical heat sink design with ribs (shelves in this work) onto which the heat producing elements are mounted on both sides. It is mounted to the aluminum cooling block into which a cooling pipe is casted, allowing the heat removal. Both components combined comprise the cooling assembly. It will be described in details further.

6.1.1. Volumetric heat transfer coefficient

To quantify the cooling performance of a cooling agent, the volumetric heat transfer coefficient is introduced in [106, 107] as follows:

$$HTC_V = \frac{Q}{V_{tube} \cdot (\Delta T_{\Delta P} + \Delta T_{HTC})}, \quad (6.1)$$

where Q is the total thermal power transferred, V_{tube} is the inner volume of the tube which characterizes the amount of coolant material available for the heat

transfer process, $\Delta T_{\Delta P}$ is the change of the involved parts' temperature coming from change of the coolants pressure occurring in the process, and ΔT_{HTC} is a temperature gradient along the cooling tube due to the heat transfer. According to eq. (6.1), the tube diameter should be optimized with respect to pressure drop and heat transfer temperature gradients to ensure the optimal volumetric heat transfer.

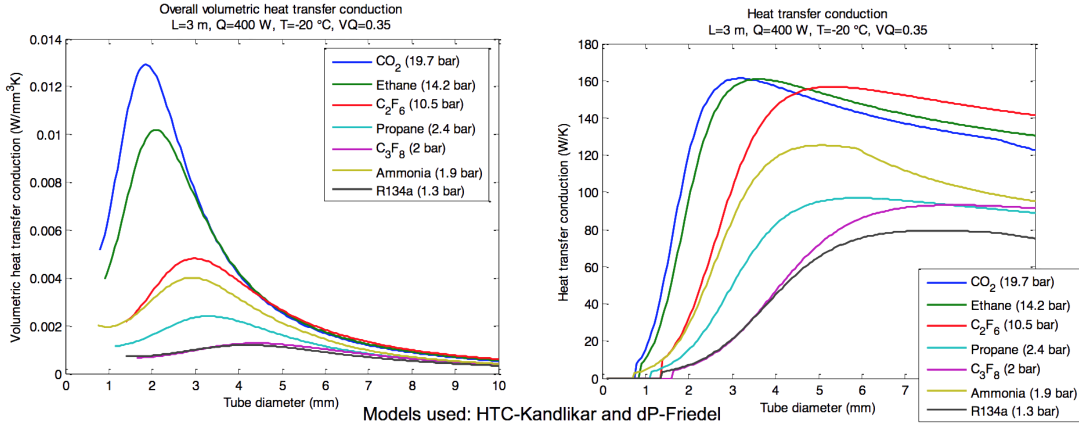

Figure 6.2.: Comparison of different coolants based on their volumetric heat transfer coefficient. The referenced models are described in [108] and [109]. Courtesy of [107].

Fig. 6.2 shows the comparison of the volumetric heat transfer coefficient of different cooling agents (left panel) and heat transfer conduction (right panel) vs. tube inner diameter for 400 W dissipated. The left panel shows that volumetric heat transfer coefficient of carbon dioxide is almost an order of magnitude better in comparison with very widely used R134a cooling agent. This figure gives a hint for a high volumetric heat transfer of carbon dioxide. In this work we implement the thermodynamical models and the equation of state of CO_2 to calculate the same parameters for the targeted cooling regimes of the STS detector in sections 6.1.4 and 6.1.5.

Carbon dioxide has a high latent heat, which allows to reduce the flow needed. The low viscosity lowers the frictional pressure drop inside the tubes. On the other hand CO_2, compared with other coolants, has to be operated at higher pressures. This forces one to utilize high pressure compatible equipment and to certify the cooling plants for security of operation. However, higher pressure means as well, that the vapor stays more compressed reducing the needed volume and increasing the mass flow, which in turn increases the pressure drop along the tube.

The advantages of carbon dioxide over other cooling agents has motivated the further investigation of CO_2 bi-phase cooling for the STS Detector. The following sections in this chapter will cover the thermodynamical properties of carbon dioxide, its equation of state, the cooling pipe diameter and length optimization.

Furthermore, in order to calculate the flow pattern, pressure drop and heat transfer coefficient of the boiling CO_2 for the foreseen cooling regimes of the STS

detector, the works of Thome *et.al*([110, 111, 112]), which are most widely used in cooling technical applications are adopted in this work.

6.1.2. CO_2 phase diagram

The usage of the two-phase evaporative CO_2 cooling implies the precise knowledge of the thermodynamical properties. Most notably its current phase, pressure and temperature.

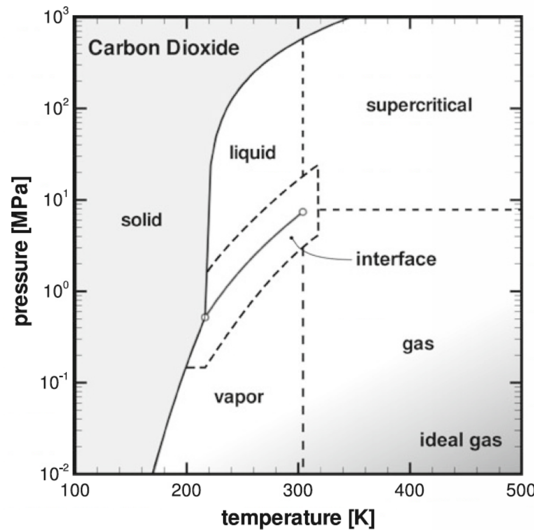

Figure 6.3.: Phase diagram of carbon dioxide depicted in terms of pressure and temperature [113].

Fig. 6.3 shows the Pressure-Temperature diagram of the CO_2 [113]. Much like water, CO_2, which is normally found in the gaseous phase in the nature, can undergo the phase transitions (most prominently) from gaseous to liquid, to solid state. The existence of other states such as supercritical fluid is possible at high pressures and temperatures. The most important transition in this work is the liquid-vapor phase transition in which the carbon dioxide can be found consisting simultaneously of two phases — saturated liquid and saturated vapor.

In technical applications it is more common to use Pressure-Enthalpy phase diagram, also known as Mollier Chart (shown in Fig. 6.4). It depicts well the transition region between liquid and vapor stages. This region represents the temperature, enthalpy and pressure range between the triple point and the critical point. The change of Enthalpy [114] is the amount of heat per mass unit needed to be added to or removed from the system to change the system's internal energy and pressure-volume product. The full difference in enthalpy between fully liquid and fully gaseous system is called heat of vaporisation and is one of the most important properties in bi-phase cooling applications since it characterizes the substance cooling performance in terms of how much heat the boiling coolant

could take away from the heat source. The heat of vaporisation is about 320 kJ/kg for the carbon dioxide at -40 °C, which is targeted to be the coolant temperature for the STS detector.

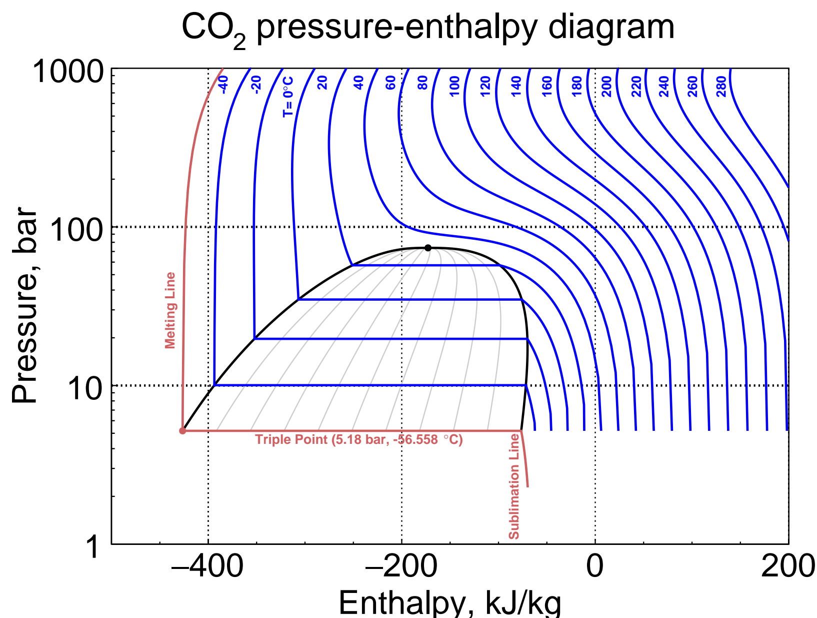

Figure 6.4.: Phase diagram of carbon dioxide depicted in terms of pressure and enthalpy. The graph is plotted with the equation of state implemented in this work (cf. section 6.1.4).

6.1.3. Vapor quality

The liquid-vapor phase transition process happens at constant pressure in the cooling pipe (isobaric process) and constant temperature (isothermal process) and undergoes different sub-phases of boiling as the ratio between liquid and vapor (vapor quality) changes from 0 to 100%. According to Bejan *et al.* [115] there are 7 main boiling sub-phases in horizontal tubes: bubbly, stratified, stratified-wavy, intermittent (combination of plug and slug flows), annular and mist flow. The boiling phases are shown in Figs. 6.5 and 6.6.

Further, according to Bejan *et al.*, we describe the phases in the order of increasing vapor quality.

In bubbly flow, small bubbles of vapor are dispersed in the continuous liquid phase, with tube walls being wet.

In plug flow, elongated liquid plugs, which are smaller than the tube diameter, are separated by elongated bubbles of vapor, the liquid phase is continuous along the bottom of tube.

In slug flow, the bubbles continue to grow in size forming bullet-like shapes of size comparable with the tube diameter.

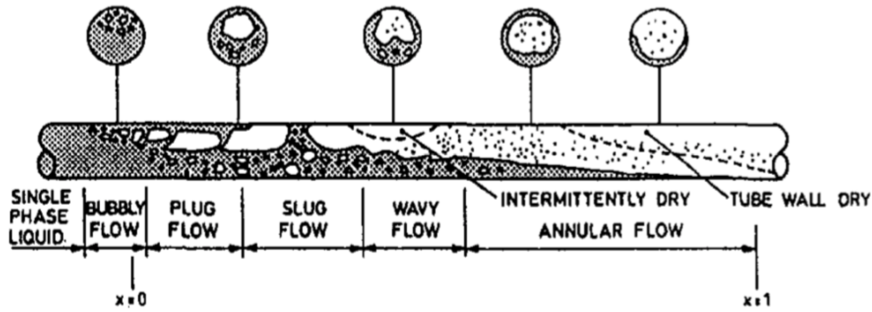

Figure 6.5.: Flow pattern of a boiling liquid inside the tube in relation with the vapor quality [115].

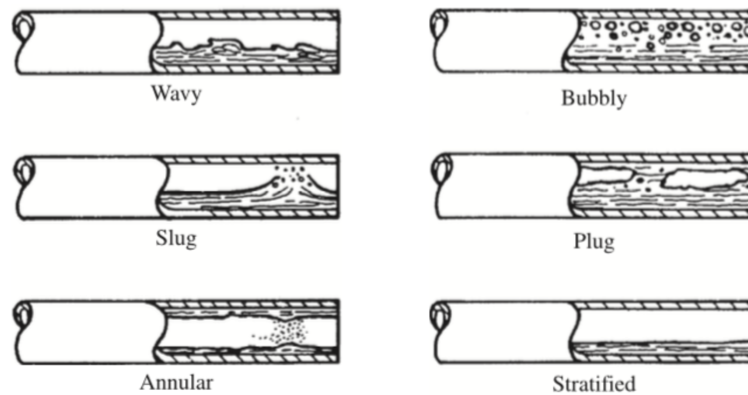

Figure 6.6.: Different flow patterns found in the tubes during evaporative cooling [115].

Stratified flow pattern is typical for low mass flows. It has distinct separation between liquid and vapor phase.

In stratified-wavy flow, as the flow increases in comparison to stratified flow, the formation of liquid waves occurs. These waves are traveling in the direction of flow and eventually wetten the sides of the tube, forming thin liquid films on the tube walls. These waves do not reach the top of the tube.

In the intermittent flow, as the mass flow further increases, the waves grow in height and start wetting the full perimeter of the tube almost continuously.

In annular flow, as the vapor quality grows, the wall perimeter stays wetted with continuous liquid film.

As the dryout inception vapor quality being reached, the tube wall start to dryout gradually with less and less surface of the tube wetted. Finally, at the dryout completion vapor quality the tube wall becomes completely dry and liquid phase is present only in small liquid bubbles flowing in a vapor medium.

The boiling process is very favorable for the cooling applications, since the boiling medium is being constantly mixed and additional turbulence contributions are being introduced which increase the overall heat exchange between the cooling substance and the heat producing interface. However the vapor quality inside the

cooling pipeline needs to be be carefully controlled and optimized. Since at high vapor qualities, as the dryout completes, the heat exchange properties severely drops down, one has a cooling regime which is more similar to forced gaseous cooling. It is much less effective compared to bi-phase or liquid cooling. This may result in uneven heat removal, temperature gradients over the cooled body as possible drawbacks.

As seen in the pressure-enthalpy diagram the lower inlet saturation pressures and temperatures are more effective for cooling purposes, since the latent heat of vaporization and temperature differences are greater at these regimes improving the overall cooling performance. However the close proximity to the triple point makes the cooling systems prone to clogging. This happens if additional frictional pressure drop inside the piping will bring the pressure of the carbon dioxide below the triple point (5.18 bar, 216.592 K). The clogging effect is due to liquid carbon dioxide changes to solid phase decreasing or fully stopping the flow of coolant in the system. This temporary effect can lead to excessive heating of heat producing components, eventually exposing damage to parts of the system. This phenomenon should be avoided at all means.

6.1.4. Equation of state for carbon dioxide

The Thome model [110] relies heavily on the knowledge of the input thermodynamical parameters of carbon dioxide and the cooling system parameters. Tab. 6.1 shows the minimum required parameters calculated from the equation of state.

Calculated Parameter	Description
P_s	Saturation pressure, Pa
ρ_V	Saturated vapor density, kg/m^3
ρ_L	Saturated liquid density, kg/m^3
h_V	Enthalpy of vapor, J/kg
h_L	Enthalpy of liquid, J/kg
c_{pV}	Isobaric heat capacity of vapor, J/kg K
c_{pL}	Isobaric heat capacity of liquid, J/kg K

Table 6.1.: The minimum required list of thermodynamical parameters of the CO_2 which are calculated from the equation of state.

In order to have precise predictions of major parameters, like pressure drop, volumetric and ordinary heat transfer coefficients, a good description of thermodynamic properties of carbon dioxide at any point of the phase diagram is needed. These properties and parameters are obtained from the equation of state (EOS). There is a certain amount of the equation of state formulations (e.g. in functional form) available in literature, differing in precision to describe the experimental data. The most discrepancy is observed in the critical region, where some

properties exhibit the asymptotic-like behavior. This subsection summarizes the implementation of the equation of state for this work.

First, as mentioned above, an adequate and precise equation of state should be chosen.

The ideal gas EOS is applicable only at low pressures and temperatures higher than T_c thus giving large deviation from the real gas behavior.

$$PV_m = RT \tag{6.2}$$

The first EOS for the real gas was introduced by van der Waals in 1873 [116]. It involves two additional parameters where a describes the attraction forces between molecules and b — the finite volume of the gas molecules which compensates the linear correlation between pressure and temperature at lower pressures and higher temperatures.

$$P = \frac{RT}{V_m - b} - \frac{a}{{V_m}^2} \tag{6.3}$$

A further development of the van der Waals' EOS, a cubic EOS of Redlich-Kwong [117], modified by G. Soave [118] (eq. (6.4)), takes into account the ω (eq. (6.5)) — an acentric factor to characterize the non-sphericity (centricity) of molecules [119]:

$$P = \frac{R\,T}{V_m - b} - \frac{a\;\alpha(\omega)}{V_m(V_m + b)}, \tag{6.4}$$

where

$$\omega = -\log_{10}\left(\frac{P_s(T/T_c = 0.7)}{P_c}\right) - 1 \tag{6.5}$$

Despite its complex form the Soave cubic EOS allows to solve for analytical roots, which is used in iterative approaches to the calculation of saturated vapor and liquid densities.

Another representation of EOS was proposed by Kamerlingh Onnes in 1901, where the pressure and compressibility factor Z of a system in equilibrium are expressed as a power series of the density (so called virial expansion [120]):

$$\frac{P(T,\rho)}{\rho RT} = Z(T,\rho) = 1 + B(T)\rho + C(T)\rho^2 + D(T)\rho^3 + \cdots, \tag{6.6}$$

where the coefficients B, C, D... are fitted against experimental data.

The further development of this EOS are the "BWR-type equation of state" introduced by Benedict *et al.* (1940) and "DMW-type" introduced by Duan-Møller-Weare (1992) which feature a truncated form of the virial expansion with addition of the exponential density dependency.

Finally, the most complex, yet most accurate, type of equation of states is the multiparameter equation of state, which is based on the derivation of the

Helmholtz free energy to describe the relation between thermodynamical properties:

$$\frac{a(T,\rho)}{RT} = \frac{a^o(T,\rho) + a^r(T,\rho)}{RT} = \alpha^o(\tau,\delta) + \alpha^r(\tau,\delta), \tag{6.7}$$

where $a^o(T,\rho)$ is the specific or molar Helmholtz energy of ideal gas and $a^r(T,\rho)$ is the residual contribution to the total Helmholtz energy of real gas. $\alpha^o(\tau,\delta)$ and $\alpha^r(\tau,\delta)$ are their reduced counterparts with inverse reduced temperature $\tau = T_c/T$ and reduced density $\delta = \rho/\rho_c$. Knowing the Helmholtz energy of a system, nearly all other thermodynamical properties of it could be described in terms of $\alpha^o(\tau,\delta)$ and $\alpha^r(\tau,\delta)$ and their respective derivatives. The $\alpha^o(\tau,\delta)$ is usually obtained from equation of the isobaric heat capacity of the ideal gas $c_p^o(T)$ and parametrized by fitting against world data.

The most fundamental, so called *reference* notations of multiparameter equation of states can contain up to 583 terms for residual part of the Helmholtz free energy as shown in [121]. This is however a full bank of terms, which is normally reduced to more meaningful amount preserving the good accuracy of experimental data description, which as well saves the computation time.

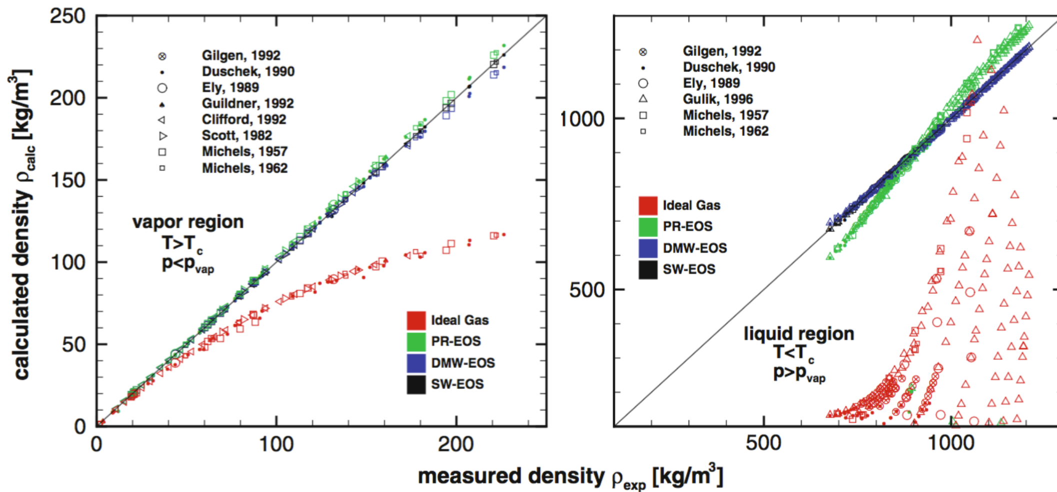

Figure 6.7.: Comparison of various EOS in terms of calculated density [113].

Fig. 6.7 shows the performance comparison of the CO_2 equations of state found in Böther *et al.* [113]. It is based on the comparison of the calculated density with the density measured both in subcritical and supercritical regions. The Span and Wagner [121, 122] multiparameter equation of state shows the best description of the experimental data. Fig. 6.8 shows the relative deviation of the density calculated from EOS to experimental measurements from different datasets, as presented in [113].

The Span-Wagner equation of state is adopted in this work for the calculation of various thermodynamic properties. However, the iterative approaches

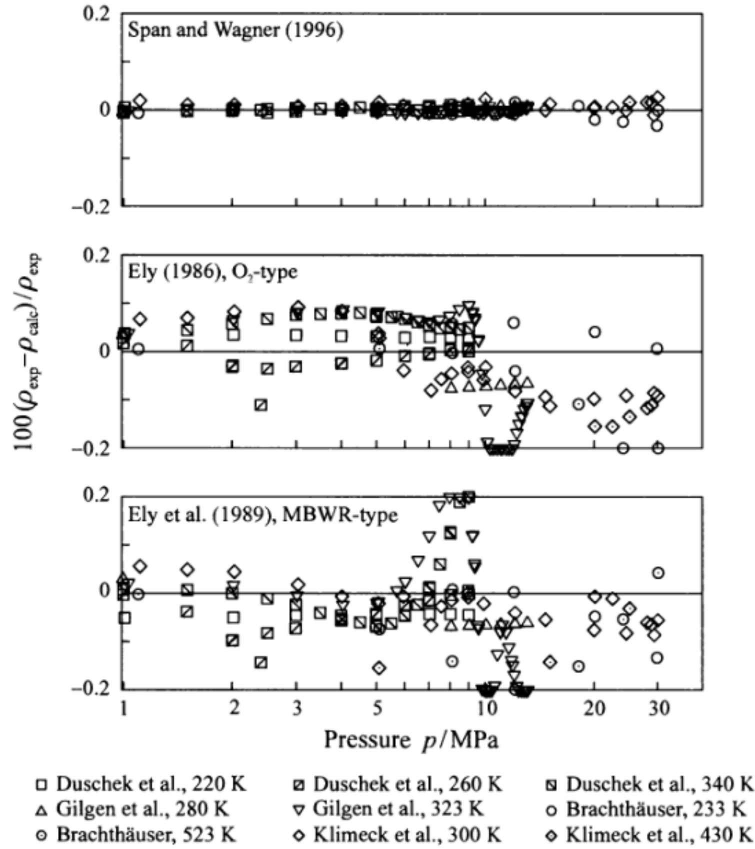

Figure 6.8.: Relative deviation of density calculated from EOS to experimental measurements from different datasets [121].

used in [121] to calculate the density and saturation pressure of the carbon dioxide based on the *regula falsi* [123] minimization, have been replaced by the MIGRAD [76] minimization algorithm from the MINUIT [77] package. The MIGRAD minimization is based on the variable metric method [124] and is a standard tool for the minimization problems in high energy physics.

The calculated properties are not limited to the Thome model requirements. They additionally include the reduced Helmholtz energy a, entropy s, isochoric heat capacity C_v, Gibbs free energy G, isentropic and isothermal expansion coefficients k_s and k_t, isentropic and isothermal compressibility coefficients κ_s and κ_t, etc.

The implemented equation of state could not describe *ab initio* all thermodynamical parameters of carbon dioxide, which are needed for the Thome model calculation. Tab. 6.2 shows the thermodynamical parameters which are extracted from the auxiliary correlations.

These correlations are obtained by fitting the effective models against global measurement data. The viscosity correlations are taken from [125, 126, 127], the surface tension correlations are taken from [128, 129], the thermal conductivity

Estimated Parameter	Description	Value at -40 °C
μ_V	Dynamic viscosity of vapor	$1.18 \cdot 10^{-5}$ N s/m^2
μ_L	Dynamic viscosity of liquid	$1.93 \cdot 10^{-4}$ N s/m^2
σ	Surface tension	$1.24 \cdot 10^{-2}$ N/m
k_V	Thermal conductivity of vapor	$1.22 \cdot 10^{-2}$ W/m K
k_L	Thermal conductivity of liquid,	0.1603 W/m K

Table 6.2.: The thermodynamical parameters of the CO_2 which are extracted from the auxiliary equations and correlations.

correlations are taken from [125, 127, 130].

The implemented equation of state and auxiliary correlations allow to extract many thermodynamical parameters of the carbon dioxide. The pressure-enthalpy diagram shown in Fig. 6.4 is plotted using the implemented framework.

6.1.5. Thome model

The Thome model [110, 112] allows to calculate the flow patterns, important vapor quality and mass flux regions as well as extract the pressure drop along the cooling line. It provides the way to analytically connect the thermodynamical properties such as the heat transfer coefficient and the pressure drop of the liquid and gaseous cooling regimes. These properties are normally very different for liquid and gaseous phase cooling.

The model allows to predict the two-phase flow patterns, pressure drop along the cooling pipe and extract the heat transfer coefficient of the boiling carbon dioxide. We use this model additionally to optimize the dimensions of the cooling pipes of the cooling bodies. The model considers the boiling phases at different vapor qualities (see section 6.1.3), coolant mass velocities, cooling temperatures and heat fluxes. Tab. 6.3 shows the input for the Thome model. The model internally uses the calculations of the carbon dioxide properties (listed in Tabs. 6.1 and 6.2) extracted from the equation of state and auxiliary correlations as described above.

Input Parameter	Description
T	Coolant temperature, K
x	Vapor quality, unitless
D_{eq}	Equivalent diameter, m
q	Heat flux, W/m^2
G	Coolant mass flux, kg/m^2 s

Table 6.3.: Input parameters for the Thome model.

The model is used to estimate the volumetric heat transfer coefficient as described above in eq. (6.1) and extract the optimal cooling pipe inner diameter. For this work 200 W of heat power (Q) should be removed by a single cooling body, the tube length (L) has been chosen to be 2 m and the maximum volumetric flow (f) is limited to 32 l_n/min by the flow meter chosen.

In order to translate this to the Thome model input, the following conversion for heat flux q

$$q = Q/S \tag{6.8}$$

and mass flux G

$$G = \dot{m}/A = \rho\dot{V}/A = 3.296 \cdot 10^{-5}\ \mathrm{kg/m^3} \cdot \mathrm{f/A} \tag{6.9}$$

is used. Here $S = \pi DL$ is the tube total inner surface area and $A = \pi D^2/4$ is the tube cross-sectional area. The factor $3.296 \cdot 10^{-5}$ arises from the volumetric to mass flow conversion. The conversion principles can be found for example in [131].

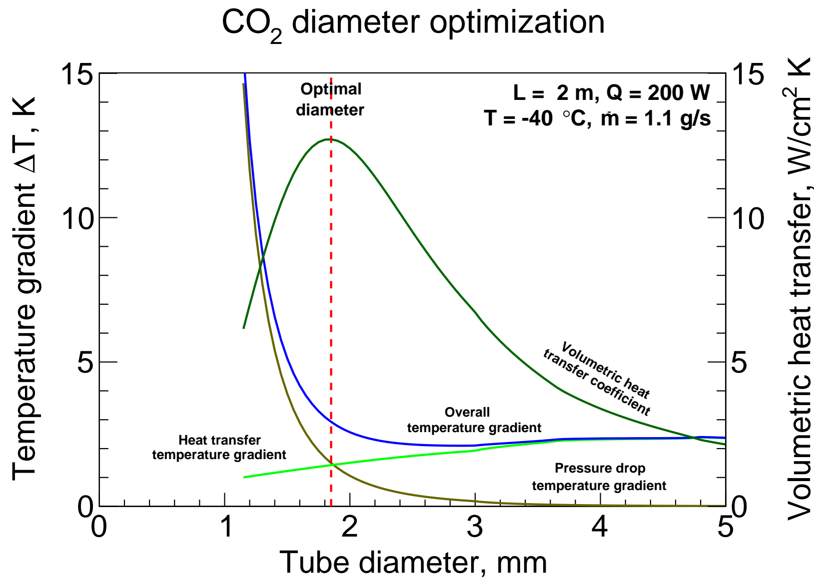

Figure 6.9.: Optimization of the tube diameter based on calculations of the temperature gradients and the volumetric heat transfer coefficient. The Thome model and CO_2 equation of state implemented in this work are used for the calculations. Both vertical axes have the same scale.

Fig. 6.9 shows the optimal diameter scan based on the Thome model and the CO_2 equation of state implemented in this work. The light green and brown lines denote the temperature gradients arising from the calculated bi-phase heat transfer coefficient and pressure drop, respectively. The blue line is their sum and denotes the overall temperature gradient.

The dark green curve denotes the volumetric heat transfer coefficient calculated for the set cooling system properties from the overall temperature gradient. The curve peaks around the optimal cooling tube inner diameter. The optimal diameter extracted is 1.85 mm. This value is taken for the experimental verification described in the following sections.

Having optimal tube inner diameter established and fixed, the Thome model allows to predict the boiling phases of the two-phase carbon dioxide. These boiling phases are further referred to as flow patterns. Fig. 6.10 shows the flow pattern map obtained for the cooling conditions used in this work.

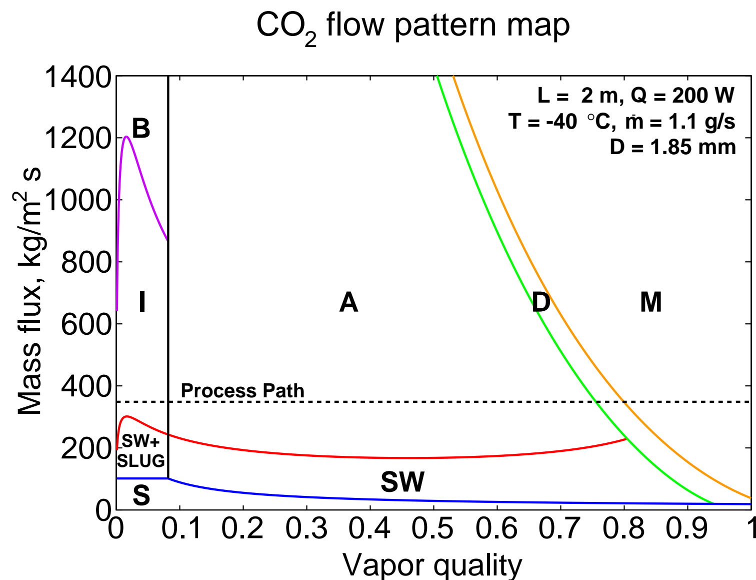

Figure 6.10.: The flow pattern of a boiling liquid inside the tube in relation with vapor quality calculated from the Thome model and CO_2 equation of state implemented in this work.

For high mass fluxes, the x_{IA} (plotted as a black vertical line around 0.08 vapor quality) defines the vapor quality boundary where the intermittent (I) to annular (A) flow pattern transition happens. The x_{di} (plotted as a green curve) defines the dryout inception vapor quality where the annular (A) to dryout (D) flow pattern transition happens. The x_{de} (orange curve) denotes the completion of the cooling tube wall dryout and the transition to the mist (M) flow pattern. At this condition the tube walls remain completely dry and mostly evaporated coolant flows inside the tube. This vapor quality is most important for bi-phase cooling applications since the heat transfer coefficient drops rapidly in this region hindering the heat removal.

For low mass fluxes, the flow patterns alter (blue curve denote the transition boundary) from slug (SW+SLUG), stratified (S) and stratified-wavy (SW) flow patterns. The x_{IA} vapor quality denoting the transition from stratified-wavy and slug to purely stratified-wavy flow pattern.

For very high mass fluxes and typically high heat fluxes instead of intermittent the bubbly (B) flow pattern (purple curve) can be observed before the transition to the annular flow pattern.

The Thome model is used to calculate the frictional pressure drop inside the cooling tube and the two-phase heat transfer coefficient. Fig. 6.11 shows the calculated properties, respectively.

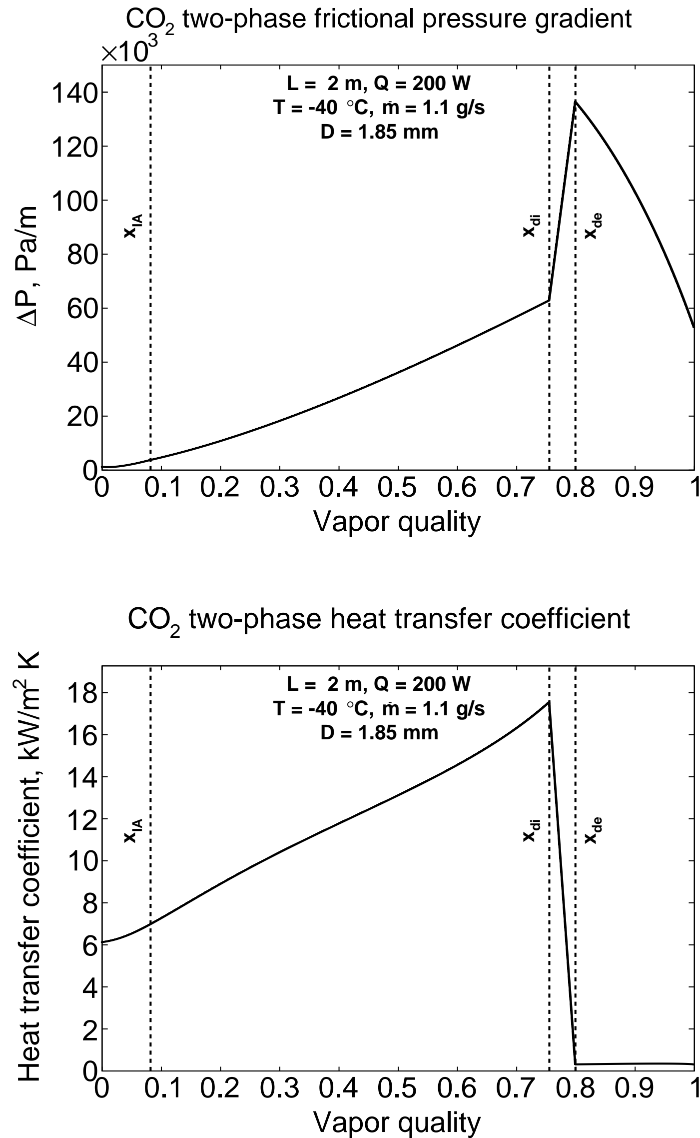

Figure 6.11.: The frictional pressure drop (top panel) and the heat transfer coefficient (bottom panel) of a two-phase carbon dioxide inside the cooling tube versus the vapor quality calculated from the Thome model and the CO_2 equation of state implemented in this work.

The figures have flow pattern transition vapor qualities denoted as vertical

dashed lines. Most important here is the dryout inception vapor quality. It indicates the drastic change in the thermodynamical properties of the coolant. The frictional pressure gradient increases here by a factor of 2. This leads to a situation where the overall pressure of the carbon dioxide decreases, which as well lowers its temperature due to expansion. If the pressure and temperature drop below the triple point (5.18 bar, -56.5 ℃, see Fig. 6.4) for reference), the formation of a solid state occurs, which in turn clogs the system reducing the mass flow to zero. Furthermore the heat transfer coefficient in this region drops rapidly by a factor of ≈ 20, which will introduce the temperature gradients among the cooled bodies. Taking into account these effects, the evaporation of the CO_2 beyond vapor quality of 0.7 should be avoided in the cooling bodies.

6.2. Thermal simulations of cooling bodies

6.2.1. Motivation

During the building phase of the open CO_2 system (see section 6.3), a number of FEM (Finite Element Method) simulations have been carried out to envision the working regimes of the setup and predict possible outcome of the measurements. The FEM simulations as well helped to understand the thermal interfaces problem and improve the experimental results later on.

6.2.2. Front-end board box simulations

The front-end boards (FEB) will dissipate up to 200 W of thermal power from an assembly of 10 read-out front-end electronic boards. The power needs to be cooled away. The holding structures holding the read-out boards are called front-end board boxes.

To find out the best geometry for the FEB boxes a series of FEM thermal simulations were conducted employing the SolidWorks [132] software package. It allows to set up the thermal parameters on an arbitrary body (in our case a 3D model drawn in AutoCAD [133] and imported into SolidWorks) such as set temperature, convection, heat flux, heat power and heat radiation and configure them flexibly.

The first input for the FEB box geometry is the geometry of the front-end board PCB. in Fig. 6.12 a CAD design of a FEB box is show.

A FEB box accommodates 10 such boards. The front-end boards are mounted to the shelves on both sides, two additional outermost shelves are added to lower the radiative heat loss and add “cold mass”. The distance between shelves should be wide enough to accommodate the electronics and the micro-cables bundled together, which connect the sensors on the ladders with readout STS-Xyter ASICs on the front-end board. Enough space should be provided for mounting purposes — a FEB box should be tightly mounted onto the cooling plate to ensure the

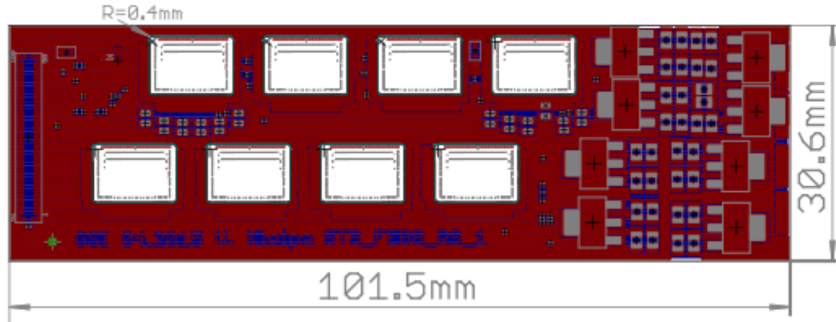

Figure 6.12.: CAD drawing of the front-end electronics board as of April 2015 [134].

best heat conductivity. The box should be made out of a material with excellent and isotropic heat conductivity which will not be activated in the radioactive environment and withstand a range of temperature regimes without becoming brittle when cold or too soft when hot. The shelves thickness has to be optimized to provide enough "cold mass" and allow a sufficient heat transfer from the most distant points to the base, where it is connected to the cooling plate. Lastly, it should be compact enough to fit inside very limited space of the STS detector.

Having this input, three major designs were considered based on the shelf thickness: $105 \times 35.6 \times 65$ mm^3, $105 \times 35.6 \times 75$ mm^3 and $105 \times 35.6 \times 85$ mm^3 aluminum boxes with shelf thicknesses from 1 to 3 mm.

A large number of FEM thermal simulations have been conducted to find out proper thermal interfaces, their geometrical parameters and materials to be used. Most of the intermediate studies are omitted here and only the final results for the most important cases are presented.

6.2.2.1. SolidWorks setup

A variety of custom defined materials are used in the FEM simulations conducted in this work. An overview of these materials and their properties is shown in appendix E. It was assumed that the base cooling plate to which the cooling bodies are attached stay at the constant coolant temperature (e.g. -40 ℃, as it is targeted for the STS detector).

A thin layer of thermally conductive grease is always simulated between the cooling plate and any cooling body. The thermal grease mitigates the effects of the material roughness and the presence of micro-cavities filled with air, which reduce overall thermal contact area dramatically. The thermal grease when put between two bodies closing these cavities and ensures the overall better thermal contact despite its relatively low thermal conductivity. Thermal grease is also applied to the interfaces between the shelves of the cooling bodies and heat producing elements (e.g. PCB with ASICs). The thermal grease is taken into account in the simulations.

6.2.2.2. Thermal studies of the FEB boxes

The final version of the cooling assembly features all above mentioned interfaces with additional introduction of the copper and kapton interfacing layers between cooling body's shelves and PCBs. The kapton layer is needed for the electrical insulation between the shelves and PCBs. Kapton has bad thermal conduction properties, however, only a thin layer (25 µm) of it is needed to electrically decouple the interfaces. A thin copper layer simulates the copper layer of a PCB and provides improved overall lateral heat distribution on the sink, since the most of the heat is produced locally in places where ASICs are located, thus increasing the cooling performance. The obtained simulation results are shown in Tab. 6.4. A sample simulation result for 3 mm thick shelves, -40 °C coolant temperature and 140 Watts of heat power dissipated is shown in Fig. 6.13.

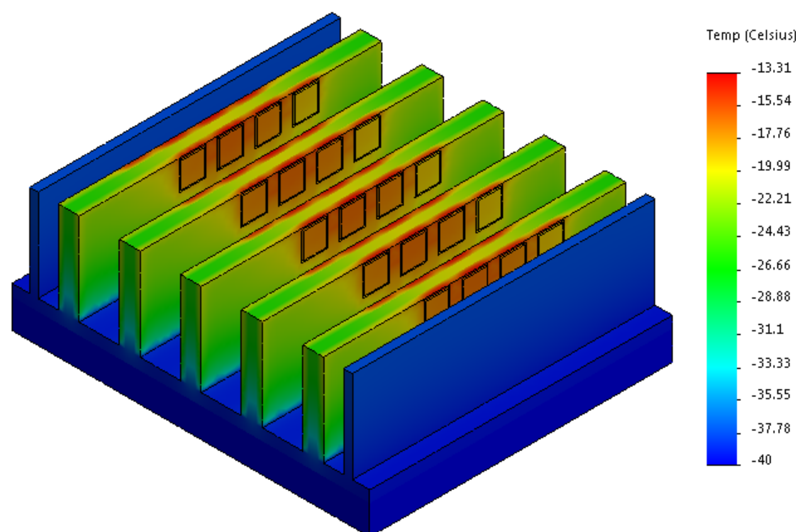

Figure 6.13.: FEM simulation result for 3 mm thick shelves, -40 °C coolant temperature and 140 Watts of heat power dissipated.

T	1 mm		2 mm		3 mm	
	200 W	140 W	200 W	140 W	200 W	140 W
-40	4.57	-3.21	-5.68	-11.2	-11.2	-13.3
-30	8.36	0.58	-0.45	-6.45	-5.2	-10.2
-20	12.16	4.38	4.77	-1.23	0.8	-4.2
-10	15.96	8.17	9.99	3.99	6.9	1.81
0	19.75	11.97	15.22	9.22	12.9	7.83

Table 6.4.: The maximum temperature simulated on the cooling assembly depending on the heat power load and cooling plate temperature.

6.2.2.3. Study of AlN heat sinks

The aim of this simulation is to introduce an Aluminum Nitride (AlN) interface between cooling body shelves, PCBs and ASICs and to see the potential improvement of the cooling performance. The Aluminum Nitride is synthesized as a powder and then compressed and formed into ceramic sheets. It has very good heat conductivity properties and is electrically insulating.

The aim of this simulation was to investigate the difference in the cooling performance when using only half the contact area of the ASICs to the AlN (see Fig. 6.14). The reduced heat sink geometry would allow a more flexible electrical line routing on the PCB.

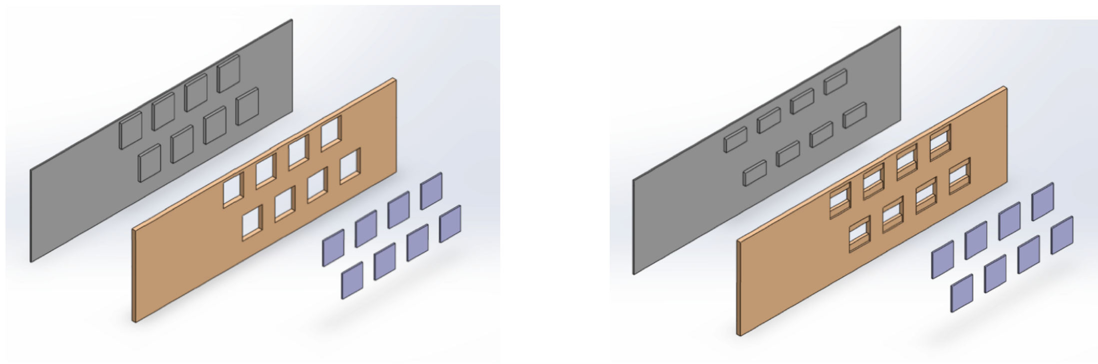

Figure 6.14.: Input geometries for FEM simulations with normal AlN heat sink (left panel) and halved heat sink (right panel). Both panels show the exploded view of the front-end board — the AlN layer (gray color), the PCB with cut-outs (brown) and 8 ASICs (purple).

In this study only 3 mm thick shelves were simulated, since this thickness was adopted as the base line design for the FEB box. Two power dissipation regimes (140 and 200 Watts) and a cooling plate temperature range from -40 ℃ to 0 ℃ were simulated. The results are summarized in the Tab. 6.5. A sample result for the reduced heat sink area geometry is shown in Fig. 6.15

T	Full area		Half area	
	200 W	140 W	200 W	140 W
-40	-19.57	-21.96	-17.8	-21.01
-30	-13.54	-16.12	-10.82	-14.84
-20	-6.53	-9.79	-3.62	-7.69
-10	0.88	-2.38	3.57	-0.49
0	8.31	5.05	10.77	6.7

Table 6.5.: Maximum temperature simulated on the cooling assembly in dependence from heat power load and cooling plate temperature.

From these measurements the conclusion can be drawn, that, firstly, the AlN

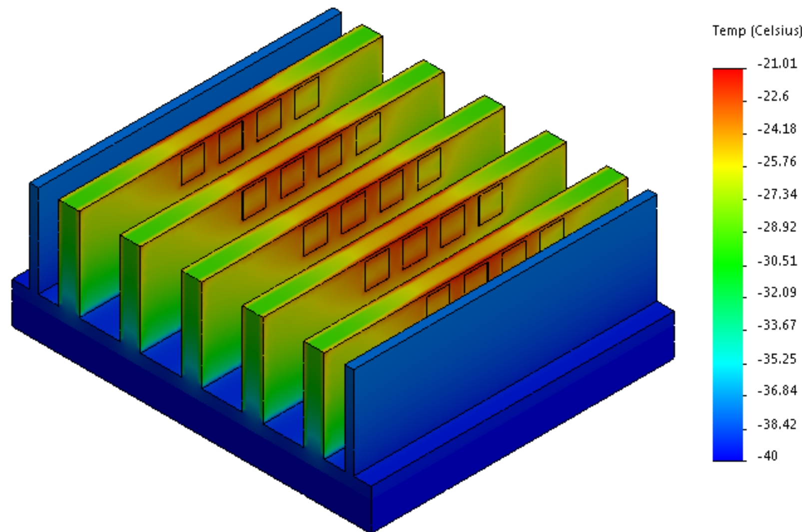

Figure 6.15.: FEM simulation result for a reduced heat sink area, 140 Watts power dissipation and -40 °C cooling plate temperature.

heat sinks greatly increase the cooling performance compared to ordinary PCBs, and, secondly, that only a minor temperature difference is observed between full and reduced area AlN heat sinks, respectively. This can be explained by a very high heat conductivity of AlN.

Thus reducing the AlN heat sink area by 50% is a viable option. It will not deteriorate the cooling performance of the FEB box significantly. The overall conclusion of this study is that one should use AlN interfacing instead of copper/kapton. This also avoids the copper activation in the CBM radiation environment.

6.2.3. Read-out board simulations

The read-out boards (ROB) will collect digital signals from the front-end boards and aggregate them into data packets and transmit them for further online processing.

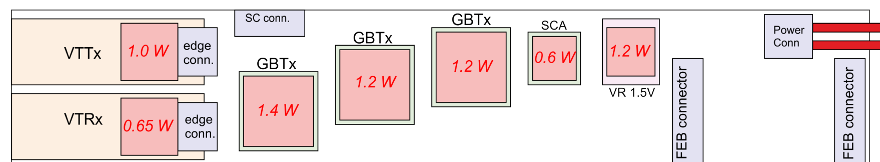

Figure 6.16.: Placement of components on the ROB together with the dissipated power.

Fig. 6.16 together with Tab. 6.6 define the components for ROB thermal simulations. The ROB is a FR4 PCB board with dimensions $196 \times 36 \times 1.6$ mm^3.

Device	Center, mm	Dimensions, mm^3	Power, W
VTTx	(31.5; 26.5)	$13 \times 13 \times 10$	1.0
VTRx	(31.5; 9.5)	$13 \times 13 \times 10$	0.65
GBTx	(61; 13)	$16 \times 16 \times 3$	1.4
GBTx	(83; 19)	$16 \times 16 \times 3$	1.2
GBTx	(105; 23)	$16 \times 16 \times 3$	1.2
SCA	(124; 25)	$10 \times 10 \times 2$	0.6
VR 1.5 V	(141.5; 26.6)	$11 \times 11 \times 2.5$	1.2

Table 6.6.: ROB component definitions.

The ROB assembly has to hold 10 read-out boards on 5 shelves. It is depicted in Fig. 6.17.

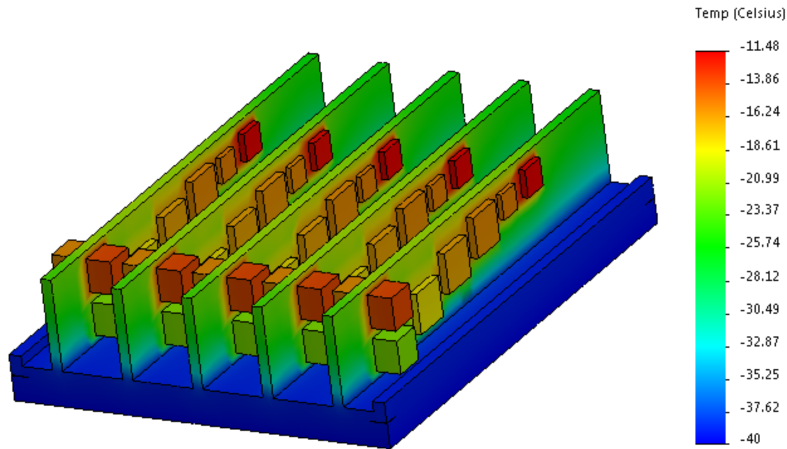

Figure 6.17.: ROB assembly to hold 10 boards on 1 mm thick shelves.

Configuration	Maximum temperature on the ROB box vs. simulated CO_2 temperature, ℃				
	-40	-30	-20	-10	0
1 mm	-11.48	-6.49	-1.49	3.49	8.723
2 mm	-16.16	-10.01	-3.85	2.31	8.63
3 mm	-18.2	-11.51	-4.81	1.87	8.62

Table 6.7.: FEM simulation results for a ROB assembly with various cooling plate temperature and shelve thickness.

Tab. 6.7 summarizes the FEM simulation results for ROB boxes of different shelve thickness and different cooling plate temperatures.

From the results obtained one can draw the conclusion that at the coolant temperature targeted for operation of the STS (-40 ℃) the smallest ROB box (with 1 mm shelf thickness) will be an adequate solution. The cooling power will be enough to avoid the heat dissipation into active volume of the STS detector.

6.3. Open CO_2 cooling system

6.3.1. Motivation

In order to verify the model calculations and the simulation results obtained in Finite Element Analysis (section 6.2) and find the optimal design of the cooling assembly experimentally, a series of experimental measurements was conducted. The main source of the discrepancies between simulations and measurements was expected to be observed due to boiling bi-phase CO_2 cooling regimes, which depend on the vapor quality and boiling phases.

From the initial requirements, that the STS detector will dissipate more than 40 kW of thermal power, the overall heat production was estimated to be 200 W and later, after separation of the FEB and ROB (Read Out Board), 140 W per cooling block. The aim of this study were absolute comparative measurements on the cooling efficiency when changing the shelf thickness. Due to the lack of space available for the cooling in the STS detector, the cooling assemblies should be as compact and as efficient as possible.

6.3.2. Cooling assembly

In order to estimate the cooling performance of the FEB boxes, which will be used in the STS detector, cooling assemblies with FEB box shelf thicknesses of 1 mm, 2 mm and 3 mm have been produced.

The cooling assembly shown in Fig. 6.18 consists of a cooling body (FEB box) with 10 mounted front-end board simulators and a cooling block.

The cooling bodies were built according to the CAD models used for the FEM simulations.

The cooling block shown in Fig. 6.18 is produced based on the design shown in Fig. 6.1. A 2.1 meter long 1.9 mm inner diameter and 2.5 mm outer diameter stainless tube was chosen based on the model calculations described in the section 6.1.5. The tube was casted into an aluminum block. The resulting dimensions of the produced cooling block are $65 \times 30 \times 105$ mm^3. To the input and output of the pipe 1/8 inch VCR female adapters were welded to provide the compatibility with the rest of the system's piping based on the imperial size VCR connectors. Thermal grease is used as an interface between the cooling block and the cooling body.

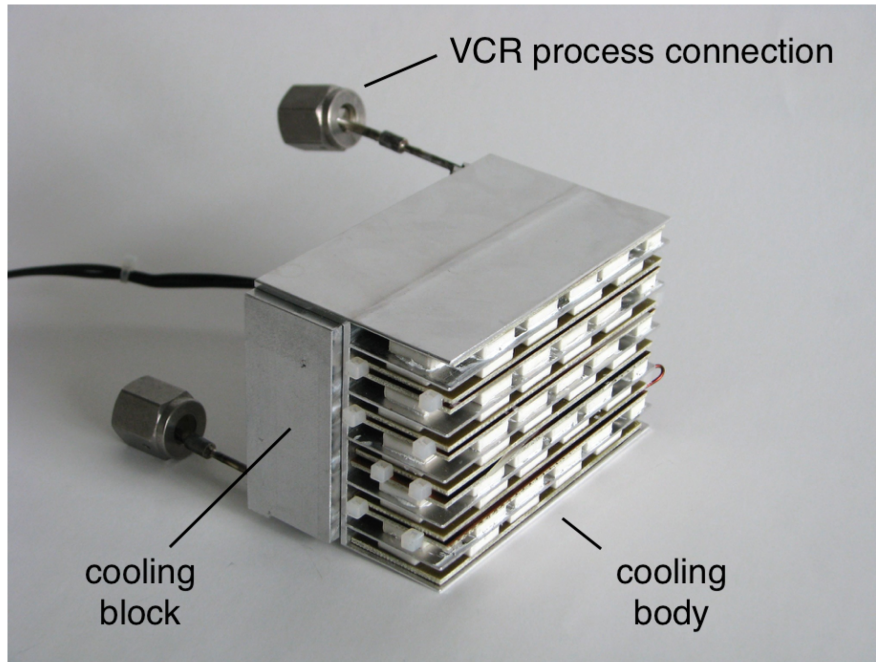

Figure 6.18.: The cooling assembly, consisting of a FEB box with front-end board simulators and a cooling block.

Fig. 6.19 shows the front-end board simulator boards used in this work. Each board consists of a PCB with 10 ceramic resistors connected in series. Each resistor produces up to 2 W of thermal power. The cooling assembly has 10 such boards, which are connected in series and mounted to the shelves.

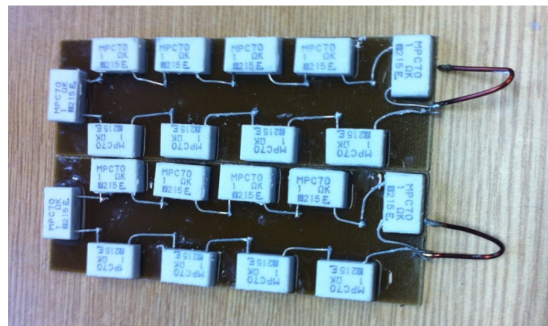

Figure 6.19.: A pair of front-end board simulators.

6.3.3. Cooling setup

In order to verify various cooling assembly designs, a bi-phase CO_2 cooling system was built. An open system was chosen due to its conceptual simplicity and the possibility to have it readily available for the tests before a closed-loop system will

be available in the future. Similar systems have also been built for the cooling tests of ATLAS [135], ALICE [136], BELLE II [137] and other experiments.

Fig. 6.20 and 6.21 show the thermodynamical process targeted by this system and the schematic of the open system designed, respectively.

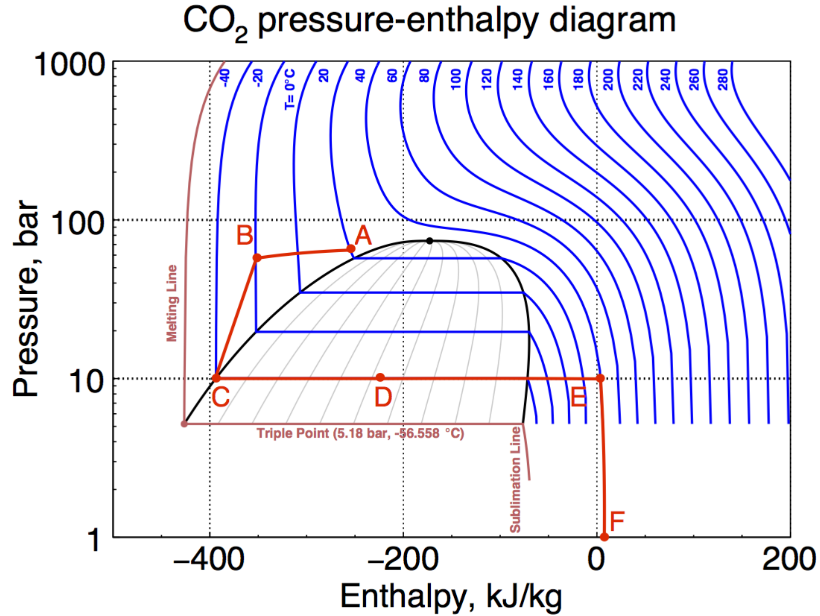

Figure 6.20.: The thermodynamical process targeted by the cooling system.

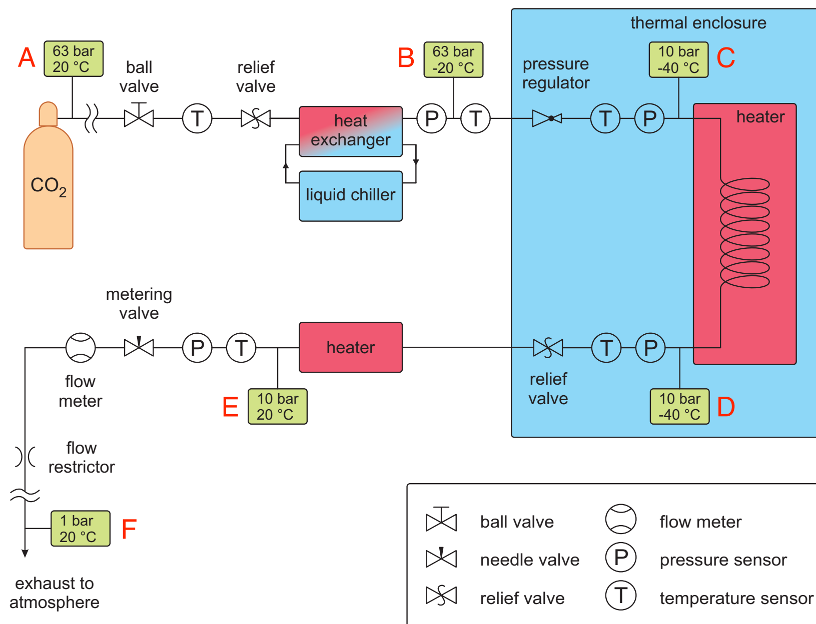

Figure 6.21.: A schematic of the open CO_2 cooling system.

Both diagrams show (denoted in red latin letters from A to F) the intermediate states of the carbon dioxide.

State A corresponds to the liquid state of CO_2 at 20 ℃ and 63 bar, stored in a bottle.

The transition A-B happens in a heat exchanger connected to the liquid chiller. In the state B the CO_2 is cooled down to -20 ℃ and is in supercooled liquid state.

At the B-C transition the supercooled CO_2 is expanded to the targeted cooling temperature of -40 ℃ and pressure of $\approx$ 10 bar. In the state C the CO_2 is on the phase transition border with the vapor quality of 0. This state is also called the saturated liquid state.

The transition C-D is the most important in this application. Here the saturated liquid CO_2 is fed into the cooling body. During the gradual phase transition under the same pressure (isobaric process) the ratio between liquid and vapor phase changes, thus the vapor quality increases. The vapor quality should not exceed the dryout inception (x_{di}) for the best cooling performance, as shown in section 6.1.5. The state D on the pressure-enthalpy diagram corresponds to a vapor quality of about 0.5. This state corresponds to the output of the cooling body. Though the rest of the liquid-vapor cooling mixture can be used for cooling purposes, this is not advisable. This leads to the change of CO_2 heat conductivity properties and the temperature gradients over the cooling body.

After exiting the cooling block, the mixed-phase carbon dioxide is evaporated completely and heated (transition D-E) back to 20 ℃. This is needed to make sure, that during further expansion to 1 bar at the atmosphere exhaust point (system output), no solid phase formation happens.

Transition E-F corresponds to the expansion of the fully gaseous CO_2 to 1 bar and its exhaust to the atmosphere.

6.3.3.1. Cooling setup equipment

The described above cooling setup uses a liquid CO_2 pressure bottle (63 bar at 20 ℃, state A in Figs. 6.20 and 6.21). The CO_2 bottle is stored in a safety cabinet in an adjacent laboratory room. The cooling system is connected to the bottle by a two-way ball valve.

The CO_2 flows (transition A-B) though a pre-cooling stage which brings it to -20 ℃. This stage consists of a Lauda RK-8 liquid chiller circulating the KRYO 40 heat transfer liquid, which is an aqueous solution of a carbon alkali salt containing inhibitors. The Lauda chiller is set to keep the coolant at -40 ℃, which flows through a custom made heat exchanger from Alfa-Laval®. After pre-cooling the liquid CO_2 is supplied to the cooling assembly.

The cooling assembly is housed in a thermally insulated volume (see Fig. 6.22). The photograph shows the interior of the thermal insulation enclosure. The cooling assembly with the temperature sensors attached to the cooling body's shelves

is shown. The cooling assembly and the relative humidity sensor are resting on a red PVC platform for mechanical stability. The central part of the figure shows the inlet and outlet of the cooling line with temperature and pressure sensors attached. Another red PVC plate at the bottom left of the figure hosts the feed-throughs for power, sensor cabling and cooling pipes. The enclosure is connected to N_2 bottle and is flushed by the gaseous nitrogen in order to reduce the relative humidity. The relative humidity inside the enclosure is measured by a Honeywell® sensing station (gray-black box on the top right of the photograph).

Figure 6.22.: The interior of the thermal insulation enclosure.

A pressure regulator is placed after the insulating box inlet and serves as an expansion valve. This pressure regulator assures that, independently from the input pressure, the output pressure of the medium will be set to a predefined value, in our case to 10 bar. Expanding the liquid CO_2 to the 10 bar brings it to the temperature of -40 ℃ at the phase boundary (state C), from whereon the latent heat of the medium can be utilized for cooling. Though the set points below -40 ℃ can be utilized, a safety span of roughly 5 bar pressure difference should be kept. This safety span allows to mitigate additional pressure drops along the system tubes, since the CO_2 pressure could reach the triple point (5.18 bar, -56.5 ℃). Beyond the triple point the phase of the carbon dioxide changes to solid, thus clogging the tubes. Thus the set point of 10 bar/-40 ℃ is chosen. At this state

the liquid CO_2 is supplied to the inner piping of the cooling assembly, depicted as a “heater” with a coiled line inside the thermal enclosure in the Fig. 6.21.

Upon leaving the thermal enclosure the mixed-phase CO_2 has to be evaporated fully in order to make the flow meter downstream detect the flow correctly. Additionally, if the CO_2 would not be evaporated fully, it would expand to the atmospheric pressure of 1 bar at the outlet leading to an undesired production of a solid CO_2, which could also lead to a clogging of the exhaust. The “heater” outside of the thermal enclosure is a thermal bath with 8 meter of stainless steel tubing wrapped into a spiraling helix submerged into a water thermal bath.

After the thermal bath a metering valve is placed which controls the overall CO_2 flow in the whole system. The flow is read-out by a Bronkhorst gas flow meter. The flow restrictor just before the exhaust controls the upper limit of the medium flow in the system. The CO_2 is finally safely exhausted to the atmosphere to prevent the asphyxiation risks.

It should be noted here, that every potentially closed volume of the system is equipped with a burst disk due to the risk of liquid trapping. The liquid trapping of the cold CO_2 is potentially dangerous, because the pressure within the closed volume can reach up to 720 bar when the CO_2 is warming up to the ambient temperature. The equipment is not designed to withstand this pressure which constitutes a safety hazard. To avoid the risk, the potentially closed volumes were protected with bust disks or, alternatively, relief valves, which open upon at a predefined pressure threshold. Also, one has to avoid valves which, upon switching, could trap the cold CO_2 liquid (see Fig. 6.23).

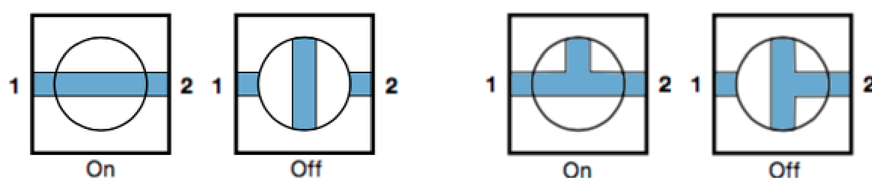

Figure 6.23.: The flow paths inside a valve: straight flow path with possibility of liquid trapping (left panel) and intrinsically safe flow path (right panel) [138].

The full list of equipment used for building the cooling setup is show in appendix F.

The setup piping is based on the Swagelok® VCR fittings. It is described in detail in appendix H. The summary of the Swagelok parts used is given in appendix I.

6.3.3.2. Cooling setup control and readout

To control the parameters of the cooling system and ensure the design properties of the CO_2 in different states of the cooling thermodynamical process, its temperature, pressure and flow should be measured and controlled.

Temperature sensors

Standard Class A pt100 temperature sensitive resistors were taken as a temperature sensors. The resistors were attached to the cooling pipes to measure the temperature of the carbon dioxide as it flows through the cooling system.

In order to ensure stable measurements and good thermal contact to the cooling pipe, a special copper block was designed and manufactured in the mechanical workshop. These blocks ensure the flat contact surface for the temperature sensors as opposed to line-like tangent contact between the tube and sensor. The sensors are glued with composite thermal glue WMK-10 to the copper blocks and additionally insulated with Armaflex® [139] insulation tape. Here the part of the sensor's wiring is insulated together with the sensor being in thermal contact with the material being measured to exclude the influence of the ambient environment to the measurements. Fig. 6.24 shows the copper block assembly used to measure the temperature on the cooling system piping section. Left panel shows the bottom part of the block with a cylindrical cut-out to accommodate the pipe. The right panel shows the assembled part. The screws ensure the tight thermal contact between the pipe and the block. Inside the cut-out a layer of thermal grease is applied which ensures that the micro-cavities of rough material surface will be filled and the thermal contact is optimal. The temperature sensors are glued on top of the block's surface and wrapped with insulation tape.

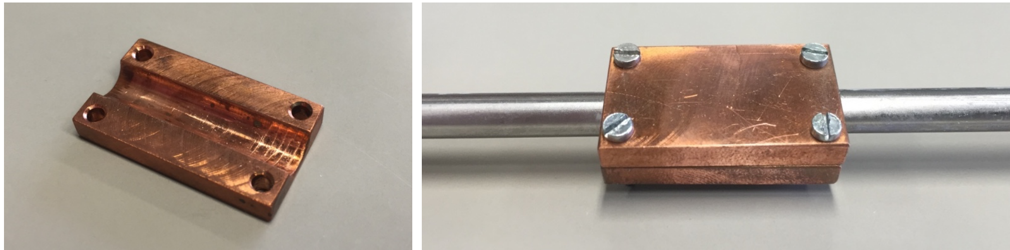

Figure 6.24.: Copper block assembly for on-tube temperature measurements.

Tab. 6.8 shows the summary for 8 temperature sensors controlling the tube temperatures and their corresponding states on the pressure-enthalpy diagram. The sensors T2, T3 and T6, T7 are placed in pairs to ensure that there are no additional temperature gradients present along the longest tube arms leading to and from the temperature enclosure.

In order to measure the temperature distribution on the cooling assembly further 8 temperature sensors are used. Fig. 6.25 and Tab. 6.9 show the sensor connection scheme and their positions on the cooling block, respectively.

The sensors are glued with a thermal glue to 1 mm thick copper plates. The copper plates have a thermal grease applied and are pressed against the shelves to ensure good heat conductivity. The sensors are insulated from other hot surfaces with an Armaflex insulating band.

Sensor	Diagram state	Position
T1	A	Before Alfa-Laval HX
T2	B	After Alfa-Laval HX
T3	B	Thermal enclosure inlet
T4	C	Cooling assembly inlet
T5	D	Cooling assembly outlet
T6	E	Thermal enclosure outlet
T7	E	Before heat bath
T8	F	Exhaust

Table 6.8.: Listing of the temperature sensors on the tubes with their positions.

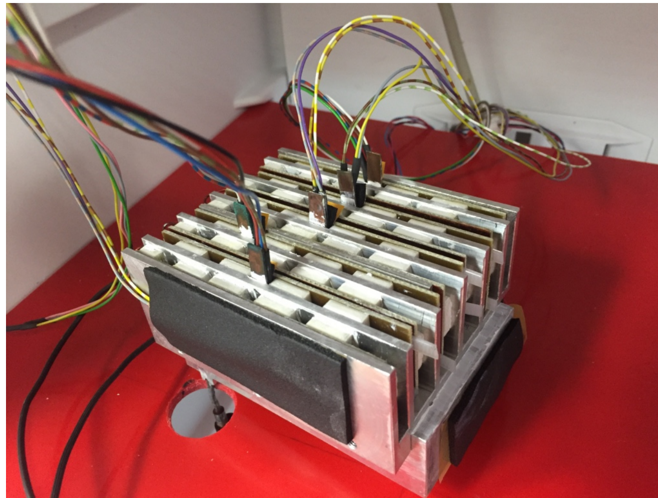

Figure 6.25.: A closeup picture of the cooling assembly with temperature sensors connected.

Sensor	Position
T9	Cooling block
T10	Cooling body outer shelf
T11-T15	Cooling body inner shelves
T16	Ambient

Table 6.9.: Listing of the temperature sensors on the cooling assembly with their positions.

An additional sensor T16 measures the ambient air temperature of the cooling assembly.

The temperature sensors are read out with an NI cDAQ-9188 chassis universal network read out device. The chassis is equipped with 4 NI-9217 RTD readout plug-in modules each reading out 4 individual pt100 sensors by 4-wire connection

scheme to cancel the voltage drop in the sensor wires and improve the reading precision compared to the 2-wire method.

In order to improve the measurement precision, the temperature sensors were calibrated against a reference sensor. The offsets of the calibration curves were extracted and corrected to (Fig. 6.26). The measurement error of these sensors, compared to the reference sensor, were estimated to be not larger than ± 0.1 ℃.

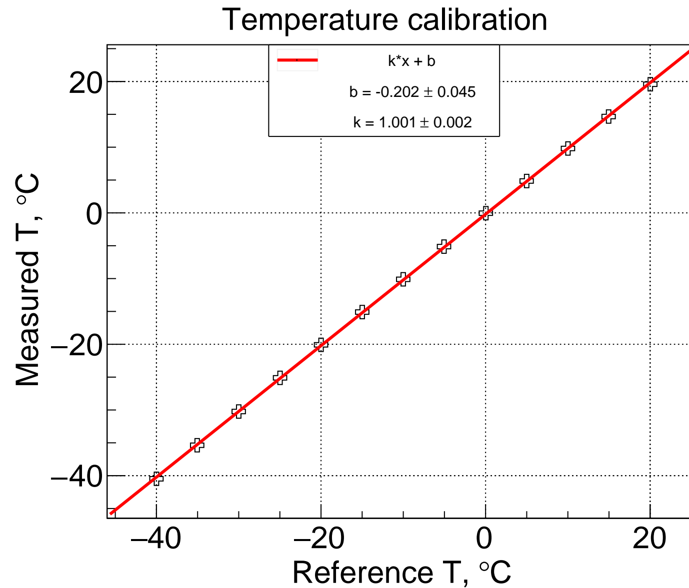

Figure 6.26.: Calibration curve for one of the temperature sensors.

Pressure sensors

The pressure sensors are used throughout the system to control the carbon dioxide pressure in the cooling system and ensure the right parameters of the thermodynamic cycle (see Fig. 6.20).

The pressure sensors used in this work are PTI-S-AG100 relative pressure transducers from Swagelok with a working pressure rating from 0 to 100 bar. They are mounted directly in the piping of the cooling system using a T-piece. One sensor is installed directly after the CO_2 bottle to control its pressure. Two sensors are installed at the inlet and outlet, respectively, of the cooling assembly. The inlet sensor controls the state C pressure, which is regulated by the expansion valve. The outlet sensor controls D and allows to measure the pressure drop in the tube of the cooling block. The last fourth sensor is installed before the exhaust of the system to control the pressure of the fully evaporated gaseous carbon dioxide as it is about to leave the system. The summary of the pressure sensor usage is given in Tab. 6.10.

Sensor	Diagram state	Position
P1	A	next to CO_2 bottle
P2	C	cooling assembly inlet
P3	D	cooling assembly inlet
P4	E	after heat bath

Table 6.10.: Listing of the pressure sensors with their positions.

The output of the pressure sensors is a signal from 0 to 10 V. They are read out with two NI USB-6009 multipurpose DAQ boards, which provide enough precision and speed for the current work's purposes. The sensors are powered by a 10 V direct current provided by the lab power supplies.

The pressure sensors come calibrated from the manufacturer. The additional correction was done to ensure the same offset reading for all the sensors. This base-line correction was done against a reference sensor.

Flow meter

The flow meter from the Bronkhorst® company is installed before the exhaust of the system. This position corresponds to the state F on the thermodynamic cycle as seen in Fig. 6.20). The flow meter together with the metering valve allow to control the amount of the carbon dioxide flowing through the system, thus the cooling power. It detects the volumetric flow in a range from 0 to 32 l_n/min which corresponds to a mass flow of 0 to 1 g/s.

The flow meter has its own integrated readout and control board and is physically connected to by the custom wired D-Sub DE-9 port. It is powered with 24 V direct current provided by the lab power supply.

The flow meter comes calibrated. However its output is defined in terms of the volumetric flow rate and is measured in l_n/min. Thus, for the best precision, it is important to ensure that the carbon dioxide flows through it at room temperature (20 ℃).

Liquid chiller

The liquid chiller together with the heat exchanger allow to pre-cool the CO_2 before expansion, while maintaining its liquid phase. We use the Lauda® RK-8 liquid chiller in this work. It circulates the KRYO 40 heat transfer liquid at temperatures down to -40 ℃. The circulation loop is interconnected with the cooling setup by a brazed plate heat exchanger. Together with the expansion valve the liquid chiller controls the set point of the cooling process.

The liquid chiller is read out and controlled by an RS232 interface. It allows to remotely read and set its various parameters, such as liquid temperature, thermal

cycling, etc.

Relative humidity control

The operation of the cooling setup at low CO_2 temperatures requires special care to be taken to prevent condensation on the cooling assembly. Thus, if the cooling set point is at -40 ℃ and the relative humidity has to be below 0.5% (at room temperature) for the dew point lower than -40 ℃.

During the measurements the thermal enclosure of the cooling system was flooded with dry nitrogen at a flow rate of 16 l_n/min. The nitrogen was supplied from the 200 bar bottle residing in the safety cabinet.

The relative humidity is measured with a Honeywell HIH-3602-C sensor placed near the cooling assembly. It comes calibrated and has a linear voltage output. The sensor is read out with a NI-6009 USB DAQ board. It is powered with 5 V direct current provided by a lab power supply.

A sample measurement of the relative humidity reduction was carried out to estimate the time to reach the minimum relative humidity and the dry nitrogen consumption. In this measurement the thermal enclosure was flooded with the dry nitrogen, replacing the air inside. The relative humidity saturates at the level of about 3% within about 1.5 hours as shown in Fig. 6.27.

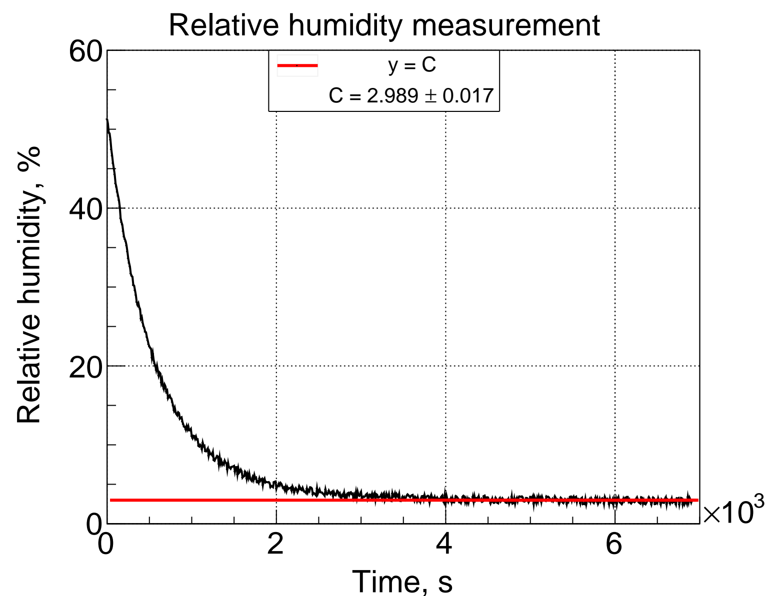

Figure 6.27.: Relative humidity dependence on the nitrogen flooding time.

The relative humidity below 3% was not achievable due to the low precision of the sensor at low temperatures. For the future measurements a high precision humidity meter will be used.

6.3.3.3. Control software

A very important part of the experimental setup are the readout and control software which aggregates all data taken from the sensors and other equipment, visualizes, processes and stores it for further analysis.

The control software is based on a data acquisition program written in LabVIEW 2013. It polls the last values read in parallel from all available external sensing devices every second. It sends the control actions to the controllable external devices, such as, for example, the Lauda liquid chiller bath.

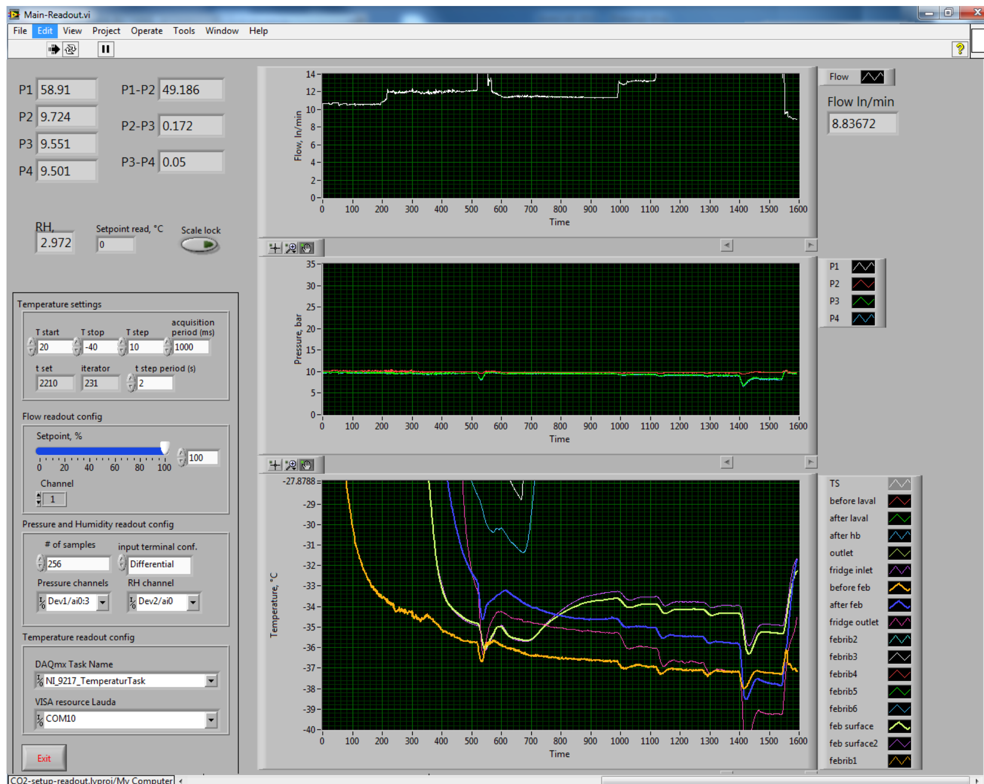

Figure 6.28.: The front panel of the setup control software.

Fig. 6.28 shows a screenshot of the readout and control program's front panel during the flow adjustment procedure. Here the acquisition parameters are set and data is aggregated and visualized. The graphs show time dependencies of (from top to bottom) the carbon dioxide volumetric flow, reading from pressure and temperature sensors. The Lauda liquid chiller could be configured from here to cycle through a set of predefined temperatures to change the input temperature of the CO_2 cooling process. The communication is done by exchanging messages with the device via a COM port. The data from other sensors is collected by NI DAQmx device drivers. Upon exiting the program, the measurement protocol in form of a comma separated values (CSV) file together with the obtained graphs is stored to disk for further analysis.

The sensor readings allow a precise adjustment of the system parameters, such as the Lauda liquid chiller set temperature, the pressure regulators output pressure, the heat bath temperature or medium mass flow. An example of wrongly tuned system parameters is shown in the Fig. 6.29. Here the heat load on the cooling FEB box simulator was low, the medium flow above normal and thermal bath temperature set to 30 ℃. In this regime the cooling process happening in the cooling assembly is either a liquid cooling, or a mixed-phase cooling with very low vapor quality, due to a low heat load and high coolant mass flux. Instead the main bi-phase cooling process appears to have "moved" downstream and happen in the thermal bath, where the bi-phase CO_2 is fully evaporated and most of the heat exchange happens. The large enthalpy of the CO_2 in the bi-phase regime is nicely visualized if the 30 ℃ warm water coexists with a thick layer of ice formed around the CO_2 line.

Figure 6.29.: Ice formation in the heat bath as a result of wrongly tuned system parameters.

The full list of the devices read out in the cooling system's control program and their characteristics is shown in appendix G.

6.3.4. FEB Box Measurement results

With the built cooling system, a lot of experimental measurements have been conducted, mainly to test the different front-end board box designs and the thermal interfaces applied to the components of the cooling assembly. Tab. 6.11 shows the summarized results obtained for a CO_2 temperature of -40 °C and different FEB box designs.

Heat Power Applied, W	Maximum Temperature, °C		
	1 mm	2 mm	3 mm
140	15	-14.2	-22.6
200	24	0.2	-15

Table 6.11.: Experimentally measured maximal temperature on the FEB box in dependence of power applied and shelf thickness

A further measurement was carried out to test the influence of the ambient environment on the measurement results. In this study the cooling assembly was additionally enclosed in the thermal enclosure made from 2 cm thick insulating foam plates (see Fig.6.30). The comparative measurements with and without the insulation allow to observe the influence of the convective and radiation heat losses.

Tab. 6.12 shows the obtained experimental results with the cooling assembly enclosed by additional foam thermal insulation.

Heat Power Applied, W	Maximum Temperature, °C		
	1 mm	2 mm	3 mm
140	19.1	-10.5	-20.1
200	30.4	5.7	-11.8

Table 6.12.: Experimentally measured maximal temperature on the FEB box in dependence of power applied and shelf thickness with the insulating box.

The results obtained show higher temperatures measured on the cooling assembly's shelves (see Tab. 6.11). This indicates, that the undesired radiative and convective heat losses to the ambiance play a role. This was taken into account in the further designs of the cooling bodies, where its top is additionally covered with an aluminum cover connected to the cooling plate. However, the full enclosure of the FEB boxes in the STS detector is not possible due to the cable connections.

Figure 6.30.: The Armaflex insulating foam enclosure around the cooling assembly to reduce the influence of the convective and radiation heat losses.

As a result of these experimental studies, the STS detector has adopted the 3 mm thick shelf FEB design. This allows the efficient heat removal from the heat producing elements with a safety margin.

6.4. Further experimental work with the cooling system

With the cooling system described above the absolute comparative measurements were conducted and the FEB box design was optimized. The cooling system is currently rebuild, preserving 80% of its components, into a water based cooling system. This allows to conduct further relative measurements of the thermal interfaces of the cooling assembly, for example, to test out the performance of different thermal greases, compounds and pads and determine the best thermal glue for the ASIC chips.

For the future studies, it is planned to build a more realistic cooling demonstrator. It will comprise a half unit cooling station with 6 FEB boxes attached

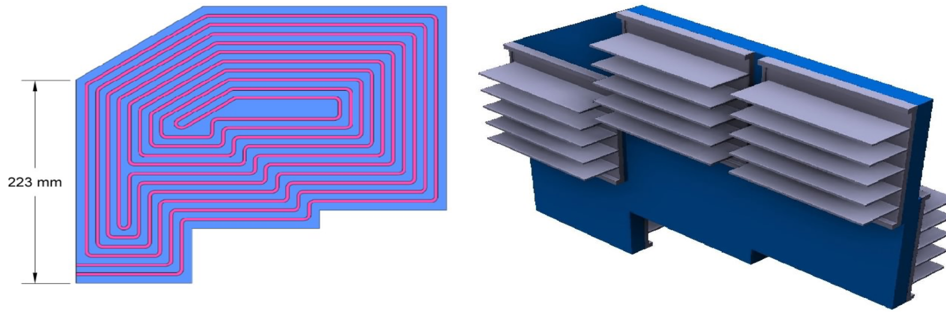

Figure 6.31.: The STS half unit cooling plate.

to the both sides of the cooling plate as illustrated in Fig. 6.31. The left panel of the figure shows the inner tubing of the plate and the path the carbon dioxide flows inside it. The right panel shows the conceptual design of the cooling plate with the front-end electronic boxes attached to it.

7. Conclusions and Outlook

7.1. Conclusions

To ensure the proper performance of the STS detector, its basic building blocks, silicon microstrip sensors, must be quality assured before assembly. During operation they have to be kept at a working temperature of about -5 ℃ at all times. For this purpose two research and development projects have been carried out in the framework of this thesis.

To qualify and control the quality of silicon microstrip sensors at different steps ranging from procurement to installation a number of optical quality assurance methods and procedures were developed. A flexible experimental setup to implement these methods and procedures was built at the University of Tübingen. It allows to scan along single sensors, collect and process images of different regions at various magnification factors. The application of a number of specialized machine vision algorithms allows to detect defects and other features of the object under investigation. These algorithms employ, e.g., image filtering and transformations, pattern and texture matching, edge detection and contour tracing. Machine learning and deep learning algorithms are applied to control the presence and integrity of important electrical elements of the sensor, the detection and classification of the defects, defect contexts, etc. The application of the machine learning algorithm allows to further improve the quality assurance. The information collected during the sensor scan and image analysis includes the detailed data on defects or other features. It is classified to decide on the sensor's overall quality.

The collected data is sent to the central database for long term storage as well as for later use, e.g. when analyzing the experimental data obtained with the sensors. The corresponding data storage schemes were developed within the FairDB framework. Various data storage technologies were analyzed and the usage of the GSI high performance computing clusters was proposed.

The setup has proven to be flexible and extensible as it was modified and adapted to check the quality of sensor microcables. The methods and procedures applied are mostly the same as those used to control the quality of silicon microstrip sensors with certain adaptations and modifications. It was recognized that, in order to improve the quality of the microcables, the developed methods have to be adopted on the microcable production site at LTU company located in Kharkov. The corresponding proposal was communicated to the company.

The developed metrology methods allow to characterize the geometrical pa-

rameters of the sensor such as its warp, thickness, cutting edge quality and parallelism, etc. The metrology methods were applied to measure the spatial positioning and orientation of the sensors on the ladders. The methods developed will be used at two detector assembly sites: at GSI, Darmstadt and JINR, Dubna. Another sensor quality assurance center in MSU, Moscow has expressed its interest to adopt the methods developed.

In order to find out the proper and optimal design of the cooling elements for the STS detectors cooling system, an equation of state and a thermodynamical model have been implemented to optimize the bi-phase cooling regimes and to find out the optimal diameter of the tubes and to predict the boiling phases of the carbon dioxide. After establishing the conceptual design of the cooling body, a number of finite element method simulations for the Front-End Board (FEB) and Read-Out Board (ROB) boxes were carried out. To verify the simulations of the FEB box, an open bi-phase CO_2 cooling system was built. It allowed to test different FEB boxes' designs and study the heat distributions on them at different heat loads and cooling powers applied.

7.2. Outlook and project continuation

The optical inspection setup allows to inspect silicon microstrip sensors of all sizes (up to 6×12 cm^2) and designs from the two manufacturers. The metrology and microscopy methods developed were so far applied only to the sensors on a ladder assembled at GSI, Darmstadt. It is subject to further investigation to apply them to the ladders produced at JINR, Dubna, where the assembly procedures are different from those at GSI.

Parts of the inspection algorithms have also been implemented in the electrical quality assurance setup built at University of Tübingen, among others, the pattern recognition for the system calibration and sensor warp measurements along the AC pad line.

The open CO_2 cooling system has shown to be a robust and simple, yet flexible system to utilize the bi-phase cooling principle. It is already in use for further research and development regarding the STS detector cooling. A 1 KW closed cycle cooling CO_2 plant will be used to test and measure the temperature distributions of a full cooling module for a half unit of the STS detector.

The thermodynamical models for the bi-phase CO_2 cooling implemented allow to calculate the cooling regimes for arbitrary cooling bodies. They will be used for the investigation of the bi-phase CO_2 cooling for the Micro-Vertex Detector of the CBM experiment.

7.3. 1 kW closed cooling system TRACI XL

In order to test the cooling demonstrator mentioned above, a prototype 1 kW closed loop bi-phase CO_2 cooling plant TRACI XL (Fig. 7.1), based on the TRACI multipurpose CO_2 [140], cooling system was built and is currently being commissioned at GSI. It utilizes the so-called 2PACL[1] principle developed for CERN LHCb's VELO (Vertex Locator) detector and also for the AMS (Alpha Magnetic Spectrometer) experiment located on the International Space Station. TRACI XL is a closed loop CO_2 circulation system combined with the compressor and accumulator, in which the partially evaporated CO_2 is reliquefied with the help of a chiller based on R404A as cooling agent.

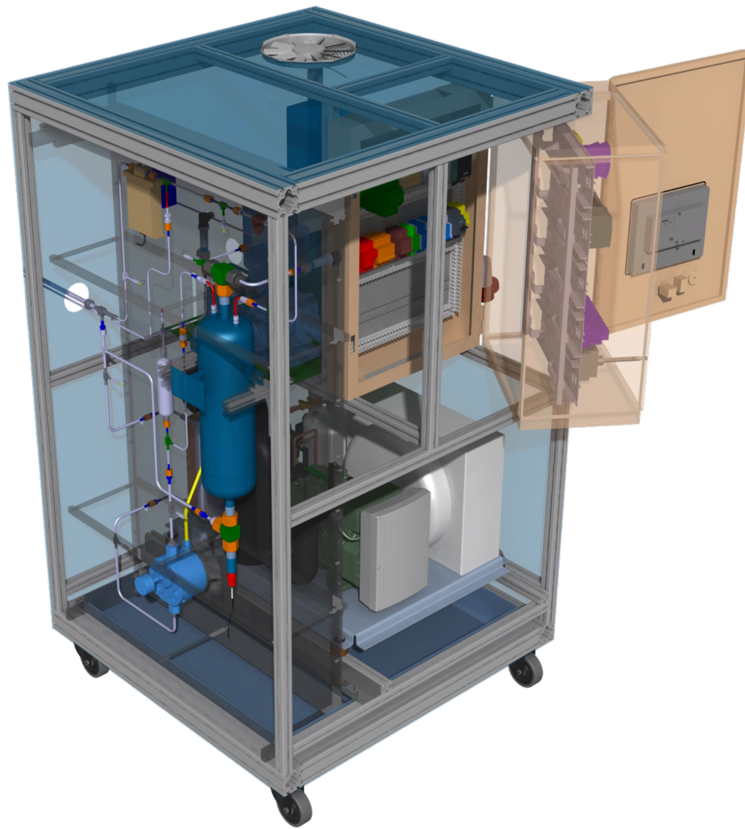

Figure 7.1.: The TRACI XL 1 kW cooling system [142].

Fig. 7.2 shows the thermodynamical cycle that carbon dioxide undergoes in the 2PACL system. The state *A* here is considered as the start point. Here the sub-cooled CO_2 is compressed (state *B*) and fed into the cooling distribution system (state *C*). It is then expanded back to the working pressure (state *D*) and fed to the cooling plate. The transition *D*-*E* corresponds to the cooling cycle

[1] 2-Phase Accumulator Controlled Loop [141]

in the heat exchanger. The mixed phase CO_2 is then reliquefied as shown in transition *E-F-A*.

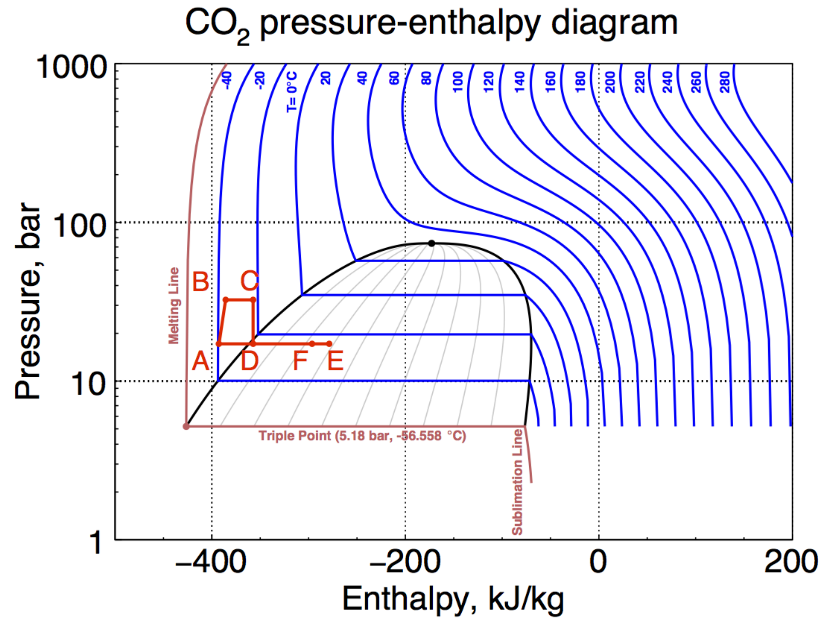

Figure 7.2.: The thermodynamical process corresponding to the closed loop cooling system [142].

The TRACI XL will be used to test the cooling efficiency of a 1 kW STS quarter station cooling plate demonstrator as described in the previous section. A demonstrator is shown in the Fig. 6.31.

Appendix A.

Optical setup hardware and equipment

Hardware	Manufacturer	Model	Characteristics
Microscope camera	Motic Europe S.L.U.	Moticam 5	5 MP CMOS C-ring connection
Servomotors	Faulhaber/ Movtec	SMC-300	Linear servomotors 190/70/70 mm XYZ movement range
Vacuum pump	Gebr. Becker GmbH	VT 4.4	150 mbar abs. underpressure
Zoom and Focus	Navitar	1-52002	Motorized 3 mm Fine Focus with ∅15 mm coaxial direct light connection
Direct light source	Starlight	Roma LED3-PC	590 lm, 5700 K
Ring light source	Starlight	RL-12 series	4 zone source, controllable brightness
Vacuum Chuck 3 zones	Custom made		12.2×12.2 cm^2
Energy management	Energenie	EG-PM2 USB	4 controllable power sockets for light and vacuum bypass control
Mounting Frame	item Industrietechnik GmbH	Profil 6 60×60 leicht	60×60 mm^2

Table A.1.: Optical setup hardware and equipment.

Appendix B.

Neural networks architecture

The description and usage of the neural networks is given in the section 5.4.6.3.

Tab. B.1 shows the neural network architecture used for the defect context detection.

The convolutional and pooling layers were described previously.

The routing layers provide the possibility to pass through and account for the fine grain features from the layer 16 (512 x 3 x 3) to the latest convolution layers of the network [86].

The reorganization layers allow to match the dimensions of the routed layers to those of the latest convolution layers by resizing them accordingly [86].

The global average pooling is described in [143]. It allows to substitute the fully connected layers, thought to be prone to overfitting, with the layer computing the average of each feature map, which provides the input for the softmax layer.

Id	Layer Type	Number of filters	Filter size/ stride	Input dimensions	Output dimensions
0	Convolutional	32	3 x 3 / 1	448 x 448 x 3	448 x 448 x 32
1	Max. pooling		2 x 2 / 2	448 x 448 x 32	224 x 224 x 32
2	Convolutional	64	3 x 3 / 1	224 x 224 x 32	224 x 224 x 64
3	Max. pooling		2 x 2 / 2	224 x 224 x 64	112 x 112 x 64
4	Convolutional	128	3 x 3 / 1	112 x 112 x 64	112 x 112 x 128
5	Convolutional	64	1 x 1 / 1	112 x 112 x 128	112 x 112 x 64
6	Convolutional	128	3 x 3 / 1	112 x 112 x 64	112 x 112 x 128
7	Max. pooling		2 x 2 / 2	112 x 112 x 128	56 x 56 x 128
8	Convolutional	256	3 x 3 / 1	56 x 56 x 128	56 x 56 x 256
9	Convolutional	128	1 x 1 / 1	56 x 56 x 256	56 x 56 x 128
10	Convolutional	256	3 x 3 / 1	56 x 56 x 128	56 x 56 x 256
11	Max. pooling		2 x 2 / 2	56 x 56 x 256	28 x 28 x 256
12	Convolutional	512	3 x 3 / 1	28 x 28 x 256	28 x 28 x 512
13	Convolutional	256	1 x 1 / 1	28 x 28 x 512	28 x 28 x 256
14	Convolutional	512	3 x 3 / 1	28 x 28 x 256	28 x 28 x 512
15	Convolutional	256	1 x 1 / 1	28 x 28 x 512	28 x 28 x 256
16	Convolutional	512	3 x 3 / 1	28 x 28 x 256	28 x 28 x 512
17	Max. pooling		2 x 2 / 2	28 x 28 x 512	14 x 14 x 512
18	Convolutional	1024	3 x 3 / 1	14 x 14 x 512	14 x 14 x1024
19	Convolutional	512	1 x 1 / 1	14 x 14 x1024	14 x 14 x 512
20	Convolutional	1024	3 x 3 / 1	14 x 14 x 512	14 x 14 x1024
21	Convolutional	512	1 x 1 / 1	14 x 14 x1024	14 x 14 x 512
22	Convolutional	1024	3 x 3 / 1	14 x 14 x 512	14 x 14 x1024
23	Convolutional	1024	3 x 3 / 1	14 x 14 x1024	14 x 14 x1024
24	Convolutional	1024	3 x 3 / 1	14 x 14 x1024	14 x 14 x1024
25	Routing	16			
26	Reorganization		/ 2	28 x 28 x 512	14 x 14 x 2048
27	Routing	26	24		
28	Convolutional	1024	3 x 3 / 1	14 x 14 x 3072	14 x 14 x1024
29	Convolutional	35	1 x 1 / 1	14 x 14 x 1024	14 x 14 x 45
30	Global average pooling		Global		45
31	Softmax classification				Object class probability

Table B.1.: Architecture of the convolutional neural network used in this work for the defect context detection.

Appendix C.

Sensor warp data

Sensor Id	p-side, μm	n-side, μm
CBM01B1-PDTF02	14	19
CBM05CBaby-bb1.ptbs	13	5
CBM05CBaby-bb3.ptds	11	8
CBM05CBaby-bb4.pobn	16	9
CBM05CBaby-bb5.am4ta	11	8
CBM03C6-302193-18	35	37
CBM06C6-331827-3-SM	19	34
CBM06C6-331827-18-SM	18	18
CBM06C6-331827-22-SM	24	17
CBM06C6-350191-04	78	68
CBM06C2-350714-06-1	50	26
CBM06C2-350714-18-2	51	31
CBM06C2-350714-22-2	45	25
CBM06C4-351135-08	48	47
CBM06C4-351135-09	61	46
CBM06C4-351135-23	71	63
CBM06C6-353090-11	78	73
CBM06H4-S10938-1609-5	44	27
CBM06H6-S10938-2695-2-SM	27	29
CBM06H6-S10938-4440-58	56	38
CBM06H6-S10938-4440-60	54	46
CBM06H2-S10938-4723-001-3	43	31
CBM06H2-S10938-4723-001-7	44	33
CBM06H12-S10938-4723-1-001	52	56

Table C.1.: Maximum value of the sensor warp measured on both p- and n-sides of the prototype sensors.

Appendix D.

Sensor thickness measured with the autofocusing approach

Sensor Id	Thickness, µm	Error, µm
302193-18	279.9	2.3
322312-18	270.1	2.4
331827-3-SM	286.9	2.8
331827-18-SM	291.5	2.5
331827-22-SM	299.6	2.6
350191-04	288.6	2.7
350714-06-1	279.1	2.5
350714-18-2	284.8	2.6
350714-22-2	267.7	2.6
351135-08	274.3	2.4
351135-09	274.4	2.3
351135-23	288.5	2.6
353090-08	306.3	3.0
353090-09	305.9	3.1
353090-10	305.3	2.5
353090-11	305.7	2.5
353090-12	303.8	3.1

Table D.1.: Sensor thickness measured for CiS produced sensors. Nominal thickness is 285 ± 15 µm.

Sensor Id	Thickness, μm	Error, μm
2695-2-SM	319.5	2.2
4440-58	320.9	2.2
4440-60	317.9	2.1
4723-3	321.0	2.3
4723-7	329.2	2.1
4723-1	315.4	2.2

Table D.2.: Sensor thickness measured for Hamamatsu produced sensors. Nominal thickness is 320 ± 15 μm.

Appendix E.

FEM Simulated materials

Assembly part	Material	Heat conductivity, W/m·K	Thickness if applicable, mm
Cooling plate	Aluminum Alloy1060	200	
Cooling body	Aluminum Alloy1060	200	
Interface between plate&body	Thermal grease	0.8	0.1
Interface between shelve and others	Thermal grease	0.8	0.03
PCB	FR4	0.29	1.5
Thermal interface to PCB	AlN ceramic	285	0.5
ASIC chips	Silicon-like material	100	0.5
Thermal glue	WMK-10	10	0.03
Insulation layer	Kapton	0.12	0.025

Table E.1.: Thermal properties of the materials used in FEM simulations.

Appendix F.

Cooling system equipment

Hardware	Manufacturer	Model	Characteristics
Liquid Chiller	Lauda	RK-8 CS	KRYO-40 -50..150 °C
Heat Exchanger	Alfa-Laval	AXP10-10H-F	Custom made brazed plate
Ceramic Resistors	Fukushima Futaba	MPC70	1 Ohm, 2 W
Temperature sensors	otom Group	Class A pt100	100 Ohm at 0 °C
Pressure sensors	Swagelok	PTI-S-AG100-32AO-Y	Metal thin-film sensor, 0..100 bar
Gas flow meter	Bronkhorst	F-111AC-50K-ABD-88-V	0..32 l_n/min, up to 100 bar
RH Sensor	Honeywell	HIH-3602-C	0..100%, non-condensing
DAQ Chassis	National Instruments	cDAQ-9188	8 slot chassis, LAN
Temperature Readout	National Instruments	NI-9217	RTD readout plug-in modules
DAQ board	National Instruments	NI USB-6009	14-bit 48 kS/s
Energy management	Energenie	EG-PMS2 LAN	4 controllable power sockets

Table F.1.: List of equipment used in the cooling system and their characteristics.

Appendix G.

List of devices read out by the cooling system's control software

Device	Read-out by	Communication
Pressure sensors	2x NI-6009 USB	NI DAQmx
RH sensor	NI-6009 USB	NI DAQmx
Temperature sensors	4x NI-9217	NI DAQmx
Liquid chiller	Own read-out board	RS232 interface
Gas flow meter	Own read-out board	MS DDE, RS232
Energy management	Custom LabVIEW driver	LAN HTTP client/server

Table G.1.: Equipment read out and/or controlled by the acquisition software

Appendix H.

Cooling system piping and process connections

Firstly, it has to be mentioned that a CO_2 bottle contains liquid in equilibrium with the vapor phases of carbon dioxide. The liquid to vapor proportion changes with medium usage. In order to ensure that only the liquid phase is supplied to the system, a special vessel with a rising pipe has to be used. To mitigate the stiffness of the connection and simplify the replacement of the bottles a flexible braided metal hose is used as an interface between the bottle outlet and the system inlet. This interface uses the 6 mm Swagelok fittings, whereas the cooling system uses as a standard 1/4 inch VCR type connection. To mitigate this problem, a special 6 mm fitting to 1/4 inch VCR adapter was created in the mechanical workshop.

Fig. H.1 shows the Swagelok tube fittings. A typical fitting consists of a pair of fitting ferrules which are pressed against the fitting body with a female nut with the advantage of no torque being transmitted to tubing during installation. The front ferrule creates a seal against the fitting body and on the tubing outside diameter. The back ferrule, as the nut is turned, axially advances the front ferrule and radially applies an effective tube grip. The tube is being deformed in the process, as seen on the right panel of the figure, and the ferrule assembly remains on the tube end. This type of connection applies well in cases when no reassembly is required, as every reassembly iteration tends to make the connection more prone to the leaks. To restore the connection quality the only option would be to cut the end of the tube, where the ferrule assembly located and reintroduce it back. The disadvantage here is clear — the piping should be accustomed to the new piping dimensions, which is not always available.

When designing modular systems such as one being described, the usage of reusable connections is preferred. The Swagelok VCR (Vacuum Coupling Radiation) face seal fittings allow such flexibility buy using the expendable metal gaskets. When tightening the nuts, the gland receive an axial motion towards each other squishing the gasket and effectively sealing the connection. Despite its name it is not purpose-made for vacuum applications, the pressure ratings span from vacuum to the pressure of 771 bar according to specification. Fig. H.2 shows the typical VCR type connection assembly.

The interface from cooling assembly to the rest of the system with 1/4 inch

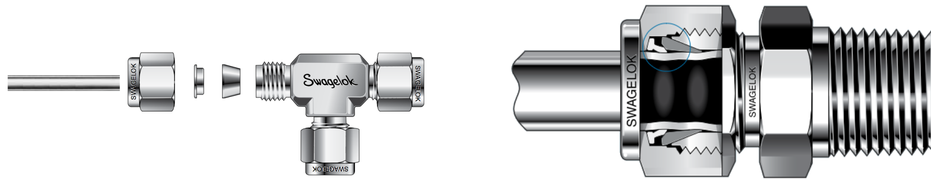

Figure H.1.: Swagelok gaugeable tube fittings. Left panel shows the constituent components of a fitting. Right panel shows the assembled and swaged fitting in place [138].

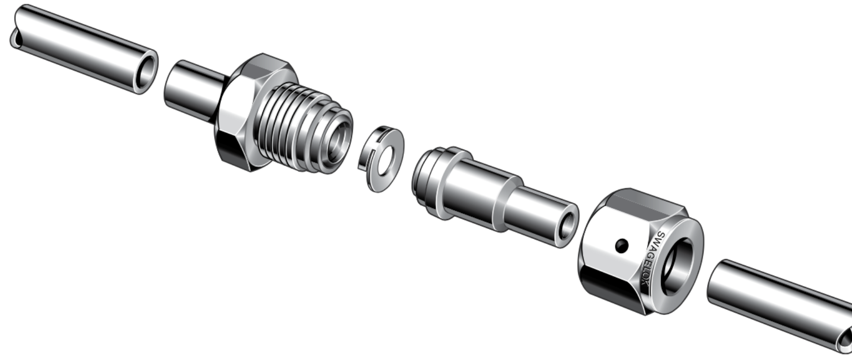

Figure H.2.: VCR metal gasket connection featuring from left to right: input piping branch to be butt welded to the VCR type gland with the male nut placed on it, a metal gasket (here with retainer), another gland with a female nut to be welded to the output piping branch [138].

piping has been realized by a custom made adapters. These adapters feature the combination of socket and butt welded piping from 2.5 mm OD pipe cast in aluminum and 1/8 to 1/4 inch adapter gland.

To allow usage of other components with the NPT[1] process connection type (for example the Swagelok PTI-S-AG100 pressure sensors) the male and female 1/4 inch NPT to 1/4 inch VCR adapters were used. The teflon tape wrapped on the threads ensures the leak tightness when connecting the male NPT threads to their adapters.

[1] American National Standard Taper Pipe Thread. The thread has a conical form with a 60° included angle with flattened peaks and valleys.

Appendix I.

Swagelok parts for cooling system

Part number	Description	Properties
SS4-GUF-4	Needle valve	
PTI-S-AG100-32AO-Y	Pressure sensor	Thin metal film sensor 0-100 bar rating, 0-10 V dc, 1/4 in. male NPT
SS-T4-S-035-6ME	Stainless steel tube	1/4" OD, 0.18 ID, up to 350 bar
SS-4-VCR-1	Female nut	
SS-4-VCR-2	Gasket	
SS-4-VCR-3	Socket weld gland	
SS-4-VCR-4	Male nut	
SS-RTM4-F4-1	burst disk	
SS-4-VCR-7-4	VCR male to NPT female adapter	
SS-43GHLVCR4	2-way ball valve	HL flow path to avoid liquid trapping
KPR1GLA411A20000	Pressure regulator	Control range 0..17.2 bar, max inlet pressure 68.9 bar

Table I.1.: Swagelok parts for cooling system

List of Figures

1.1. 3-dimensional representation of the QCD phase diagram at high net-baryonic μ_B and moderate isospin μ_I densities. Different phases of the nuclear matter and critical end points (CEP) are shown [4]. . . . 7

2.1. A conceptual view of the FAIR facility [10]. 9
2.2. The CBM experimental setup including, from left to right, Dipole Magnet, MVD, STS, RICH, MUCH, TRD, TOF, ECAL and PSD detector systems [11]. 10
2.3. A comparison of interaction rates and center of mass collision energies of high energy physics experiments [19]. 13
2.4. Particle yields depending on the collision energy for central Au+Au and Pb+Pb collisions [23]. 13
2.5. Net baryon density evolution of the fireball at 5 (left panel) and 10 (right panel) AGeV [19]. 14
2.6. Evolution of the excitation energy density and net-baryon density of a fireball. The step between data points is 1 fm/c [19]. 14
2.7. The difference in elliptic flow v_2 of particles and antiparticles as a function of the collision energy for the 10%-40% central Au+Au collisions measured by the STAR collaboration [19]. 15
2.8. The excess kurtosis times variance ($k\sigma^2$) of the proton, antiproton and net-proton distributions for most central Au+Au collisions as a function of collision energy measured at RHIC [26]. 16
2.9. Invariant-mass spectra of electron-positron pairs radiated in central Au+Au collision at 20 AGeV. Color coded are the contributions from different underlying decay processes [19, 29]. 17
2.10. The yields of hypernuclei depending on the collision energy for 10^6 central Au+Au collisions calculated with thermal model [30]. 18

3.1. View of the STS detector without thermal enclosure and services [33]. 19
3.2. Layout of the silicon sensors from CiS (left panel) and Hamamatsu (right panel) in the corner region, n side. Legend: 1) Alignment mark 2) Guard ring 3) Strip numbering panel 4) Polysilicon bias resistor 5) DC pad 6) Bias ring pad 7) AC pad 8) Aluminum read-out strip. . . 21
3.3. The diagram of the STS detector production from procurement to the assembly [36]. 22
3.4. A barcode and QR code to identify the sensor. 23

3.5. Silicon microstrip cross section. The ionizing particle traversing the silicon bulk creates the electron-hole pairs which are drifting in the electrical field to the respective sensor side [36]. 23
3.6. A sketch of the Frenkel pair creation mechanism. 25
3.7. Displacement damage functions normalized to 95 MeV · mb for neutrons, protons, pions and electrons. The inset displays a zoomed part of the figure [44]. 26
3.8. Deterioration of charge collection efficiency with increasing particle fluence [45]. 26
3.9. Increase of inverse trapping time with fluence (top panel) and time (bottom panel) [44]. 27
3.10. Change of detector depletion voltage and effective charge carrier concentration with respect to fluence (top panel) and annealing time (bottom panel) [44]. 29
3.11. Change of detector leakage current with fluence (top panel) and damage parameter with annealing time (bottom panel) [44]. 30

4.1. The I-V (top panel) and C-V (bottom panel) characteristics of the prototype sensors measured during the electrical characterization at the University of Tübingen [50, 51]. 34
4.2. The results of a per strip pinhole test for a prototype sensor [51]. . . 35
4.3. Total cable capacitance distribution measured for a prototype microcable stack [51]. 36

5.1. Setup for the optical QA consisting of an XY-table and a microscope system. 38
5.2. The rotation correction of an image taken from misaligned sensor. The left panel shows the source image, the right panel shows the corrected image rotated by about 2.5 degrees clockwise. 39
5.3. The color adjustment principle of an image taken with a wrong exposure value of the camera, here overexposed. The source image (left panel) is adjusted for its brightness and contrast yielding sharper edges and more saturated colors (right panel). 40
5.4. The use of the Color Operator tool illustrated. The AC pads on the source image (left panel) are detected and overlaid with the per-pixel addition (right panel). 41
5.5. An overview of different color planes extracted. Image is taken in the corner region of the CBM06C6-353090-11 prototype sensor. 41
5.6. An overview of different image filters applied to a source grayscale image. 43
5.7. An overview of different edge detection algorithms. 43
5.8. An alignment mark detected on the corner of the prototype sensor from CiS (left panel) with a template (right panel). 44

5.9. Source image with a defect on a texture (larger panel) and calculated Haralick features, as seen in the Texture training interface of NI Vision. The features extracted are (from top to bottom, from left to right) dissimilarity, contrast, homogeneity, correlation, entropy. . . . 45
5.10. A scratch defect detected with the texture matching algorithm. . . . 46
5.11. Example of the color thresholding for gray objects. 46
5.12. Example of the binary morphology algorithms applied in series. . . . 47
5.13. Detection of the scratched pads. 48
5.14. An overview of the image lens distortions. The panels show the source image, barrel, pincushion and mustache(a combination of barrel and pincushion) distortions. 49
5.15. An example of a dot array calibration plate. 50
5.16. Correction for the barrel distortions of the image. The errors are scaled by a factor of 45 for presentation purposes. 51
5.17. Example of the Niblack correction for the bright field distortion. . . 52
5.18. Principles of the correction for the flat field distortions. The images are downsampled artificially for the presentation purposes. This allows to illustrate the unevenness of the light spot. The left panel shows the source image of the background with the light spot from the coaxial lighting visible. The middle panel shows the thresholded image. The right panel shows the corrected image. 53
5.19. The autofocus values measured for different object heights. 53
5.20. A close-up image of the reference calibration cross used for various measurements in the zoom calibration. 54
5.21. The dependence of the camera exposure time on the zoom value extracted from the calibration. 55
5.22. The close-up visualization for the parcentricity discrepancy measurement. The center of an acquired image is denoted by a white dashed line. The distances are measured to the fitted edges of the cross. . . 56
5.23. Parcentricity deviation in X and Y directions measured in pixels (top left and top right panels, repsectively) and absolute distance deviation measured in micrometers (bottom panel)). 56
5.24. The dependence of the Z-stage position of a linear motor stage on zoom value extracted from the calibration. It provides the means of parfocality corrections. 58
5.25. A closeup of the calibration cross with its edges fitted to extract the object horizontal and vertical size. 58
5.26. Dependence of the optical system's magnification power (left panel) and observed 100 μm wide object width (right panel) on the zoom value. 59
5.27. The dependence of the projected field of view on the zoom value extracted from the calibration. 60

5.28. The dependence of the optical system's depth of field on the zoom magnification power (left panel) and the zoom value (right panel). . 61
5.29. The dependencies of Lorentzian distribution amplitude on the focus motor stage observed at minimal (left panel) and maximal (right panel) magnification power of the optical system. Solid red line denotes the Lorentzian fit, dashed blue line denotes the Gaussian fit. . 61
5.30. The dependence of the Lorentzian distribution's parameters half width at half maximum and amplitude on the zoom value extracted from the calibration. 62
5.31. The dependence of the Lorentzian distribution's parameters half width at half maximum and amplitude on the optical system's depth of field extracted from the calibration. 62
5.32. Estimation of motor stage positioning repeatability by measuring the actual arrival position vs targeted position. 64
5.33. Error vector field. The errors are scaled by a factor of 1000. 65
5.34. Sensor misalignment calibration principle. Black rectangle denotes the motor coordinate space, blue rectangle denotes the sensor coordinate space. The initial search for the alignment mark is denoted by the dashed purple line. Further scan over four corner alignment marks is denoted by the red arrows. 67
5.35. Sensor scan movement pattern scheme. Black rectangle denotes the motor coordinate space, blue rectangle denotes the sensor coordinate space. The actual surface scan is done in the sensor coordinate space. Scan movement pattern is denoted by the red arrows. 68
5.36. Detection example of a dust particle covering a large area and 4 strips on a p side of a prototype sensor. The left panel shows the source image, the right panel shows the detected defect. 69
5.37. Detection example of a scratch traversing many strips on an n side of a prototype sensor. The left panel shows the source image. The right panel shows the scratch defect detected. 70
5.38. Detection example of a metal break region on a prototype sensor. Left panel shows the source image, right panel shows the processed image with edges detected, edge numbering is suppressed. 71
5.39. Detection example of a metal short between two strips of a CMS-OB2 silicon strip sensor used in the LHCb experiment. The left panel shows the source image. The right panel shows the detected defect. . 72
5.40. Detection example of a metal short caused by a discharge. Left panel shows the source image. Right panel shows the defect detected by edge detection algorithms. 72
5.41. Detection example of second metal line defects for CiS (top panels) and Hamamatsu (bottom panels) sensors. Left panels show the source images, right panels show the defects detected and overlaid. 73

5.42. Detection example of the implant strip break. Left panel shows source image, right panel shows the detected defect. 74
5.43. Strip coupling capacitance measured during the electrical inspection. Low value measured for the strip 58 indicates the defect. Data measured by I. Panasenko [79]. 74
5.44. Detection example of the implant opening defect type. 75
5.45. A close-up photograph of the p-stop implantation defect. 76
5.46. Interstrip capacitance (left panel) and strip leakage current (right panel) characteristics measured in the defective region. The deviation from the average values indicate the presence of a defect. Data measured by I. Panasenko [79]. 76
5.47. A simplified sketch of a cross section of a CiS sensor. Left panel shows the non-defective layer configuration, right panel shows the defect of a Si_3N_4 dielectric deposition. 77
5.48. Detection example of a dielectric defect on an n-side of a prototype 6.2×4.2 cm^2 sensor from CiS. Left panel shows the source image, right panel shows the processed image with the edges detected, edge numbering is suppressed. 77
5.49. Detection example of an implant opening defect over the bias ring (top row) and near the edge of a sensor (bottom row). Left panels show the source images of the defects. Middle panels show the defect detected with contour tracing. Right panels show the defect detected with color thresholding. 78
5.50. Detection example of a passivation layer opening due to manufacturing process faults. The left panel shows the source image. The right panel shows the defects detected. 79
5.51. Detection example of a passivation layer opening due to its degradation found on the n-side of a prototype sensor from CiS. The left panel shows the source image. The right panel shows the defects detected. 80
5.52. Detection example of sensor surface chips found on prototype Hamamatsu sensors. Left panels show the source image, right panels show the defects detected. 80
5.53. The electrical element integrity principle based on the pattern matching. The defective elements are not detected here due to the high, thus strict, matching score threshold. 82
5.54. The sketches of the edge region of the CiS (left panel) and Hamamatsu (right panel) sensors. 83
5.55. Detection example of the deeply scratched guard ring of a CiS sensor (top panels) and a foreign object laying over bias and guard ring of a Hamamatsu sensor (bottom panels), potentially shortening them. . . 84
5.56. A simplified sketch of the neural network architectures used in this work. 85

5.57. Activation functions used for data propagation between the neural network layers. The sigmoid (a), hyperbolic tangent (b), rectified linear unit (c) and parametrized rectified linear unit (d) functions are shown. This work uses the PReLU activations between convolution layers. 86
5.58. A sketch of the maximum pooling principle. Left panel shows the source image. Middle and right panels show the result of a pooling filter with a size of 2×2 and stride of 1 and 2, respectively. 87
5.59. Different metrics used to estimate the performance of the region proposal networks: precision (left panel), recall (middle panel) and intersection over union (IOU, right panel). 88
5.60. Training progress illustrated in terms of training loss (left panel) and intersection over union (right panel). 89
5.61. Different contexts of the sensor identified with a neural network. . . 90
5.62. The dust particles and scratches identified with a neural network. . . 90
5.63. Summary for the sensor quality inspected. The sensor quality score and grade range from lowest (0, D) to highest (4, A), respectively. . 91
5.64. The object height measurement principle by adjusting the focus of the system in a calibrated fashion (middle panel) or by adjusting the vertical position of the optical system (right panel). Optical tube CAD drawing used here is taken from [91]. 92
5.65. Image frequency response vs. motor step. 94
5.66. An instant cut of the autofocusing process at 3 different motor positions, corresponding to non-focused image (top row), more focused image (middle row) and fully focused image (bottom row). 94
5.67. The results of the autofocusing method characterization — the autofocus value measured (left panel), the fit errors (right panel) and the single measurement time (bottom panel) depending on the motor step size. 95
5.68. Image frequency response vs. motor step for an approach parameter value of 2. 96
5.69. The results of the adaptive method characterization — the autofocus value measured (left panel), the fit errors (right panel) and the single measurement time (bottom panel) depending on the approach parameter. 97
5.70. Method comparison for the stepping and adaptive approaches in terms of fit errors (left panel) and measurement times (right panel). 98
5.71. Log-log dependence of single measurement time vs. approach parameter value. 99
5.72. Height profile of a most central 7×7 cm region of the vacuum chuck obtained with autofocusing method to measure object heights. The left panel shows uncorrected map. The right panel shows the corrected one. 99

5.73. The warp of the prototype 6×4 cm^2 sensor measured without and with vacuum supplied to the chuck. The maximum warp value measured without vacuum is 44 μm and with vacuum applied 19μm. 100
5.74. Summary of a measured warp of the n side of the prototype sensors available. 100
5.75. Sensor warp measured for a prototype silicon sensor from CiS. . . . 101
5.76. A sensor edge profile analyzed using machine vision algorithms. . . . 102
5.77. Deviation of a measured edge along a single side of a sensor (left panel) and its distribution (right panel). 102
5.78. Illustration of the edge parallelism measurement principle. 103
5.79. Summary of the parallelism measured for available prototype sensors. Top panel shows the absolute values measured. Bottom panel shows the values normalized to the edge length expressed in microradians. . 104
5.80. A comparison of the sensor edges by their type and manufacturer. . 106
5.81. Sensor thickness **W** and distance to the top edge **D** measured using machine vision algorithms. 107
5.82. Summary of the thickness profiles measured for four prototype sensors which were presented in Fig. 5.80. 107
5.83. Summary of the sensor thickness measured with electrical characterization for the Hamamatsu sensors. Courtesy of Iaroslav Panasenko [79]. 108
5.84. Summary of the sensor warp measured along a single edge of four prototype sensors which were presented in Fig. 5.80. 109
5.85. Sensor thickness measurement principle based on the differential height measurement of a outermost sensor feature. Here the metal print with the pad number **P2** is used. 110
5.86. Sensor thickness obtained by autofocusing height measurements for the prototype silicon sensors from CiS (top panel) and Hamamatsu (bottom panel). 111
5.87. A schematical representation of the FairDB architecture [97]. 112
5.88. The FairDB integration into FairROOT [97]. 113
5.89. The concept of the FairDB versioning [97]. 114
5.90. The developed FairDB database schema for the data storage. 115
5.91. A photograph of a prototype sensor module [101]. 119
5.92. A principal scheme of the cable stack connected to the sensor [101]. . 119
5.93. A photograph of the polyimide meshed spacer with removable test structures [101]. 119
5.94. The original (left panel) and the processed images (right panel) of the cable with a broken trace. 121
5.95. Trace break detection by constraining the pixel color value. The left panel shows the saturation color plane extracted for the original picture. The right panel shows the pixel value histogram for the region of interest selected. 122

5.96. The original (left panel) and processed image (right panel) of the cable traces with thinnings. 122
5.97. Trace thinning detection by constraining the pixel color value. Left panel shows the contrast plane of the source image extracted. Right panel shows the pixel value histogram for the region of interest selected 123
5.98. The original and processed image of the cable traces lifted off (top panels) and a dust grain (bottom panels). 124
5.99. The original (left panel) and processed (right panel) image of the cable metal surface defects. 124
5.100. The microscope image taken of the same region of interest with low (left panel) and high (right panel) camera exposure. 125
5.101. A CAD view of the ladder assembly tool. The carbon fiber (CF) ladder frame (black color) is fixed on the holding and alignment structure (grey color). The silicon microstrip sensors (red color) are glued to the L-Legs previously glued to the CF frame. Image courtesy of O. Vasylyev, GSI [104]. 127
5.102. A macro photograph of the fiberglass L-Legs carrying the sensor (left panel) [105]. A CAD drawing of a L-Leg (right panel) [103]. 127
5.103. The ladder assembly tool integrated into optical inspection setup. . . 128
5.104. The spatial configuration of the sensors mounted on the ladder. The red arrows denote the readout plane orientation. 128
5.105. A sketch of sensor overlap. Top panel shows the overlap in the corner region in the sensor plane. Bottom panel shows the side view of the sensor spatial configuration out of the sensor plane. 129
5.106. The spatial configuration of the sensors mounted on the ladder relative to the mounting base plane. 130
5.107. Height map (warp) of the sensors on the ladder. 131
5.108. The graphical user interface of the optical inspection setup. 133
5.109. Configuration panels of the optical inspection graphical program. . . 134
5.110. Inspection overview program. 135
5.111. Interface for the region of interest preview. 136
5.112. Rolling shutter effects. From left to right: undistorted image, sudden start of motor movement, fly-by at a set speed, arrival moment. . . . 137

6.1. Schematic view of a cooling body (left panel) and cooling block (right panel). 139
6.2. Comparison of different coolants based on their volumetric heat transfer coefficient. The referenced models are described in [108] and [109]. Courtesy of [107]. 140
6.3. Phase diagram of carbon dioxide depicted in terms of pressure and temperature [113]. 141

6.4. Phase diagram of carbon dioxide depicted in terms of pressure and enthalpy. The graph is plotted with the equation of state implemented in this work (cf. section 6.1.4). 142
6.5. Flow pattern of a boiling liquid inside the tube in relation with the vapor quality [115]. 143
6.6. Different flow patterns found in the tubes during evaporative cooling [115]. 143
6.7. Comparison of various EOS in terms of calculated density [113]. . . . 146
6.8. Relative deviation of density calculated from EOS to experimental measurements from different datasets [121]. 147
6.9. Optimization of the tube diameter based on calculations of the temperature gradients and the volumetric heat transfer coefficient. The Thome model and CO_2 equation of state implemented in this work are used for the calculations. Both vertical axes have the same scale. 149
6.10. The flow pattern of a boiling liquid inside the tube in relation with vapor quality calculated from the Thome model and CO_2 equation of state implemented in this work. 150
6.11. The frictional pressure drop (top panel) and the heat transfer coefficient (bottom panel) of a two-phase carbon dioxide inside the cooling tube versus the vapor quality calculated from the Thome model and the CO_2 equation of state implemented in this work. 151
6.12. CAD drawing of the front-end electronics board as of April 2015 [134]. 153
6.13. FEM simulation result for 3 mm thick shelves, -40 °C coolant temperature and 140 Watts of heat power dissipated. 154
6.14. Input geometries for FEM simulations with normal AlN heat sink (left panel) and halved heat sink (right panel). Both panels show the exploded view of the front-end board — the AlN layer (gray color), the PCB with cut-outs (brown) and 8 ASICs (purple). 155
6.15. FEM simulation result for a reduced heat sink area, 140 Watts power dissipation and -40 °C cooling plate temperature. 156
6.16. Placement of components on the ROB together with the dissipated power. 156
6.17. ROB assembly to hold 10 boards on 1 mm thick shelves. 157
6.18. The cooling assembly, consisting of a FEB box with front-end board simulators and a cooling block. 159
6.19. A pair of front-end board simulators. 159
6.20. The thermodynamical process targeted by the cooling system. 160
6.21. A schematic of the open CO_2 cooling system. 160
6.22. The interior of the thermal insulation enclosure. 162
6.23. The flow paths inside a valve: straight flow path with possibility of liquid trapping (left panel) and intrinsically safe flow path (right panel) [138]. 163
6.24. Copper block assembly for on-tube temperature measurements. . . . 164

6.25. A closeup picture of the cooling assembly with temperature sensors connected. 165
6.26. Calibration curve for one of the temperature sensors. 166
6.27. Relative humidity dependence on the nitrogen flooding time. 168
6.28. The front panel of the setup control software. 169
6.29. Ice formation in the heat bath as a result of wrongly tuned system parameters. 170
6.30. The Armaflex insulating foam enclosure around the cooling assembly to reduce the influence of the convective and radiation heat losses. . 172
6.31. The STS half unit cooling plate. 173

7.1. The TRACI XL 1 kW cooling system [142]. 177
7.2. The thermodynamical process corresponding to the closed loop cooling system [142]. 178

H.1. Swagelok gaugeable tube fittings. Left panel shows the constituent components of a fitting. Right panel shows the assembled and swaged fitting in place [138]. 194
H.2. VCR metal gasket connection featuring from left to right: input piping branch to be butt welded to the VCR type gland with the male nut placed on it, a metal gasket (here with retainer), another gland with a female nut to be welded to the output piping branch [138]. . . 194

List of Tables

3.1. Specification summary of the silicon microstrip sensors used in the STS detector [36]. 21
3.2. Annealing time dependence from detector operation temperature . . 29

5.1. Summary for the dot array estimation for a 50 μm dot size and 100 μm dot spacing 49
5.2. Extracted motor stages' positioning errors. 65
5.3. Silicon sensors acceptance criteria 66
5.4. Fit parameters for Fig. 5.65 93
5.5. Overview and analysis of the data storage technologies 117
5.6. Microcable production yield by microcable type as is and with traces repaired [101]. 120
5.7. Information on the cable defects from the manual inspection enclosed in the package. 126
5.8. Summary of the information extracted from the sensor overlap. . . . 129
5.9. Summary of the angular misalignment of the sensors relative to each other. 130
5.10. The sensor cutting edge quality of the sensors on the ladder. 131

6.1. The minimum required list of thermodynamical parameters of the CO_2 which are calculated from the equation of state. 144
6.2. The thermodynamical parameters of the CO_2 which are extracted from the auxiliary equations and correlations. 148
6.3. Input parameters for the Thome model. 148
6.4. The maximum temperature simulated on the cooling assembly depending on the heat power load and cooling plate temperature. . . . 154
6.5. Maximum temperature simulated on the cooling assembly in dependence from heat power load and cooling plate temperature. 155
6.6. ROB component definitions. 157
6.7. FEM simulation results for a ROB assembly with various cooling plate temperature and shelve thickness. 157
6.8. Listing of the temperature sensors on the tubes with their positions. 165
6.9. Listing of the temperature sensors on the cooling assembly with their positions. 165
6.10. Listing of the pressure sensors with their positions. 167

6.11. Experimentally measured maximal temperature on the FEB box in dependence of power applied and shelf thickness 171
6.12. Experimentally measured maximal temperature on the FEB box in dependence of power applied and shelf thickness with the insulating box. 171

A.1. Optical setup hardware and equipment. 179

B.1. Architecture of the convolutional neural network used in this work for the defect context detection. 182

C.1. Maximum value of the sensor warp measured on both p- and n-sides of the prototype sensors. 183

D.1. Sensor thickness measured for CiS produced sensors. Nominal thickness is 285 ± 15 µm. 185
D.2. Sensor thickness measured for Hamamatsu produced sensors. Nominal thickness is 320 ± 15 µm. 186

E.1. Thermal properties of the materials used in FEM simulations. 187

F.1. List of equipment used in the cooling system and their characteristics. 189

G.1. Equipment read out and/or controlled by the acquisition software . . 191

I.1. Swagelok parts for cooling system 195

Bibliography

[1] W. Greiner, S. Schramm, and E. Stein, *Quantum chromodynamics*. Springer-Verlag Berlin Heidelberg, 3rd edition, 2007, http://dx.doi.org/10.1007/978-3-540-48535-3.

[2] K. G. Wilson, Confinement of Quarks, *Physical Review D*, 10(2445), 1974.

[3] D. J. Gross and F. Wilczek, Ultraviolet Behavior of Non-Abelian Gauge Theories, *Phys. Rev. Lett.*, 30:1343–1346, 1973, http://dx.doi.org/10.1103/PhysRevLett.30.1343.

[4] A. Bracco, G.-E. Körner, B. Krusche, et al., NuPECC Long Range Plan 2017 Perspectives in Nuclear Physics, Technical report, European Science Foundation, 2017, http://www.nupecc.org/lrp2016/Documents/lrp2017.pdf.

[5] G. Brianti, Large Hadron Collider in the LEP Tunnel: A Feasibility Study of Possible Options, *Conf. Proc. C*, 8405141(207), 1984.

[6] M. Harrison, T. Ludlam, and S. Ozaki, RHIC project overview, *Nuclear Instruments and Methods in Physics Research Section A: Accelerators, Spectrometers, Detectors and Associated Equipment*, 499(2-3), 2003.

[7] P. Senger, B. Friman, C. Höhne, et al., *The CBM Physics Book, Compressed Baryonic Matter in Laboratory Experiments*. Springer-Verlag Berlin Heidelberg, 2011, http://dx.doi.org/10.1007/978-3-642-13293-3.

[8] FAIR Baseline Technical Report, Executive Summary, Technical report, GSI, Darmstadt, 2006, http://www.fair-center.eu/fileadmin/fair/publications_FAIR/FAIR_BTR_1.pdf.

[9] P. Senger and V. Friese, Nuclear Matter Physics at SIS-100, Technical report, GSI, Darmstadt, 2012, http://www.fair-center.de/fileadmin/fair/experiments/CBM/documents/CBMatSIS100.pdf.

[10] *Experiments - The Four Pillars of Physics at FAIR*, http://www.fair-center.eu/for-users/experiments.html, retrieved February 2017.

[11] *The Compressed Baryonic Matter Experiment*, http://www.fair-center.eu/for-users/experiments/nuclear-matter-physics/cbm/introduction.html, retrieved February 2017.

[12] A. Malakhov et al., editors, *Technical Design Report for the CBM Superconducting Dipole Magnet*. GSI, Darmstadt, 2013.

[13] J. Heuser, W. Müller, V. Pugatch, et al., editors, *[GSI Report 2013-4] Technical Design Report for the CBM Silicon Tracking System (STS)*. GSI, Darmstadt, 2013, http://repository.gsi.de/record/54798.

[14] C. Höhne et al., editors, *Technical Design Report for the CBM Ring Imaging Cherenkov Detector (RICH)*. GSI, Darmstadt, 2013.

[15] S. Chattopadhyay et al., editors, *Technical Design Report for the CBM Muon Chambers (MuCh)*. GSI, Darmstadt, 2014.

[16] N. Herrmann et al., editors, *Technical Design Report for the CBM Time-of-Flight System (TOF)*. GSI, Darmstadt, 2014.

[17] F. Guber et al., editors, *Technical Design Report for the CBM Projectile spectator detector (PSD)*. GSI, Darmstadt, 2014.

[18] *HPC - High Performance Computing*, https://www.gsi.de/en/work/research/it/hpc.htm, retrieved February 2017.

[19] T. Ablyazimov et al., Challenges in QCD matter physics –The scientific programme of the Compressed Baryonic Matter experiment at FAIR, *The European Physical Journal A*, 53(3):60, 2017, http://dx.doi.org/10.1140/epja/i2017-12248-y.

[20] T. Ablyazimov et al., *Baryonic Matter at Nuclotron, Conceptual Design Report*. JINR, Dubna, 2012, http://nica.jinr.ru/files/BM@N/BMN_CDR.pdf.

[21] P. Salabura et al., HADES - a high acceptance di-electron spectrometer, *Nucl. Phys. B*, 44:705, 1995.

[22] I. Meshkov and A. Sidorin, editors, *Design and Construction of Nuclotron-based Ion Collider fAcility (NICA), Conceptual Design Report*. JINR, Dubna, 2008, http://nica.jinr.ru/files/NICA_CDR.pdf.

[23] C. Blume, Energy dependence of hadronic observables, *Journal of Physics G: Nuclear and Particle Physics*, 31(4):S57, 2005, http://stacks.iop.org/0954-3899/31/i=4/a=008.

[24] I. C. Arsene, L. V. Bravina, W. Cassing, et al., Dynamical phase trajectories for relativistic nuclear collisions, *Phys. Rev. C*, 75:034902, 2007, http://dx.doi.org/10.1103/PhysRevC.75.034902.

[25] A. Bzdak, V. Koch, and N. Strodthoff, Cumulants and correlation functions versus the QCD phase diagram, *Phys. Rev. C*, 95:054906, 2017, http://dx.doi.org/10.1103/PhysRevC.95.054906.

[26] J. Thäder, Higher Moments of Net-Particle Multiplicity Distributions, *Nuclear Physics A*, 956:320 – 323, 2016, the XXV International Conference on Ultrarelativistic Nucleus-Nucleus Collisions: Quark Matter 2015, http://dx.doi.org/10.1016/j.nuclphysa.2016.02.047.

[27] P. M. Hohler and R. Rapp, Is ρ-meson melting compatible with chiral restoration?, *Physics Letters B*, 731:103 – 109, 2014, http://dx.doi.org/10.1016/j.physletb.2014.02.021.

[28] R. Rapp and H. van Hees, Thermal dileptons as fireball thermometer and chronometer, *Physics Letters B*, 753:586 – 590, 2016, http://dx.doi.org/10.1016/j.physletb.2015.12.065.

[29] R. Rapp and J. Wambach, Low-mass dileptons at the CERN-SpS: evidence for chiral restoration?, *The European Physical Journal A - Hadrons and Nuclei*, 6(4):415–420, 1999, http://dx.doi.org/10.1007/s100500050364.

[30] A. Andronic, P. Braun-Munzinger, J. Stachel, et al., Production of light nuclei, hypernuclei and their antiparticles in relativistic nuclear collisions, *Physics Letters B*, 697(3):203 – 207, 2011, http://dx.doi.org/10.1016/j.physletb.2011.01.053.

[31] A. Adare, S. Afanasiev, C. Aidala, et al. (PHENIX), J/ψ Production versus Centrality, Transverse Momentum, and Rapidity in Au + Au Collisions at $\sqrt{s_{NN}} = 200$ GeV, *Phys. Rev. Lett.*, 98:232301, 2007, http://dx.doi.org/10.1103/PhysRevLett.98.232301.

[32] B. Abelev, J. Adam, D. Adamová, et al. (ALICE), J/ψ Suppression at Forward Rapidity in Pb-Pb Collisions at $\sqrt{s_{NN}} = 2.76$ TeV, *Phys. Rev. Lett.*, 109:072301, 2012, http://dx.doi.org/10.1103/PhysRevLett.109.072301.

[33] J. Heuser, Private communication, 2017.

[34] *CiS Forschungsinstitut für Mikrosensorik GmbH*, http://www.cismst.de/en/, retrieved February 2017.

[35] *Hamamatsu Photonics K.K.*, http://www.hamamatsu.com/eu/en/index.html, retrieved February 2017.

[36] O. Bertini, E. Friske, J. Heuser, et al., Specifications for Quality Assurance of Microstrip Sensors in the CBM Silicon Tracking System, Technical report, GSI, 2016.

[37] F. Hartmann, Silicon tracking detectors in high-energy physics, *Nuclear Instruments and Methods in Physics Research Section A: Accelerators, Spectrometers, Detectors and Associated Equipment*, 666:25 – 46, 2012, advanced Instrumentation, `http://dx.doi.org/10.1016/j.nima.2011.11.005`.

[38] S. Tavernier, *Experimental Techniques in Nuclear and Particle Physics*. Springer-Verlag Berlin Heidelberg, 1 edition, 2010.

[39] J. L. Beeby, The Density of Electrons in a Perfect or Imperfect Lattice, *Proceedings of the Royal Society of London A: Mathematical, Physical and Engineering Sciences*, 302(1468):113–136, 1967, `http://dx.doi.org/10.1098/rspa.1967.0230`.

[40] P. Lloyd and P. Smith, Multiple scattering theory in condensed materials, *Advances in Physics*, 21(89):69–142, 1972, `http://dx.doi.org/10.1080/00018737200101268`.

[41] R. Wunstorf, *Systematische Untersuchungen zur Strahlenresistenz von Silizium-Detektoren für die Verwendung in Hochenergiephysik-Experimenten*, PhD Thesis, Universität Hamburg, 1992.

[42] I. S. Esqueda, *Modeling of Total Ionizing Dose Effects in Advanced Complementary Metal-Oxide-Semiconductor Technologies*, PhD Thesis, Arizona State University, 2011.

[43] J. Frenkel, Über die Wärmebewegung in festen und flüssigen Körpern (About the thermal motion in solids and liquids), *Zeitschrift für Physik*, 35(8):652–669, 1926, `http://dx.doi.org/10.1007/BF01379812`.

[44] M. Moll, *Radiation damage in silicon particle detectors: microscopic defects and macroscopic properties*, PhD Thesis, Universität Hamburg, 1999.

[45] A. Affolder, Silicon Strip Detectors for the ATLAS HL-LHC Upgrade, *Physics Procedia*, 37:915 – 922, 2012, proceedings of the 2nd International Conference on Technology and Instrumentation in Particle Physics (TIPP 2011), `http://dx.doi.org/10.1016/j.phpro.2012.02.429`.

[46] J. Meese, Neutron Transmutation Doping in Semiconductors, *Proc. 2nd Int. Conf. Columbia, Missouri*, 1979.

[47] J. Guldberg, Neutron-Transmutation-Doped Silicon, *Proc. 3rd Int. Conf. Copenhagen*, 1981.

[48] V. Perevostchikov and V. Skoupov, *Gettering Defects in Semiconductors*. Advanced microelectronics. Springer, 2005.

[49] B. Hartiti, J. C. Muller, and P. Siffert, Defect generation and gettering during rapid thermal processing, *IEEE Transactions on Electron Devices*, 39(1):96–104, 1992, `http://dx.doi.org/10.1109/16.108217`.

[50] I. Panasenko, E. Lavrik, A. Lymanets, et al., A Custom Probe Station for Microstrip Detector Quality Assurance of the CBM Experiment, *Journal of Physics: Conference Series*, 742(1):012037, 2016, `http://stacks.iop.org/1742-6596/742/i=1/a=012037`.

[51] I. Panasenko, Private communication, 2017.

[52] *Systemdesignsoftware LabVIEW - National Instruments*, `http://www.ni.com/labview/`, retrieved August 2016.

[53] *NI Vision - Machine Vision for Any Application*, `http://www.ni.com/vision/`, retrieved August 2016.

[54] L. G. Shapiro and G. C. Stockman, *Computer Vision*. Pearson, 1st edition, 2011.

[55] J. Canny, A Computational Approach To Edge Detection, *IEEE Trans. Pattern Analysis and Machine Intelligence*, 8(6):678–698, 1986.

[56] R. Brunelli, *Template Matching Techniques in Computer Vision: Theory and Practice*. Wiley, 1st edition, 2009.

[57] S. Tanimoto and T. Pavlidis, A hierarchical data structure for picture processing, *Computer Graphics and Image Processing*, 4(2):104 – 119, 1975, `http://dx.doi.org/10.1016/S0146-664X(75)80003-7`.

[58] T. Chan and J. Shen, *Image Processing And Analysis: Variational, Pde, Wavelet, And Stochastic Methods*. Society for Industrial and Applied Mathematic, 1st edition, 2005.

[59] R. Haralick and L. Shapiro, *Computer and Robot Vision*, volume 1. Addison-Wesley Publishing Company, Inc., 2002.

[60] R. C. Gonzalez and R. E. Woods, *Thresholding. Digital Image Processing*. Pearson Education, 2nd edition, 2003.

[61] M. Sezgin and B. Sankur, Survey over image thresholding techniques and quantitative performance evaluation, *Journal of Electronic Imaging*, 13(1):146–168, 2004, `http://dx.doi.org/10.1117/1.1631315`.

[62] L. Devroye and G. T. Toussaint, A note on linear expected time algorithms for finding convex hulls, *Computing*, 26(4):361–366, 1981, http://dx.doi.org/10.1007/BF02237955.

[63] F. P. Preparata and M. I. Shamos. *Convex Hulls: Basic Algorithms*, pages 95–149. Springer New York, New York, NY, 1985. http://dx.doi.org/10.1007/978-1-4612-1098-6_3.

[64] C. W. Piper, *A first book of the lens : an elementary treatise on the action and use of the photographic lens*. Hazell, Watson and Viney London, 1901.

[65] C. W. Piper, *The Optics of Photography and Photographic Lenses*. Whittaker & Co, 1892.

[66] A. E. Conrady, Decentred Lens-Systems, *Monthly notices of the Royal Astronomical Society*, 79:384–390, 1919.

[67] D. C. Brown, Decentering distortion of lenses, *Photogrammetric Engineering*, 32:444–462, 1966.

[68] Y. Zheng, S. Lin, C. Kambhamettu, et al., Single-Image Vignetting Correction, *IEEE Trans. Pattern Anal. Mach. Intell.*, 31(12):2243–2256, 2009, http://dx.doi.org/10.1109/TPAMI.2008.263.

[69] P. B. Catrysse, X. Liu, and A. El Gamal, QE reduction due to pixel vignetting in CMOS image sensors, *Proc. SPIE*, 3965:420–430, 2000, http://dx.doi.org/10.1117/12.385460.

[70] W. Niblack, *An Introduction to Digital Image Processing*. Prentice-Hall International Inc., 1986.

[71] J. Sauvola and M. Pietikäinen, Adaptive document image binarization, *Pattern Recognition*, 33(2):225 – 236, 2000, http://dx.doi.org/10.1016/S0031-3203(99)00055-2.

[72] W. C. Porter, B. Kopp, J. C. Dunlap, et al., Dark current measurements in a CMOS imager, *Proceedings of SPIE - The International Society for Optical Engineering*, 6816, 2008, http://dx.doi.org/10.1117/12.769079.

[73] R. Widenhorn, M. M. Blouke, A. Weber, et al., Temperature dependence of dark current in a CCD, *Proceedings of SPIE - The International Society for Optical Engineering*, 4669:193–201, 2002.

[74] *Mitutoyo Measuring Instruments*, http://www.mitutoyo.co.jp/eng/, retrieved February 2017.

[75] R. Brun and F. Rademakers, ROOT - An object oriented data analysis framework, *Nuclear Instruments and Methods in Physics Research Section A: Accelerators, Spectrometers, Detectors and Associated Equipment*, 389(1):81 – 86, 1997, new Computing Techniques in Physics Research V, `http://dx.doi.org/10.1016/S0168-9002(97)00048-X`.

[76] *MIGRAD algorithm description at TMinuit Class Reference*, `https://root.cern.ch/doc/master/classTMinuit.html`, retrieved August 2016.

[77] F. James and M. Roos, Minuit - a system for function minimization and analysis of the parameter errors and correlations, *Computer Physics Communications*, 10(6):343 – 367, 1975, `http://dx.doi.org/10.1016/0010-4655(75)90039-9`.

[78] G. Baumann, D. Boeni, L. Buchmann, et al., Quality assurance of 100 CMS-OB2 sensors for LHCb Trigger Tracker, Technical report, CERN, 2004.

[79] I. Panasenko, *Development of electrical quality assurance methods for the silicon sensors of the STS detector*, PhD Thesis in preparation, Universität Tübingen, 2017.

[80] Y. Jia, E. Shelhamer, J. Donahue, et al., Caffe: Convolutional Architecture for Fast Feature Embedding, 2014, arXiv:1408.5093.

[81] *TensorFlow, An open-source software library for Machine Intelligence*, `https://www.tensorflow.org`, retrieved February 2017.

[82] *mxnet, A Flexible and Efficient Library for Deep Learning*, `http://mxnet.io`, retrieved February 2017.

[83] L.-G. Pang, K. Zhou, N. Su, et al., An EoS-meter of QCD transition from deep learning, 2017, arXiv:1612.04262.

[84] Y. Rath, *Search for Top Quark Pair Associated Higgs Bosons Decaying into Bottom Quarks Using Deep Neural Networks with the CMS Experiment*, Master Thesis, Rheinisch-Westfälische Technische Hochschule Aachen, 2016.

[85] T. Fuchs, Development of a Machine Learning Based Analysis Chain for the Measurement of Atmospheric Muon Spectra with IceCube, 2017, arXiv:1701.04067.

[86] J. Redmon and A. Farhadi, YOLO9000: Better, Faster, Stronger, 2016, arXiv:1612.08242.

[87] S. Ren, K. He, R. Girshick, et al., Faster R-CNN: Towards Real-Time Object Detection with Region Proposal Networks, 2016, arXiv:1506.01497v3.

[88] C. M. Bishop, *Pattern Recognition and Machine Learning.* Information science and statistics. Springer, 1st ed. 2006. corr. 2nd printing edition, 2006.

[89] *CUDA, NVIDIA Accelerated Computing*, https://developer.nvidia.com/cuda-zone, retrieved February 2017.

[90] R. Girshick, Fast R-CNN, 2015, arXiv:1504.08083v2.

[91] *Navitar Imaging and Projection Optics*, https://navitar.com, retrieved February 2017.

[92] M. Heideman, D. Johnson, and C. Burrus, Gauss and the history of the fast fourier transform, *IEEE ASSP Magazine*, 1(4):14–21, 1984, http://dx.doi.org/10.1109/MASSP.1984.1162257.

[93] L. Johnson, S. Kotz, and N. Balakrishnan, *Continuous Univariate Distributions*, volume 1. Wiley, 1994.

[94] K. Levenberg, A Method for the Solution of Certain Non-Linear Problems in Least Squares, *Quarterly of Applied Mathematics*, 2:164–168, 1944.

[95] D. Marquardt, An Algorithm for Least-Squares Estimation of Nonlinear Parameters, *SIAM Journal on Applied Mathematics*, 11:431–441, 1963, http://dx.doi.org/10.1137/0111030.

[96] *Stealth Dicing Technology and Applications, Technical Information, Hamamatsu Photonics K.K., Mar. 2005*, http://www.hamamatsu.com/resources/pdf/etd/SD_tech_TLAS9004E.pdf, retrieved February 2017.

[97] D. Bertini, FairROOT Virtual Database, User Manual, Technical report, GSI Helmholtzzentrum für Schwerionenforschung GmbH, 2013, https://cbm-wiki.gsi.de/foswiki/pub/STS/STSComponentsDatabase/FairDB_Manual.pdf.

[98] *FairDB Object Relational Mapping library*, https://github.com/denisbertini/dbase, retrieved February 2017.

[99] *The FairRoot framework*, https://fairroot.gsi.de, retrieved February 2017.

[100] H. Goeringer, gStore: GSI Archive Storage System, User Manual, Technical report, GSI Helmholtzzentrum für Schwerionenforschung GmbH, 2015.

[101] C. J. Schmidt, Private communication, 2016.

[102] *LED Technologies of Ukraine, Ltd.*, http://ltu.ua/en/, retrieved February 2017.

[103] O. Chikalov, V. Elsha, A. Sheremetev, et al., On the positioning of the L-legs on the CBM/BM@N STS DSSDs, Internal note, Technical report, JINR, 2017.

[104] O. Vasylyev, Private communication, 2016.

[105] U. Frankenfeld, Private communication, 2017.

[106] B. Verlaat, CO_2 cooling for the LHCb-VELO experiment at CERN, *Proceedings of the 8th IIF/IIR Gustav Lorentzen Conference on Natural Working Fluids*, 2008.

[107] B. Verlaat and J. Noite, Design considerations of long length evaporative CO_2 cooling lines, *Proceedings of the 10th IIR Gustav Lorentzen Conference on Natural Working Fluids*, 2012.

[108] S. Kandlikar, A general correlation for saturated two-phase flow boiling heat transfer inside horizontal and vertical tubes, *Journal of Heat and Mass Transfer*, 112:219–228, 1990.

[109] L. Friedel, Improved friction drop correlations for horizontal and vertical two-phase pipe flow, *European Two-phase Flow Group Meeting, Paper E2, Ispra, Italy*, 1979.

[110] L. Cheng, G. Ribatski, J. M. Quibén, et al., New prediction methods for CO_2 evaporation inside tubes: Part I - A two-phase flow pattern map and a flow pattern based phenomenological model for two-phase flow frictional pressure drops, *International Journal of Heat and Mass Transfer*, 51(1-2):111 – 124, 2008, http://dx.doi.org/10.1016/j.ijheatmasstransfer.2007.04.002.

[111] L. Cheng, G. Ribatski, J. M. Quibén, et al., Erratum to 'New prediction methods for CO_2 evaporation inside tubes: Part I - A two-phase flow pattern map and a flow pattern based phenomenological model for two-phase flow frictional pressure drops' [Int. J. Heat Mass Transfer 51 (1-2) (2008) 111-124], *International Journal of Heat and Mass Transfer*, 55(19-20):5378 –, 2012, http://dx.doi.org/10.1016/j.ijheatmasstransfer.2012.05.044.

[112] L. Cheng, G. Ribatski, and J. R. Thome, New prediction methods for CO_2 evaporation inside tubes: Part II - An updated general flow boiling heat transfer model based on flow patterns, *International Journal of Heat and Mass Transfer*, 51(1-2):125 – 135, 2008, http://dx.doi.org/10.1016/j.ijheatmasstransfer.2007.04.001.

[113] N. Böttcher, J. Taron, O. Kolditz, et al., Evaluation of thermal equations of state for CO_2 in numerical simulations, *Environmental Earth Sciences*, 67(2):481–495, 2012, http://dx.doi.org/10.1007/s12665-012-1704-1.

[114] M. W. Zemansky, *Heat and Thermodynamics*. McGraw-Hill, 5th edition, 1968.

[115] A. Bejan and A. D. Kraus, *Heat Transfer Handbook*. Wiley-Interscience, 1st edition, 2003.

[116] J. D. van der Waals, *Over de Continuiteit van den Gas- en Vloeistoftoestand*, PhD Thesis, Hoogeschool te Leiden, 1873.

[117] O. Redlich and J. N. S. Kwong, On the Thermodynamics of Solutions. V. An Equation of State. Fugacities of Gaseous Solutions., *Chemical Reviews*, 44(1):233–244, 1949, http://dx.doi.org/10.1021/cr60137a013.

[118] G. Soave, Equilibrium constants from a modified Redlich-Kwong equation of state, *Chemical Engineering Science*, 27(6):1197 – 1203, 1972, http://dx.doi.org/10.1016/0009-2509(72)80096-4.

[119] K. Pitzer, Corresponding States for Perfect Liquids, *J. Chem. Phys.*, 7:583–590, 1939.

[120] H. Goldstein, *Classical Mechanics*. Addison-Wesley, 2nd edition, 1980.

[121] R. Span, *Multiparameter Equations of State*. Springer-Verlag Berlin Heidelberg, 1st edition, 2000.

[122] R. Span and W. Wagner, A New Equation of State for Carbon Dioxide Covering the Fluid Region from the Triple-Point Temperature to 1100 K at Pressures up to 800 MPa, *Journal of Physical and Chemical Reference Data*, 25(6):1509–1596, 1996, http://dx.doi.org/10.1063/1.555991.

[123] J.-L. Chabert, *A History of Algorithms: From the Pebble to the Microchip*. Springer, 1999.

[124] W. C. Davidon, Variable Metric Method for Minimization, *SIAM Journal on Optimization*, 1(1):1–17, 1991, http://dx.doi.org/10.1137/0801001.

[125] V. Vesovic, W. A. Wakeham, G. A. Olchowy, et al., The Transport Properties of Carbon Dioxide, *Journal of Physical and Chemical Reference Data*, 19(3):763–808, 1990, http://dx.doi.org/10.1063/1.555875.

[126] V. Vesovic, A. Fenghour, and W. A. Wakeham, The Viscosity of Carbon Dioxide, *Journal of Physical and Chemical Reference Data*, 27(1):31–44, 1998, http://dx.doi.org/10.1063/1.556013.

[127] J. Luettmer-Strathmann, J. V. Sengers, and G. A. Olchowy, Non-asymptotic critical behavior of the transport properties of fluids, *The Journal of Chemical Physics*, 103(17):7482–7501, 1995, http://dx.doi.org/10.1063/1.470718.

[128] J. R. Brock and R. B. Bird, Surface tension and the principle of corresponding states, *AIChE Journal*, 1(2):174–177, 1955, http://dx.doi.org/10.1002/aic.690010208.

[129] P. Jianxin and L. Yigang, Estimation of the surface tension of liquid carbon dioxide, *Physics and Chemistry of Liquids*, 47(3):267–273, 2009, http://dx.doi.org/10.1080/00319100701824389.

[130] R. Span, G. Scalabrin, P. Marchi, et al., A Reference Multiparameter Thermal Conductivity Equation for Carbon Dioxide with an Optimized Functional Form, *Journal of Physical and Chemical Reference Data*, 35(4):1549–1575, 2006, http://dx.doi.org/10.1063/1.2213631.

[131] First Sensor AG, *Mass flow versus volumetric flow*, https://www.first-sensor.com/cms/upload/appnotes/AN_Massflow_E_11153.pdf, retrieved February 2017.

[132] *3D CAD Design Software - SOLIDWORKS*, https://solidworks.com, retrieved November 2016.

[133] *AutoCAD For Mac and Windows | CAD Software | Autodesk*, http://www.autodesk.com/products/autocad/overview, retrieved November 2016.

[134] J. Lehnert, Private communication, 2015.

[135] G. Hemink, *CO_2 Cooling Studies for the ATLAS Upgrade*, Master Thesis, University of Twente/NIKHEF, 2010.

[136] M. G. Marzoa, *Innovative low-mass cooling systems for the ALICE ITS Upgrade detector at CERN*, PhD Thesis, École Polytechnique Fédérale de Lausanne, 2016.

[137] A. Frankenberger, *Development of an Open CO_2 Cooling System for Belle II*, Master Thesis, University of Wien, 2013.

[138] *Swagelok - Product Catalog*, https://www.swagelok.com/en/Resources/Product-Catalog, retrieved November 2016.

[139] Armacell LLC, *Armacell LLC Web Page*, http://www.armacell.us/home/, retrieved February 2017.

[140] B. Verlaat, TRACI, a multipurpose CO_2 cooling system for R&D, *Proceedings of the 10th IIF/IIR Gustav Lorentzen Conference on Natural Working Fluids*, 2012.

[141] B. Verlaat, 2PACL: controlling a two-phase CO_2 loop using at two-phase accumulator, *Proceedings of the 22nd International Congress of Refrigeration*, 2007.

[142] J. S. Rosado, Private communication, 2016.

[143] M. Lin, Q. Chen, and S. Yan, Network In Network, 2014, arXiv:1312.4400v3.

Acknowledgements

I would like to thank Prof. Dr. Hans Rudolf Schmidt for the exciting opportunity to work in such an interesting and challenging field of research and be able to participate in many projects around the central detector of the CBM experiment — the Silicon Tracking System. Working in his group gave me better understanding of the high-energy physics field and many insights into the ALICE and RHIC experiments.

Furthermore, I want to thank Prof. Dr. Josef Jochum for his supervision and mentoring of my work from the particle physics point of view.

I would like to express my deep and sincere thanks to PD Dr. habil. Roland Speith for his technical support of my work. We have had many technical discussions and have ruled out a plentiful of difficulties allowing to establish the well functioning laboratory environments.

I greatly appreciate the opportunity to participate in the Helmholtz Graduate School for Hadron and Ion Research (HGS-HIRe). The access to the soft-skill courses, lecture and power-weeks gave me the confidence and expertise in the research field.

I express my deep gratitude to Dr. Anton Lymanets for his supervision of the early stages of my work. We have implemented many brilliant technical ideas while establishing the cooling and optical inspection setups. His deep knowledge of the electronics and read-out chains have sped up the development dramatically.

I owe many special thanks to Iaroslav Panasenko for sharing his expertise on technical details of silicon sensors. The electrical characterization data he shared with me allowed me to further improve the defect detection methods.

For many insights into the field of particle physics and into the WASA experiment at COSY facility I would like to thank Prof. Dr. Heinz Clement, Dr. habil. Mikhail Bashkanov and Dr. Tatiana Skorodko.

Many thanks are addressed to my colleagues from GSI for the fruitful discussions and their ideas on how to improve and extend the quality assurance and metrology methods I have implemented in this work.

I thank the colleagues from the fine mechanical workshop for their technical help in realization of the cooling setup.

Special thanks to Dr. Maksym Zyzak, Dr. Martin Völkl, Dr. Denis Bertini, Dr. Vladimir Lavrik, Iaroslav Panasenko and Tina Schlosser for their proofreading of this work and many helpful comments.

This work is dedicated to my family who supported and encouraged me at all times.